



**HAL**  
open science

# Study of the single electron charge signals in the XENON100 direct Dark Matter search experiment

M. Le Calloch

► **To cite this version:**

M. Le Calloch. Study of the single electron charge signals in the XENON100 direct Dark Matter search experiment. Physics [physics]. Université de Nantes, 2014. English. NNT: . tel-01081007

**HAL Id: tel-01081007**

**<https://theses.hal.science/tel-01081007>**

Submitted on 6 Nov 2014

**HAL** is a multi-disciplinary open access archive for the deposit and dissemination of scientific research documents, whether they are published or not. The documents may come from teaching and research institutions in France or abroad, or from public or private research centers.

L'archive ouverte pluridisciplinaire **HAL**, est destinée au dépôt et à la diffusion de documents scientifiques de niveau recherche, publiés ou non, émanant des établissements d'enseignement et de recherche français ou étrangers, des laboratoires publics ou privés.

UNIVERSITÉ DE NANTES  
FACULTÉ DES SCIENCES ET TECHNIQUES

ÉCOLE DOCTORALE  
MATÉRIAUX, MATIÈRE ET MOLÉCULE DES PAYS DE LA LOIRE

Année : 2014

N° attribué par la bibliothèque

|  |  |  |  |  |  |  |  |  |  |
|--|--|--|--|--|--|--|--|--|--|
|  |  |  |  |  |  |  |  |  |  |
|--|--|--|--|--|--|--|--|--|--|

# Study of the single electron charge signals in the XENON100 direct Dark Matter search experiment

THÈSE DE DOCTORAT

Discipline : Physique

Spécialité : Physique des Particules

*Présentée et soutenue publiquement par*

**Maxime Le Calloch**

*Le 7 octobre 2014, devant le jury ci-dessous*

*Président* M. Stavros Katsanevas, *Professeur, Université de Paris Diderot*  
*Rapporteurs :* M. Daniel Lellouch, *Senior Staff Scientist, Weizmann Institute of Science*  
Mme Sylvie Rosier-Lees, *Directrice de Recherche, CNRS*  
*Examineurs :* M. Thierry Gousset, *Professeur, Université de Nantes*  
M. Stavros Katsanevas, *Professeur, Université de Paris Diderot*  
M. Luca Scotto Lavina, *Chargé de Recherche, CNRS*  
M. Dominique Thers, *Maître-assistant, École des Mines de Nantes*

*Directeur de thèse :* M. Thierry Gousset, *Professeur, Université de Nantes*  
*Co-encadrant :* M. Luca Scotto Lavina, *Chargé de Recherche, CNRS*



*A mes parents,  
pour leur indéfectible soutien.*



# Contents

|  |          |
|--|----------|
| <b>I English part</b>  | <b>1</b> |
| <b>Introduction</b>  | <b>3</b> |
| <b>1 A universe between light and darkness</b>                             | <b>7</b> |
| Introduction . . . . .   | 7        |
| 1.1 First indications of hidden matter . . . . .                           | 8        |
| 1.1.1 F. Zwicky and the Coma cluster . . . . .                             | 8        |
| 1.1.2 Anomalies in galaxies rotation curves . . . . .                      | 9        |
| 1.2 Cosmological Standard Model and dark matter . . . . .                  | 10       |
| 1.2.1 Short reminder on General Relativity and Cosmological Standard Model | 11       |
| 1.2.1.1 Few words of History . . . . .                                     | 11       |
| 1.2.1.2 Lorentz's transformations . . . . .                                | 12       |
| 1.2.1.3 From Special Relativity to General Relativity . . . . .            | 14       |
| 1.2.2 Einstein's field equation . . . . .                                  | 16       |
| 1.2.3 Friedmann equations . . . . .  | 18       |
| 1.3 Evidences for dark matter presence . . . . .                           | 20       |
| 1.3.1 Type Ia supernovae . . . . .   | 20       |
| 1.3.1.1 Stress energy-momentum tensor $T^{\mu\nu}$ . . . . .               | 21       |
| 1.3.1.2 Radiation-domination and matter-domination eras . . . . .          | 22       |
| 1.3.1.3 Cosmological parameters and the redshift . . . . .                 | 23       |
| 1.3.1.4 From supernovae to cosmological parameters . . . . .               | 25       |
| 1.3.2 Galaxies rotation curves . . . . .                                   | 26       |
| 1.3.3 Galaxies clusters . . . . .  | 28       |
| 1.3.4 Primordial nucleosynthesis . . . . .                                 | 29       |
| 1.3.5 Baryonic acoustic oscillations in primordial plasma . . . . .        | 30       |
| 1.3.6 Cosmic microwave background . . . . .                                | 30       |
| 1.3.7 Structure simulations . . . . .                                      | 33       |
| 1.4 Dark matter candidates . . . . .                                       | 35       |
| 1.4.1 Baryonic dark matter . . . . .                                       | 35       |
| 1.4.2 Non-baryonic dark matter . . . . .                                   | 35       |
| 1.4.2.1 Hot dark matter . . . . .  | 35       |
| 1.4.2.2 Cold dark matter . . . . .   | 36       |
| 1.5 Detection channels . . . . .   | 41       |

|          |   |           |
|----------|---|-----------|
| 1.5.1    | Supersymmetric particles production in particules colliders . . . . . | 41        |
| 1.5.2    | Dark matter indirect detection . . . . .                              | 41        |
| 1.5.3    | Dark matter direct detection . . . . .                                | 43        |
| 1.6      | Direct dark matter experiments . . . . .                              | 46        |
| 1.6.1    | Directional detection . . . . .                                       | 46        |
| 1.6.2    | Bubble chambers . . . . .   | 47        |
| 1.6.3    | Annual interaction rate modulation . . . . .                          | 47        |
| 1.6.4    | Cryogenic detectors . . . . .   | 48        |
| 1.6.4.1  | Cryogenic semiconductor bolometers . . . . .                          | 49        |
| 1.6.4.2  | Cryogenic scintillating bolometers . . . . .                          | 50        |
| 1.6.5    | Noble gas detectors . . . . .   | 51        |
| 1.6.5.1  | Argon dark matter detectors . . . . .                                 | 51        |
| 1.6.5.2  | Xenon single phase detectors . . . . .                                | 52        |
|          | Conclusion . . . . .  | 53        |
| <b>2</b> | <b>The XENON experiment</b>   | <b>55</b> |
|          | Introduction . . . . .  | 55        |
| 2.1      | General principle . . . . .   | 56        |
| 2.2      | Interaction of radiation with noble gas . . . . .                     | 57        |
| 2.2.1    | Photoelectric effect . . . . .  | 58        |
| 2.2.2    | Compton scattering . . . . .  | 59        |
| 2.2.3    | Liquid xenon as a detector . . . . .                                  | 59        |
| 2.3      | From Interaction to light signals . . . . .                           | 61        |
| 2.3.1    | Stopping power in liquid xenon . . . . .                              | 61        |
| 2.3.1.1  | Electronic recoils . . . . .  | 61        |
| 2.3.1.2  | Nuclear recoils . . . . .   | 63        |
| 2.3.2    | Charge separation under electric field . . . . .                      | 66        |
| 2.3.3    | Scintillation and ionization signals . . . . .                        | 69        |
| 2.3.3.1  | Scintillation signal . . . . .  | 69        |
| 2.3.3.2  | Ionization . . . . .  | 70        |
| 2.4      | Detailed description of the XENON detector . . . . .                  | 72        |
| 2.4.1    | Drift field . . . . .   | 72        |
| 2.4.1.1  | Drift of the electronic cloud . . . . .                               | 73        |
| 2.4.1.2  | Ionization signal . . . . .   | 75        |
| 2.4.1.3  | Drift fields during science runs . . . . .                            | 75        |
| 2.4.2    | Photomultipliers tubes . . . . .                                      | 76        |
| 2.4.3    | External shielding . . . . .  | 78        |
| 2.4.4    | The xenon cryogenics . . . . .  | 80        |
| 2.4.5    | Gas system . . . . .  | 81        |
| 2.4.6    | Trigger and data acquisition . . . . .                                | 83        |
| 2.5      | Detector calibrations . . . . .                                       | 85        |
| 2.5.1    | First science run . . . . .   | 85        |

|          |   |            |
|----------|---|------------|
| 2.5.2    | Second science run . . . . .                                      | 86         |
| 2.5.3    | Third science run . . . . .                                       | 87         |
| 2.5.4    | Additional detector calibration for R&D . . . . .                 | 87         |
|          | Conclusion . . . . .  | 88         |
| <b>3</b> | <b>Direct dark matter search with the XENON100 experiment</b>     | <b>89</b>  |
|          | Introduction . . . . .  | 89         |
| 3.1      | From light signals to physical quantities . . . . .               | 90         |
| 3.1.1    | Charge and light signals correction . . . . .                     | 90         |
| 3.1.1.1  | S1 light signal correction . . . . .                              | 90         |
| 3.1.1.2  | S2 light signal correction . . . . .                              | 92         |
| 3.1.2    | Estimation of the energy deposit . . . . .                        | 94         |
| 3.1.2.1  | Deposited energy in combined energy scale . . . . .               | 95         |
| 3.1.2.2  | Deposited energy in nuclear recoil energy scale . . . . .         | 96         |
| 3.1.3    | Example of an interaction signal . . . . .                        | 98         |
| 3.1.4    | Nuclear and electronic recoils discrimination . . . . .           | 98         |
| 3.2      | Expected background . . . . .                                     | 99         |
| 3.2.1    | The radon background . . . . .                                    | 100        |
| 3.2.2    | The krypton background . . . . .                                  | 100        |
| 3.3      | Data analysis . . . . .   | 101        |
| 3.3.1    | Dark matter data blinding strategy . . . . .                      | 101        |
| 3.3.2    | Data selection cuts . . . . .                                     | 102        |
| 3.3.3    | Statistical methods . . . . .                                     | 105        |
| 3.3.3.1  | Profile likelihood analysis . . . . .                             | 105        |
| 3.3.3.2  | Analysis with benchmarked signal region . . . . .                 | 106        |
| 3.4      | Limits on WIMP interaction cross section . . . . .                | 107        |
| 3.4.1    | Spin-independent scattering . . . . .                             | 108        |
| 3.4.2    | Spin-dependent scattering . . . . .                               | 110        |
| 3.5      | Search for axions . . . . .                                       | 111        |
| 3.6      | Towards next detector generation . . . . .                        | 115        |
|          | Conclusion . . . . .  | 116        |
| <b>4</b> | <b>Single electrons charge signals</b>                            | <b>117</b> |
|          | Introduction . . . . .  | 117        |
| 4.1      | Single electrons charge signal description . . . . .              | 118        |
| 4.1.1    | Single electron and signal electrons emission processes . . . . . | 118        |
| 4.1.2    | Previous studies . . . . .  | 120        |
| 4.1.3    | Time features . . . . .   | 120        |
| 4.1.4    | Low energy S2 signals . . . . .                                   | 123        |
| 4.2      | Properties of single electrons signals . . . . .                  | 125        |
| 4.2.1    | Rates . . . . .   | 125        |
| 4.2.2    | Time distribution . . . . .                                       | 127        |

|              |   |            |
|--------------|---|------------|
| 4.2.3        | Example of a three electrons S2 signal . . . . .                                  | 129        |
| 4.3          | Low energy S2 spectrum analysis . . . . .   | 130        |
| 4.3.1        | Parametrisation . . . . .   | 130        |
| 4.3.2        | Primary selection cuts . . . . .  | 132        |
| 4.3.3        | Potential fit biases . . . . .  | 134        |
| 4.4          | Study of secondary scintillation gain . . . . .                                   | 137        |
| 4.4.1        | Dependency on single electron depth emission . . . . .                            | 137        |
| 4.4.2        | Dependency on single electron radial location emission . . . . .                  | 139        |
| 4.4.3        | Influence on the number of S2 signals per waveform . . . . .                      | 142        |
| 4.5          | Systematic effects in the determination of the gain . . . . .                     | 146        |
| 4.5.1        | Notations and conventions . . . . .   | 147        |
| 4.5.2        | Consistency check of the model . . . . .  | 148        |
| 4.5.3        | Consistency between constrained and unconstrained fits . . . . .                  | 150        |
| 4.5.4        | Fit stability against number of Gaussian distributions . . . . .                  | 152        |
| 4.5.5        | Fit stability against intensity threshold description . . . . .                   | 154        |
| 4.5.6        | Correlation between the parameters of the fit . . . . .                           | 157        |
| 4.5.7        | Dependency on the initial values of the parameters of the fit . . . . .           | 158        |
| 4.5.8        | Fit stability against lower boundary of the energy range . . . . .                | 158        |
| 4.5.9        | Fit stability against upper boundary of the energy range . . . . .                | 160        |
| 4.5.10       | Fit stability against main S2 signal intensity threshold . . . . .                | 161        |
| Conclusion   | . . . . .   | 161        |
| <b>5</b>     | <b>Secondary scintillation gain of single electron signals</b>                    | <b>163</b> |
| Introduction | . . . . .   | 163        |
| 5.1          | Time stability . . . . .  | 164        |
| 5.2          | Dependency on the calibration source . . . . .                                    | 167        |
| 5.3          | Single electrons signals occurring between the main S1 and S2 signals . . . . .   | 170        |
| 5.4          | Dependency on the electric field . . . . .  | 174        |
| 5.4.1        | Field calculation . . . . .   | 175        |
| 5.4.2        | Measurement of the dependency . . . . .   | 177        |
| 5.4.3        | A dedicated single electron calibration run . . . . .                             | 180        |
| 5.5          | S2 signal repartition over top and bottom PMTs arrays . . . . .                   | 183        |
| 5.5.1        | Data selection . . . . .  | 184        |
| 5.5.2        | Results and stability checks . . . . .  | 185        |
| 5.6          | Outcome of the analysis: electrons extraction yield . . . . .                     | 187        |
| 5.7          | Outcome of the analysis: from S1 and S2 to drifting electrons and emitted photons | 193        |
| 5.8          | Applications and perspectives . . . . .   | 195        |
| 5.8.1        | Detector detector settings optimisation . . . . .                                 | 195        |
| 5.8.2        | Multiple scattering rejections . . . . .  | 197        |
| 5.8.3        | An homogeneously distributed source of events for light correction . . . . .      | 197        |
| 5.8.4        | Charge signal modelling simulation . . . . .                                      | 198        |
| 5.8.5        | Single electrons signals for background estimation . . . . .                      | 199        |

---

|          |  |            |
|----------|--|------------|
| 5.8.6    | A S2-only analysis for Low-mass WIMP . . . . .                             | 201        |
| 5.8.7    | Application to the detection of coherent neutrino-nucleus scattering . . . | 202        |
|          | Conclusion . . . . .   | 203        |
|          | <b>Conclusion</b>  | <b>205</b> |
|          | <b>II Partie Française</b>   | <b>209</b> |
| <b>6</b> | <b>Analyse des signaux d'électrons uniques dans l'expérience XENON100</b>  | <b>211</b> |
|          | Introduction . . . . .   | 211        |
| 6.1      | Le détecteur XENON100 . . . . .  | 212        |
| 6.2      | La recherche des WIMP avec XENON100 . . . . .                              | 214        |
| 6.3      | Signaux de charge d'électron uniques . . . . .                             | 216        |
| 6.3.1    | Origines des signaux de charge d'électron uniques . . . . .                | 216        |
| 6.3.2    | Caractérisation des signaux de charge d'électron uniques . . . . .         | 217        |
|          | Conclusion . . . . .   | 219        |
|          | <b>List of Figures</b>   | <b>221</b> |
|          | <b>List of Tables</b>  | <b>227</b> |
|          | <b>Bibliography</b>  | <b>229</b> |
|          | <b>Remerciements / Acknowledgments</b>                                     | <b>243</b> |



# **Part I**

## **English part**



# Introduction

The present document details the thesis work performed at the Subatech laboratory during three consecutive years. It has been achieved under the scientific advices of Dr. Luca Scotto Lavina and the supervision of Prof. Thierry Gousset, in strong contact with the XENON Collaboration. The subject treated here refers to the single electron charge signals observed by the XENON100 detector, whose main goal is the direct search of dark matter. In order to fully understand this subject, it is needed to start from the end of the title, thanks to an introduction of the dark matter hypothesis and its search through the direct channel.

Planets, stars, galaxies, black holes... This is usually what people know about the Universe components. However, since the first part of the twentieth century, many astronomical and cosmological observations have indicated that an invisible mass is missing to allow the description of their dynamics. Because of its non-luminous property, this hidden mass is usually called *dark matter*. Since it has not yet been discovered and must still be present 14 billion years after the Big Bang, dark matter is usually assumed to have a very low probability of interaction with regular matter and with itself.

This additional component of the Universe is also in very good agreement with the Cosmological Standard Model, which aims at describing the Universe's evolution from the Big bang up to nowadays. Some recent measurements of the Cosmological Microwave Background (CMB) made by the Planck satellite have established the contribution of dark matter to the total energetic budget of the Universe to be of the order of 27 %. The matter that is known would represent about only 5 %. The remaining part would thus belong to another undetected quantity, the dark energy, that would be responsible for the Universe expansion.

Among all the candidates commonly used to describe the dark matter, the most favourite one has the generic name of Weakly Interacting Massive Particle (*WIMP*). Their detection could be performed through different channels, by using either their production at collider experiments, or their annihilation products, but also by using the scattering of WIMPs from the Universe inside a target material. The description of the dark matter hypothesis, from evidences, models and candidates up to a review of detection technique and direct dark matter search experiments will be done in the first chapter.

In this context, the XENON program is a phased approach project which aims to achieve the direct detection of WIMPs by using a cylindrical dual-phase time projection chamber (*TPC*) of ultra-pure liquid xenon (*LXe*) used as both target and detection medium, surmounted by a gaseous

xenon phase ( $GXe$ ). Due to the expected low interaction rate of dark matter particles, this design enables thus to combine the high stopping power of liquid xenon and its low intrinsic radioactivity with the high reconstruction power of TPCs for the position of scatterings, in order to reach a very high sensitivity to rare events thanks to an efficient background rejection. Moreover, using xenon as target medium allows to take benefits of its high atomic mass  $A$  to which the WIMP-nucleus scattering cross-section is proportional.

An interaction within the active volume of the detector induces the recoil of the encountered particle that creates ionization electrons and prompt scintillation photons. A part of the released electrons escapes to recombination and drifts towards the gas phase thanks to a constant electric field. Close to the interface, electrons are accelerated by a stronger field and extracted into the gaseous phase, where they generate proportional scintillation photons. The photon emission in liquid phase is called the *scintillation signal* ( $S1$ ), while the photon emission in the gas phase is called the *ionisation signal* ( $S2$ ). Both of them are detected by two PhotoMultiplier Tubes (PMT) arrays placed at the top and the bottom of the TPC.

The current phase of the XENON program is the XENON100 detector. The presentation of this detector and the strategies developed by the XENON Collaboration for background rejection will be detailed in the second chapter. It also includes the description of the physical processes that lead to the emission of the two detectable light and charge signals.

XENON100 has been taking data at the Gran Sasso underground National Laboratory (LNGS), in Italy, since 2008. The design of this experiment has made XENON100 the most sensitive detector for WIMP-nucleus coupling from Spring 2011 up to Autumn 2013, when LUX, another detector based of the same technology but with a larger sensitive mass, has provided slightly better limits. As a complement, details on the procedure used for the calibrations of the detector response to both nuclear and electronic recoils during each of the dark matter search periods are also given.

The third chapter gives then an explanation of the different intensities of each signal for either nuclear recoils ( $NR$ ) induced by WIMPS or background neutrons off nuclei, or for electronic recoils ( $ER$ ) induced by the scattering of background  $\gamma$  rays and  $\beta$  particles off electrons from xenon atoms. It also presents the establishment of the quality cuts developed from calibration data and used for the search of dark matter. This is also followed by details on the calculation of the sensitivity limits provided by XENON100. It concerns not only the WIMP-nucleus coupling, which does not depend on the spin of the particle encountered by the WIMP, called *Spin Independent* analysis ( $SI$ ), but it concerns also the coupling of WIMPs with either the protons or the neutrons of the nucleus, and thus depending on the spin of the nucleon. This analysis is then called *Spin Dependent* analysis ( $SD$ ). In addition, very recent results on the search of axions and axion-like particles ( $ALP$ ), another well motivated cold dark matter candidate, performed with the XENON100 experiment is also presented.

The results presented in this third chapter are mainly focused on the second science run achieved by the detector, since it corresponds to the most sensitive one, and since the data acquired during the third science run have not been released yet. At the time of writing, the results provided by XENON100 for WIMP-neutron coupling and axions search are the most sensitive one.

As it will be seen all along these three first chapters, the dark matter search requests an accurate

knowledge of the experimental background due to the expected low scattering rate. Moreover, a full understanding of the two detectable signals is also mandatory, especially for the search of low-mass WIMPs performed with the S2 signal only, or in order to be able to combine data acquired during different science runs, and for which different running conditions could have been set. As a result, even the tiniest signals identified on the recorded waveforms need to be understood.

In this context, the very low energy part of the spectrum of S2 signals is investigated. It corresponds thus to a region below 150 photoelectrons detected by PMTs. In this domain of the S2 spectrum, several structures appear regularly, and belong to the distribution of S2 signals emitted by one up to about five electrons extracted in time coincidence in the gas phase. Each of these electrons is released by the photoelectric effect of ultraviolet photons – coming mainly from the S2 signal but also from S1 signal in lower proportions – over electrons of xenon atoms in liquid phase. The method and data selection cuts developed during this thesis in order to determine the average S2 signal induced by each of these groups of few electrons are thus presented in the fourth chapter. It also includes a description of the contribution of each identified source of systematical error to the total error associated to these average values.

Thanks to this full understanding of the systematical errors, all the data acquired during each science run can be combined in order to reduce the statistical error. The latest chapter gives thus with a very high precision the average value of the S2 signal induced by a single electron drifting in the gaseous phase for each of the three science runs performed by XENON100. This average S2 signal at low energy is also named the *secondary scintillation gain* in this thesis. Such an analysis exhibits the stability of the detector response for low energy charge signals for a long time period of stable running conditions.

In addition, the evolution of the secondary scintillation gain as a function of the electric field in the gas phase is also presented, including the analysis of data from a dedicated calibration campaign. These results have been also used for analysing the evolution of the electron extraction yield from the liquid to the gas phase as a function of the electric field. This study is an opportunity to perform the measurement the average energy *W-value* needed for a recoiling particle to produce an electron-ion pair. Such a measurement is in very good agreement with previous published measurements and has been obtained with a higher precision thanks to lower systematical effects.

The last section of this fifth chapter presents then a list of several applications of the single electron charge signals, among which are the optimisation of the detector running conditions, an application to Monte Carlo simulations for charge signal estimation, and some applications to dark matter analysis such as mentioned above.

The XENON100 experiment is almost over. The latest data that are currently taken are only used to perform R&D in view of the next step of the XENON program, the XENON1T detector. For this new experiment, the background exposition is expected to be reduced by a factor 100 with respect to XENON100. It will thus allow to explore a wide signal region predicted by theoretical model. Thanks to this higher sensitivity, some new regions at low-mass WIMP could be also investigated. For this purpose, a very good knowledge of the charge signal is mandatory, especially for signals at very low energy such as those induced by a cloud of very few electrons, and for which single electrons signals such as studied in this thesis can be a source of background. It is then needed to fully understand all low energy charge signals, and to be able to clearly identify those

that are produced by few individuals single electron signals occurring in time coincidence. For this purpose the work presented in this document will thus help to this understanding, identification and rejection.

In agreement with the rules of the University of Nantes, this thesis is written in English. It also contains a short summary of few pages written in French in the second part of this document.

# Chapter 1

## A universe between light and darkness

In this first chapter will be discussed all the aspects of the dark matter hypothesis. The several evidences that have indicated up to date the presence of dark matter in the Universe's content are firstly reviewed, including an introduction to the metric and equations that rule the Universe. The main possibles candidates that could describe dark matter are then described, and by focusing on the WIMPs candidates, the different way to detect them are approached. More details are then given for the direct detection channel, with a short description of most of the corresponding experiments.

### Contents

---

|  |           |
|--|-----------|
| <b>Introduction</b> . . . . .                                    | <b>7</b>  |
| <b>1.1 First indications of hidden matter</b> . . . . .          | <b>8</b>  |
| <b>1.2 Cosmological Standard Model and dark matter</b> . . . . . | <b>10</b> |
| <b>1.3 Evidences for dark matter presence</b> . . . . .          | <b>20</b> |
| <b>1.4 Dark matter candidates</b> . . . . .                      | <b>35</b> |
| <b>1.5 Detection channels</b> . . . . .                          | <b>41</b> |
| <b>1.6 Direct dark matter experiments</b> . . . . .              | <b>46</b> |
| <b>Conclusion</b> . . . . .                                      | <b>53</b> |

---

### Introduction

Dark matter is assumed to be a non-luminous component of the Universe that would represent more than a quarter of its total energy. However, the nature of this element is still unknown and many efforts are made to discover it. In the present chapter will be discussed all the aspects of the dark matter hypothesis, from observable evidences up to the description of the experiments built for its detection.

The presentation starts first by a brief review of the historical observations that have led to the development of the missing mass concept, nowadays known as *dark matter*. The metric and equations that rule the Universe will be then introduced, followed by a complete review of all the

observables that indicate dark matter existence. Thanks to this latter, an identity card of the best dark matter candidate can be drawn.

In a second time, a review of the several historical main candidates that have been tested as dark matter candidates will be made. It will be then seen that the most favourite one up to date, the *Weakly Interacting Massive Particles (WIMP)*, are also the candidates that follow the best constraints drawn from dark matter evidences.

The different channels investigated for the dark matter detection will be then introduced, with more details given on direct detection principle. For this latter, a review of the different main experiments will be made, excluding experiments that use liquid xenon in dual phase time projection chamber, since this will be more deeply detailed in the second chapter.

## 1.1 First indications of hidden matter

The dark matter search is an old quest, that took its roots in the first part of the twentieth century, in parallel to the development of the Cosmological Standard Model. In the present section will be redrawn all the main historical steps that have led to the establishment of the dark matter theory.

### 1.1.1 F. Zwicky and the Coma cluster

The first time the concept of dark matter was highlighted was at the beginning of the 1930's. At that time, a Swiss astronomer, Fritz Zwicky, started to study the well known galaxy cluster in the Coma Berenice constellation, with the aim to determine the mass of each galaxy using the velocity dispersion [1]. He used then the virial theorem that links together kinetic energy  $E_c = Mv^2/2$  and potential energy  $E_p = -M^2G/2R$ :

$$2E_c + E_p = 0 \tag{1.1}$$

where  $M$  corresponds to the mass of the considered galaxy,  $v$  corresponds to its dispersion velocity respect to the others,  $R$  is the radius at which the velocity dispersion is measured, and  $G$  is the gravitational constant.

Zwicky compared then the masses deduced in this way to the ones deduced from luminosity. He has found thus that the mass of the whole cluster deduced from velocity was more than 400 times bigger than the mass obtained from luminosity. Nowadays, thanks to more accurate knowledges and measurements, this value has been lowered to few tens, but the consequence remains valid: there is matter that can not be detected by light. In order to explain it, Zwicky introduced several hypothesis, like a possible different behaviour of the stars in the Coma cluster than in the Milky Way. And among all of them, he proposed then the possibility to have some non-luminous matter to describe the missing mass, and that he called dark matter (*dunkle Materie* in the original paper).

Since then, the same phenomenon was confirmed for many galaxy clusters, confirming that this was not a localized anomaly. However, at the time Zwicky has presented his results, his

conclusions and hypothesis did not convinced the scientific community, partially because of measurement uncertainties that have led to several criticism against his results.

Few years later, in 1936, an American astronomer Sinclair Smith presented the same analysis with the Virgo cluster [2], and found a dynamic mass about 200 times bigger than Hubble's estimation from luminosity of an average mass of a nebula<sup>1</sup> [3]. Referring to Zwicky's analysis of the Coma cluster, Smith postulated intergalactic material (called *internebulular* material), either uniformly distributed or in the form of clouds of low luminosity surrounding the galaxies to explain this distribution, supposing that both analyses of the Virgo mass were correct.

At that time, the scientific community also thought in majority that huge structures like galaxies clusters were rather temporary than stable, and for them such discrepancies was a good argument to confirm galaxies clusters as a temporary behaviour. As a consequence, the dark matter case was closed and fell into oblivion for the next decades. It was only in the 1970's that dark matter came back on stage, this time at the galaxy's scale, thanks to several analysis on the galaxies rotation curves, as it is reported in the next section.

### 1.1.2 Anomalies in galaxies rotation curves

Before jumping to the 1970's, it is necessary to stay more longer in the 1930's. At that time, an American astronomer, Horace Babcock reported in 1939 during his Ph.D. thesis that the mass over light ratio in the Andromeda galaxy increased as a function of the radial position from the center [4]. He suggested then that this could be explained either by light absorption in the galaxy or by modified gravity, and never referred to non-luminous matter. His analysis however highlighted for the first time a strange behaviour in the relationships between mass and light at the galactic scale.

Twenty years later, Louise Volders, a Dutch astronomer, presented her results on the study of the evolution of the stars velocity as a function of the galactic center in the M33 and M101 galaxies [5]. As expected according to the Newtonian mechanic and the Kepler laws, the stars velocity profile  $v(r)$  as a function of the galactic center, called *galaxy rotation curve*, should decrease according to:

$$v(r) = \sqrt{\frac{GM(r)}{r}} \quad (1.2)$$

where  $M(r)$  is the mass of the part of the galaxy inside the radius  $r$ , as it is the case for the planets in our solar system, or also for the moons rotating around our giant planets. However, she noticed that the rotation curves did not followed the expected trend, as it was also noticed by her colleague Jan Oort in 1940 for the velocities of stars in the neighbourhood of the Sun [6]. Then, with the improvement of telescopes and observations techniques, the 1970's brought some complements and suggestions to those observations.

At that period, the American astronomer Vera Rubin, started also to study the velocity of stars in spiral galaxies. She first began with Andromeda galaxy [7], where she noticed that stars velocities were higher than expected. She co-published then several papers on this topic dur-

---

<sup>1</sup>Virgo galaxies were identified only few years earlier as galaxies beyond the Milky Way, and not nebulae

ing the decade, like in 1978 where she investigated the possibility to have massive dark halo of non-luminous material around the galaxy up to high radius [8], as it was suggested by different independent numerical analysis in the previous years, like in [9]. Her results showed then that the galaxies rotation curves of high-luminosity spherical galaxies were almost flat at high radii, or at least much higher than the expected trend, such as in Figure 1.1(a). However, she concluded that this did not allowed to confirm the absolute necessity to add non-luminous massive halo to describe the galaxies rotation curves.

A later analysis that she co-published in 1980, on the analysis of a set of 21 galaxies selected for their very large ranges of luminosity and radii [10] has then confirmed the lack of matter to describe the observed galaxies rotation curves:

*"The conclusion is inescapable that the non-luminous matter exists beyond the optical galaxy."*

The year after, in 1981, Albert Bosma, presented is own analysis of galaxy rotation curve in NGC3198 [11]. By using a dark matter halo for the reproduction of the rotation curve, he found a very good agreement between observed velocities and fit function, as illustrated by Figure 1.1(b).

This figure corresponds to one of the early success of the dark halo. Starting from that point, the dark matter became one of the hottest topics of research in physics, with many other indications on its presence and abundance that were discovered in the following years, as it is detailed in the next section. As a complement, a recent analysis of the dark matter halo around the Milky Way [12] illustrates also very well the success of the dark halo model.

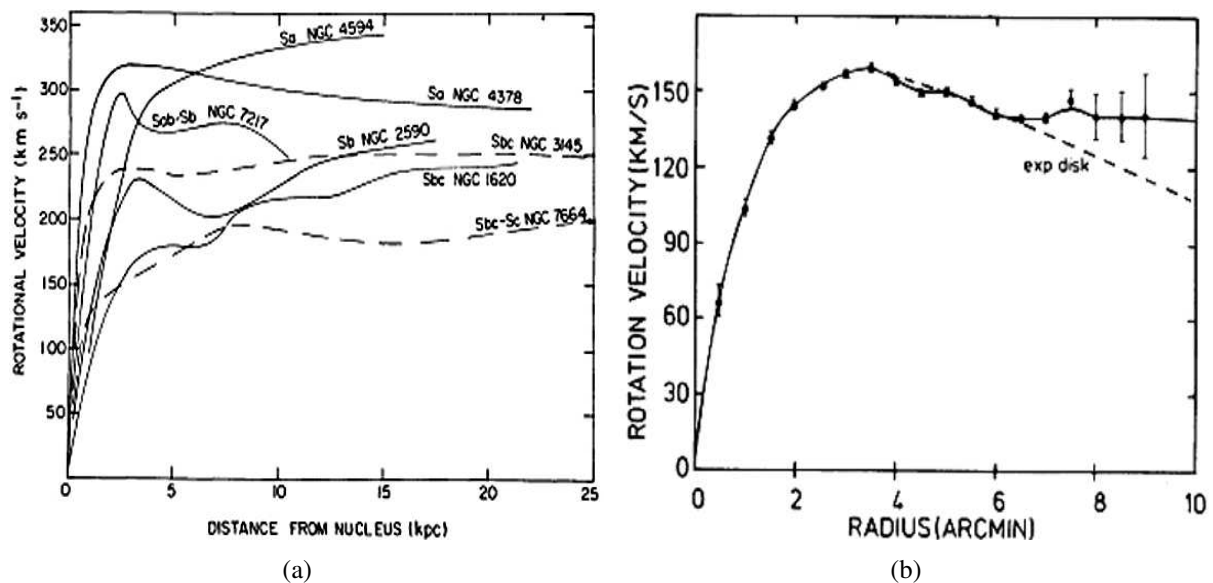


Figure 1.1: (a) Several galaxies rotation curves from [8], (b) Galaxies rotation curves fit using dark matter halo compared to expected trend from keplerian laws (dashed line), from [11].

## 1.2 Cosmological Standard Model and dark matter

Thanks to these two indications of non-luminous missing mass described in the previous section, the concept of dark matter was born. However, if it was the observation of the Universe

that has induced this concept, it could be asked whether it was in good agreement with the model that explains the evolution of the Universe. This latter, developed in the first part of the twentieth century, is called *Cosmological Standard Model*, and worked with a very good success up to that point.

As a result, the contribution of dark matter to the Universe composition according to this Cosmological Standard Model will be presented in this section. For this purpose, two preliminary steps will be first reminded. The first one consists in the demonstration of the need to add a temporal coordinate to each object. The purpose of this new coordinate is to always allow their description when they are in movement with respect to a reference frame, whatever are their velocities in this frame.

The second one consists then in an introduction to the General Relativity, thanks to position equations that include this additional coordinate. This step will thus present the modification of trajectories due to gravitation. The equations of the evolution of the Universe, and the description of its different components could be then developed starting from this introduction to the General Relativity.

## 1.2.1 Short reminder on General Relativity and Cosmological Standard Model

The Cosmological Standard Model has been built by using the General Relativity. However, this latter has the aim of studying time-space, where the time is inextricably linked to the space. As a result, the present section develops first the mechanisms that have led to add this fourth coordinate, and then introduces the mathematics that rule General Relativity.

### 1.2.1.1 Few words of History

Since the Cosmological Standard Model was born in the beginning of the twentieth century, it is needed to start by going earlier in time to understand its development. Thus, in the middle of the nineteenth century, a well known physicist, the Scottish James Maxwell, developed his famous equations that allow to describe the behaviour of electromagnetic waves while they are travelling, and that has shown that they were travelling at light velocity.

These laws were one of the greatest success of physics at that time, since it worked perfectly for many applications like with Hertz antennas. However, the only one type of reference frame known at that time were Galilean's reference frames, in which those laws were not invariant by reference frame transformation, such as the one illustrated the next section. More especially, according to the Newtonian mechanic that rules this reference frames' family, the light velocity does not remain constant. This phenomenon was then a huge problem for the understanding of the Universe. In order to solve it, three hypothesis were suggested:

1. Maxwell's equations were wrong
2. There was a way to conciliate the Galilean's reference frame and Maxwell laws: space was filled by *aether*

3. Galilean's reference frame and Newtonian mechanic were not always true, and a more extendible theory is needed

As said before, the Maxwell's equations were successfully confirmed by experimental observations, so the first hypothesis could not be right. The second one was also excluded by the different experiments of interferometry made by Michelson and Morley in the 1880's, and that have shown that velocity at light scale were not addable. It has also demonstrated that aether did not exist since there was no perceptible "wind" of aether due to the motion of the Earth around the sun. This leads to the last hypothesis.

### 1.2.1.2 Lorentz's transformations

In 1904, the Dutch physicist Hendrick Lorentz rewrote the transformation of coordinates for reference frame transformation, previously expressed for Galilean's reference frames by adding a time dilation. The present section shows then the main steps needed to move from Galilean's transformations to Lorentz's transformations. The aim of this part is to illustrate the need to add a fourth coordinate to describe each object in the Universe. The developments presented here are inspired from [13].

Two different reference frames,  $R = \{t, x, y, z\}$  and  $R' = \{t', x', y', z'\}$  are considered here. They are defined such that  $R'$  is in translation along the  $x$  axis, toward high  $x$  values with velocity  $\vec{v}$ . Each axis of the two reference frame that are respectively parallels. At  $t = t' = 0$ , both reference frame origins are mixed. This situation is illustrated with Figure 1.2.

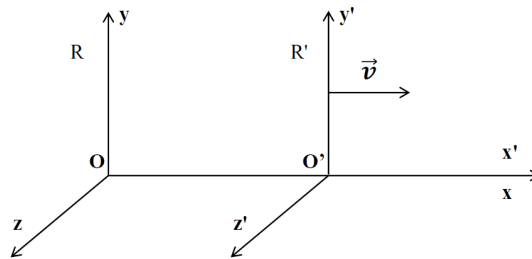


Figure 1.2: Example of two reference frames linked together by Lorentz's transformations

Galilean reference frames follows the transformations 1.3, that are always true for  $v \ll c$ :

$$t' = t, x' = x - vt, y' = y, z' = z \quad (1.3)$$

If it is assumed that there is a pointlike light source in  $O$ , the origin of the reference frame  $R$ , that emits light at  $t = 0$ , then at a time  $t$ , the sphere that contains all the light has a radius:

$$r = \sqrt{x^2 + y^2 + z^2} = ct \quad (1.4)$$

where  $x$ ,  $y$ , and  $z$  are the coordinates at the time  $t$  of a photon emitted at the time  $t = 0$  in the reference frame  $R$ . This is illustrated by the sphere in Section 1.2.1.3.

The same sphere in the reference frames  $R'$  defined previously has then the following radius:

$$r' = \sqrt{x'^2 + y'^2 + z'^2} = ct' \quad (1.5)$$

It can be then noticed that  $c$  is not written as  $c'$  since it should be the same quantity whatever the considered reference frame is. The following relationships for the transformations from  $R'$  to  $R$  can be then defined:

$$t = t(x', y', z', t'), \quad x = x(x', y', z', t'), \quad y = y(x', y', z', t'), \quad z = z(x', y', z', t') \quad (1.6)$$

They will be calculated later in this section. For the sphere example, these relationships are however defined such as Equations 1.4 and 1.5 are equivalent, leading to:

$$c^2t^2 - x^2 - y^2 - z^2 = c^2t'^2 - x'^2 - y'^2 - z'^2 \quad (1.7)$$

Since one of the easiest transformations is considered here, as represented in Figure 1.2, only two coordinates will change ( $x$  and  $t$  here). The formula 1.7 could be then simplified as follows:

$$c^2t^2 - x^2 = c^2t'^2 - x'^2 \quad (1.8)$$

In Galilean reference frame, it has been seen in relations 1.3 how the general relationships 1.6 could be expressed. By analogy and by including a modification on the time coordinate as expressed in 1.8, a linear relationships with constant coefficients between the two concerned coordinates can be also applied:

$$ct = Act' + Bx', \quad x = Cct' + Dx', \quad y = y', \quad z = z' \quad (1.9)$$

where, according to 1.8:

$$A^2 - C^2 = 1, \quad B^2 - D^2 = -1, \quad AB - CD = 0 \quad (1.10)$$

This system can be solved by using this solution:

$$A = \cosh(\theta), \quad B = \sinh(\phi), \quad C = \sinh(\theta), \quad D = \cosh(\phi) \quad (1.11)$$

where  $\theta$  and  $\phi$  are two numbers. The last equation in relation 1.10 implies that  $\sinh(\theta - \phi) = 0$ , which is only possible if  $\theta = \phi$ .

At each time, the origin  $O' = (ct', 0, 0, 0)$  of the reference frame  $R'$  has the coordinates  $(ct, vt, 0, 0)$  in  $R$ . So, according to the Relationships 1.9 and 1.10:

$$ct = \cosh(\theta)ct' + \sinh(\theta) \times 0, vt = \sinh(\theta)ct' + \cosh(\theta) \times 0 \quad (1.12)$$

This leads to:

$$\beta = \frac{v}{c} = \tanh(\theta), \cosh(\theta) = \frac{1}{\sqrt{1 - \frac{v^2}{c^2}}} = \gamma, \sinh(\theta) = \frac{\frac{v}{c}}{\sqrt{1 - \frac{v^2}{c^2}}} \quad (1.13)$$

where the two parameters  $\beta$  and  $\gamma$  are the *Lorentz parameters*.

The relations 1.9 can be thus rewritten in a simplest way, that is called *Lorentz's transformations* and where the time dilation appears:

$$ct = \gamma(ct' + \beta x'), x = \gamma(x' + \beta ct'), y = y', z = z' \quad (1.14)$$

While these relationships correspond to simplest case of transformation between  $R$  and  $R'$ , there are always possibilities for more complicated transformations to reach similar relationships by following the same development. Moreover, they can always describe each object, whatever is the velocity of  $R'$  compared to  $R$ . These mathematics that include time dilation are at the base of the *Special Relativity* and *General Relativity* developed by Albert Einstein in 1905 and 1915. They are both approached in the next section.

### 1.2.1.3 From Special Relativity to General Relativity

In the previous section were presented the way to translate an event in one frame to another one that is in motion compared to the first one. This kind of analysis has led Einstein to make two postulates to define the *Special Relativity*:

1. The physical laws that are true in one frame are always true in whatever else frame.
2. The light velocity is always independent from the movement state of its source

In other words, the first postulate says that the only one motion that can be measured is a relative motion from one object to another one. This is what the *relativity* means. Then, the second one means that, as illustrated in the previous section, the time is not an absolute quantity, but a quantity that belongs to the concerned frame.

As a consequence, Einstein defined the infinitesimal difference  $ds$  between two infinitely close objects  $(t, x, y, z)$  and  $(t + dt, x + dx, y + dy, z + dz)$  in the space-time frame:

$$ds^2 = c^2 dt^2 - (dx^2 + dy^2 + dz^2), = c^2 dt^2 - dl^2 \quad (1.15)$$

As said above, this relation is true for two infinitely close objects, and this represents the *Special Relativity*. Now, in order to enlarge this definition to the entire Universe for the *General*

*Relativity*, it is needed to take into account the gravity that creates curvature in the space-time frame at larger scale.

For introducing the notion of curvature, the frame that will be used consists in a 2-dimensional surface of a sphere, such as shown in Figure 1.3. The developments presented below are inspired from [14–16].

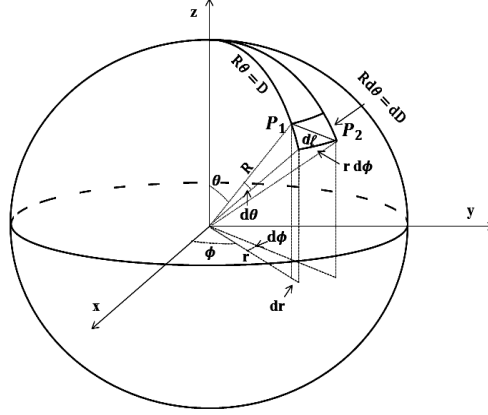


Figure 1.3: Distance  $dl$  as measured for the surface of a sphere.

$D = \theta R$  is then the distance along the sphere of radius  $R$  between the object  $P_1$  and the North pole. If a second object  $P_2$  is infinitely close to  $P_1$ , then the distance  $dl$  between them along the sphere is:

$$dl^2 = (dD)^2 + (rd\phi)^2, = (rd\theta)^2 + (rd\phi)^2 \quad (1.16)$$

And  $r = R\sin(\theta)$ , meaning that  $dr = R\cos(\theta)d\theta$ . Thus:

$$Rd\theta = \frac{dr}{\cos(\theta)} = \frac{Rdr}{\sqrt{R^2 - r^2}} = \frac{dr}{\sqrt{1 - \frac{r^2}{R^2}}} \quad (1.17)$$

Equation 1.16 could be then rewritten as:

$$dl^2 = \left( \frac{dr}{\sqrt{1 - \frac{r^2}{R^2}}} \right)^2 + (rd\phi)^2 = \left( \frac{dr}{\sqrt{1 - Kr^2}} \right)^2 + (rd\phi)^2 \quad (1.18)$$

where  $K = 1/R^2$  is the curvature associated to the considered 2-dimensional elementary surface defined between  $P_1$  and  $P_2$ . Because of the homogeneity of the geometry, this curvature is always there and constant whatever are the locations of the  $P_1$  and  $P_2$  objects on the same sphere.

The formula 1.18 defined for a 2-dimensional elementary surface of a 3-dimensional volume defined in  $\mathcal{R}^3 = \{x, y, z\}$  space can be then extended to a 3-dimensional elementary volume of a

4-dimensional hypervolume defined in  $\mathcal{R}^4 = \{t, x, y, z\}$  space by doing the extension from polar coordinate to spherical coordinate:

$$dl^2 = \left( \frac{dr}{\sqrt{1-Kr^2}} \right)^2 + (rd\theta)^2 + (r\sin(\theta)d\phi)^2 \quad (1.19)$$

where the parameter  $r$  corresponds to the 3-dimensional extension of the 2-dimensional radial distance from the origin that is defined in Figure 1.16. In the same way, the parameter  $K$  corresponds to the curvature of each considered 3-dimensional elementary volume. As for  $\mathcal{R}^3$  space,  $K$  is valid and constant everywhere in the space-time frame. This is the cosmological principle:

*The Universe is spatially homogeneous and isotropic*

This result can be now injected into the Equation 1.15 by following the convention  $c = 1$ :

$$ds^2 = (dt)^2 - \left( \frac{dr}{\sqrt{1-Kr^2}} \right)^2 + (rd\theta)^2 + (r\sin(\theta)d\phi)^2 \quad (1.20)$$

The remaining step is then to express this relationship in terms of the dimensionless scale factor,  $a(t) = r(t)/\rho$ , where  $\rho$  is the comoving coordinate that follows a given object as the Universe expands, and  $t$  is a universal time that measures the time spent since the Big Bang. Then, because of the expansion of the Universe that modifies all its geometrical properties, including also the curvature, the time-independent parameter  $\kappa = K(t)a^2(t)$  for the expression of the curvature is introduced. The final relationship is thus:

$$ds^2 = (dt)^2 - a^2(t) \left[ \left( \frac{d\rho}{\sqrt{1-\kappa\rho^2}} \right)^2 + (\rho d\theta)^2 + (\rho \sin(\theta) d\phi)^2 \right] \quad (1.21)$$

This relationship is known in its full name as the *Friedmann-Lemaître-Robertson-Walker* metric (FLRW). The constant  $\kappa$  describes the general shape of the Universe:

- $\kappa = -1$  : The Universe is *open*, with a saddle shape, and will expand forever.
- $\kappa = 0$  : The Universe is *flat*, and its expansion will slow down.
- $\kappa = 1$  : The Universe is *closed*, with a spherical shape, and will expand up to the point where gravitational attraction will overcome the expansion, leading to a collapse of the Universe, that is sometimes known as the *Big Crunch* in opposition to the Big Bang.

## 1.2.2 Einstein's field equation

By starting from the equation 1.21, the developments presented here aim to show the different contribution to the Universe composition, among which the dark matter contribution can be clearly identified. These developments are inspired from [14–20].

The relation 1.21 can be also expressed in another way<sup>2</sup>:

$$ds^2 = g_{\alpha\beta} dx^\alpha dx^\beta \quad (1.22)$$

where  $g_{\alpha\beta}$  is the *metric tensor* that includes gravitation, and  $x^\alpha$  is the quadrivector associated to an object, with the time as its first coordinate.

In General Relativity, the trajectory in space-time frame of an object without any interaction except gravity is called a *geodesic*, and is ruled by the following law:

$$\frac{d^2 x^\alpha}{ds^2} + \Gamma_{\beta\gamma}^\alpha \frac{dx^\beta}{ds} \frac{dx^\gamma}{ds} = 0 \quad (1.23)$$

where the  $\Gamma_{\beta\gamma}^\alpha$  are the Christoffel symbols that are mathematical tools used for the change of a metric and defined as follows:

$$\Gamma_{\beta\gamma}^\alpha = \frac{1}{2} g^{\alpha\rho} (g_{\rho\beta,\gamma} + g_{\rho\gamma,\beta} - g_{\beta\gamma,\rho}) \quad (1.24)$$

The comma used in the expression of the metric tensor is a simple way to express derivation:  $g_{\rho\beta,\gamma} = \partial_\gamma g_{\rho\beta}$ . In General relativity, the curvature of the space-time is represented through the Riemann-Christoffel tensor:

$$R_{\alpha\beta\gamma\delta} = \frac{1}{2} (-g_{\beta\gamma,\alpha\delta} - g_{\alpha\delta,\beta\gamma} + g_{\beta\delta,\alpha\gamma} + g_{\alpha\gamma,\beta\delta}) + g_{\mu\nu} (-\Gamma_{\alpha\delta}^\mu \Gamma_{\beta\gamma}^\nu + \Gamma_{\alpha\gamma}^\mu \Gamma_{\beta\delta}^\nu) \quad (1.25)$$

with:

$$R_{titi} = \frac{\ddot{a}}{a} g_{ii} \quad \text{and} \quad R_{ijij} = \left( \left( \frac{\dot{a}}{a} \right)^2 + \frac{\kappa}{a^2} \right) g_{ii} g_{jj}, \quad i, j = r, \theta, \phi \quad (1.26)$$

The trace associated to this tensor is called *Ricci tensor*:

$$R_{\alpha\beta} = R_{\alpha\mu\beta}^\mu = -\Gamma_{\alpha\beta,\rho}^\rho + \Gamma_{\alpha\rho,\beta}^\rho - \Gamma_{\gamma\rho}^\rho \Gamma_{\alpha\beta}^\gamma + \Gamma_{\beta\gamma}^\rho \Gamma_{\alpha\rho}^\gamma \quad (1.27)$$

with:

$$R_{tt} = 3 \frac{\ddot{a}}{a} \quad \text{and} \quad R_{ii} = \left( \frac{\ddot{a}}{a} + 2 \frac{\dot{a}^2 + \kappa}{a^2} \right) g_{ii}, \quad i, j = r, \theta, \phi \quad (1.28)$$

Again, the trace associated to this last tensor is called Ricci scalar:

---

<sup>2</sup>The summation over all index is implicit

$$R = g^{\alpha\beta} R_{\alpha\beta} = R_{\alpha}^{\alpha} = 6 \frac{\ddot{a}}{a} + 6 \frac{\dot{a}^2 + \kappa}{a^2} \quad (1.29)$$

For the FLRW metric, these two mathematical tools were used by Einstein in his field equation that links together the Ricci tensor (for the space-time curvature) and the stress-energy-momentum tensor  $T_{\mu\nu}$  (for the matter and energy distribution) thanks to:

$$R_{\mu\nu} - \frac{1}{2} g_{\mu\nu} R - g_{\mu\nu} \Lambda = -8\pi G T_{\mu\nu} \quad (1.30)$$

which is a generalisation of the Poisson's equation  $\Delta\phi = 4\pi G\rho$ , and where  $G$  is the Newtonian gravitational constant. In order to keep a static universe, Einstein introduced later the third term in the left member of the equation, containing  $\Lambda$ , known as *cosmological constante*.

Nowadays, recent measurements have indicated an acceleration of the Universe's expansion. The cosmological constant is then a way to cope with it. It introduces then a new concept that is complementary to dark matter, called *dark energy*, and that represents an hypothetical and unknown energy that will play the opposite role to dark matter by accelerating the Universe's expansion<sup>3</sup>.

### 1.2.3 Friedmann equations

For the metric defined in Section 1.2.1.3 and developed in Section 1.2.2, the Equation 1.30 gives the scale factor  $a$  for a Universe filled with a perfect fluid. The corresponding associated stress-energy-momentum tensor is:

$$T_{\mu\nu} = (\rho + p)u_{\mu}u_{\nu} - pg_{\mu\nu} \quad (1.31)$$

where  $\rho$  and  $p$  are respectively the energy density and pressure associated to this fluid. This leads to:

$$\left(\frac{\dot{a}}{a}\right)^2 = \frac{8\pi G}{3}\rho - \frac{\kappa}{a^2} + \frac{\Lambda}{3} \quad (1.32)$$

and

$$\frac{\ddot{a}}{a} = -\frac{4\pi G}{3}(\rho + 3p) + \frac{\Lambda}{3} \quad (1.33)$$

that are known as the *Friedmann equations*, corresponding to the use of the Einstein equation

---

<sup>3</sup>This effect has been observed by two research teams, respectively under the leadership of S. Perlmutter [21], and A. Riess and B. Schmidt [22] that received all of the three the Nobel Prize in 2011 for their works on this subject

assuming the cosmological principle. It is then also common to introduce a time-dependant term, called *Hubble's constant*  $H(t) = \dot{a}/a$ . The critical density  $\rho_c$  needed for a flat universe ( $\kappa = 0$ ) without any cosmological constant  $\Lambda$  can be calculated as a function of this term  $H(t) = \dot{a}/a$ :

$$H^2 = \left(\frac{\dot{a}}{a}\right)^2 = \frac{8\pi G}{3}\rho_c \iff \rho_c = \frac{3H^2}{8\pi G} \quad (1.34)$$

By using this definition of critical density  $\rho_c$ , Equation 1.32 becomes:

$$H^2 = \left(\frac{\dot{a}}{a}\right)^2 = H^2 \frac{\rho}{\rho_c} - H^2 \frac{\kappa}{a^2 H^2} + H^2 \frac{\Lambda}{3H^2} \quad (1.35)$$

The three terms in the right member can be separated into three variables  $\Omega_m$ ,  $\Omega_\kappa$ , and  $\Omega_\Lambda$ , that correspond to the densities associated to matter, curvature and vacuum energy that compose the Universe respectively.

$$\Omega_m = \frac{\rho}{\rho_c}, \quad \Omega_\kappa = -\frac{\kappa}{a^2 H^2}, \quad \Omega_\Lambda = \frac{\Lambda}{3H^2} \quad (1.36)$$

The matter density  $\Omega_m$  could be then decomposed into two additional components: the baryonic matter density  $\Omega_b$  for all visible matter like stars, planets and others visible components, and the non-baryonic matter density  $\Omega_{DM}$  that corresponds to non-luminous matter that can be highlighted through an analysis of the motions of some objects such as those mentioned in Section 1.1.

Thanks to the notation introduced in Relationships 1.36, the final equation for the several components of the Universe is:

$$\Omega_m + \Omega_\kappa + \Omega_\Lambda = 1 \quad (1.37)$$

Thus, assuming a flat universe means that the total amount of available energy in the Universe is shared between matter density and cosmological constant. This hypothesis is well motivated and confirmed by very recent measurement from the Planck satellite [23] that has yield to  $100 \Omega_\kappa = 0.10_{-0.65}^{+0.62}$ . The other results on the several densities  $\Omega_i$  are presented in Section 1.3.6.

Furthermore, the Relationship 1.37 highlights also the contribution to the Universe composition of both the dark energy through the cosmological constant  $\Omega_\Lambda$ , and the dark matter through the term  $\Omega_{DM}$  that is included in  $\Omega_m$ . This is then how the Cosmological Standard Model includes *dark* components to the Universe description.

In the next section are presented all the majors evidences from dark matter that constrain its contribution to the Universe available amount of energy.

### 1.3 Evidences for dark matter presence

As presented in Section 1.1, many optical observables evidences have indicated the dark matter existence. A review of the main observations that have constrained the several values of the  $\Omega_i$  parameters presented above is thus made in the present section. All of these evidences are listed from stars' scale up to the Universe's scale.

#### 1.3.1 Type Ia supernovae

Most of the stars at the end of their life arrive at a status called *white dwarf*, which corresponds to a very dense stars, mostly composed by carbon and oxygen. They have thus stopped any internal nuclear fusion, and are then in equilibrium between their gravitational force and internal pressure. While during their life this kind of star can reach a mass few times bigger than the Sun's one, a white dwarf has a mass below the *Chandrasekhar* limit, around 1.4 solar mass,  $M_{\odot}$ .

In case such a star composes a binary system with another star, there is then the possibility that, because of its density and gravitational potential, the white dwarf star steals mass from the other star. Two different scenarii can then occur:

1. The white draft re-ignites internal nuclear fusion
2. The white draft creates a supernova thermonuclear explosion

This type of star explosion is called *supernovae Type Ia*. The peculiarity of this supernovae is that the variation of the emitted light is approximatively the same for all the observed Type Ia. Thanks to this, such supernovae are called *standard candles*, and can be used as source information for the Universe's composition and behavior. Indeed, as said earlier, such analysis have yield to the discovery of the acceleration of the Universe's expansion [21, 22]. In what follows is presented how informations on Universe's components can be inferred from type Ia supernovae analysis. These developments are inspired from [14, 15].

Due to the Universe expansion, the light emitted by an object is seen by an Earth observer with a spectral shift toward the red spectrum region. This shift  $z$  is expressed as follows:

$$z = \frac{\lambda_{obs} - \lambda_{emit}}{\lambda_{emit}} \iff 1 + z = \frac{\lambda_{obs}}{\lambda_{emit}} \quad (1.38)$$

where  $\lambda_{emit}$  and  $\lambda_{obs}$  are respectively the light wavelength at the emission point and at the observatory point. This relationship can be rewritten by using the scale factor:

$$1 + z = \frac{a(t_0)}{a(t)} \quad (1.39)$$

where  $t_0$  is the present epoch and  $t$  is an earlier time at which the light was emitted. In the next section will be presented how this redshift can be related to the current component of the Universe.

### 1.3.1.1 Stress energy-momentum tensor $T^{\mu\nu}$

Previously, by using the the Friedmann's Equation 1.32, the ratio  $\dot{a}/a$  was defined as a function of the energy density  $\rho$  that belongs to the stress-energy-momentum tensor  $T^{\mu\nu}$ . This density can be divided into two terms:

1. The density  $\rho^{NR}$  that belongs to non-relativistic matter and which includes baryonic and non-baryonic matter:

$$\rho^{NR} = \rho^B + \rho^{NB} \quad (1.40)$$

2. The density  $\rho^R$  that belongs to relativistic matter and which includes photons and neutrinos densities:

$$\rho^R = \rho^\gamma + \rho^\nu \quad (1.41)$$

Moreover, in General Relativity, the stress-energy-momentum tensor  $T^{\mu\nu}$  is conserved, implying for the covariant derivative:

$$\partial_\mu T^{\mu\nu} + \Gamma_{\mu\rho}^\mu T^{\rho\nu} + \Gamma_{\mu\rho}^\nu T^{\mu\rho} = 0 \quad (1.42)$$

Then, by using the definition of the stress-energy-momentum tensor presented in Equation 1.31, the conservation law written for  $\nu = 0$  is:

$$\partial_0 \rho + \Gamma_{\mu 0}^\mu \rho + \Gamma_{\mu\rho}^0 T^{\mu\rho} \quad (1.43)$$

Thus, for the FLRW metric, all the Christoffel  $\Gamma_{i0}^j$  and  $\Gamma_{ij}^0$  read:

$$\Gamma_{i0}^j = \delta_{ij} \frac{\dot{a}}{a}, \quad \Gamma_{ij}^0 = -\frac{\dot{a}}{a} \gamma_{ij}, \quad \Gamma_{00}^0 = 0 \quad (1.44)$$

and

$$\Gamma_{\mu 0}^\mu = 3 \frac{\dot{a}}{a}, \quad \Gamma_{\mu\rho}^0 = 3 \frac{\dot{a}}{a} p \quad (1.45)$$

This leads to:

$$\dot{\rho} + 3 \frac{\dot{a}}{a} (\rho + p) = 0 \quad (1.46)$$

The same relationship could be found if the Universe is assume to be adiabatically expanding, allowing the use of the first law of thermodynamic:

$$dU + PdV = dQ = 0 \quad (1.47)$$

where  $U$  is the internal energy in the Universe,  $P$  is the pressure and  $V$  its Volume. The energy density  $\rho = U/V$  per unit of volume is then:

$$\begin{aligned} d\rho &= d\left(\frac{U}{V}\right) \\ &= \frac{dU}{V} - U\frac{dV}{V^2} \\ &= \frac{-PdV}{V} - \rho\frac{dV}{V} \\ &= -(\rho + p)\frac{dV}{V} \end{aligned} \quad (1.48)$$

Moreover, since each length increases proportionally to  $a(t)$ , the Universe's volume expansion increases proportionally to  $a^3$ , leading to:

$$d\rho = -3(\rho + p)\frac{da}{a} \quad (1.49)$$

The Equation 1.46 can be then found back by dividing by  $dt$  on the left and on the right.

### 1.3.1.2 Radiation-domination and matter-domination eras

Since the density differential equation have been obtained in the previous section, it can be applied to the firsts two epochs of the Universe that were respectively dominated by relativistic density  $\rho^r$  and non-relativistic density  $\rho^{nr}$ , in order to establish the relationships between each of these two densities and the scale factor  $a$ .

The first epoch of the Universe was dominated by radiation energy density and known as *radiation-domination era*. At that time, the following relationships can be applied:

$$p^r = \rho^r/3, \rho^r \gg \rho^{nr} \quad (1.50)$$

that modifies Equation 1.46 into:

$$\dot{\rho}^r + 3\frac{\dot{a}}{a}\left(\rho^r + \frac{\rho^r}{3}\right) = 0 \quad (1.51)$$

which is equivalent to:

$$\dot{\rho}^r = -4\rho^r \frac{\dot{a}}{a} \quad (1.52)$$

And finally,

$$\rho^r \propto a^{-4} \quad (1.53)$$

Then, the following epoch was dominated by non-relativistic density, and is known as *matter-domination era*. In a dust filled universe approximation, in comoving coordinates, the non-relativistic matter is approximated as stationary dust particles, which produce no pressure. Thus, by analogy to *radiation-domination era*:

$$p^{nr} = 0, \rho^{nr} \gg \rho^r \quad (1.54)$$

And Equation 1.46 becomes:

$$\dot{\rho}^{nr} + 3\frac{\dot{a}}{a}(\rho^{nr} + 0) = 0 \quad (1.55)$$

leading to:

$$\rho^{nr} \propto a^{-3} \quad (1.56)$$

### 1.3.1.3 Cosmological parameters and the redshift

Thanks to the two Relationships 1.53 and 1.56 obtained in the previous section, the Equation 1.35 can be now rewritten by including the redshift, illustrating how the analysis of the type Ia supernovae can give informations about the Universe's component.

For this purpose, it is necessary to start with the Equation 1.32 that can be rewritten by separating the two contributions of the matter density, relativistic and non-relativistic:

$$\left(\frac{\dot{a}}{a}\right)^2 = \frac{8\pi G}{3}(\rho^r + \rho^{nr}) - \frac{\kappa}{a^2} + \frac{\Lambda}{3} \quad (1.57)$$

Moreover, the Equation 1.52 has shown that  $\rho^r a^4$  is constant, leading to  $\rho^r a^4 = \rho_0^r a_0^4$ . In this equation,  $\rho_0^r$  and  $a_0$  are the current relativistic matter density and the scale factor at the present time respectively. This can be rewritten as:

$$\rho^r = \rho_0^r \frac{a_0^4}{a^4} \quad (1.58)$$

And by analogy:

$$\rho^{nr} = \rho_0^{nr} \frac{a_0^3}{a^3} \quad (1.59)$$

Then, by using the definition 1.39 of the redshift, by defining the current critical density  $\rho_{c0}$  for a flat universe, in analogy to 1.34:

$$\rho_{c0} = \frac{3H_0^2}{8\pi G} \quad (1.60)$$

and by defining the current cosmological parameters  $\Omega_{\kappa 0} = -\kappa/(a_0^2 H_0^2)$  and  $\Omega_{\Lambda 0} = \Lambda/(3H_0^2)$  in analogy to Relationships 1.36:

$$\left(\frac{\dot{a}}{a}\right)^2 = H_0^2 (\Omega_{m0}^{nr} \times (1+z)^3 + \Omega_{m0}^r \times (1+z)^4 + \Omega_{\kappa 0} \times (1+z)^2 + \Omega_{\Lambda 0}) \quad (1.61)$$

In this equation, the cosmological parameter  $\Omega_{m0}^r$  is the sum of the present contribution of photons  $\Omega_{\lambda 0}$  and neutrinos  $\Omega_{\nu 0}$  to the Universe's energy budget, as detailed in relation 1.41. As reported in [24],  $\Omega_{\lambda}$  is mostly dominated by the energy of the Cosmic Microwave Background (CMB), whose temperature has been accurately measured by the COBE experiment [25] at  $T = 2.725 \pm 0.001K$ , leading to  $\Omega_{\lambda} = 2.47 \times 10^{-5} h^{-2} = 5.37 \times 10^{-5}$  with the latest value of  $h = H_0/100 km.s^{-1}.Mpc^{-1} = (67.80 \pm 0.77) \times 10^{-2}$  from the Planck satellite [23]. As it is also reported in [24],  $\Omega_{\nu}$  can be determined through the total mass of the three neutrinos flavour, according to the following relation:

$$\Omega_{\nu} = \frac{\sum m_{\nu_i}}{93eV} h^{-2} \quad (1.62)$$

The most restrictive upper limit on the total mass provided by the Planck satellite [23], combined with the results from baryonic oscillations presented later in this section and other experiments on Cosmic Microwave Background (CMB) analysis, is  $\sum m_{\nu_i} < 0.23$  eV. This leads to  $\Omega_{\nu} < 5.38 \times 10^{-3}$ . The less restrictive upper limit on the total mass provided by a combination of results from part of these experiments was of the order of 1 eV. The consequence of these two results on  $\Omega_{\lambda}$  and  $\Omega_{\nu}$  is that  $\Omega_m^r$  is negligible in comparison to the whole energy budget of the Universe. Then, assuming a flat universe as it was mentioned above, Equation 1.61 depends only on  $\Omega_{m0}^{nr}$  that contains contribution of baryonic and non-baryonic matter, including possible massive neutrino even if supposed to be relativist, and  $\Omega_{\Lambda 0}$  that refers to dark energy. For the rest of

this section on supernovae,  $\Omega_m^{nr}$  will be identified as  $\Omega_m$ .

The last step for linking type Ia supernovae and Universe's component is to see how the luminosity can be combined with redshift. This is the purpose of the next section.

### 1.3.1.4 From supernovae to cosmological parameters

The luminosity distance  $D_L$  associated to an incoming light signal is obtained by measuring the incoming luminosity flux  $F$  associated to a known luminosity  $\mathcal{L}$ , which is the particularity of type Ia supernovae, through the following formula:

$$D_L = \sqrt{\frac{\mathcal{L}}{4\pi F}} \quad (1.63)$$

If  $r$  is the radial distance between a source emitting light signal at the time  $t$  and an observer that is seeing this signal at the present time  $t_0 > t$ , then photons that have travelled across the distance  $r$  from the source have drawn at  $t_0$  the light sphere with a surface  $4\pi(ra_0)^2$ .  $ra_0$  is then the radius of this sphere by taking into account the Universe's expansion.

Moreover, during the light signal travel, the intrinsic luminosity has been reduced by a factor  $(1+z)$  due to the time cosmological dilation and by a second factor  $(1+z)$  due to the redshift. The incoming flux is then rewritten as:

$$F = \frac{\mathcal{L}}{(1+z)^2 \times (4\pi(ra_0)^2)} \quad (1.64)$$

The luminosity distance becomes:

$$D_L = (1+z)ra_0 \quad (1.65)$$

The next steps consists in expressing the radial distance as a function of the redshift and cosmological parameters. The time derivation of the redshift definition in relation 1.39 leads to:

$$dt = -\frac{dz}{H_0(1+z)\sqrt{\Omega_{m0}(1+z)^3 + \Omega_{\Lambda 0}}} \quad (1.66)$$

where  $\Omega_{m0}$  corresponds to  $\Omega_m$ . In order to simplify this expression, the function  $f(z)$  is defined:

$$f(z) = \frac{1}{\sqrt{\Omega_{m0}(1+z)^3 + \Omega_{\Lambda 0}}} \quad (1.67)$$

Then, by integrating Equation 1.66 between the present time  $t_0$  and the time  $t$  at which the light signal was emitted, the time difference  $(t_0 - t)$  is obtained as a function of the redshift  $z$ :

$$(t_0 - t) = \int_0^z \frac{f(z)dz}{H_0(1+z)} \quad (1.68)$$

Moreover, all along the geodesic followed by the light signal between the emission source and the observer,  $ds^2 = 0$ . By considering then the simplest case where  $d\theta = d\phi = 0$ , then the FLRW metric defined in 1.21 leads to:

$$\frac{dt}{a(t)} = \frac{dr}{\sqrt{1-kr^2}} \quad (1.69)$$

If  $t_1$  is the time at the light emission,  $r_1 = 0$  and  $r_0$  the radial positions associated to the emission position and the observer respectively, then by integrating the two members:

$$\int_{t_1}^{t_0} \frac{dt}{a(t)} = \int_0^{r_0} \frac{dr}{\sqrt{1-kr^2}} \quad (1.70)$$

And by using the Equation 1.68:

$$\int_{t_1}^{t_0} \frac{dt}{a(t)} = \frac{1}{H_0 a_0} \int_0^z f(z)dz \quad (1.71)$$

The Expressions 1.70 and 1.71 can be mixed in order to express  $r$  as a function of  $H_0$ ,  $a_0$ ,  $z$ ,  $\Omega_m$  and  $\Omega_\Lambda$  that are included in  $f(z)$ . This expression is finally injected into Equation 1.65. Since  $D_L$  and  $z$  can be measured, the latter relationship can be used to relate  $\Omega_m$  and  $\Omega_\Lambda$ . Such results have been recently updated in [26] as it is illustrated by the blue ellipses in Figure 1.4.

### 1.3.2 Galaxies rotation curves

As it was discussed in 1.1.2, galaxy rotation curves were one of the major evidences that have built the dark matter hypothesis. One of the most famous rotation curves that illustrates the contribution of the dark halo is represented in Figure 1.5.

To be complete on this subject, it is needed to mention also that an alternative theory to dark matter was suggested in 1983 by an Israeli physicist Mordehai Milgrom [28] to explain galaxies rotation curves through a modification of the Newtonian gravity. This theory is known as *MODified Newtonian Dynamics* (MOND).

While it works well for reproducing the stars velocities spectra, it however can not explain alone dark matter evidence at larger scale, such as galaxies clusters that are the subject of the next section. A recent relativistic adaptation of this gravity modification theory [29] seems however succeed to explain the observed behaviours at larger scale without adding a dark matter contribution.

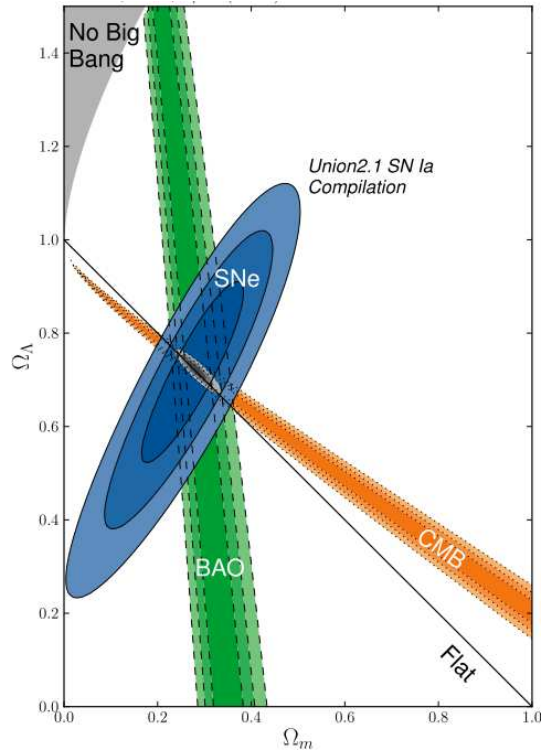


Figure 1.4: Combination of cosmological parameters  $\Omega_m$  and  $\Omega_\Lambda$  from different observables, from [26]. Blue ellipses correspond to the informations inferred from Type Ia supernovae, black line illustrates the case of a flat universe, CMB orange areas and BAO green areas correspond respectively to informations inferred from CMB analysis by WMAP as it will be discussed in Section 1.3.6 and BAO analysis as it will be discuss in Section 1.3.5. The most favoured parameters correspond to the best agreement between all of these three methods and are represented by the grey ellipses.

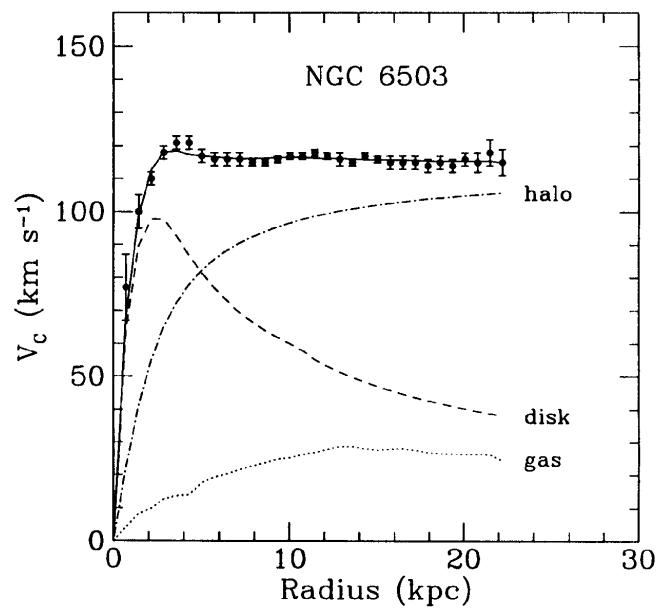


Figure 1.5: Galaxy rotation curve from NGC 6503 from [27], illustrating the contribution of the gas, luminous disc and dark halo to stars velocities, with a very good agreement between data and fit function.

### 1.3.3 Galaxies clusters

As mentioned in 1.1, galaxies clusters were the first indications of dark matter. In addition to this, galaxies cluster are also objects with particular properties, called gravitational lensing. In such objects, the light from galaxies in the background respect to the observer can be distorted through the influence of additional matter between the observer and the source, see Figure 1.6(a) for illustration. This process can lead to artificial images of the original galaxies, like Einstein's rings, as illustrated in Figure 1.6(b). The angular radius of such perturbations depends on the mass that is responsible to the light distortion, for which the process is achromatic.

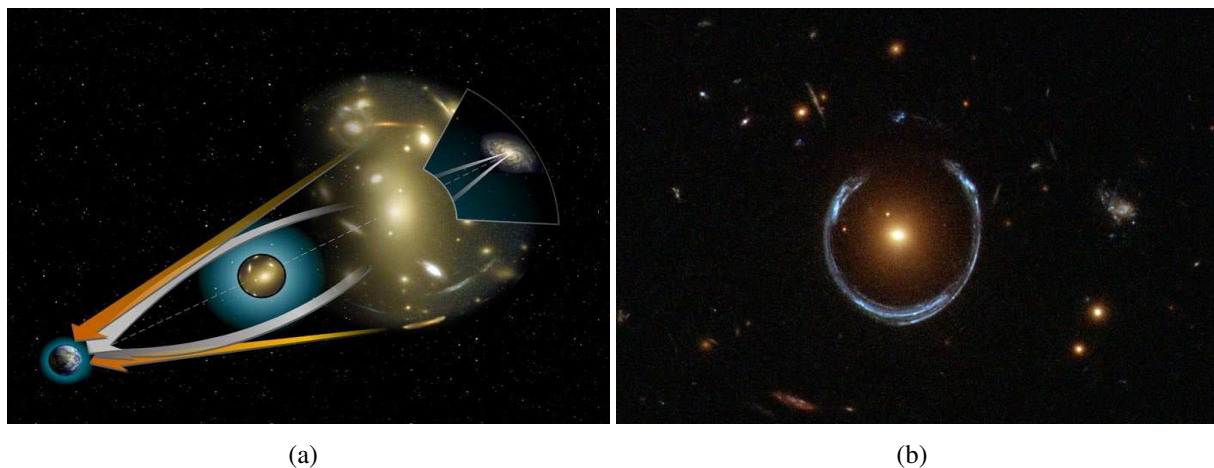


Figure 1.6: Illustration of (a) gravitational lensing, and (b) Einstein's ring. Both pictures from [30].

This phenomenon exists also for other objects such as galaxies and all other massive objects such as those described in Section 1.4.1. It correspond to a successful prediction of the General Relativity that was firstly observed in the 80's, and it has allowed to draw few years ago a 3D map of dark matter distribution [31]. In addition to this distribution reconstruction, it is also used nowadays to determine the mass of the object that deviates the light. Moreover, it corresponds to one possible way to detect planets that orbit around another star than the Sun, and usually known as *exoplanets*.

Furthermore, it is also galaxies clusters that have led to the best argument up to date on the dark matter presence. In 2006, the space telescope *Chandra* has analysed a collision of two galaxies clusters, now called *Bullet Cluster*, as represented in Figure 1.7(a). It corresponds to the optical image of the situation right after the collision of two clusters of galaxies.

Inside, around and between galaxies exist hot gases. They emit X-rays by thermal Bremsstrahlung emission. Their distribution in each of the two clusters, corresponding to most of the baryonic matter inside the whole structure, can be thus reconstructed thanks to this X-rays emission. This reconstruction is superimposed in pink color [33] on the optical image of Figure 1.7(a).

Moreover, the distribution of the total mass of each of the two structures can be also reconstructed using gravitational lensing. The corresponding regions are also superimposed in blue [34] to the optical image. The blue and pink regions are thus different.

The baryonic matter remains in the center of the collision, while there is another massive

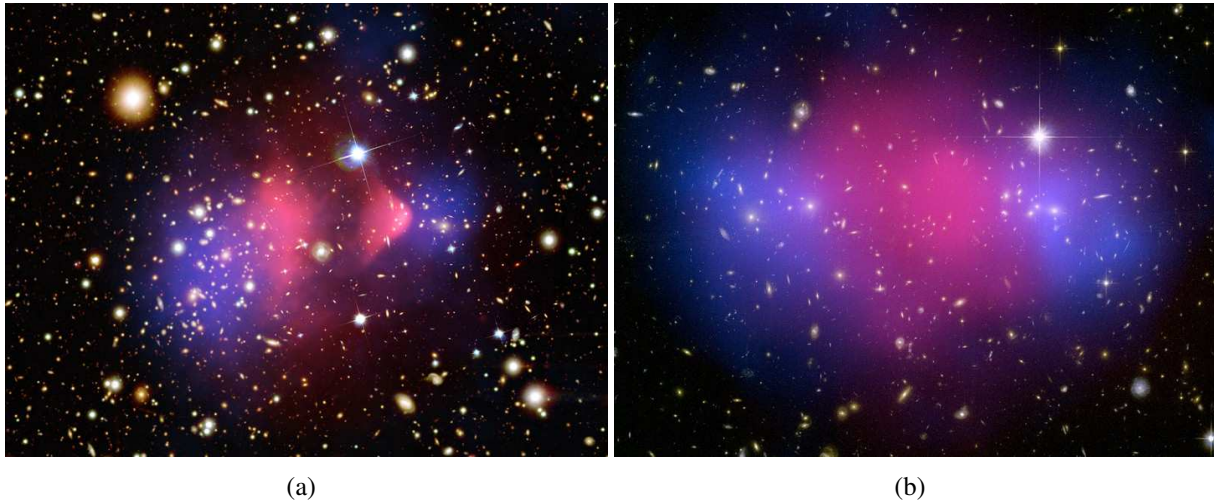


Figure 1.7: Mass distribution in galaxies clusters collisions: (a) Bullet cluster, (b) MACS J0025.4 Both pictures come from [32]. See text below for colors explanation.

matter, the dark matter, that is in the external part of the collision. This can be explained by the interactions of the baryonic matter during the collision, and that was thus slowed down, while the dark matter has gone further. This is up to date the most evidence of non baryonic dark matter existence. It also illustrates that dark matter has a very low interaction rate, which is agreement with the fact that no experiment has discovered it up to now.

Since this analysis, a few more similar object were found. Some of them, like in the *Abell 520* galaxies cluster, have a less clear differentiation in the mass distribution. This has thus let space for controverts on this argument for the dark matter existence, up to the analysis of objects with a mass distribution equivalent to bullet cluster. Such objects, like in *MACS J0025.4* galaxies cluster, represented in Figure 1.7(b), have independently confirmed the analysis of the bullet cluster.

### 1.3.4 Primordial nucleosynthesis

The primordial nucleosynthesis studies has allowed to confirmed the robustness of the Cosmological Standard Model. After light-matter decoupling, lowest elements such as hydrogen or helium isotopes started to be created, and by nuclear fusions, next heavier elements were obtained as long as the Universe's temperature allowed it. The abundance evolutions (blue curves) of all of the lightest elements can be then compared to the respective observable abundance (green areas), as it shown in Figure 1.8. These evolutions can be represented either as a function of the baryon density over light density ratio or as a function of the baryonic cosmological parameter  $\Omega_b$ .

The nice feature of this study is that almost all of the elements have provided similar values for  $\Omega_b$ , that are in good agreement with the measured values from CMB analysis from WMAP and Planck satellites. The value provided by the latter is  $\Omega_b = 0.02207 \pm 0.00027$ . As it can be seen on Figure 1.8 the  ${}^7\text{Li}$  isotope provides different value than the CMB analysis. Physics beyond the standard model, like Supersymmetry, could modify light elements abundance, as discussed in [36].

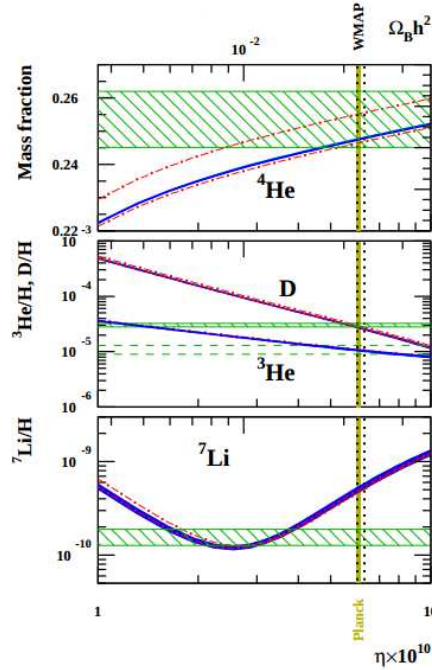


Figure 1.8: Abundance prediction for lightest elements from primordial nucleosynthesis as a function of baryonic over light ratio  $\eta$  or baryonic cosmological parameter  $\Omega_b$  (blue curves) compared with observable abundance (green areas) and CMB analysis (vertical lines). Model including respectively 3.02 and 3.70 as effective number of neutrino family are illustrated by dashed red curve. Picture from [35].

### 1.3.5 Baryonic acoustic oscillations in primordial plasma

In the primordial plasma, before the recombination between electrons and nucleus to create atoms, the opposition between baryons that created gravity potential, and photons that created radiation pressure, has induced small fluctuations in the homogeneity of the plasma. These fluctuations are known as *Baryonic Acoustic Oscillation* (BAO) and were frozen at the light-matter decoupling. Thanks to this, they can be observed in the CMB, but also in the matter distribution since it was the primary gravitational potential that participated to the creation of large structures through accretions.

The analysis of such oscillations is thus another source of informations for matter content in the Universe, with recent results provided in [37] and illustrated previously in Figure 1.4.

### 1.3.6 Cosmic microwave background

The last evidence of dark matter in the Universe concerns the anisotropies observed in the Cosmic Microwave Background analysis (CMB), already mentioned several times in the previous sections. The CMB gives a picture of the Universe at the time of the light-matter decoupling. It is visible by analysing nowadays photons that were released at that time. While at the decoupling epoch, the Universe's temperature was of the order of 3000 K. This temperature is now of the order of 2.725 K due to the Universe expansion.

The existence of the CMB was first postulated in 1948 by two American cosmologists, Alpher

and Herman [38], who estimated its temperature at 5 K. It was then discovered accidentally in 1965 by two American physicists, Penzias and Wilson [39], who received the Nobel prize in 1978 for their discovery. The CMB temperature anisotropies are of the order of  $\delta T/T \sim 10^{-5}$  and are mainly due to inhomogeneity of matter distribution at the light-matter decoupling time. The recent sky map shown in Figure 1.9, extracted from [40], for the results from the Planck satellite illustrates these temperature anisotropies.

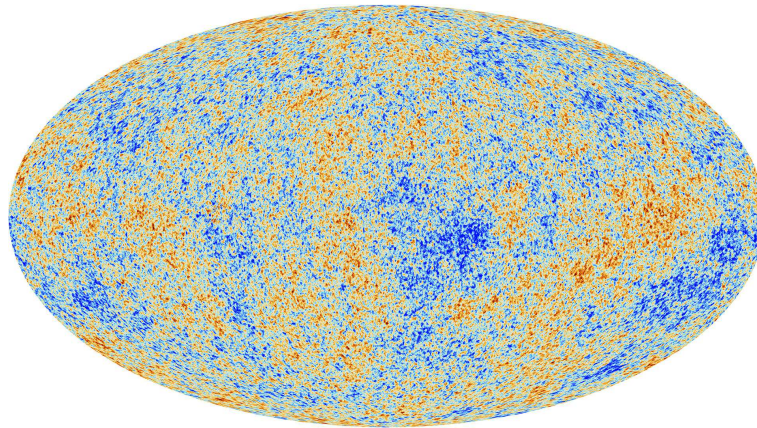


Figure 1.9: Sky map of the temperature anisotropies measured by the Planck satellite. Figure extracted from [40].

In order to infer values for cosmological parameters from this map, the fluctuations are decomposed into spherical harmonics  $Y_{lm}(\theta, \phi)$  associated to the temperature fluctuations:

$$\frac{\delta T}{T} = \sum_{l=2}^{+\infty} \sum_{m=-l}^{+l} a_{lm} Y_{lm}(\theta, \phi) \quad (1.72)$$

The variance of the amplitudes  $a_{lm}$  are then expressed through the  $C_l$  coefficients:

$$C_l = \langle |a_{lm}|^2 \rangle = \frac{1}{2l+1} \sum_{m=-l}^{+l} |a_{lm}|^2 \quad (1.73)$$

The evolution of the term  $D_l = l(l+1)C_l/2\pi$  as a function of the variable  $l$  that corresponds to the angular scale through which the sky is studied can be drawn, as it is represented in Figure 1.10 for results from the Planck collaboration [41].

Thanks to this analysis, informations about cosmological parameters, can be inferred, as it is explained in [42, 43], like the Hubble constant that helps for the evaluation of the  $\Omega_i$  parameters. The locations and heights of the regular peaks of the spectrum, named *acoustic peaks*, are used to determine the values of these cosmological parameters. As an example, the position of the first peak will give an information on the curvature of the Universe, while the enhancement of the odd peaks with respect to even peaks will indicate an increase in baryon density, and vice-versa. This is explained by the gravitational potential wells that were due to the early baryon distribution, and that has led to acoustic oscillations [44]. A modification of the dark matter density or of the

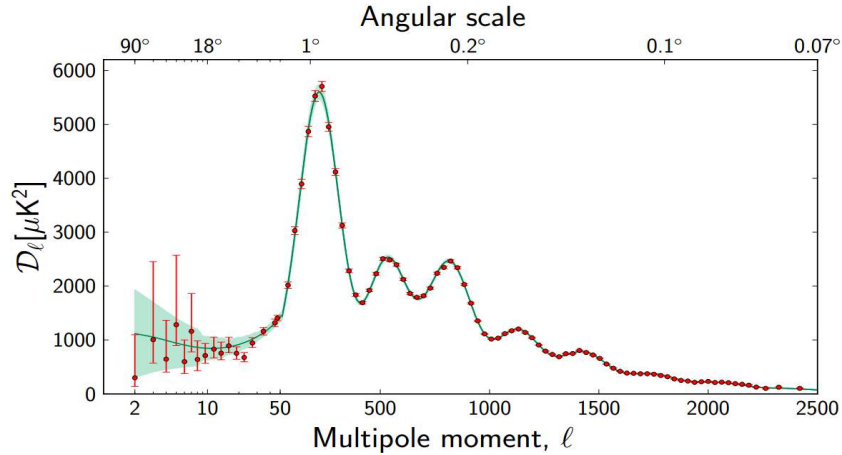


Figure 1.10: CMB power spectrum analysis by the Planck satellite. Figure from [41].

dark energy density would also change the shape of the spectrum, such as illustrated in [42].

The firsts results provided by the Planck collaboration are listed in Table 1.1, and are in very good agreement with the other observables detailed earlier.

| Cosmological parameters                                | Symbol           | Planck best-fit |
|--|------------------|-----------------|
| Baryonic density [%]                                   | $\Omega_b$       | 4.90            |
| Cold dark matter density [%]                           | $\Omega_c$       | 26.71           |
| Total matter density [%]                               | $\Omega_m$       | 31.75           |
| Dark energy density [%]                                | $\Omega_\Lambda$ | 68.25           |
| Age of the Universe [Gyr]                              | $t_0$            | 13.819          |
| Hubble Constant [ $\text{km.Mpc}^{-1}.\text{s}^{-1}$ ] | $H_0$            | 67.11           |

Table 1.1: Cosmological parameters from Planck satellite [23]

It can be noticed here the introduction of a *cold dark matter density*. As presented in the paragraph 1.3.7, the most favourite candidates for dark matter have sub-luminous velocities (*cold elements*), in comparison to candidates with velocities close to light celerity (*hot elements*) such as neutrinos. As discussed in Section 1.3.1.3, these latter were already rejected as dark matter candidate because of their small contribution to Universe's composition.

This concludes this section on all observables that have led to dark matter evidence. Several important results are:

- The *standard* matter (baryonic and relativistic matter) is not the only component of the Universe. There are other components, called dark matter and dark energy, that are both much more abundant, but up to now not identified.
- All of the independent evidences for dark matter and dark energy give coherent results.
- Dark matter is not a *local anomaly of the space*, but a clear component of the universe, that is present at all various space and time scales. This means that the dark matter candidate should be a relic of the early Universe, and should be present everywhere.

- According to those observable, it seems relevant to exclude baryonic objects as dark matter candidate. However, in order to test this hypothesis, a discussion will be done in Section 1.4.2 by investigating non luminous massive objects as dark matter candidates in galaxy halo
- Since dark matter has not been discovered yet, it can be expected to be neutral and to have also very low interaction rate with standard matter, as it is illustrated with the bullet cluster in Section 1.3.3.

In the last paragraph of this section of the evidence for dark matter and dark energy, the computing structures simulations will be approached, giving another contribution to the list of attributes to the dark matter candidate.

### 1.3.7 Structure simulations

In the last decades, several simulation programs have been developed to draw the most accurate scenario of structures formation at different scales, combining many computers and taking benefits of the most recent computing technology. Among them, there is at large scale the Millenium project (phase I, II and XXL) that used the early results on cosmological parameters from the WMAP experiment. More recently, there is also the Bolshoi program that used first the latest results from WMAP, and since last year the results from the Planck satellite. Those simulations are completed by simulations at more restrictive scale, of the order of galactic dark matter halo, like the Aquarius project. The aim of reducing the scale of simulations is to confirm results at lower scale but with more precision the results obtained with simulations at larger scale, but aim also to have a better understanding of our own galaxy.

The lessons early taken from those kind of simulations were the apparition of dark halo, and the need of cold dark matter to allow the structures formation such as those that can be optically observed, as it was also recently confirm in [45]. As an example of the power of thoses simulations, the comparison has been made [46] between a reconstructed *sky* from Millenium I and the observed sky with two of the three biggest known structures: the *Sloan Great Wall* in blue in the top part of Figure 1.11 and the *CfA2 Great Wall* in blue in the smaller piece, with the *Coma* cluster in the center. The first wall is also the biggest one, and includes about 10 000 galaxies with a total size that is over more than 1.37 billion light years. The two walls are seen in North sky. Then, the left blue part of the figure represents same order of structures, seen in South sky, with the half of the *2dFGRS* object that includes 220 000 galaxies far up to 2 billion light years. In red is represented the *sky* created by the millenium I simulation taking into account cosmological parameters from WMAP, and with a very good reproduction of the observed structures.

In addition to this, the simulation at galaxies scale has been able to confirm the galaxy structures observed with simulations at larger scale, with also same density profile inside the halo as those observed for different real galaxies. It has however led some other questions about the uniqueness of the Milky Way, since simulations have predicted about 500 dwarf galaxies around the Milky Way [47] while about only a tens of such objects has been identified so far. One possible explanation would be that some of these dwarfs galaxies are almost pure dark matter object,

corresponding to undetectable dark matter sub-halo. Unless some physical process, such as the dark matter self interaction are not accurately reproduced. This kind of question needs lots of time to be answer, especially since simulation needs precise cosmological parameters, but also because the more the requested precision is, the more it will suffer from the technology improvement.

Thanks to all of these observations, the numerical simulations of the Universe evolution have already improved our knowledge on dark matter behaviour, like confirming the cold dark matter hypothesis. With the continuous improvement of the technologies, it will continue in the next future to contribute to focus the dark matter hunt, as all the other independent analysis detailed earlier will do.

This closes this section on all the evidences of dark matter existence. The next section will present a quick review of the main candidates that were suggested for describing the dark matter.

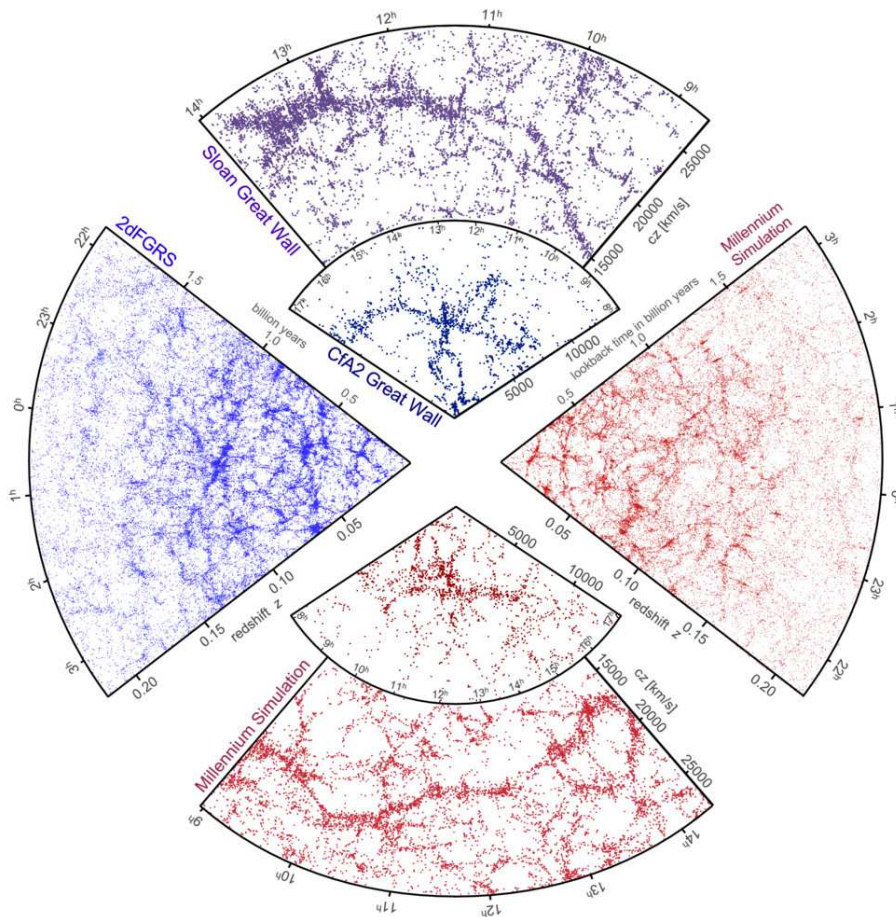


Figure 1.11: Comparison between observable galaxies distribution (blue) and Millennium I simulation (red). Top blue piece represents the observed North sky, and has to be compared with simulation on bottom red piece. The same for the left blue piece, which represents the observed South sky, and the simulations on right red piece. Picture from [46].

## 1.4 Dark matter candidates

As it has been seen in the previous section, the *standard* matter, that includes photons, neutrinos and all the visible baryonic matter, corresponds only to few percent of the Universe components, while dark matter contributes to about 27%. From the observations discussed in the previous section, the dark matter candidate is expected to be neutral, non-luminous, non-relativistic, non-localized. It should also have a relic density, a high abundance and a very low interaction rate with baryonic matter.

In what follows will be made a review of the historically favoured candidates that follow some of these expected properties, starting from simplest one, up to the one most favoured nowadays.

### 1.4.1 Baryonic dark matter

The first candidates to describe the missing mass, at least at galaxies scales, were all the massive non luminous objects, that includes planets, namely giant, brown stars<sup>4</sup>, neutrons stars, and black holes. This list could sometimes include interstellar gas clouds, red dwarfs<sup>5</sup> and white dwarfs. All of these objects can be named under the acronym of *MAssive Compact Halo Object (MACHOs)*.

At the end of the last century, different search campaigns, like the MACHO [48] and EROS [49] experiments, were led in order to have indications on the contribution of such objects to dark halo. As a results, these two experiments derived upper limits at 20% and 25% respectively of the Milky Way halo that is composed by MACHOs objects, requesting an additional component to the dark halo.

These results, combined with CMB studies on baryonic contribution to the Universe, lead to search for non-baryonic dark matter candidates, also because of the presence of dark matter at much larger scale.

### 1.4.2 Non-baryonic dark matter

As approached in the previous paragraph, the baryonic candidates are not able to describe alone the missing mass, whatever is the considered scale. This has led to the search for non-baryonic candidates, that can be split into two families: *hot* and *cold* candidates. Both of them will be approached in what follows.

#### 1.4.2.1 Hot dark matter

Among the candidates for hot dark matter, the most favoured are standard neutrinos, and the hypothetical sterile neutrinos. The former seem to be almost perfect candidates regarding to the properties summarized at the beginning of this section, except for their velocities. However, the analysis performed on the CMB spectrum has always shown that they were not enough abundant to mostly contribute to dark matter, namely because of their total mass, as discussed in

<sup>4</sup>Brown stars are objects that are more massive than giant planets, but not enough to start internal fusion as standard stars

<sup>5</sup>Red dwarfs stars are the smallest possible stars that are right enough massive to start internal fusion.

Section 1.3.1.3. Furthermore, this abundance in the Universe is very well known, strengthen the conclusion that they can not describe the missing mass.

That is why the sterile neutrino, that is expected to be more massive than standard neutrinos, and for which the abundance is absolutely unknown, can really be a good candidate for dark matter, even if it is not discovered yet. However, the most favoured scenario from numerical simulations for allowing the structures formations as the observed ones needs cold dark matter. This should thus permit gravitational accretion of matter by following the *bottom-up* scenario, and that hot dark matter would not promote. That will be then its discovery that would conclude on its contribution to dark matter, namely by concluding on its velocity since models on sterile neutrino predict this particle to be either *hot*, *warm*, or *cold* dark matter, as it is discuss here [50].

### 1.4.2.2 Cold dark matter

As for hot dark matter, several candidates were suggested to describe cold dark matter. A quick review of prediction of their mass and cross-section is shown in Figure 1.14 at the end of this section. It also includes some hot dark matter candidates. In the following developments will be presented only the two most favourite candidates: the *axions* particles and the *Weakly Interacting Massive Particles (WIMPs)*.

#### Axions

One of the most favourite candidates for cold dark matter are the axions<sup>6</sup> particles. They take their origins in the mixed invariance of charge-parity (*CP*) that is illustrated through the following relationship between electron and positron:

$$e_{up}^- \xleftrightarrow{CP} e_{down}^+ \quad (1.74)$$

Since the Universe presents an asymmetry between matter and antimatter, a violation of this mixed invariance is expected. This has however not been observed so far at the strong interactions scale in Quantum ChromoDynamic (QCD). This lack of invariance is also known as the *strong CP problem*. In order to explain it, the two physicists Roberto Peccei and Helen Quinn have suggested a QCD model in which the symmetry remains inviolated through the emission of an axion, that would work thus as a boson.

The axions particles would be then a neutral particle, with a very low mass ( $\ll$  eV), and that could switched into photon and vice-versa under the influence of a very high magnetic field. This phenomenon is known as Primakoff effect. Among the experiments that aims to detect axions through this effect, the CERN Axion Solar Telescope (*CAST*) [51] and the Axion Dark Matter eXperiment (*ADMX*) [52] can be cited.

Another way investigated to detect axion is to test the possibility of a scattering process similar to the photoelectric effect described in Section 2.2.1 between an axion and an electron of an atom.

---

<sup>6</sup>The origins of this name come from a lye brand, since axions are supposed to *clean* two problems in the modern physic: The strong-CP problem and the dark matter problem

The axion would thus extract the electron by giving it all its energy when vanishing. By analogy to the photoelectric effect, this phenomenon is also known as *axioelectric effect*, and would request a more massive axion to allow the electronic extraction and to improve detector sensitivity. Among all the experiments that are searching for axions through this channel, the recent results from the XENON100 experiment [53] can be noticed. They will be presented in Section 3.5.

### Weakly Interacting Massive Particles

The model that describes the Weakly Interacting Massive Particles (*WIMP*) [54, 55] predicts that at the earliest times of the time Universe, the WIMPs density was constant. This was allowed thank to a thermal equilibrium between annihilations into two Standard Model particles and creations by two Standard Model particles:

$$\chi\chi \longleftrightarrow P\bar{P} \quad (1.75)$$

where  $\chi$  and  $P$  represent respectively the WIMPs and the Standard Model particles. By cooling down, the Universe has reached temperature below the dark matter particle's mass. As a consequence, the creation of dark matter particles was not be possible anymore. Starting from that point, only annihilation could occur. The density decreased thus exponentially, as it is shown in 1.12(a). However, since the Universe has continued to expand, the dilatation has reached large enough to make impossible any annihilation. The WIMP density remained then almost constant. This period is known as the *freeze out* of the WIMP density, and is illustrated by the horizontal line on the right part of Figure 1.12(a).

The evolution of the WIMPs population as long as the annihilation and creation occurs can be described by the Boltzmann equation:

$$\frac{dn}{dt} = -3Hn - \langle \sigma_{A\nu} \rangle (n^2 - n_{eq}^2) \quad (1.76)$$

where:

- $n$  is the WIMP density,
- $n_{eq}$  is the WIMP density at thermal equilibrium,
- $H$  is the Hubble constant,
- $\langle \sigma_{A\nu} \rangle$  is the thermally averaged annihilation cross section

As the Universe cool down, the term  $3Hn$  becomes more and more dominant, up to the freeze out that occurs around a Universe's temperature at  $T \sim m_\chi/20$  [54]. Finally, by defining the time freeze out condition  $n_\chi \langle \sigma_{A\nu} \rangle = H$ , the relic density can be expressed as:

$$\Omega_\chi h^2 \approx \frac{3 \times 10^{-27} \text{ cm}^3 \cdot \text{s}^{-1}}{\langle \sigma_{AV} \rangle} \quad (1.77)$$

Dark matter candidates are not expected to have electromagnetic interaction. Thus, by assuming a cross-section of the order of the weak interaction  $\sigma = 10^{26} \text{ cm}^3 \cdot \text{s}^{-1}$ , the corresponding physical cold dark matter density is  $\Omega_\chi h^2 \sim 0.1$ . This is very close to the experimental values, such as  $\Omega_\chi h^2 = 0.12029$  provided by the Planck satellite [23]. This convergence between cosmology and particles physics, combined with the relic abundance, constitutes the so called *WIMP miracle*. Since no DM signature has been observed yet, there is however no more reason than for illustration to assume an WIMP annihilation cross section of the order of the electroweak cross section.

As a complement, the expected values of the WIMPs mass as a function of their contribution to dark matter is presented in Figure 1.12(b) by the brown band. It can be thus seen that, depending on the WIMPs mass, their contribution to the dark matter is either weak or strong. This explains why the direct dark matter experiments calculate cross-sections limits for a large WIMP mass range, as it presented in Section 3.4.

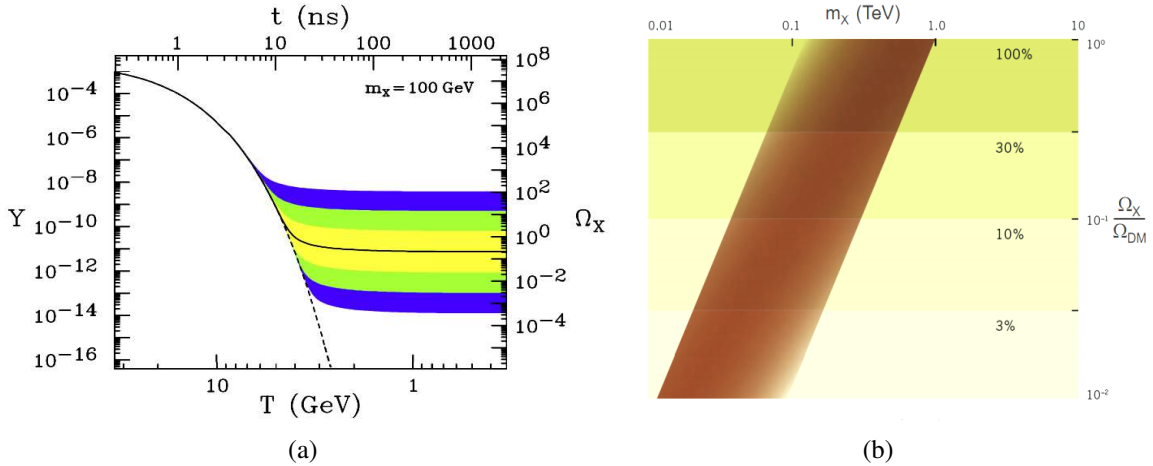


Figure 1.12: (a) Comoving number density  $Y$  and resulting thermal relic  $\Omega_\chi$  as a function of the Universe's age and temperature. The relic density is shown by the solid line using annihilation cross section value in order to get the correct relic density, while shaded regions correspond to same relic density using annihilation cross section that differ respectively by a factor 10,  $10^2$  and  $10^3$  from this value, (b) Wimp mass  $m_\chi$  as a function of the WIMP contribution to dark matter. Both Pictures from [54].

## Supersymmetric Particles

The previous paragraph have shown that cosmology provides some good candidates to describe dark matter, among which are the WIMPs candidates. However, the Standard Model (SM) does not include any of such particles. This is then some theoretical extensions of the SM that could suggest WIMPs candidates, as it is the case for the SUPerSYmmetric (SUSY) extension of

the SM.

The Supersymmetric extension of the Standard Model was introduced to solve hierarchy problem in SM. According to this theory, each particle of the SM will have a *superpartner* that have exactly the same properties, except a higher mass, and a different spin, such that bosons are associated to fermions and vice-versa. The superpartners that are bosons keep then the same name as their standard partner, starting with a prefix *s*, and the superpartners that are fermions keep then the same name as their standard partner, ending with a suffix *ino*, as it is illustrated in Figure 1.4.2.2.

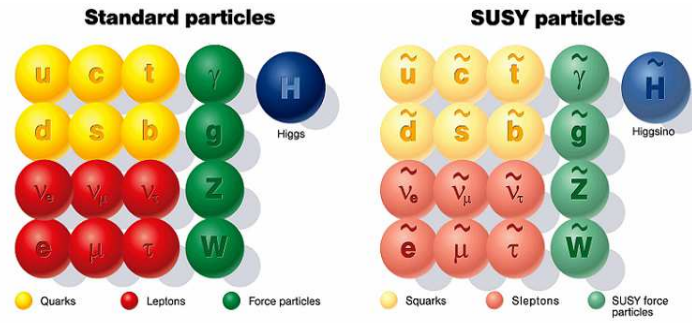


Figure 1.13: Standard Model particles and their associated theoretical superpartners.

One of the possible scenarios suggested by the SUSY theory is that all of the supersymmetric particles are unstable. They decay to the Lightest Supersymmetric Particle (*LSP*) that is supposed to be the only supersymmetric stable particle. This stability would be guaranteed thanks to the introduction of a new quantum number, the *R-parity* that should be conserved:

$$R = (-1)^{3B+L+2S} \quad (1.78)$$

where:

- $B$  is the baryonic number,
- $L$  is the leptonic number,
- $S$  is the spin

The R-parity is equal to +1 for SM particles, and –1 for SUSY particles. One of the most favourite candidate for this LSP is the lightest neutralino that comes from linear combination between neutral supersymmetric partner of the gauge bosons and Higgs bosons:

$$\tilde{\chi} = a_1 \tilde{B} + a_2 \tilde{W}^3 + a_3 \tilde{H}_1^0 + a_4 \tilde{H}_2^0 \quad (1.79)$$

Neutralino are however not the only one WIMPs candidates provided by the SUSY theory. There are also other possible candidates such as the gravitino  $\tilde{g}$  that would be the superpartner of the graviton  $g$ , even if this latter has not been discovered so far. Thus, as a conclusion to this review

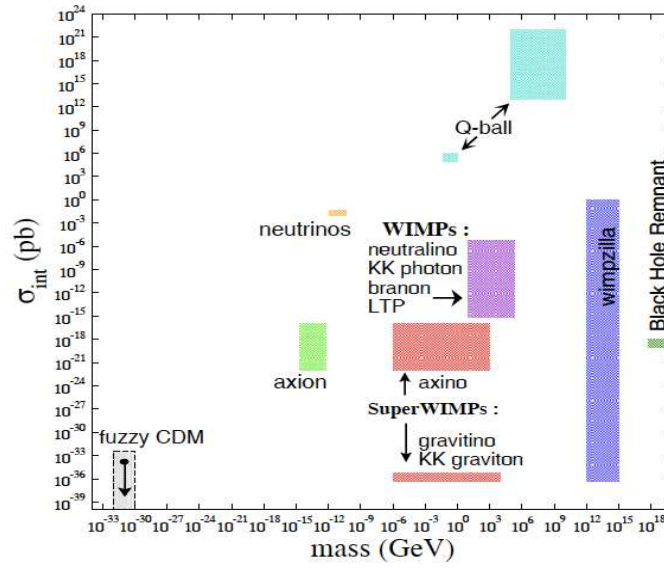


Figure 1.14: Predicted masses and nucleon interaction cross-sections areas for several dark matter candidates. Picture from [56].

of essential dark matter candidates, a larger review of the predicted masses and cross-sections for most of the dark matter candidates is presented in Figure 1.14.

Figure 1.15 presents also a table from [55] that summarizes the test of different dark matter candidates through all the possible constraints and detection channel. It illustrates thus that WIMPs, assuming to be neutralino particles, are effectively among the best candidates for the description of the dark matter.

| <i>DM candidate</i>         | I.<br>$\Omega h^2$ | II.<br>Cold | III.<br>Neutral | IV.<br>BBN | V.<br>Stars | VI.<br>Self | VII.<br>Direct | VIII.<br>$\gamma$ -rays | IX.<br>Astro | X.<br>Probed | Result |
|-----------------------------|--------------------|-------------|-----------------|------------|-------------|-------------|----------------|-------------------------|--------------|--------------|--------|
| SM Neutrinos                | x                  | x           | ✓               | ✓          | ✓           | ✓           | ✓              | -                       | -            | ✓            | x      |
| Sterile Neutrinos           | ~                  | ~           | ✓               | ✓          | ✓           | ✓           | ✓              | ✓                       | ✓!           | ✓            | ~      |
| Neutralino                  | ✓                  | ✓           | ✓               | ✓          | ✓           | ✓           | ✓!             | ✓!                      | ✓!           | ✓            | ✓      |
| Gravitino                   | ✓                  | ✓           | ✓               | ~          | ✓           | ✓           | ✓              | ✓                       | ✓            | ✓            | ~      |
| Gravitino (broken R-parity) | ✓                  | ✓           | ✓               | ✓          | ✓           | ✓           | ✓              | ✓                       | ✓            | ✓            | ✓      |
| Sneutrino $\tilde{\nu}_L$   | ~                  | ✓           | ✓               | ✓          | ✓           | ✓           | x              | ✓!                      | ✓!           | ✓            | x      |
| Sneutrino $\tilde{\nu}_R$   | ✓                  | ✓           | ✓               | ✓          | ✓           | ✓           | ✓!             | ✓!                      | ✓!           | ✓            | ✓      |
| Axino                       | ✓                  | ✓           | ✓               | ✓          | ✓           | ✓           | ✓              | ✓                       | ✓            | ✓            | ✓      |
| SUSY Q-balls                | ✓                  | ✓           | ✓               | ✓          | ~           | -           | ✓!             | ✓                       | ✓            | ✓            | ~      |
| $B^1$ UED                   | ✓                  | ✓           | ✓               | ✓          | ✓           | ✓           | ✓!             | ✓!                      | ✓!           | ✓            | ✓      |
| First level graviton UED    | ✓                  | ✓           | ✓               | ✓          | ✓           | ✓           | ✓              | x                       | x            | ✓            | $x^a$  |
| Axion                       | ✓                  | ✓           | ✓               | ✓          | ✓           | ✓           | ✓!             | ✓                       | ✓            | ✓            | ✓      |
| Heavy photon (Little Higgs) | ✓                  | ✓           | ✓               | ✓          | ✓           | ✓           | ✓              | ✓!                      | ✓!           | ✓            | ✓      |
| Inert Higgs model           | ✓                  | ✓           | ✓               | ✓          | ✓           | ✓           | ✓              | ✓!                      | -            | ✓            | ✓      |
| Champs                      | ✓                  | ✓           | x               | ✓          | x           | -           | -              | -                       | -            | ✓            | x      |
| Wimpzillas                  | ✓                  | ✓           | ✓               | ✓          | ✓           | ✓           | ✓              | ✓                       | ✓            | ~            | ~      |

Figure 1.15: Test of several dark matter candidates with all possible constraint. A ! is added if upcoming data at the publication time could probe significant areas of the parameter space. Table from [55].

## 1.5 Detection channels

In the previous section have been presented the different candidates for dark matter particle. Cosmology and observable suggest then the WIMPs as being the most favoured particles. In what follows will be reviewed the different channels available to test this hypothesis and attempt to discover WIMPs.

### 1.5.1 Supersymmetric particles production in particles colliders

By following the Relationship 1.75, such a particle can be directly produced at SM collider particles, like the Large Hadron Collider (LHC) at the European Council for Nuclear Research (written in French in the international acronym *CERN*) and represented in Figure 1.5.1. They could be then detected through missing mass in the total visible energy.

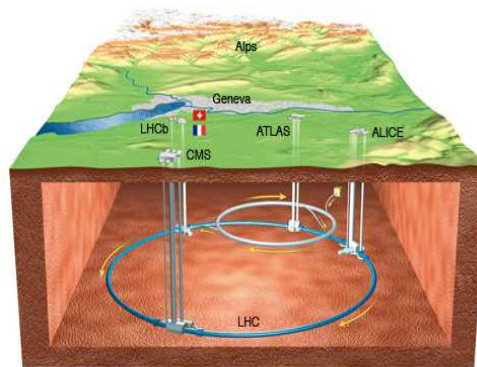


Figure 1.16: Artistic view of the Large Hadron Collider (LHC).

As it has been mentioned in Section 1.4.2.2, several supersymmetric particles have been purposed to describe dark matter. All of these possible scenarios for supersymmetric extension are currently tested at the LHC, mainly by the two experiments ATLAS (A Toroidal LHC Apparatus) and CMS (Compact Muon Solenoid). Up to date, no sign of supersymmetric extension were found [57] [58].

It is important to notice that if no sign of supersymmetric extension were found at the LHC, this would not mean that there is or there is not space for WIMPs. The opposite case, meaning SUSY discovery, is also true. SUSY and more especially neutralino, are theories in agreement with the WIMPs hypothesis, but WIMPs are not forced to be neutralino and vice-versa. In case of neutralino discovery, then only a precise measurement of their properties would gives informations on their abundance in the Universe, leading to conclusions on their contribution to dark matter.

### 1.5.2 Dark matter indirect detection

As shown by the Relation 1.75, dark matter annihilations are supposed to lead to SM particles creations. For this research channel, called *indirect dark matter detection*, excess of SM particles in cosmic rays are searched. Since annihilation rate is by definition related to dark matter density, regions with an expected high DM density will be favoured. This includes the galactic center or

neighbourhood of the sun, but also the spheroidal dwarfs satellite galaxies around the Milky Way that are supposed to be the most dark-matter-dominated objects [59].

This analysis can be run either in space, like with the FERMI-LAT satellite [59] or the AMS-02 experiment [60] [61] in the International Space Station (*ISS*), or directly on Earth, like with the Ice-Cube [62] and HESS-II [63] experiments, or with the future experiment CTA [64].

Several messengers can be thus studied through this channel. There are then charged particles, that could have provided an excess signal at high energy due to a higher fraction of positron over electron than expected, firstly seen by the PAMELA satellite [65] and confirmed then by FERMI-LAT [66] and AMS-02 [67], see Figure 1.17(a). However, this excess does not constitute a clear evidence of dark matter annihilation since some astrophysical objects like pulsars could explain it [68]. In a more general way, using charged particle leads to the loss of any possible information on the emission direction, since charged particles can be deviated during their travel.

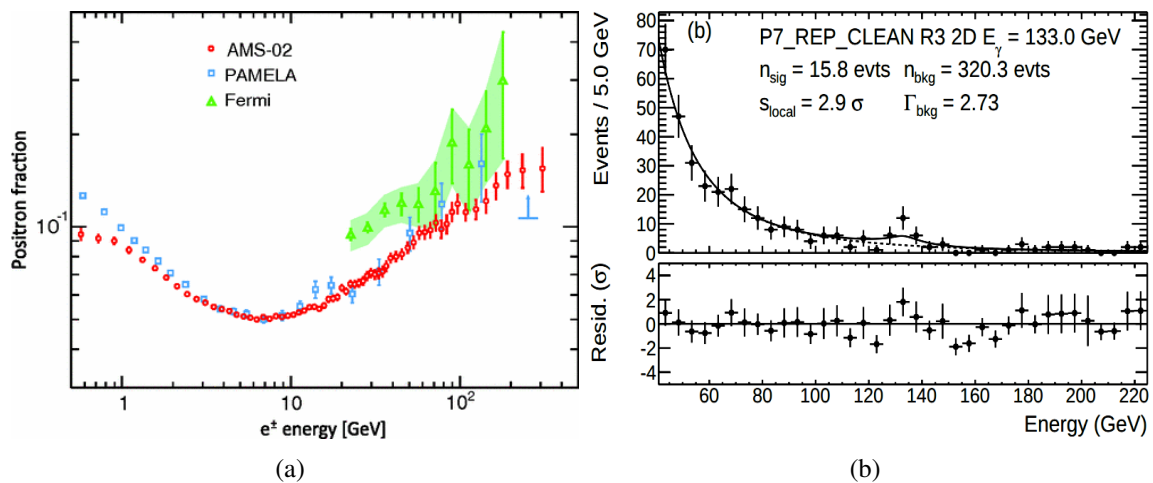


Figure 1.17: (a) Excess of positron over electron fraction at high energy, (b) Excess of  $\gamma$  ray at 133 GeV. Pictures from [67] and [69] respectively.

In addition to charge cosmic rays, neutral cosmic can be also considered. More especially, gamma rays have recently provided a nice excess signal by the FERMI-LAT satellite a  $4.5\sigma$  of local significance in a preliminary analysis after 3.7 years of data taking [69]. This significance was then successively lowered down to  $4.1\sigma$  after data reprocessing and to  $3.3\sigma$  by using a 2D fit. Finally, by adding new data acquired in the following months, this significance fell down to  $2.9\sigma$  after 4.4 years of data taking, see Figure 1.17(b). This fluctuation of  $\sim 10\%$  of the local significance by adding the new data was however in the statistical acceptance of either dark matter signal or null signal hypothesis, and only additional data could provide clear conclusion.

The last messenger are neutrinos that are interesting candidates for directional detection since they have also unperturbed propagation. However compared to photons detected with the same target, they would need a larger WIMPs annihilation rate into these neutrinos to provides same significance, because of their low scattering cross-sections.

As a conclusion on this section, while it is true that up to now no clear signal of dark matter has been seen, several channels have provided very interesting results, that are very encouraging for further researches.

### 1.5.3 Dark matter direct detection

The last possible detection channel for dark matter detection consists then in investigating dark matter elastic scattering inside target material. This process is expected to lead to nuclear recoil of the encountered atom [70] following pool principle, as it is illustrated by Figure 1.18.

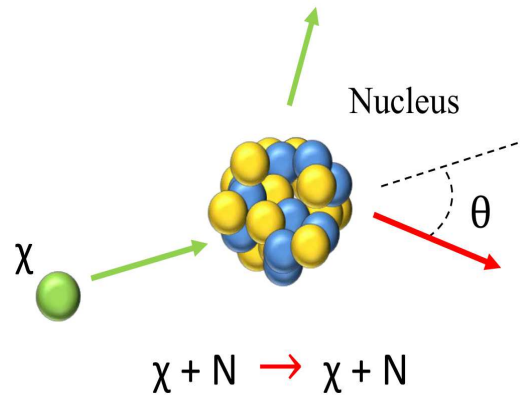


Figure 1.18: Direct dark matter detection principle.

This detection channel is known as *direct detection*, through which will be measured the associated recoil energy. Such a signal is within few keV up to about 100 keV energy range, and can be calculated using:

$$E_R = \frac{m_\chi v^2}{2} \frac{4 m_N m_{\chi}}{(m_N + m_{\chi})^2} \cos^2(\theta_r) \quad (1.80)$$

There are then different ways to detect this recoil, and the associated energy. The analysis consists then in using either one of the three possible signals among the *heat*, *ionisation* or *excitation* signals, or combining two of them. These different strategies are illustrated by Figure 1.19, including the name of the associated main experiments that will be approached in the next section.

One of the main aspect of the dark matter direct detection channel is the expected interaction rate  $R$  per unit of recoiling energy  $E_R$  that, by assuming a Boltzmann distribution of the dark matter velocities, can be expressed as [71, 72]:

$$\frac{dR}{dE_R} = \frac{\sigma_0 \rho_0}{4v_e m_\chi m_r^2} F^2(q) \left[ \text{erf} \left( \frac{v_{min} + v_e}{v_0} \right) - \text{erf} \left( \frac{v_{min} - v_e}{v_0} \right) \right] \quad (1.81)$$

where  $\sigma_0$  is the expected wimp-nucleon cross section for a zero momentum transfer, and  $v_e$  is the Earth velocity with respect to the WIMPs halo in the Milky Way. In particular, since our Solar System is travelling in the galaxy, and since the Earth is rotating around the sun, this velocity can be express through  $v_e = v_0(1.05 + 0.07\cos(\omega t))$ , with  $v_0$  usually equal to 220 km/s. The term  $1.05 \times v_0 \sim 230$  km/s expresses the galactic velocity of the Sun, while the second member expresses the velocity modulation due to Earth position around the Sun [72, 73], as illustrated by Figure 1.20.

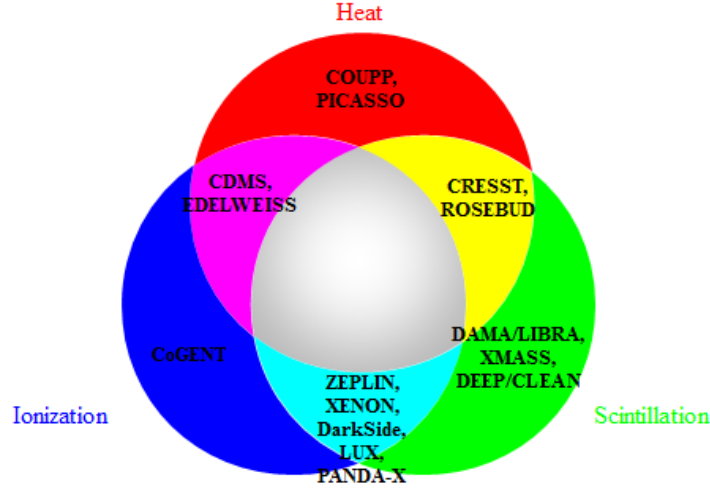


Figure 1.19: (b) Description of signal(s) used by the main direct dark matter experiments.

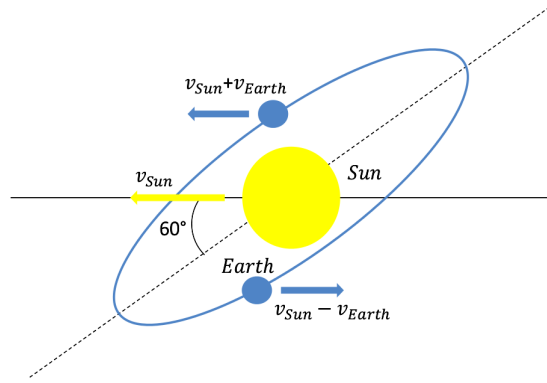


Figure 1.20: Illustration of the contribution of the Earth's motion around the Sun to the total Earth velocity respect to the WIMPs halo.

Then, the other members of the Equation 1.81 are defined such as  $\rho_0$  is the expected local WIMP mass density, and is usually  $\sim 0.3 \text{ GeV.cm}^{-3}$  like in [74],  $m_\chi$  is the WIMP mass, and  $m_r$  is the reduced mass defined through  $m_r = (M_n M_\chi)/(M_n + M_\chi)$ , where  $M_n$  is the nucleus mass. The term  $F(q)$  is the nuclear form factor associated to the momentum transfert  $q = \sqrt{2M_n E_R}$  [71], and  $v_{min} = \sqrt{(m_N E_R)/(2m_r^2)}$  is the minimal velocity requested to have impulsion transfer [72].

As a complement to this formula, in order to measure or constrain WIMP-nucleus cross-section, WIMP are assumed to follow Maxwellian distribution, with velocity smaller than the galaxy escape velocity  $v_{esc} = 544 \text{ km.s}^{-1}$  [72, 75].

Moreover, for direct detection, two kind of coupling can be considered, *scalar* and *axial*. The first one involves scattering of WIMP with nucleus as a whole, and is known as *Spin-Independent coupling (SI)*. This scattering is illustrated in Figure 1.21(a), and would lead to a Higgs boson or squark exchanged. The second coupling process involves the scattering of WIMP with only either neutron or proton of the nucleus, and is known as *Spin-Dependent coupling (SD)*, illustrated in Figure 1.21(b) with gauge boson or squark exchanged. This latter coupling implies to rewrite the nuclear form factor in order to take into account the two separated contributions of protons and

neutrons. For the two types of coupling, the squark exchange seems however to be excluded [76]. The results from the two analysis channels performed by the XENON100 experiment will be presented in Section 3.4.2.

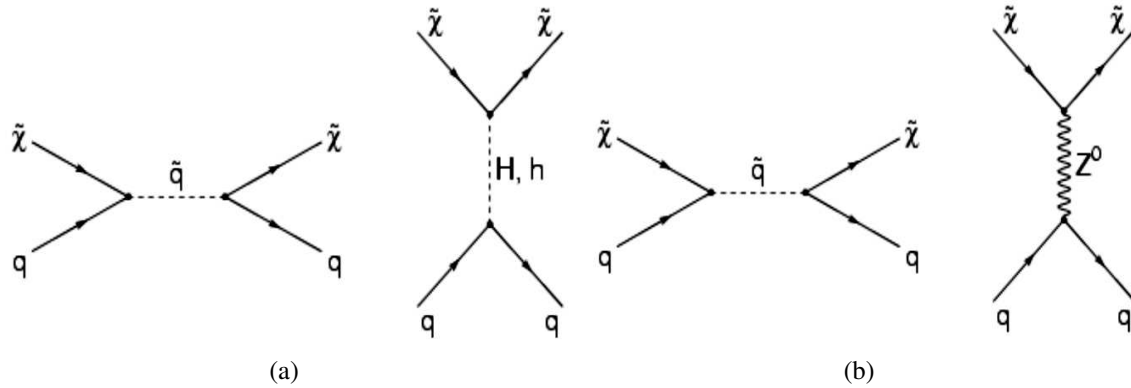


Figure 1.21: Feynmann diagrams for dark matter scattering (a) through Spin Independent scenario, (b) through Spin Dependent scenario.

By using Relation 1.81, the evolution of the expected WIMPs interaction rate as a function of the recoil energy for the different target materials used by the current experiments can be calculated, assuming WIMP mass and cross-section. This is illustrated by Figure 1.22.

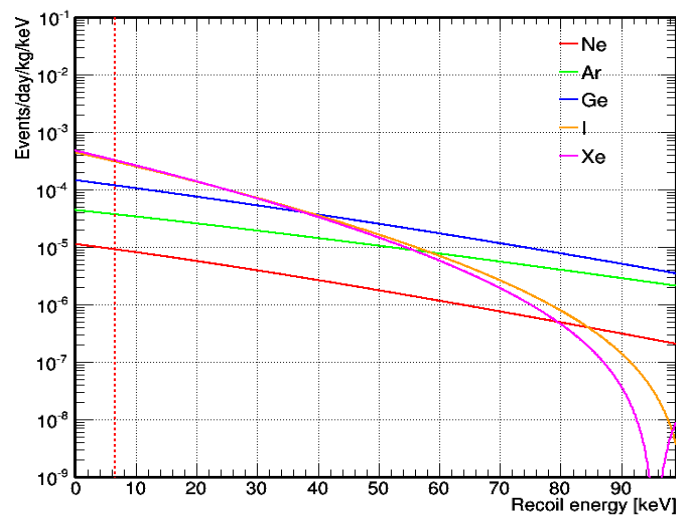


Figure 1.22: Illustration of the expected WIMPs interaction rate as a function of recoil energy for several target materials, assuming WIMP mass and cross-section at  $100 \text{ GeV} \cdot \text{c}^{-2}$  and  $10^{-44} \text{ cm}^{-2}$  respectively. The vertical dashed line illustrates the analysis threshold on the recoiling energy set at 6.6 keV for the results published in 2012 by the XENON100 experiment [74]

It shows then that heaviest target materials, such as iodine and xenon are favoured for having higher statistics. This can be understood by reducing the WIMP cross section presented in Section 3.4 to a proportional dependence with the square of the atomic mass of the target material once all astrophysical parameters are fixed:  $\sigma_0 \propto A^2$ .

Moreover, it can be seen that, whatever the target material is, the expected interaction rate is much higher at low recoil energy than at high recoil energy. Having a low recoil energy detection

threshold to take benefits of this distribution is then one of the biggest challenge of all direct dark matter experiments. As an illustration, the vertical red dashed line in Figure 1.22 represents the XENON energy threshold at 6.6 keV for results published in 2012 [74]. The feature of the xenon curve at high recoiling energy is due to the expression of the form factor [71].

As a complement, direct detection experiments aim to see ultra-rare events that would be detected among lots of interactions due to other particles. This means that this latter interactions, called background events, need to be reduced as much as possible. This is then the key point of direct dark matter experiments. These background events can be then divided into two terms, the background events from cosmic rays and the background events from the environment of the detector and from the detector components. In order to reduce the former, as it will be seen in the next section and, most of the experiments are placed underground, but this is however not always the case. For example, such experiments can also be placed deep under ice in South Pole, like with the *DM Ice* experiment. Then for the second type of background, it is only a combination of good shielding and clean materials that would allow to reduce it, as it will be discussed for XENON100 in the second chapter.

This concludes this section on dark matter detection. In what follows will be approached the different techniques developed for direct dark matter detection.

## 1.6 Direct dark matter experiments

As it has been seen in the previous section, there are different types of signals that can be measured for direct dark matter search. They consist in *heat*, *excitation* and *ionisation* signals, that can be used separately or into a combination of two of them, in order to highlight a dark matter interaction inside a detector. In the following developments will be presented how such signals are used by the several direct dark matter experiments. Most of the experiments approached here have their results presented in Section 3.4 for comparison with XENON100, with up-to-date no clear sign of a dark matter detection.

### 1.6.1 Directional detection

Before having a look to the comparison of all the different targets used for direct dark matter detection, the directional direct detection project will be presented. Among all of the experiment that aim to this detection, there are *DM – TPC* (UK-USA), *DRIFT* (UK-USA), *MIMAC* (France), or *NEWAGE* (Japan) projects, that are described in [77]. The principle of directional detection follows the illustration of dark matter interaction rate annual modulation shown in Figure 1.20, but at larger scale. Indeed, due to the Earth motion, this time not around the sun, but around the galactic center, it is expected to see a privileged incoming WIMPs direction, that background sources such as neutrons would not have.

Thus, the aim of directional direct dark matter experiments is to combine target with enough high expected WIMPs interaction rate, e.g. by using a fluorine compound, with a Time Projection Chambers (TPC) able to show in three dimensions the nuclear recoil direction, as illustrate in Figure 1.23 for the MIMAC experiment. All along the track of an incoming particle inside the

detector, some electrons/ions pair will be created by ionisation. Thanks to the application of an electric drift field, the electrons can be collected on a segmented anode. This allows the reconstruction of the  $(x,y)$  position to each scattering, while the  $z$  coordinate is obtained by knowing the electron drift velocity. Up to date, all of these experiments are still in R&D status, with some of them that have started acquiring few dark matter data, but that are currently not able to be as competitive as the other direct dark matter experiments. Moreover, since the aim of this detection channel is the reconstruction of the incoming direction for dark matter particle, it would request thus larger volume than for standard detection.

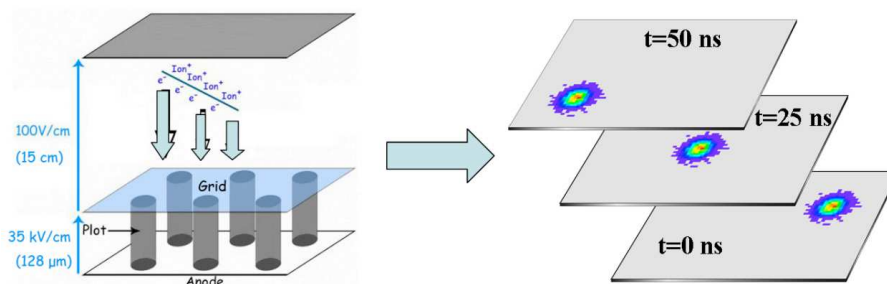


Figure 1.23: MIMAC directional direct dark matter detection principle. Picture from [77]

## 1.6.2 Bubble chambers

Among all the other different techniques developed for direct dark matter detection, there are also bubble chambers that are among the most sensitive experiments on SD analysis, especially through WIMP-proton coupling [78]. The different experiments that use this technique are *COUPP* [79] and *PICASSO* [80] experiments, installed in *SNOLAB* (extension of the Sudbury Neutrino Observatory laboratory) in Canada, and the *SIMPLE* [81] experiment installed in *LSBB* (French acronym for Low Background Underground Laboratory) in South of France. The particularity of such a technique is that in the case of the *COUPP* experiment, ultrasound analysis is combined with optical trace (one single bubble expected for a WIMP scattering) for incoming particle differentiation, while for the other experiments the differentiation is more focused on coincidence rejection (*SIMPLE*) and ionisation density rejection (*PICASSO*). All of the recent results provided by this experiments can be seen in Section 3.4, with up-to-date no sign of dark matter detection.

## 1.6.3 Annual interaction rate modulation

One of the other possibilities for a dark matter direct detection consists in analysing the annual modulation of background interaction rate in a detector, using either scintillation or ionisation signal. Indeed, considering the annual modulation of the Earth velocity with respect to dark matter halo, as described in Figure 1.20, it is expected that the WIMPs interaction rate is maximum in June and minimum in December. Such an analysis was firstly made by *DAMA* experiment, at

LNGS (Italian acronym for Gran Sasso National Laboratory) in Italy that has reported for the first time a positive signal for direct dark matter detection [82], using NaI scintillating crystals. Their several upgrades, up to the current one called *DAMA – LIBRA* have led to the same signature [83], recently independently confirmed by *CoGeNT* in case of non-Maxwellian dark matter halo velocity [84]. Both results are represented by purple and red contours respectively on Figure 1.24. In comparison to the DAMA experiment, the CoGeNT one uses the same detection principle, but with germanium detectors. As a result, while the former uses the scintillation signal, the latter uses the ionisation signal for particle detection, as previously presented in Figure 1.19.

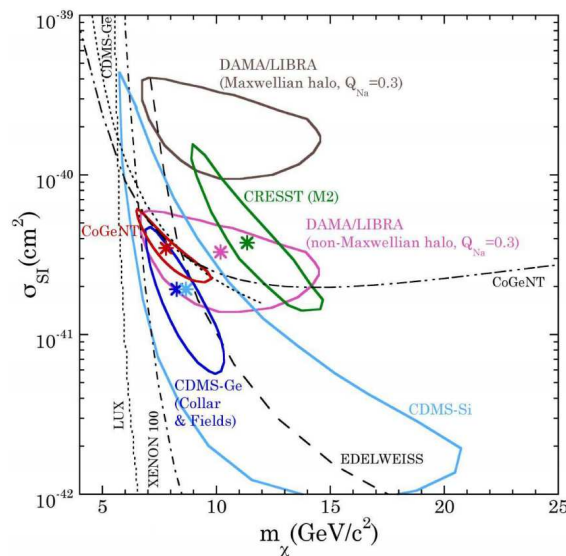


Figure 1.24: *CoGeNT* latest annual modulation results compared to other direct dark matter experiments results. Picture from [84].

The publications of positive dark matter signals by each of these two experiments have led to huge controversy, since several other direct detection experiments with higher dark matter SI interaction sensitivity, namely with xenon technology, but also some with Germanium detectors, have never seen positive signals. A possible explanation of those signals could be done by the introduction of a low mass WIMP component into dark matter halo [84]. Several other hypothesis have been proposed in order to explain these signals by a specific dark matter coupling (inelastic, WIMP-electron coupling ...). However, none of them has succeeded to convince the community, since several experiments with higher detection sensitivities have seen no sign of dark matter up to date. Among all the efforts made by direct detection community to improve their own detector sensitivity, a strong one is made to improve low energy detection threshold to give a clearer answer to such signals, as it is recently the case for the XENON collaboration by using  $^{88}\text{Y}^9\text{Be}$  calibration.

### 1.6.4 Cryogenic detectors

Cryogenic detectors are bolometers detectors, cooled down to few tens of mK. Among them, two types of detectors can be found. They combine with the *heat* signal either a *ionisation* signal (semiconductor bolometers) or a *scintillation* signal (scintillating bolometers).

### 1.6.4.1 Cryogenic semiconductor bolometers

Two main experiments use cryogenic semiconductor bolometers: *CDMS* [85] that uses silicon and germanium bolometers at the *Soudan* Underground laboratory in USA, and *EDELWEISS* [86] that uses germanium bolometers at *LSM* (French acronym for Modane Underground Laboratory) in France. A WIMP scattering inside such a detector will induce both a small temperature increases and the ionisation of the crystal, as represented in Figure 1.25(a) for the germanium bolometers.

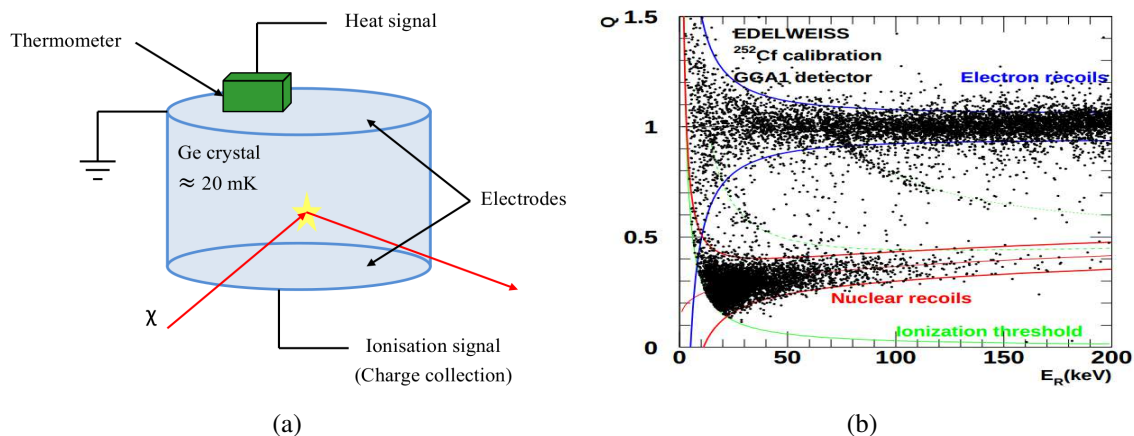


Figure 1.25: (a) Illustration of the WIMP interaction inside germanium bolometer, inspired from [87]. (b) Electronic and nuclear recoil bands obtained by *EDELWEISS I* experiment. Picture from [87].

The charges released by the ionization induced during the recoil will be collected by the electrodes, while the increase of the temperature will be monitored by thermocouples. The different ionisation rate and temperature increase will be then used to separate electronic recoil (induced by penetrating  $\beta$  particles and  $\gamma$  rays) from nuclear recoil (induced by penetrating neutron and WIMPs particles), as it is illustrated in Figure 1.25(b) for *EDELWEISS I*, where  $Q$  expresses the combination between both heat and ionisation signals as a function of the energy recoil.

As an illustration, a deposited energy of 356 keV by an electron or a  $\gamma$  ray will lead to the emission of about 100 000 electrons-ions pairs during the recoil of the encountered electron, while there will be only about 30 000 electrons-ions for a nuclear recoil induced by a neutron or a WIMP particle, with the same deposited energy [88]. For the two types of recoil, the same increase of temperature will be identified. This factor of about 1/3 between the nuclear and electronic recoil bands can be also seen of Figure 1.25(b).

Up to date, no sign of dark matter interaction has been seen by the *EDELWEISS* experiment, leading to one of the most stringent limits of WIMPs-nucleons cross-section in 2010-2011 [86], up to the strong development of noble gas detectors, and whose results are compared to the *EDELWEISS* experiment in Section 3.4. In parallel, *CDMS* has also provided its own results. While for this experiment, no sign of dark matter signal was firstly seen [89] [90], the *CDMS* Collaboration has recently claimed a positive low-mass WIMP signature [85], as shown in Figure 1.24. As for the *DAMA* and *CoGeNT* experiment, this was also never confirmed either by the *EDELWEISS* experiment or by the xenon detectors (*XENON* or *LUX*). In order to become more

competitive with respect to noble gas detector, germanium community (*EDELWEISS + CDMS*) are currently discussing about a possible collaborations merging, in order to build a bigger germanium detector: The *EUREKA* project.

#### 1.6.4.2 Cryogenic scintillating bolometers

In a similar way to cryogenic semiconductor bolometers, some collaborations, like *ROSEBUD* [91] at the beginning of the 2000's in the *Canfranc* underground laboratory (Spain) and *CRESST* [92] in LNGS, use cryogenic scintillating bolometers by combining *heat* signal with *scintillation* signal, as it is illustrated in Figure 1.26 that presents the schema of a detection module of the *CRESST* experiment. As for the *CDMS* experiment, this latter experiment has recently claimed to a positive low-mass WIMP signature [92], never confirmed by any other direct detection experiment, but still in agreement with *CoGeNT* low-mass WIMP hypothesis. Much more recently, new results from the *CRESST* experiment [93] have excluded the very low-mass WIMP signal previously claimed. This signal, known as *M2*, is represented by green contour in Figure 1.24. For the other signal previously claimed by this experiment, known as *M1* and represented by the main grey contour in the results from all direct dark matter experiment presented in Section 3.4.1, the *CRESST* Collaboration aims to acquire more data in order to clarify the nature of this signal.

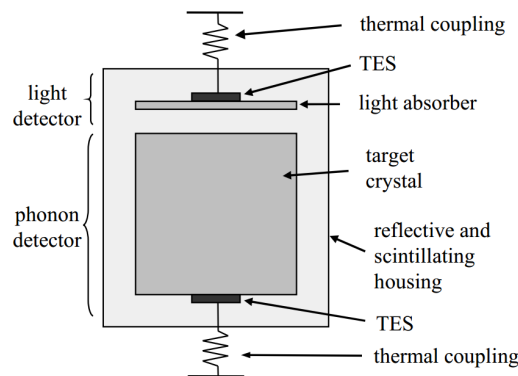


Figure 1.26: Schema of a detection module of the *CRESST* experiment. The emitted light due to the cristal excitation by the recoiling particle is seen by the light absorber, while the increase of the temperature is measured through the thermal couplings. Picture from [92].

While in a general way cryogenic bolometers present a better NR-ER bands discrimination than noble gas detector, they have however some construction size limits, namely because of cost. Indeed, for each additional module, only a small central part would contribute to the increase of the dark matter search volume: the fiducial volume. In parallel, the efforts made to keep the homogeneity of the detector from one module to another one could also partially explain this high cost, while for noble gas detector, the increase of the size of the detector is more easy simply because of requesting only the increase the device itself.

This review of direct dark matter experiments will be now concluded by noble gas detectors, starting by experiments that use argon as detector medium.

## 1.6.5 Noble gas detectors

Noble gas detectors usually use either argon or xenon (and eventually neon) in liquid phase ( $LAr$  or  $LXe$ , eventually  $LNe$ ) as target material, and can be either single phase detectors, or dual phases detectors. In this latter case, a Time Projection Chamber ( $TPC$ ) with liquid and gaseous phase of the same material will be used. The detection process presented here mainly refers to nuclear recoil. However, the same process occurs also for electronic recoils, but with different signals intensities, such as it is widely discussed in the next chapter for the xenon example.

### 1.6.5.1 Argon dark matter detectors

In this section, will be presented experiments that use argon as target material, firstly in dual phase mode, and then in single phase mode. Argon is a very interesting detector media due to its high stopping power and its high background discrimination capability. Furthermore, as all noble gases, argon allows to easily build scalable homogeneous detectors with stable cryogenic at about  $-180^\circ$ . Thanks to its self-shielding property for external liquid regions, and thanks to the accurate scattering position reconstruction, a good fiducialisation can be done in order to reduce background exposition for final search volume. Finally, its high abundance in the atmosphere ( $\sim 1\%$ ) makes it also much cheaper not only than xenon, but also than bolometers. Thus, this argon extracted from the air can be easily used for performing R&D.

However, argon has two main disadvantages. The first one consists in its small wavelength emission light ( $\lambda = 128$  nm) that requests a light shifter to allow its detection. Then, the argon extracted from the atmosphere can not be used for dark matter search, due to the isotope  $^{39}\text{Ar}$ , a  $\beta^-$  emitter, that implies intrinsic background leading to sensitivity limitation. One of the possibility for low-background experiments with argon is then to use low-radioactivity argon, such as depleted argon or argon from underground gas wells. As a results, the cost advantage with respect to xenon is strongly reduced, because of the extraction or depletion cost.

### Argon dual phases detectors

Dual phase  $TPCs$  using either xenon or argon, combine *scintillation* and *ionisation* signals. Their emissions are induced by the excitation and the ionisation of atoms of the medium used for the detection by the recoiling particle. As a results, a WIMP scattering inside liquid phase of such detectors, as illustrated in Section 2.1 for the xenon example, leads to a first scintillation signal  $S1$  emitted by relaxation of excited atoms. These atoms were either excited by the recoiling particle or indirectly via the electron/ions recombinations after the ionisation atoms by the recoiling nucleus. In parallel, part of the electrons released during this ionisation step escape to recombination thanks to an electric field. They drift toward gas phase where they emit their own light signal, the ionisation signal  $S2$ . The ratio between these two signals allows the discrimination between electronic and nuclear recoils, as it is illustrated in Section 3.1.4 for the xenon case.

Among the dark matter experiments that use argon in dual phase time projection chamber, the  $WArP$  experiment [94] in LNGS can be firstly cited. It corresponds to the first argon dark matter experiment, but has however see no sign of dark matter interactions. Two other experiments have

been recently assembled: the *DarkSide* experiment [95] in LNGS and the *ArDM* [96] experiment in Canfranc, and have started to acquire data for dark matter search.

### Argon single phase detectors

The detection process in single phase noble gas chamber is similar to dual phase, with the exception that no drift field is applied. As a consequence, all the electrons released by the ionisation of atoms during the nuclear recoil will recombine. As for dual phase experiment, two excited states of the argon atoms will be produced: the singlet and triplet state. Each of them will have its own relaxation time. An advantage of the argon with respect to xenon is that the time difference between the two relaxation times is three order times larger for the former noble gas than for the latter, leading to a clear second scintillation signal few micro-seconds after the first one, such as presented in Section 2.3.3.1. Moreover, the two excited states will be created with different proportion for electronic and nuclear recoils. As a result the proportion between these two scintillation signals that will be used for background rejection. Thus, in order to maximize the light collection, single phase noble gas chambers have usually a spherical geometry, with Photo-Multiplier Tubes (PMTs) installed all around, since *scintillation* is in this case the only one available signal.

This technology is currently used at SNOLAB by the *DEAP* [97] and *CLEAN* [98] experiments. The latter would aim to build multi-ton noble gas single phase detector able to run either with LAr or with LNe. The purpose of this design is to be able to do an additional study on the interaction rate dependency on the square of the target atomic mass in case of WIMP positive signal, such as mentioned previously in Section 1.5.3.

#### 1.6.5.2 Xenon single phase detectors

As it will be seen in the next chapter, xenon detection properties are similar to argon's. The differences consist then in the liquid phase temperature, close to  $-90^\circ$ , and a higher expected rate as illustrated in Figure 1.22, due to its much higher atomic mass. A first advantage of the xenon is a cleaner intrinsic background since most of the isotopes of natural xenon are stable. Moreover, two of its isotopes that have an unpaired neutron,  $\text{Xe}^{129}$  and  $\text{Xe}^{131}$ , representing in abundance half of the isotopes of natural xenon, lead xenon to have higher sensitivity than argon for SD analysis.

The physical processes that occur in xenon single and dual phase chambers are similar to argon detectors, and will be more detailed for dual phase chamber in the next chapter. A xenon single phase experiment is currently used in Kamioka underground Observatory (Japan) by the *XMASS* experiment. The recent results from this detector on a low-mass WIMP analysis [99] presented in 2012, consisting in only few days of data taking, have led to a lower sensitivity than other xenon experiments, as represented on Figure 1.27. During this short data acquisition period, no sign of a WIMP interaction has been seen.

More recently, the *XMASS* collaboration has also presented result for possible inelastic WIMP nucleon scattering after 165.9 days of data in a 41 kg restricted analysis volume [100] with no sign of dark matter interaction. The purpose of a such analysis was to test the hypothesis that when

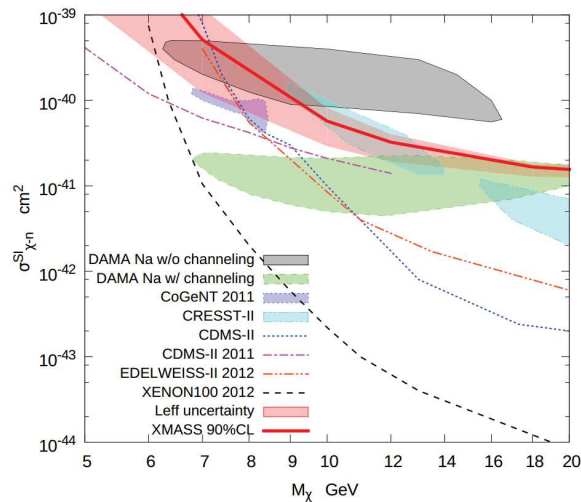


Figure 1.27: XMASS low-mass WIMP analysis results after 6.7 days with 835 kg of LXe. Picture from [99]

WIMP scatters off baryonic matter, this latter becomes excited, as it was previously suggested in order to explain *DAMA/LIBRA* observed annual modulation [101] [102].

The presentation of the detection principle for xenon dual phase detector, with an introduction to current and future experiments will be done in the next chapter.

As a conclusion to this section, it is important to notice that several detection techniques have been developed with the aim of a direct dark matter detection. For this purpose, several scenarios are always investigated by each experiment. These scattering channels are thus SI and SD WIMP coupling, but also low-mass WIMP or WIMP inelastic scattering analysis, WIMP-electrons coupling, axions ... None of them has provided a clear signature of dark matter so far, even if some experiments have claimed for positive signatures of possible low-mass WIMPs. It is then further detection improvements, mostly thanks to the oncoming new detectors generation, that would give clear answers, not only for such signals, but also for higher mass WIMPs.

## Conclusion

In this first chapter it has been presented many independent evidences that have led to not only the indication of dark matter and dark energy presence, but also to very consistent values between their expectations on the respective contribution of these two dark components to the Universe composition. Moreover, it has been also demonstrated the robustness of the cosmological WIMP hypothesis as a dark matter candidate, since particle physics provides independently some candidates through Standard Model extensions, such as neutralino, that have coherent expected properties with WIMP hypothesis. The final answer would be then obtained with their discovery, either according to the WIMP hypothesis or according to neutralino hypothesis.

To do this, huge efforts have been made now and in the past, investing many channels detection and WIMP interaction hypothesis. Up to now, no clear signals has been obtained, but several indications at the edges of the Standard Model appeared, either in indirect or in direct detection.

It will be then the acquisition of more and more data, and above all the improvements of the used detectors that would allow to get a clear answer on dark matter hypothesis.

In this context, it will be explained in the next chapters how the *XENON100* experiment works and contributes to lift the veil on this dark matter. It will be also seen how the next xenon detectors generation, leaded by the *XENON1T* experiment, would improve the sensitivity to such rare events.

# Chapter 2

## The XENON experiment

The operation of a dual-phase rare gas Time Projection chamber (TPC) through the example of the XENON100 detector is presented. After a presentation of the best models that describe the scintillation processes and charge attenuation during electrons drift, the main components of the TPC are detailed. It is also introduced the different background sources that affect XENON100, and which are common to most underground low background experiments. Then, the strategies developed for the xenon purification and cryogenic in the XENON100 experiment are presented, completed by details on the calibration procedure.

### Contents

---

|   |           |
|---|-----------|
| <b>Introduction</b> . . . . .                                   | <b>55</b> |
| <b>2.1 General principle</b> . . . . .                          | <b>56</b> |
| <b>2.2 Interaction of radiation with noble gas</b> . . . . .    | <b>57</b> |
| <b>2.3 From Interaction to light signals</b> . . . . .          | <b>61</b> |
| <b>2.4 Detailed description of the XENON detector</b> . . . . . | <b>72</b> |
| <b>2.5 Detector calibrations</b> . . . . .                      | <b>85</b> |
| <b>Conclusion</b> . . . . .                                     | <b>88</b> |

---

### Introduction

In the previous chapter were discussed all the experimental facts that have made dark matter one of the hottest topics in today's physics, including a review of almost all the techniques developed for the dark matter discovery. The present chapter will complete this review by describing the case of a rare gas low background dual phase TPC through the example of the XENON100 experiment.

The principle of the XENON100 TPC that transforms an interaction in the liquid phase of the detector into two measurable luminous signals will be firstly presented. A brief reminder on the main interaction processes of  $\gamma$  rays with matter will be then done, since they will be often

mentioned in the rest of this document. It will be followed by details on the models that describe the emission of the two signals.

The description of the main components of the detector will then allow to explain their detection. It will include a presentation of the processes used in XENON100 for the xenon purification and cryogenic. Details on the triggering and data acquisition are also given.

The presentation of the calibration procedure is then done, completed by a description of calibrations performed or planned post science run for R&D purpose.

## 2.1 General principle

The XENON dark matter program is a phase approach research program. It has started in the beginning of the 2000's, firstly with a very small dual phase xenon detector built as demonstrator (between few tens of grammes and few kilogrammes of LXe as target mass). Then, after a couple of years with the XENON10 detector, that contained about 15 kg of LXe (10 kg after fiducialisation). It has provided the first dark matter search results for the XENON program after a deployment at the LNGS underground laboratory in 2006 [103]. The data taken by this detector and re-analysed in 2011 [104] have also made XENON10 one of the most sensitive low mass WIMP detector still up to date.

Among all the others direct dark matter experiments with a LXe dual phase TPC, the experiments LUX [105], and very recently PandaX-I [106] for present examples and ZEPLIN-III [107] for a past example can be cited. These three detectors use or have used the same detector configuration than XENON100, with 250 kg (118 kg), 120 kg (37 kg) and 12 kg (5 - 6 kg) of LXe as target material (fiducial volume) respectively.

The current phase of the XENON program corresponds to the XENON100 detector that is illustrated in Figure 2.1. It corresponds to a 61 kg LXe dual-phase TPC surrounded by a veto volume of 99 kg of LXe as active shield. The diving bell process is then used to allow a Gaseous Xenon ( $GXe$ ) pocket inside LXe, as discussed in Section 2.4.5.

When an ionizing particle interacts inside the LXe, the encounter target, electron for a scattering  $\gamma$  ray or  $\beta$  particle, or nucleus for a scattering neutron or WIMP, will recoil. During this recoil, it will excite and ionize encountered xenon atoms. The recombination of part of electron-ion pairs will create additional excited xenon atoms. The relaxation of all these excited atoms will lead to a first scintillation signal in the LXe, called  $S1$ , following the process illustrated in Figure 2.2 and presented with more details in Section 2.3.3.1. Then, part of the released electrons will escape to recombination with ions thanks to a drift field of about 0.5 kV/cm created by potential difference between cathode and ground mesh as described at the end of this section. They will drift then toward the gas phase where they will be extracted and will emit a second scintillation signal, called  $S2$ . The intensities of the  $S1$  and  $S2$  signals will depend of the type of the recoil, i.e nuclear or electronic. The processes that leads to such difference will be explained in the next section. As a result to this difference, the discrimination between nuclear recoils and electronic recoils will be done thanks to a different  $S2/S1$  ratio.

As a complement, it is also important to mention that xenon TPCs are also used for other research topics such as neutrinoless double beta decay physics with the EXO-200 experiment [109]

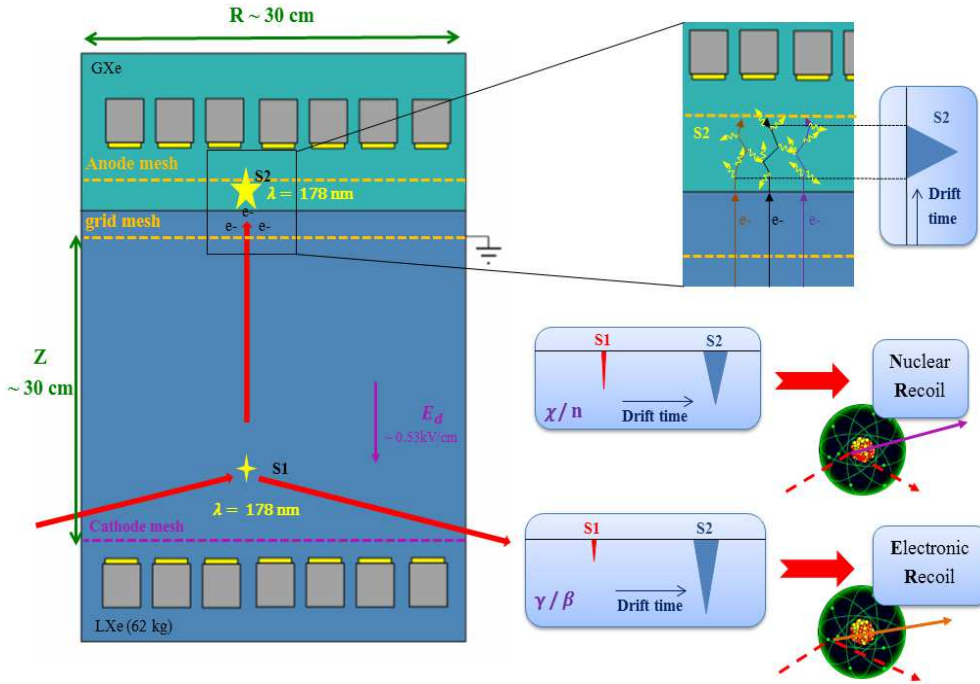


Figure 2.1: XENON100 TPC principle

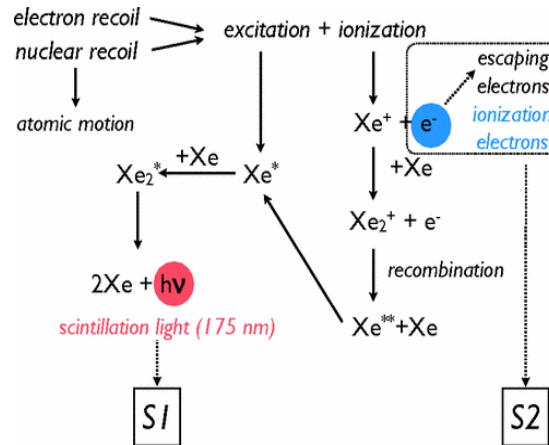


Figure 2.2: Scintillation and ionisation signals emission scenario, from [108].

that used single phase TPC with  $\sim 130$  kg of LXe enriched in  $^{136}\text{Xe}$ , but also for medical imaging with a Compton telescope, as is currently developed for the XEMIS project by the SUBATECH xenon group [110], consisting in a single phase xenon TPC with  $\sim 16$  kg of LXe for the prototype XEMIS1 and with  $\sim 130$  kg of LXe for the small animal imager XEMIS2.

## 2.2 Interaction of radiation with noble gas

In the XENON100 TPC, the background is mostly dominated by electronic background, corresponding to recoiling electrons in the LXe. This background is mostly induced by  $\gamma$  rays, but also by  $\beta$  particles. Most of them are coming from components of the detector. Due to this high contribution of  $\gamma$  rays to the total background, it is important to discuss about the two main inter-

actions processes of  $\gamma$  rays in the LXe, the photoelectric effect and the Compton scattering. Their relative contribution to the photons scattering process in LXe as a function of the energy of these photons is illustrated by Figure 2.3. The purpose of this reminder is to ease the understanding of the rest of this thesis since there will be several references to these scattering processes.

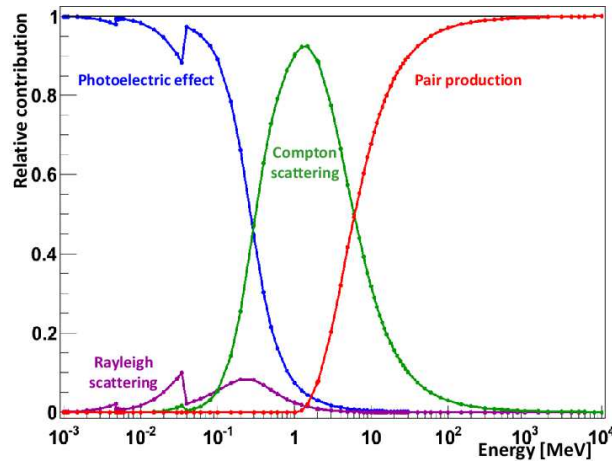


Figure 2.3: Relative contribution of the main photon interaction processes in xenon, picture from [111] with data from [112].

### 2.2.1 Photoelectric effect

The photoelectric effect corresponds to the interaction of an incoming  $\gamma$  ray with an electron from an external energetic layer of the encountered atoms, and during which the full energy of the  $\gamma$  ray is transferred to the electron. As a consequence, the  $\gamma$  ray vanishes and the electron is ejected with a kinetic energy that is equal to the difference between the original energy  $h\nu$  of the incoming  $\gamma$  ray and the energy needed to extract an electron from its energetic layer. This phenomenon is illustrated in Figure 2.4(a)

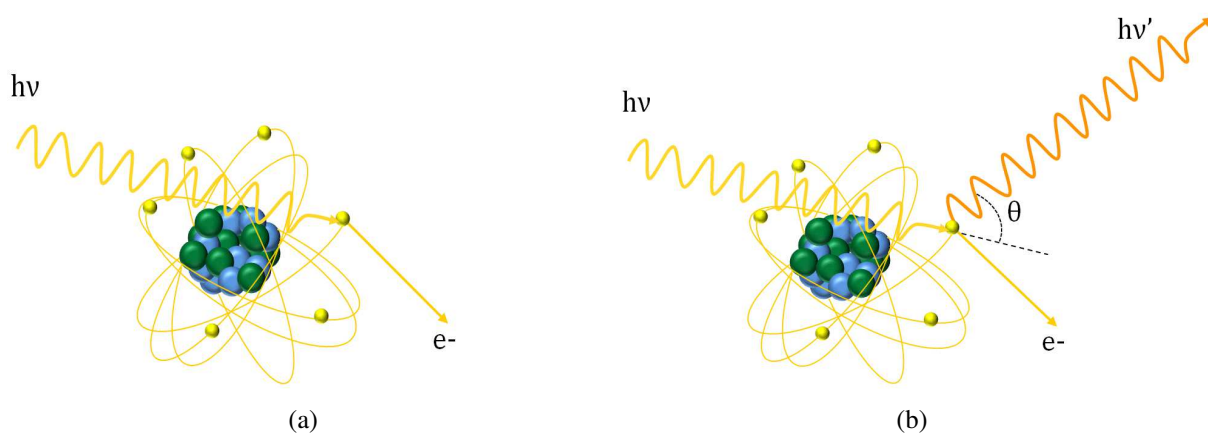


Figure 2.4: (a) Sketch of the photoelectric effect, (b) sketch of the Compton effect.

### 2.2.2 Compton scattering

In the case of the Compton scattering, the incoming  $\gamma$  ray does not transfer all of its energy, and is then re-emitted with a lower energy  $h\nu'$  that depends on its diffusion angle  $\theta$ :

$$h\nu' = \frac{h\nu}{1 + \alpha(1 - \cos \theta)} \quad (2.1)$$

where  $\alpha = h\nu/m_e c^2$ . Through this scattering process, the transferred energy  $T_e$  to the released electron after its extraction is then defined as follow:

$$\begin{aligned} T_e &\sim h\nu - h\nu' \\ &\sim h\nu \frac{\alpha(1 - \cos \theta)}{1 + \alpha(1 - \cos \theta)} \end{aligned} \quad (2.2)$$

The maximum value is obtained for  $\theta = 180^\circ$  (back scattering), and is equal to:

$$T_{e,max} = h\nu \frac{2\alpha}{1 + 2\alpha} \quad (2.3)$$

Since only part of the energy of the original  $\gamma$  ray is transferred, few successive scatterings can occur in the same target material, until the full transfer of the energy of the original  $\gamma$  ray. The Compton scattering is illustrated in Figure 2.4(b). Several others  $\gamma$  ray scattering processes can also occurs, but at the [0.1 - 10] MeV energy range, the typical energy range of background  $\gamma$  rays in XENON100, they have much less probability to occur in LXe, as illustrated in Figure 2.3.

Moreover, at the typical energies of  $\beta$  particles in the XENON detectors, *i.e* also at the [0.1 - 10] MeV energy range, a process similar to the Compton scattering mostly occurs when involving an electron as incoming particle. The encountered electron will be then extracted by carrying part of the energy of the scattered electron. The latter will thus continue its way with a diffusion angle and a lower kinetic energy down to thermalization after successive scatterings.

It is also important to notice that all the processes mentioned above for both  $\beta$  particles and  $\gamma$  rays lead to the ionization of the encountered atom by energy transfer, if the amount of transferred energy is sufficient to extract electron from the xenon atom. Vice-versa, if the transferred energy is not enough, then no electron-ion pair will be created and the encountered atom will remain in an excited energy state. In such case, the relaxation down to the atomic energy ground state is made thanks to photon emission, as it is discussed in Section 2.3.3.1.

### 2.2.3 Liquid xenon as a detector

As presented in Section 1.6.5.1, noble gases are in general very good media for particles detection, not only thanks to their fast response for the scattering of a particle through the simultaneous emission of both a scintillation signal and an ionization signal, but also thanks to their high stopping power that is related to their atomic masses (apart helium).

Among all of them, the heaviest one is the radon *Rn*. However, due to its very high intrinsic radioactivity, it would not be a good candidate for particle detection. The best noble gas candidate as detector media that appears then is the xenon *Xe*. A review of the main physical properties of the liquid xenon is made in Table 2.1. Some of them, such as the average ionization energy  $W$ , will be discussed in the following chapters.

| <b>Xenon properties</b>  | <b>Values</b> |
|--|---------------|
| Atomic number  | 54            |
| Average atomic mass [g.mol <sup>-1</sup> ]   | 131.3         |
| Density [g.cm <sup>-3</sup> ] [113]  | 2.827         |
| Ionization potential in liquid phase [114] [eV]                                    | 9.28          |
| Average ionization energy $W$ [115] [eV]   | 15.6 ± 0.3    |
| Energy needed for scintillation photon creation in LXe from $\beta$ ray [114] [eV] | 21.6          |
| Scintillation peak [114] [nm]  | 178           |
| Dielectric constant in LXe [116]   | 1.96          |
| Singlet energetic state $1\Sigma_u^+$ time relaxation [114] [ns]                   | 3             |
| Triplet energetic state $3\Sigma_u^+$ time relaxation [114] [ns]                   | 27            |

Table 2.1: Xenon main properties

On the other hand, the lightest noble gas, the helium *He*, is not enough dense with respect to other target materials in general to be usually used for particles detection. It is however a very interesting and useful noble gas for particle physics. Indeed, thanks to its fast diffusion in air due to its very light mass, helium can be used for detector leak check. It is also used for the cooling of many detectors and medical devices such as Magnetic Resonance Imaging (*MRI*) thanks to its very low liquefaction temperature<sup>7</sup>. By taking advantage of this property, this gas is used for the cooling of the xenon with the Pulse Tube Refrigerator (PTR), such as mentioned in Section 2.4.4.

As detector media, all noble gases from neon *Ne* up to xenon present similar advantages, such as the possibility to create homogeneous detection volumes at a reasonable cost, with high particle stopping powers that depend roughly on the density of the material. They present also the advantage of an accurate interaction position reconstruction thanks to fast scintillation response and ionisation signal in presence of drift field, and the low transverse diffusion for drifting electrons. This allows the exploitation of their self-shielding capacity through fiducialisation.

Finally, in case of the xenon, in addition of being the noble gas with the best stopping power - radon excluded for the reason explained above - it also presents the property of having almost no intrinsic radioactivity, since all isotopes of xenon found in nature are stable, or long-life double-beta emitter (<sup>136</sup>Xe, Half-life:  $\tau \sim 10^{21}$  yr). This property is crucial for low background experiments. As an illustration, the natural abundance of xenon isotopes in atmosphere is given by Table 2.2.

Moreover, xenon is also able to provide SD cross section sensitivity as discussed in Section 1.6.5.2. A comparison of different properties of the several noble gases is made in Table 2.3.

In a more practical point of view, xenon presents also the property of having a very stable and simple cryogenic at about -91°, while lighter noble gas will request lower temperatures for their

<sup>7</sup>Helium is liquefied at 4.2 K at atmospheric pressure

| Isotope               | $^{124}\text{Xe}$ | $^{126}\text{Xe}$ | $^{128}\text{Xe}$ | $^{129}\text{Xe}$ | $^{130}\text{Xe}$ | $^{131}\text{Xe}$ | $^{132}\text{Xe}$ | $^{134}\text{Xe}$ | $^{136}\text{Xe}$ |
|-----------------------|-------------------|-------------------|-------------------|-------------------|-------------------|-------------------|-------------------|-------------------|-------------------|
| Natural abundance [%] | 0.09              | 0.09              | 1.92              | 26.44             | 4.08              | 21.18             | 26.89             | 10.44             | 8.87              |

Table 2.2: Xenon isotopes natural abundance, table from [117].

| Element (liquid phase)                         | LHe   | LNe   | LAr   | LKr  | LXe   |
|--|-------|-------|-------|------|-------|
| Atomic number                                  | 2     | 10    | 18    | 36   | 54    |
| Atomic mass [ $\text{g}\cdot\text{mol}^{-1}$ ] | 4.0   | 20.18 | 39.95 | 83.8 | 131.3 |
| Density [ $\text{g}\cdot\text{cm}^{-3}$ ]      | 0.145 | 1.2   | 1.40  | 2.41 | 3.06  |
| Average ionization energy $W$ [eV]             | 40    | 26    | 23.3  | 20.5 | 15.6  |

Table 2.3: Several properties of noble gas, table from [118].

cryogenic.

## 2.3 From Interaction to light signals

In the present section will be detailed the processes that rule the energy deposition for electron and nucleus in LXe during their recoil. The purpose of this section is to explain the proportion of the scintillation signal  $S1$  and of the ionisation signal  $S2$ , that is induced by the electrons that drift toward the gas phase thanks to the applied drift field. This will then demonstrate that the relative intensities of these two signals depend on the type of the recoiling particle, providing thus an observable quantity, the  $S2/S1$  ratio, that has a good discrimination power for the identification of the type of the recoiling particle.

It will be thus seen that the processes that occur are not always very well known or understood, because of the low recoil energy range that is between few keV up to 100 keV for the application considered here, and because of the type of the recoiling particle, especially for nuclear recoils where for the present example a xenon nucleus is involved.

### 2.3.1 Stopping power in liquid xenon

In this section will be considered separately the two types of recoil, electronic and nuclear, that are induced by the scattering of an incoming particle inside the liquid phase of the XENON100 detector. As a result, only energies between few keV up to about 1 MeV for the recoiling particle will be considered.

#### 2.3.1.1 Electronic recoils

Electronic recoils correspond to scatterings off electrons of the encountered atoms, and are produced by  $\gamma$  rays or  $\beta$  particles. When  $\gamma$  rays interact in the liquid phase, in most of the cases photoelectric effects or Compton scatterings occur, as illustrated by Figure 2.3 from [112], due to their energies that are mostly at the [0.1 – 10] MeV energy range. In case of electron as ionizing particle, part of its energy is transmitted to one electron of the encountered atom [111]. This latter

electron will be then more energetic than its orbital state and will thus move to a higher one. If the energy received by this electron is enough to allow the extraction, then the atom becomes ionized and the released electron will follow one of the two scenarios illustrated in Figure 2.2, i.e. recombination or drift toward the gas phase.

In the opposite case, the excited atom will release additional energy by ultraviolet photon emission, also as illustrated in Figure 2.2. Such phenomenon occurs not only for the initial ionizing electron, but also for all of the recoiling electrons, including those released by  $\gamma$  rays, and that are enough energetic to escape to either recombination with xenon ions or capture by electro-negativity, as long as they keep enough energy to not drift toward the gas phase due to the electric field.

For charged particle in motion inside a media, their energy deposition per length unit  $dE_c/dx$ , that is due to interactions with electrons from atoms of the media, can be expressed by using the Bethe formula. In the energy range of 10 keV – 1 MeV, and for the case of the electron as being the charged particle since the electronic recoil is considered here, this formula can be simplified as:

$$-\frac{dE_c}{dx} = \frac{4\pi nZ(\alpha\hbar)^2}{m_e v^2} L \quad (2.4)$$

where  $n$  is the electron density of the material,  $Z$  is the charge of the atoms that constitute this material.  $v$  is the velocity of the scattering particle, hence the recoiling electron, and  $m_e$  is the electron rest mass.  $\alpha$  is the fine structure constant and  $\hbar$  is the reduced Planck constant. The term  $L \approx \ln(m_e v^2)/(2\hbar\langle\omega\rangle)$  is the stopping number, where  $\hbar\langle\omega\rangle$  is the average energy needed for the excitation of the encountered atom by the particle in motion. In the present section, only recoiling electrons will be considered as such particles.

Moreover, for the case of the liquid xenon,  $nZ = 7.6 \cdot 10^{29} \text{ e}^-/\text{m}^3$ , and  $\hbar\langle\omega\rangle \approx 0.5 \text{ keV}$  leading to the expression:

$$-\frac{dE_c}{dx} [\text{MeV}/\text{cm}] = \frac{0.39 [\text{MeV}/\text{cm}]}{\beta^2} L \quad (2.5)$$

where  $\beta = v/c$  with  $c$  the light celerity, and with  $L$  that varies between 3 and 7. As an illustration, the energy deposition per length unit for a recoiling electron in LXe as a function of its energy is presented in Figure 2.5.

Thus, the loss of energy follows the Bohr model, where the scattering particle transfers its energy to a target electron that is considered to be in rest state. There are then kinematic possibilities for a high deviation of the propagation direction of the recoiling particle after the scattering with respect to its original propagation direction. By taking into account that electrons can be exposed to such a high deviation, the loss of energy can be understood as a thickness covered by the recoiling particle, usually known as *practical range*. It varies from few micrometers up to few millimeters for an original energy of the recoiling electron within the [10 keV – 1 MeV] energy range.

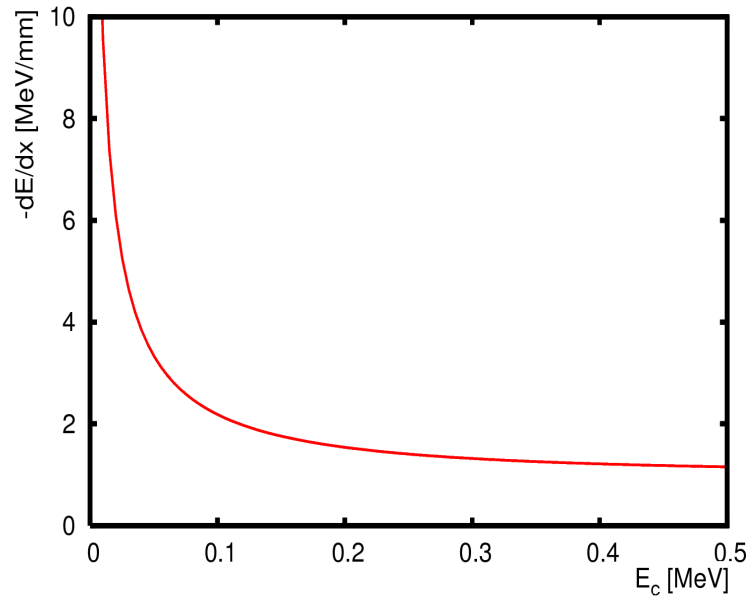


Figure 2.5: Illustration of the energy deposition per length unit for a recoiling electron in LXe as a function of its energy.

In order to be more precise on the way how the energy is deposited all along the particle range, a model based on two behaviours can be considered [119], such as illustrated by Figure 2.6.

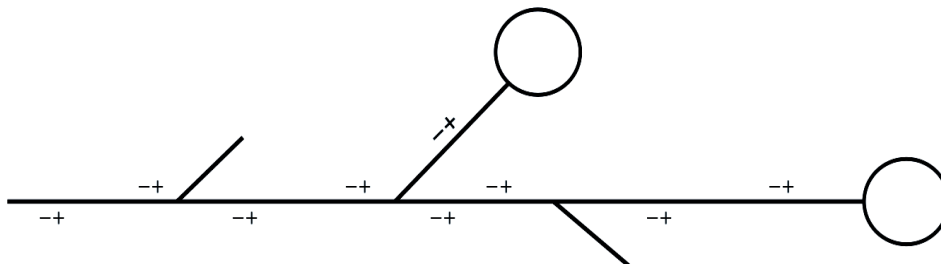


Figure 2.6: Illustration of the two components energy deposition model. See the text below for explanations.

The lines illustrate random walk from left to right, for an electron that is still energetic ( $E_c > [25 - 50]$  keV), and for which each energy loss is of the order of the minimum ionisation potential of the encountered atoms. The electron-ion pair that are thus created are represented by  $-+$  symbols. Some  $\delta$  emissions can also sometimes occur. Such emissions are represented by the additional secondary lines with respect to the main one.

The ending regions represented by circle illustrate then the second behaviour of the ionising particle track. These regions are usually named *blob*, and correspond to a high energy loss because of high ionisation density for electrons that have kinetic energy between 1 keV and 25 – 50 keV.

### 2.3.1.2 Nuclear recoils

Nuclear recoils correspond to scatterings on nuclei of the encountered atoms, and are expected to be produced by WIMP scatterings inside detector, following an early suggestion of direct detec-

tion of certain dark matter candidates [70], such as sterile neutrinos or supersymmetric candidates like sneutrino and photino.

Unfortunately, nuclear recoils do not belong only to dark matter particles. Neutrons can also perfectly mimic this signature thanks to elastic scattering with nucleus, corresponding to the main interaction process at energies close to MeV [120], the typical energies of incoming neutron that led to signals similar to the expected WIMP signature. At such energies, this process is combined with a non-negligible but distinguishable neutron inelastic scattering probability, as illustrated by Figure 2.7(a). These inelastic scatterings mostly involve  $^{129}\text{Xe}$  and  $^{131}\text{Xe}$  isotopes, but also possible  $^{19}\text{F}$  impurities, as illustrated in Figure 2.7(b).

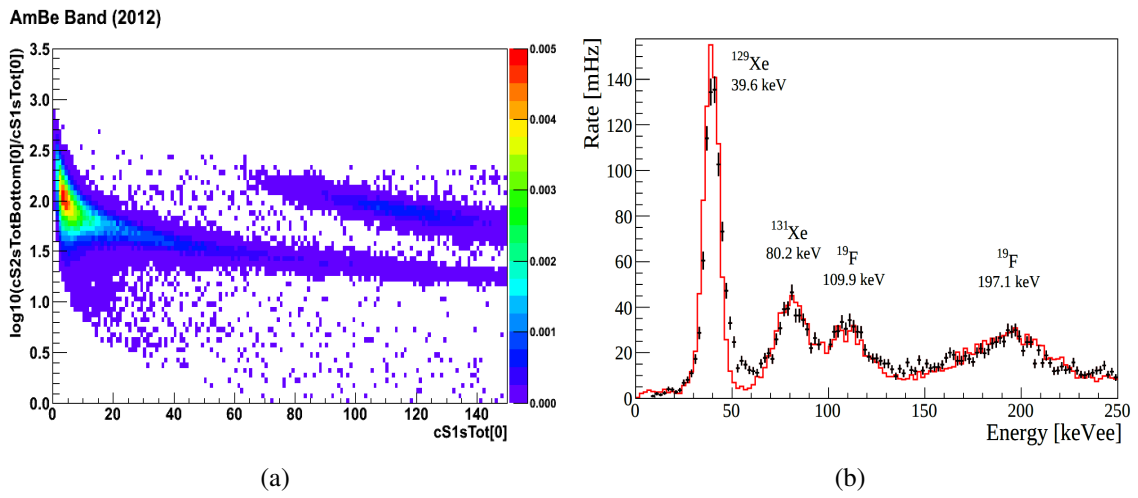


Figure 2.7: (a) Nuclear recoil band for XENON100 after  $^{241}\text{Am}^9\text{Be}$  calibration in spring 2012 with the additional 40 keV  $\gamma$  ray emission due to inelastic scattering over  $^{129}\text{Xe}$  isotope (cloud in the right top), (b)  $^{241}\text{Am}^9\text{Be}$  calibration spectrum (black marker) in combined energy scale corresponding only to electronic recoil interactions. Results from Monte Carlo simulations (red curve) are in very good agreement. Pictures respectively from [121] and [122].

For the two types of particle responsible to the nuclear recoil considered here, i.e. neutrons and WIMP, the velocity of a xenon nucleus in LXe is:

$$\beta = \sqrt{\frac{2E_c}{m_{\text{Xe}}c^2}} = (0.4 - 4) \cdot 10^{-3} \quad (2.6)$$

In such velocity range, an ion can capture some electrons very easily, and then can do its recoil with a charge state close to neutrality. During its recoil, two types of interaction can occur: either a scattering with an electron from an atom, or a scattering with a nucleus from an atom. As it will be seen below, the probability that one of these two processes occurs with respect to the other one depends on the velocity of the recoiling nucleus. Thus, the stopping power  $(dE_c/dx)_e$  by the electrons is [123]:

$$\left(-\frac{dE_c}{dx}\right)_e = 8\pi n \frac{(\hbar c)^2}{m_e c^2} K_e \frac{zZ}{z^{2/3} + Z^{2/3}} \frac{v}{\alpha c} \quad (2.7)$$

$$\Leftrightarrow \left(-\frac{dE_c}{dx}\right)_e [\text{MeV}/\mu\text{m}] = 0.14 [\text{MeV}/\mu\text{m}] \times 10^3 \beta$$

where  $K_e$  is a constant,  $z$  is the charge of the recoiling nucleus and  $v$  is its velocity. The other quantities have been already defined for Equation 2.4. When the velocity is very low, the present process of the energy transfer from the recoiling nucleus to the encountered electron is less efficient than the transfer from the recoiling nucleus to the encounter one, as it is illustrated by red and blue curves for the xenon case in Figure 2.8.

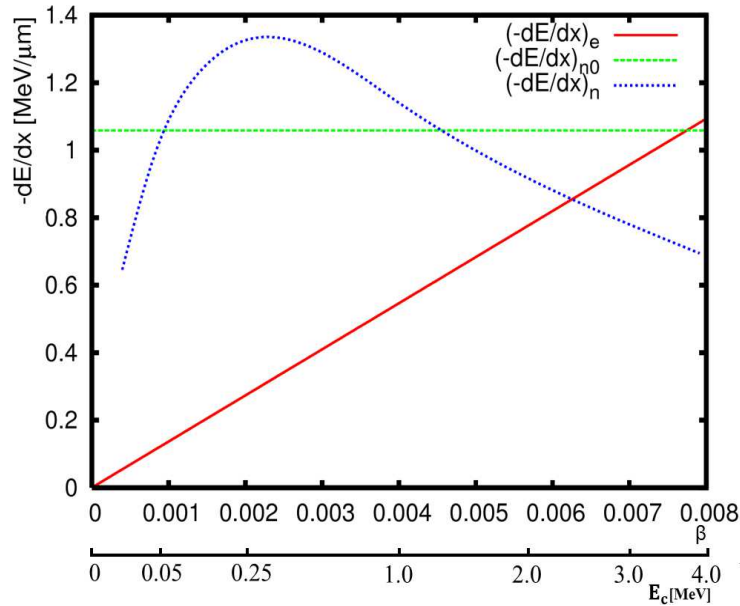


Figure 2.8: Illustration of the relative contributions of each interaction process for a recoiling nucleus as a function of its energy, based on results from [123]. See the text for explanation.

In this figure has been also reported in blue for comparison the stopping power  $(dE_c/dx)_n$  of the recoiling xenon nucleus by other xenon nuclei of the medium, calculated with a Thomas-Fermi potential [123], and demonstrating thus a higher interaction rate with nuclei than with electrons for recoiling nucleus with a low kinetic energy. In the whole energy range considered here, the order of size of the stopping can be approximated by an ion-dipole potential [123]:

$$\left(-\frac{dE_c}{dx}\right)_{n0} = \frac{\pi^2}{2.7183} n \frac{(\hbar c)^2}{m_e c^2} \frac{m}{m+M} \frac{zZ}{z^{2/3}} \frac{v}{\alpha c} \quad (2.8)$$

$$\Leftrightarrow \left(-\frac{dE_c}{dx}\right)_{n0} [\text{MeV}/\mu\text{m}] = 1.1 [\text{MeV}/\mu\text{m}]$$

where  $m$  is the mass of the recoiling nucleus, and  $M$  is the mass of the encountered atoms. For the present example, they are very close. The other terms have been previously defined.

Thus, the difference between the range covered by recoiling electrons and nuclei with the same original amount of energy is mainly due to the order of size of the stopping power  $dE_c/dx$ . The covered range is then between few  $\mu m$  for an initial energy of 1 MeV, and decreases roughly as a function of the energy, for decreasing ones. Moreover, the competition between  $(dE_c/dx)_n$  and  $(dE_c/dx)_e$  leads also to the consequence that for the recoiling nucleus, the main part of the original kinetic energy is deposited during scattering with other nuclei. This energy will be then released in term of heat, instead of contributing to the excitation or ionisation of the encountered atoms. This phenomenon is named as *quenching*. Moreover, such energy deposition leads also to a lateral dispersion of the track: the ionisation distribution is not concentrated on the recoiling nucleus track.

As a result, the combination of all these phenomenon leads to different excitation and ionisation densities of the encountered atoms for recoiling electrons and nuclei. These are however not all the processes that are responsible to such differences between the ratio of the charge over light signal for the two types of recoils with the same initial energy, as it will be seen in the next section.

### 2.3.2 Charge separation under electric field

When no electric field is applied in the medium, all the electron-ions pairs recombine. As a results, all the energy depositions previously described lead to a scintillation signal, as it will be seen later in the next section. Moreover, for the case of the nuclear recoil, a large amount of the deposited energy can not be seen by light emission, since it has been transferred under thermal agitation. Up to this point, it is not possible to clearly distinguish nuclear and electronic recoils just by having a look to the total production of light, even if the spacial distribution of the energy deposition between the two types of recoil are different. One possibility consists thus in investigating more deeply the feature of the light production.

Indeed, as it will be seen later, the electron-ion recombination leads to the production of an excited di-xenon molecule that will be produced with a certain delay from the one directly produced by excited xenon atoms. The relaxation of the dimers produced either directly or via recombination will thus lead to two different scintillation signals in the liquid phase, with a time delay of about 3 ns for the second one with respect to the first one. It is then only the proportion of the intensity of one of these signals with respect to the other one that can provide a discrimination criteria if no drift field is applied. However, due to the low time delay between these two signals for xenon, it is then better to investigate another way for their discrimination. This is the purpose of the application of an electric drift field in the LXe.

As a consequence of this drift field, a part of the secondary electrons produced during the recoil of each particle will be collected. The proportion of electrons that will drift with respect to the total amount of electrons released during the recoil depends on the size of the track. The separation will be thus more efficient for long tracks, induced by electronic recoils, than for short tracks, induced by nuclear recoils. This distinction between the two different proportions of electrons contributes then also to the difference between the ratio of the charge over light signal for the two types of recoils.

Thus, several different models have been developed in order to describe electrons-ions recombinations, depending of *e.g.* the size of the particle track, or the detection medium. In the case of LAr and LXe, the most accurate one is known as the *box model* [124], which corresponds to an improvement of a much earlier model, the *Jaffé's model*, that will not be presented here, but that is detailed in [125].

According to this model, by neglecting coulomb forces, it is assumed that all along the track of the ionizing particle a cloud of ions and electrons is created. By applying a drift field  $\vec{E}$ , both quantities start to move in opposite direction, in parallel to the electrons-ions recombinations. The numbers of two types of charges are then ruled according to:

$$\begin{aligned}\frac{\partial N_+}{\partial t} &= -\mu_+ E \nabla N_+ + d_+ \nabla^2 N_+ - \alpha N_+ N_- \\ \frac{\partial N_-}{\partial t} &= \mu_- E \nabla N_- + d_- \nabla^2 N_- - \alpha N_+ N_-\end{aligned}\quad (2.9)$$

where  $N_+$  and  $N_-$  correspond to the number of ions and electrons respectively,  $\mu_+$  and  $\mu_-$  are the associated mobilities due to the applied drift field. In the same way,  $d_+$  and  $d_-$  correspond to the associated diffusion coefficients. The last term  $\alpha$  is the recombination coefficient. The term  $\alpha N_+ N_-$  describes thus the part of the electrons that recombines, while the term  $\mu_- E \nabla N_-$  describes the part of electrons that drift thanks to the application of an electric field.

One of the suggestions brought by Thomas and Imel [124] was then to simplify this equation. Indeed, since ions drift velocity is few order of magnitude smaller than electrons' one, and since the diffusions terms are very small in both liquid argon and xenon, these terms can be then neglected, leading to:

$$\begin{aligned}\frac{\partial N_+}{\partial t} &= -\alpha N_+ N_- \\ \frac{\partial N_-}{\partial t} &= \mu_- E \nabla N_- - \alpha N_+ N_-\end{aligned}\quad (2.10)$$

where the recombination between one electron and one ion from the same initial atom can be almost excluded under drift field application, as previously mentioned in another earlier model, the *Onsager's model* [126]. Due to the different recombination regimes that depend on the ionisation density along the track of the recoiling particle, Thomas and Imel suggested to apply the box model boundaries conditions. In the opposition to Fano's correction factor, this model means that each produced electron-ion pair is isolated from all others, and that all of them are uniformly distributed in a box with dimension  $a$ . Moreover, due to the assumption that Coulomb forces are neglected, only drift field is applied to each individual charge. The system 2.10 can be then solved in order to obtain the collected charge fraction:

$$\frac{Q}{Q_0} = \frac{\ln(1 + \xi)}{\xi} \quad (2.11)$$

where  $Q/Q_0$  represents the proportion of the collected electrons thanks to the drift field compared to the population of created ions, before any possible electron-ion recombination. The parameter  $\xi$  corresponds then to the only one parameter from which the model is depending. It corresponds to:

$$\xi = \frac{N_0 \alpha}{a^2 v} \quad (2.12)$$

where  $N_0$  is the number of electron-ion pairs created inside the box and  $v = \mu_- E$  is the electrons drift velocity for a given electric field  $\vec{E}$ . As an illustration, Figure 2.9 shows the evolution of the term  $\ln(1 + \xi)/\xi$ , hence the fraction of charge collected, as a function of  $1/\xi$ .

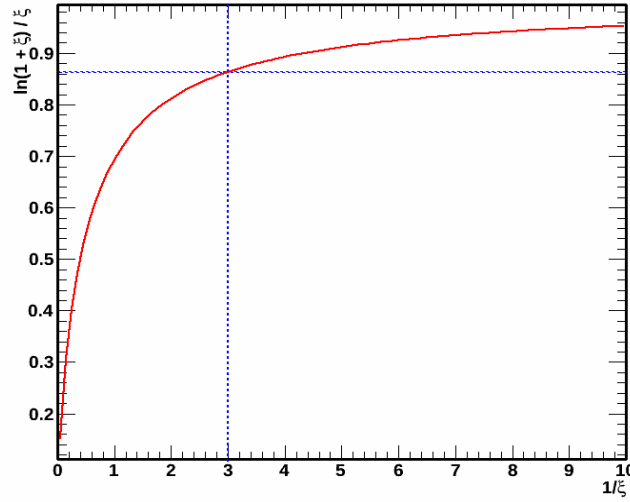


Figure 2.9: Illustration of the evolution of the charge collection as a function of the parameter  $1/\xi$ . The two dashed lines represent the best value of the  $\xi$  parameter for the fit of the charge collection in LXe performed in [124] on data acquired with electrons produced by a  $^{113}\text{Sn}$  radioactive source, for a drifting electric field of about 0.5 kV/cm.

The two dashed lines represent the best value of the  $\xi$  parameter for the fit of the charge collection in LXe performed in [124] on data acquired with electrons produced by a  $^{113}\text{Sn}$  radioactive source, for a drifting electric field of about 0.5 kV/cm. The difference between the charge collection of about 86 % (horizontal dashed line) for a drift field of 0.5 kV/cm (vertical dashed line) in Figure 2.9 and the charge collection for data acquired with  $\gamma$  ray produced by a  $^{137}\text{Cs}$  presented in Section 5.6 is explained by the difference between the energy of each of the two types of involved ionising particles.

Furthermore,  $\xi \rightarrow 0$  in case of a drift field strong enough such that no recombination occurs and for a perfect electron collection, while  $\xi \rightarrow \infty$  if no drift field is applied and all electrons recombine with ions. Moreover, this parameter is higher for nuclear recoils than for electronic recoil, because of the high rate of recombination [124]. This leads thus to an electron collection factor that is lower for the former case than for the latter one.

This model allows the description of charge and light production in both xenon and argon. In the next section will be then detailed the processes that lead to the emission of light in liquid and gas phases.

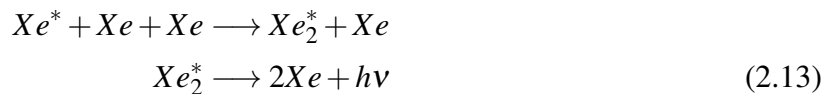
### 2.3.3 Scintillation and ionization signals

The present section details the different steps that lead to the scintillation and ionisation signals emission.

#### 2.3.3.1 Scintillation signal

As detailed in Figure 2.2, two processes, xenon atom excitation and electron recombination with a xenon ion, lead to the emissions of ultraviolet photons in the liquid phase, usually known in literature as Vacuum UltraViolet photons (*VUV*), and create the scintillation signal S1. In this section, only the ultraviolet photons emission from atom excitation is detailed, while the emission from electron-ion recombination will be presented in the next section.

The process that leads to ultraviolet photons emission from atom excitation is expressed by the following relationships [114]:



When the recoiling particle excites the encountered atoms, the latter will combine itself with another xenon atom, creating an excited di-xenon molecule (*dimer*). The two xenon atoms will then come back to energetic ground state through their separation and with a ultraviolet photon emission at 178 nm. The typical time needed for this dimer formation is of the order of few picoseconds.

Two different energetic states of the dimer can occur, the singlet state  $1\Sigma_u^+$  and the triplet state  $3\Sigma_u^+$ . The associated relaxation times are then different due to these energetic states, and are respectively 3 ns and 27 ns in case of electrons [114], and more generally respectively at few nanoseconds and few tens of nanoseconds, depending of the recoiling particle. Indeed, as detailed in Section 2.3.1, the lose of energy per unit length for heavy particles such as  $\alpha$  or others ions is much higher than for electron, leading to a much higher ionisation density. Since there are more ions and electrons in a more restrictive space, the recombination yield will be higher and recombinations will occur faster for heavy recoiling ions than for recoiling electrons. All of these recombinations will contribute to the two states of the dimer, each time with a certain delay due to the recombination time compared to dimer directly produced by atom excitation. The measured decay times of each state take into account these contributions, that is why they differ from one type of recoiling particle to another.

Moreover, the proportion between the two excited states depends again on the recoiling particle [127]. Thus, and combined with the time relaxation, both energetic states of dimers provide a good background discrimination quantity for dark matter search, as seen in Section 1.6.5.2 with

the XMASS experiment. However, the time difference between both xenon dimer energetic states is not as long as for other noble gas used for dark matter research, as illustrated by Table 2.4. Therefore, most of the xenon dark matter experiments like the XENON program use a time projection chamber, usually as double phase TPC, instead of using a single phase with no drift field. Single phase xenon TPC could also be considered by following the set up of the XEMIS detector developed for medical imaging and mentioned in Section 2.1. However, as justified in [128], dual-phase TPC provides a S2 signal that is amplified. This allows a lower energy threshold, which is a crucial point for increasing both the dark matter scattering sensitivity and the dark matter interaction statistics in case of discovery, as reminded in Section 1.5.3, while keeping the same energy resolution as for single phase TPC. Thanks to this technology, the two dimers relaxation times can be replaced by S1 and S2 signals as discriminant factor for electronic and nuclear recoil discrimination.

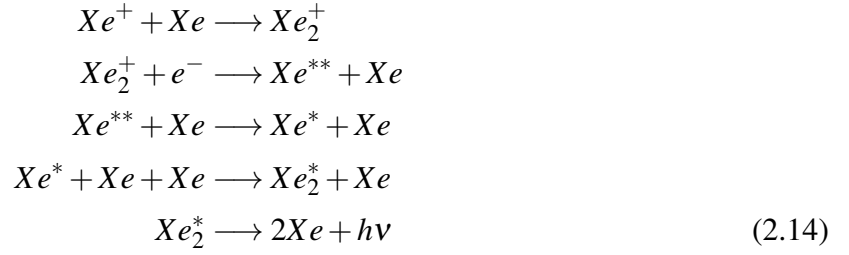
| Noble gas | Singlet lifetime [ns] | Triplet lifetime [ns] |
|-----------|-----------------------|-----------------------|
| Neon      | $< 18.2 \pm 0.2$      | $14900 \pm 300$       |
| Argon     | $7.0 \pm 1.0$         | $1600 \pm 100$        |
| Xenon     | $4.3 \pm 0.6$         | $22.0 \pm 2.0$        |

Table 2.4: Singlet and triplet lifetime comparison between several noble gas, from [129].

In a more practical point of view, using a xenon TPC instead of using a single phase chamber with no drift field requires a much lower quantity of LXe as a veto volume surrounding the fiducial one. This is due to a higher discrimination power of the scintillation and ionisation signals with respect to dimers relaxation time. Indeed, as presented in Section 1.6.5.2, the current dark matter sensitivity of the XMASS experiment is much lower than the results from XENON100. If for the former it corresponds only to few days of cumulated data compared to more than two hundred days for the second science run of XENON100, the total LXe mass used by the former is more than 800 kg compared to 160 kg respectively. These volumes include a fiducial volume of the order of few tens of kg for the two experiments. The current cost of commercial xenon is of the order of 1-2 k\$ per kg, increasing considerably the xenon furniture cost for the former with a lower sensitivity compared to the latter.

### 2.3.3.2 Ionization

In parallel to the excitation process, ionization of the encountered atoms can occur. The released electrons can then partially (with applied drift field) or almost totally (no drift field) recombine with xenon ions through the process described in Relationships 2.14 [114], leading to *heat* and ultraviolet photons emission.



The energy deposited by the scattering particle ( $\gamma$ , WIMP, ...) on the future recoiling particle (electron or nucleus) is linked to the two numbers of excited and ionized xenon atoms through the Platzman equation [130]:

$$E_{dep} = N_{ex}E_{ex} + N_iE_i + N_i\varepsilon \tag{2.15}$$

where  $N_{ex}$  and  $N_i$  are respectively the number of excited and ionized xenon atoms during the recoil of either the electron or the nucleus. The two energies  $E_{ex}$  and  $E_i$  correspond then respectively to the average energy needed to create either excited xenon atom or an electron-ion pair. The remaining term  $\varepsilon$  corresponds to the kinetic energy of the sub-excitation electrons. This latter term can be sometimes neglected in a simplified version of Platzman equation, like in [131]. The Equation 2.15 can be rewritten as:

$$E_{dep} = N_i(\alpha E_{ex} + (E_i + \varepsilon)) \tag{2.16}$$

with  $\alpha = N_{ex}/N_i$ . The two numbers  $N_{ex}$  and  $N_i$  can be then explicitly expressed as a function of the deposited energy and the two average energies  $E_{ex}$  and  $E_i$ :

$$\begin{aligned}
N_i &= \frac{E_{dep}}{\alpha E_{ex} + (E_i + \varepsilon)} \\
N_{ex} &= \alpha N_i
\end{aligned} \tag{2.17}$$

This number  $N_i$  of produced ions corresponds to an average value for a given transferred energy. The observed number of ions will then fluctuate around this value. In a first approach, it can be then expected that this number fluctuates according to Poisson statistic, but the Italian physicist U. Fano has shown that such statistics can not be applied [132], due to the correlation between the different scattering steps of the recoiling particle that does not allow to treat them independently. He introduced then the *Fano factor*  $F$  defined such that the fluctuation  $\sigma_n$  of the number  $N_i$  of produced ions is defined as follows, and depends on the considered target material:

$$\sigma_n = \sqrt{FN_i} \tag{2.18}$$

The energy resolution of a TPC detector, corresponding to the full width at half maximum, can be then inferred from this factor through the following formula:

$$\begin{aligned} R &= 2.35 \frac{\sqrt{FN_i}}{N_i} \\ &= 2.35 \sqrt{\frac{FE_i}{E_{dep}}} \end{aligned} \quad (2.19)$$

where the factor 2.35 comes from the relation between a Gaussian spread and its FWHM. In the case of LXe, the Fano factor has been theoretically estimated at about few hundredth, allowing to calculate the resolution for a given energy. These estimations are however underestimated since several contributions such as ionisation density are missing. As a complement of this section, the Equation 2.17 can be also used for explaining the total number of emitted photons and the number of electrons that escape to recombination and start to drift toward the gas phase:

$$\begin{aligned} N_{ph} &= N_{ex} + rN_i \\ N_e &= N_i(1 - r) \end{aligned} \quad (2.20)$$

where  $r$  is the electron recombination probability that can be estimated by using the model described in Section 2.3.2.

As a complement, it can be noticed that such equations are very well summarized in [131] on *NEST*, a computing tool for Monte Carlo simulation of noble gas detector, and widely used for dark matter search.

## 2.4 Detailed description of the XENON detector

The description of the main components of the XENON100 TPC is made in the present section, while the description of the shielding and devices that are placed around the chamber is done in the next one. This detector components review is divided into several parts. It first starts by the description of the drift field and the S2 attenuation during the drift of the electronic cloud, followed by the description of the PMTs arrays and the light detection. The presentation of the detector external shielding, the xenon cryogenic and the recirculation gas system is then made, completed by the description of the triggering of the data acquisition.

### 2.4.1 Drift field

The total drift length in LXe is about 30 cm, thanks to a potential difference between cathode mesh at the bottom of the detector and a ground mesh placed few millimeters below the gas phase. The TPC was originally drawn to provide a field up to 1 kV/cm, but running conditions were then optimised at about 0.53 kV/cm, corresponding to about 176  $\mu$ s for the full electron drift length. In these conditions, the cathode voltage is set at -16 kV.

The cathode and ground meshes are respectively  $75\ \mu\text{m}$  and  $50\ \mu\text{m}$  thick, both with a 5 mm pitch hexagonal pattern. The drift field is kept constant thanks to 40 field shaping copper rings, visible in Figures 2.10(a) and in the bottom of Figure 2.10(b) as parallel horizontal planes alternated with a cylindrical PTFE shield (The plastic white element used to create a light cage for ultraviolet photons thanks to his high reflectivity property for such photons). A higher electric field is then applied between the ground mesh and the anode mesh 5mm above, usually set at 4.4 kV voltage, leading to an electric field in this region around 11 – 12 kV/cm. This anode mesh is made by an hexagonal pattern of 5 mm pitch and  $125\ \mu\text{m}$  thick. Finally, two additional ground meshes identical to the previous one are placed 12 mm below the cathode and 5 mm above the anode, in order to protect the top and bottom PMTs arrays. The anode and the two ground meshes 5 mm upper and below are represented in Figure 2.10(b).

The optical transparency of the three meshes on the top of the TPC and of the two meshes on bottom of the TPC for photons are 47.7% and 83.4% respectively [122]. The transparency of the ground mesh between cathode and anode meshes for drifting electron is close to 100% [133].

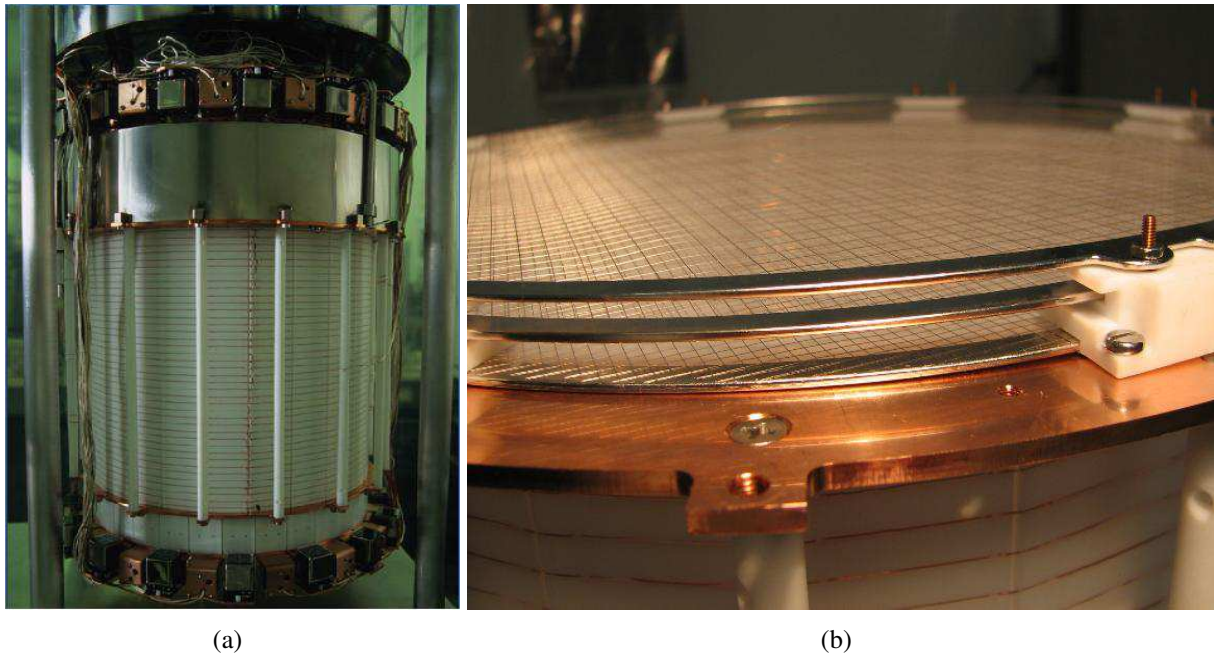


Figure 2.10: (a) XENON100 TPC, (b) XENON100 top meshes : top and bottom correspond to ground meshes, while the anode is in the middle.

Furthermore, the TPC is mounted in a double-walled  $^{316}\text{Ti}$  stainless steel cryostat. This stainless steel is also used for several components of the TPC, such as the diving bell or the meshes, and was selected for its low activity, especially in  $^{60}\text{Co}$ , as presented in Section 3.2 for the related internal background. In the next section is presented the drift of the electrons in LXe.

#### 2.4.1.1 Drift of the electronic cloud

An electronic cloud reaches the top of a TPC with usually less electrons than what were originally created at the interaction point. This is due to the presence of electronegative impurities (mainly oxygen) diluted in the LXe, that trap the electrons during their drift. Such effect can be

observed with the evolution of the charge signal as a function of the drift length, corresponding to the depth of the interaction point of impurities in the TPC, for a known deposited energy  $E$ , see Figure 2.11(a), by assuming a uniform distribution.

The evolution of the S2 signal as a function of the drift time can be written as [122]:

$$S2(\Delta t, \vec{E}) = S2_0(\vec{E}) \exp\left(-\frac{\Delta t}{\tau_e}\right) \quad (2.21)$$

where  $S2(E)$  is the charge signal that is measured after the electron drift, while  $S2_0(E)$  is the charge signal that should have been seen if no impurities were present in the LXe.  $\Delta t$  is then the drift time associated to the drift length, corresponding to the time difference between the scintillation S1 and ionization S2 signals. The parameter  $\tau_e$  is called *electron lifetime*, and depends on the nature of the impurity, i.e. its ability to trap electrons, and its concentration. This is the parameter which allows to describe the charge loss during the drift, as illustrated by the exponential curve on Figure 2.11(a). Such effect leads to a z-correction of the signal, as mentioned in Section 3.1.1.2. Since it depends on the xenon purity, it needs to be monitored regularly: when the detector is running in stable conditions, the LXe purity is improving, that is why there is a need of a regular measurement. For this purpose, a radioactive caesium calibration source ( $^{137}\text{Cs}$ ) is used once a week, or more frequently in case of high variation of LXe purity, to monitor this evolution through similar plots to the one presented on Figure 2.11(a). The advantage of the  $^{137}\text{Cs}$  is that it decays by releasing a monochromatic  $\gamma$  ray at 662 keV which could be totally absorbed in the LXe by photoelectric effect. Such a full absorption peak can be very easily identified in S2 versus S1 map, as illustrated by the main cloud in Figure 2.11(b).

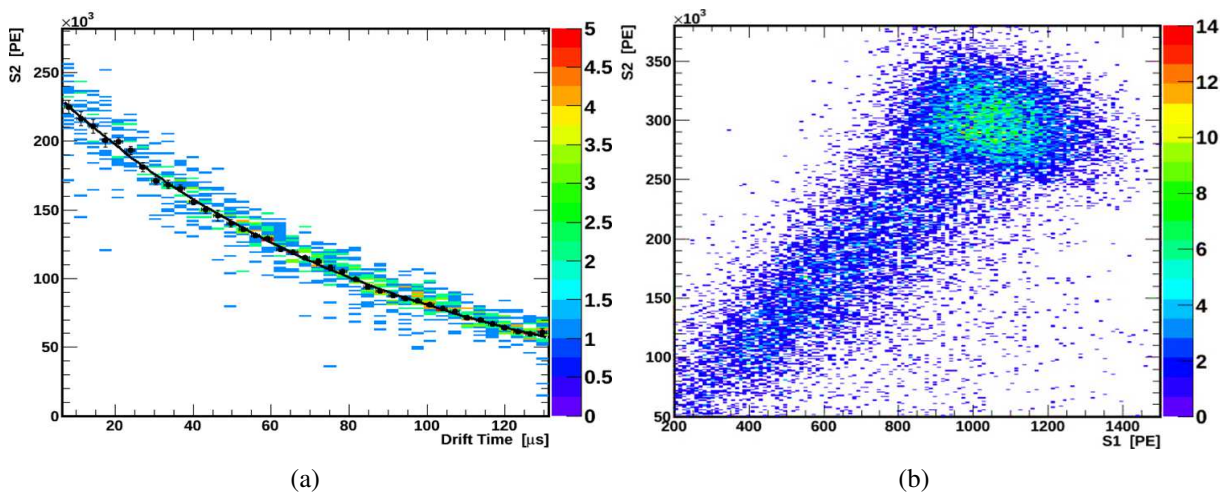


Figure 2.11: (a) Evolution of S2 signals for the  $^{137}\text{Cs}$  full absorption peak of a 662 keV  $\gamma$  ray as a function of the scattering depth, (b) S2 versus S1 map for  $^{137}\text{Cs}$ . The full absorption peak corresponds to the main cloud at the top right of the plot.

### 2.4.1.2 Ionization signal

In general, there are two different ways to collect charges that are drifting in a TPC. The first one consists in using a single phase TPC. In this case, the electrons are collected by an anode plane, that should be segmented in order to allow the  $(x, y)$  reconstruction, as discussed in Section 2.1 for the XEMIS detector. The second one consists then in using a dual phase TPC, like in the XENON detectors. In this case, an electric field higher than the drift one is required to extract electrons from liquid to gas phase.

In the XENON100 detector, the drift field  $E_d$  created between cathode and ground mesh is equal to about  $\sim 0.53$  kV/cm. Then, the higher electric field created between that ground mesh and the anode is about 11 – 12 kV/cm. During special running conditions, as it will be extensively explained in Chapter 5, this field is let to vary in the gas phase from  $\sim 5$  kV/cm up to  $\sim 15$  kV/cm, by changing both liquid level above the grid and the anode voltage.

As a complement on this electric field, it can be mentioned that if the field in the liquid phase above the grid is higher than below the grid, usually set around 6 kV/cm, it is however lower than the electric field in the gas phase. The calculation of the electric fields in liquid and gas phases above the grid will be presented by Formula 5.7 and Formula 5.8 respectively. The zero of the liquid level in the XENON100 detector is set 5 mm below the position of the ground mesh. It is important to notice that having the field in liquid phase above the grid is a crucial requirement, meaning that the liquid level should be above the grid, in order to allow the electron extraction to the gas phase. This corresponds to the only one possibility to have a S2 signal in dual-phase, as it has been reported here [128].

After their extraction into gas phase, the electrons are accelerated and create a second scintillation signal, the *ionisation* signal S2, by following the same excitation and ionisation process as in the liquid phase, as illustrated in Figure 2.1. In case of an enough strong drift field in the gas phase, an electronic avalanche can occur, corresponding in a first time to the excitation and ionisation of xenon atoms by electrons previously released by the one extracted from liquid phase. Then, the more the electric field is strong, the more such phenomenon at the second, third or higher order can occur. This is a similar process to the electronic amplification in the PMTs. The results presented in Section 5.4.2 will show that no electronic avalanche will occur for electric field in gas below about 12 kV/cm.

### 2.4.1.3 Drift fields during science runs

As an illustration, the Table 2.5 summarizes the cathode and anode voltage configuration,  $V_C$  and  $V_A$ , during each science run. In practice, the cathode voltage has a negative value. However, for clarity reasons, only the corresponding absolute value for each science run is presented here. Furthermore, Table 2.5 also summarizes the configuration of the liquid level  $d_L$  above the ground mesh, and the gas gap  $d_G$  between the liquid surface and the anode mesh. In practice, the measurement of the liquid level is performed with the origin of the  $z$  axis that is set 0.5 cm below the ground mesh. Thus, to be compared to real liquid level measurements, the data presented here need to be increased by 0.5 cm.

The drift field  $E_d$  between the cathode and the ground mesh is then indicated, as it is also the

case for the two fields in liquid  $E_L$  and in the gas phases  $E_G$  between the ground mesh and the anode. These two fields are calculated by using the formula presented in Section 5.4.1.

| Science run   | $V_C$ [kV] | $V_A$ [kV] | $d_L$ [cm] | $d_G$ [cm] | Electric fields |               |               |
|---------------|------------|------------|------------|------------|-----------------|---------------|---------------|
|               |            |            |            |            | $E_d$ [kV/cm]   | $E_L$ [kV/cm] | $E_G$ [kV/cm] |
| <b>First</b>  | 16.0       | 4.5        | 0.25       | 0.25       | 0.53            | 6.08          | 11.9          |
| <b>Second</b> | 16.0       | 4.4        | 0.15       | 0.35       | 0.53            | 5.26          | 10.3          |
| <b>Third</b>  | 15.0       | 4.4        | 0.24       | 0.26       | 0.50            | 5.87          | 11.5          |

Table 2.5: Summary of the drift fields during each science run.

## 2.4.2 Photomultipliers tubes

The PMTs used in XENON100 are 1" square Hamamatsu. 98 of them are placed in concentric circles on the top array in order to optimise the  $(x,y)$  position reconstruction, while the 80 PMTs of the bottom array are all arranged in a more compact way in order to optimise the light collection, especially for improving the sensitivity to S1 signal. An illustration of the PMTs arrays is presented in Figure 2.12 and by grey squares in Figure 2.1.

In addition to these two arrays, 64 others PMTs are placed in the veto all around the TPC, in order to reject all single scattered events in the TPC related to a scattering in the veto. This corresponds to a very efficient factor for background reduction, and it is one of the main improvements from XENON10 experiment. The veto PMTs can be seen in Figure 2.10(a), where they correspond to the boxes all around the TPC, on the top and on the bottom.

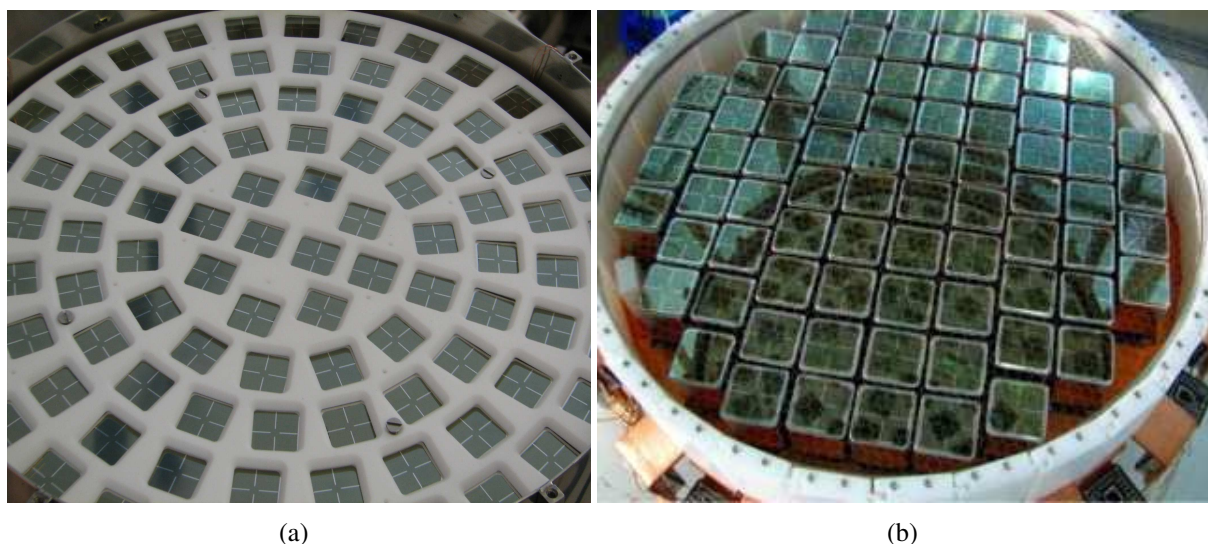


Figure 2.12: XENON100 PMTs arrays: (a) top, (b) bottom.

In order to optimise the light collection, the walls of the TPC are made with 1/4 inch-thick polytetrafluorethylen (*PTFE*) that was selected for its property of being a very good reflector for the ultraviolet scintillation light [134]. Thanks to this PMTs configuration, XENON100 is able to

distinguish two successive scatterings if they have a relative position larger than 3 mm in the (x-y) plan and a relative depth larger than 0.3 mm [122].

The processes that lead to the emission of the two signals, S1 and S2, and their different intensities have been developed in the previous sections. The emitted light during these two signals have a 178 nm wavelength, corresponding to the xenon scintillation peak [114], and are seen by the two PMTs arrays presented above.

S1 and S2 are induced by all the photons that are collected by the PMTs, as illustrated by Figure 2.13 for one scattering photon. Once a photon passes through the PMT window and will heat the photocathode, it will vanish by photoelectric effect, releasing one electron. This latter will be accelerated toward the opposite edge of the PMT thanks to successive drift fields in a vacuum chamber, in order to be collected by the anode. A focussing electrode is used to center all the electrons that could have been released on the borders of the photocathode.

During its drift, the electron will collide several intermediate dynodes, usually between 10 and 14 [118], releasing each time new electrons that will follow it down to the anode. This step is called the amplification of the signal and corresponds to the gain of the PMT, that is between  $10^6$  and  $10^8$ . The PMTs used for the XENON100 experiment have 10 dynodes per PMTs, leading to an average gain of  $\sim 2.0 \cdot 10^6$  for each of them [122].

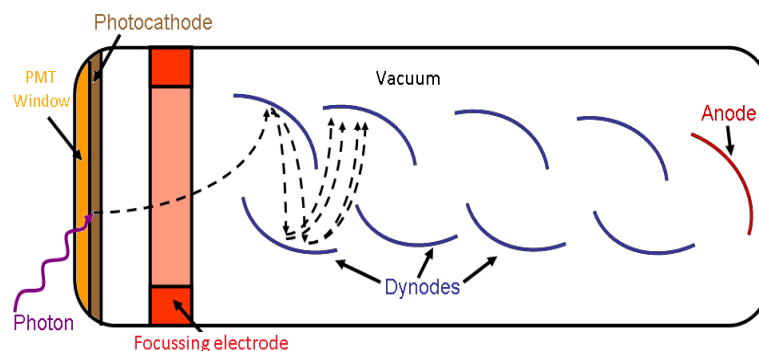


Figure 2.13: Illustration of PMT principle, adapted from [111].

After this amplification, all the released electrons are collected by the anode. The sudden increase of the voltage at the end of each PMTs is monitored. Each S1 and S2 signal corresponds to a pulse in the base line current and can be then expressed in volt, see Figure 2.14(a). However, it is more common to normalize such signals in photoelectron (*PE*). 1 PE corresponds to the average voltage induced by one electron extracted from the photocathode by an incident photon. It is expressed in term of the gain, i.e. the number of electrons reaching the anode after the photon scattering, as illustrated by Figure 2.14(b). This gain is usually measured once a week for each PMTs of the detector thanks to a dedicated monochromatic blue LED source ( $\lambda = 470\text{nm}$  [122]). In the standard notation, S1 and S2 signals correspond to the sum of all the signals seen in coincidence by each PMT of the detector. It is however possible to access to each waveform, and thus to each S1 and S2, registered by each individual PMT.

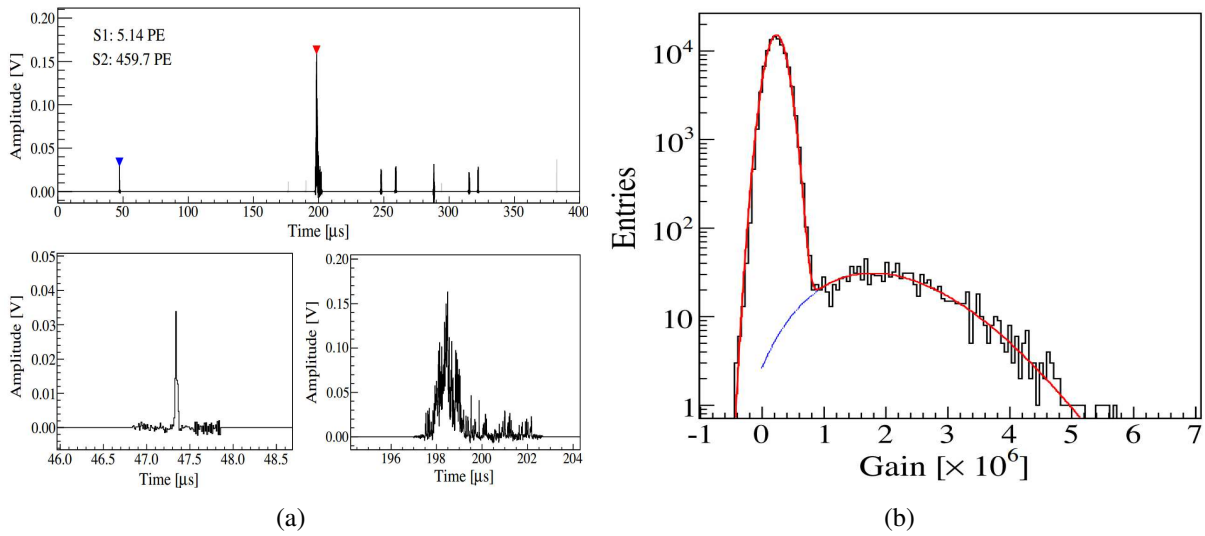


Figure 2.14: (a) Example of a low-energy event recorded in XENON100, the two plots on the second row correspond to zooms on blue and red marker on the first row respectively, i.e. S1 and S2 signals. (b) Example of a single photoelectron spectrum expressed in terms of gain, fitted by a sum of two Gaussians that correspond to noise (first peak) and the photoelectron signal respectively. The value associated to the PMT gain corresponds to the average of the second Gaussian, which is in the present example  $2.06 \cdot 10^6$ . Both pictures are from [122].

### 2.4.3 External shielding

As seen in Section 1.5.3, dark matter direct detection experiments are placed underground in order to drastically reduce the exposition to astroparticles and their products in the Earth's atmosphere. The LNGS underground laboratory provides then a very good natural shielding thanks to a 1.4 km rock thickness, that corresponds to 3700 m water equivalent (*mwe*), reducing the muon flux by a factor  $10^6$  with respect to the ground level [122, 135]. As an illustration, Figure 2.15 show the approximative muon flux received by experiments in several underground laboratories as a function of their depth. It is also added the name of the noble gas dark matter experiments that are placed in each of these underground laboratories.

However, such a shielding does not prevent from exposition to local environment background, such as the natural radioactivity from rocks – the very same rocks that also prevent from astroparticles exposition – or from buildings and concrete used underground. Moreover, there is still a residual part of the cosmic rays that could reach underground detectors. Thus, all underground low background experiments need additional shieldings around their detectors.

In the case of the XENON100 experiment, to prevent exposition mostly from external  $\gamma$  radioactivity, an external 20 cm thick shield of lead is used, combined with an additional internal 5 cm thick layer of lead with low  $^{210}\text{Pb}$  contamination. Then, two others additional internal layers of polyethylene and copper, 20 cm and 5 cm thick respectively, are used to prevent XENON100 detector from lead layers' radioactivity.

Finally, the full shielding is mounted on a 25 thick polyethylene layer, and surrounded on the top and on 3 sides by 20 cm of water and polyethylene layer, in order to reduce exposition mostly from *muon-induced neutrons*, i.e. neutrons released by muons scattering off rocks.

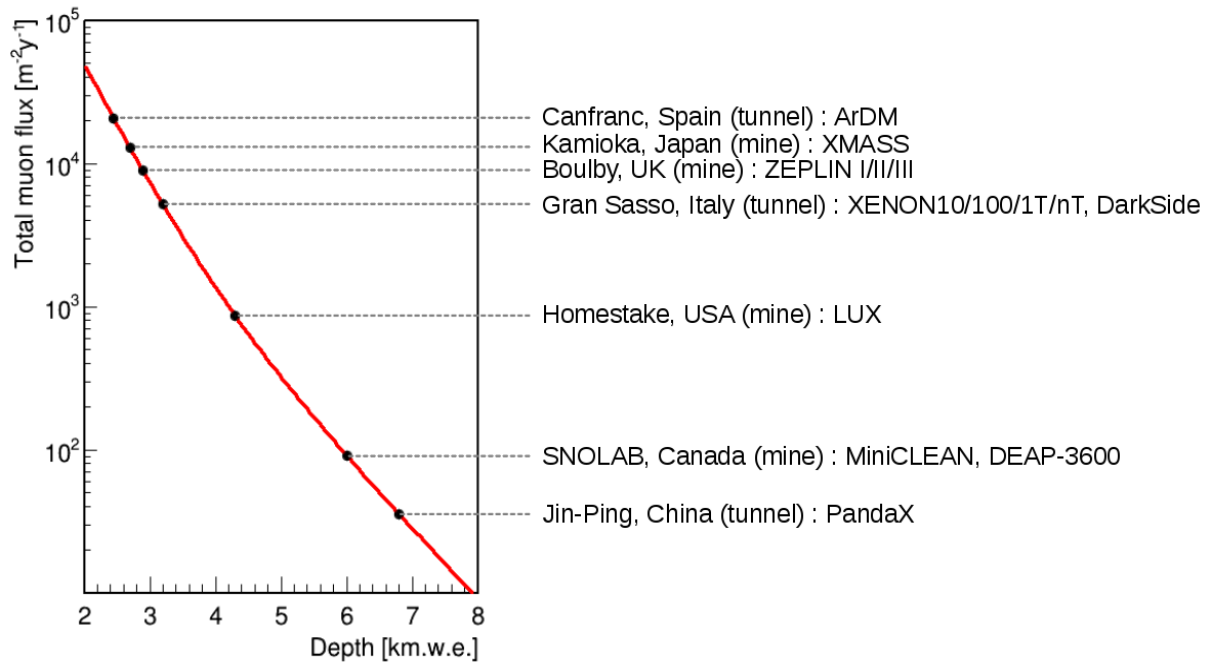


Figure 2.15: Illustration of a muon flux reduction as a function of the depth of underground laboratories.

A sketch of the different layers of the shielding is presented in Figure 2.16(a). The water and polyethylene layer from the back of the detector is represented in 2.16(b).

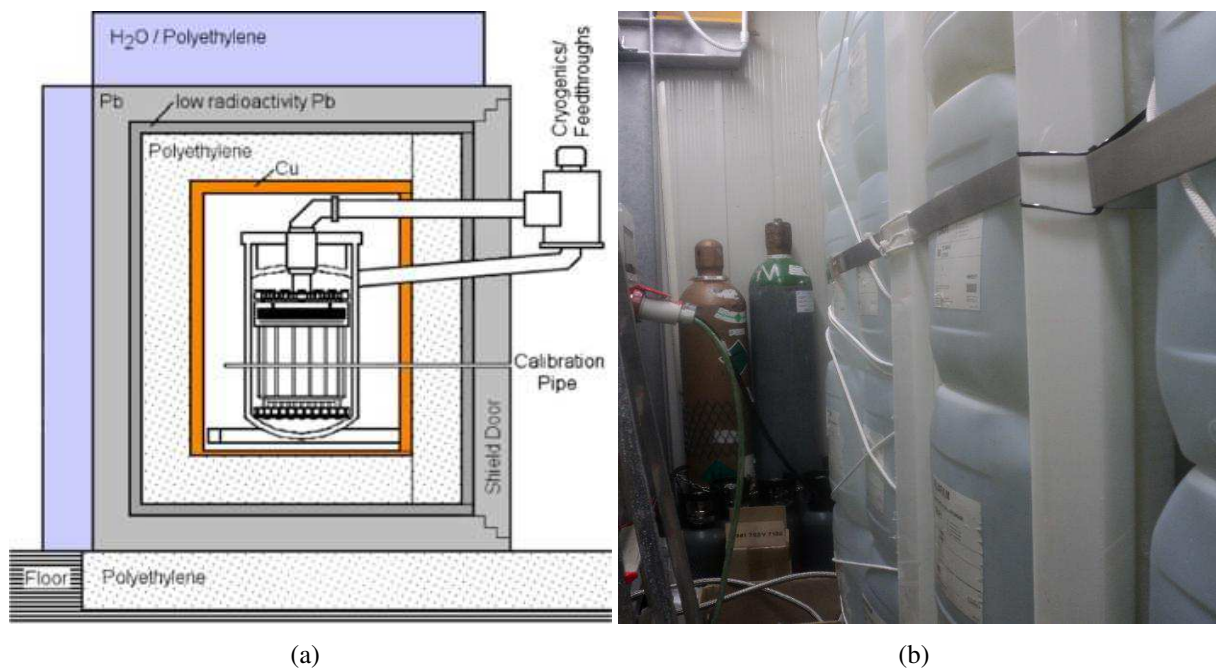


Figure 2.16: (a) Illustration of the several layers of the XENON100 passive shield, from [122], (b) picture of the back side of the XENON100 shield.

For the future XENON1T detector, a different shielding strategy has been drawn, in order to reduce by about 100 times the exposition to background. It consists in a cylindrical ultra-pure

water muon veto with a 10 m diameter and a 10 m height, as it is represented in Figure 3.17 in Section 3.6.

### 2.4.4 The xenon cryogenics

As already approached previously and as presented with more details in the next chapter, the more the XENON100 acquires data, the more its sensibility to dark matter scattering increases, as it is also the case for all other direct dark matter experiments. As a consequence, such a detector is expected to be able to run in continuous operation for long time, typically at least of the order of one or two years. This was the case for the second science run, that has consisted in about 225 lives days of cumulated data [74], and has corresponded to more than thirteen months in continuous operation. This corresponds up to date to the longest running period for a liquid xenon TPC.

Due to this extended running period, a high detector stability is mandatory, in order to be able to easily compute together all the acquired data. For this purpose, XENON100 use a Pulse Tube Refrigerator (PTR) specifically designed for liquid xenon temperatures, i.e. at about  $-95^\circ$  for a 2 bar pressure. This device is illustrated in Figure 2.17, and consists in providing up to 200 W of cooling power to xenon in gaseous state thanks to a cold finger thermally connected to a cold head, cooled down by helium relaxation, taking advantage of the already known applications of this noble gas such as mentioned in Section 2.2.3. In order to have a more adjustable temperature, a copper resistor is placed between cold head and cold finger. Thanks to this, the temperature is monitored with high precision and stabilized with fluctuations lower than 0.04% during the five months of the first science run [122], as it will be illustrated in Section 2.4.5.

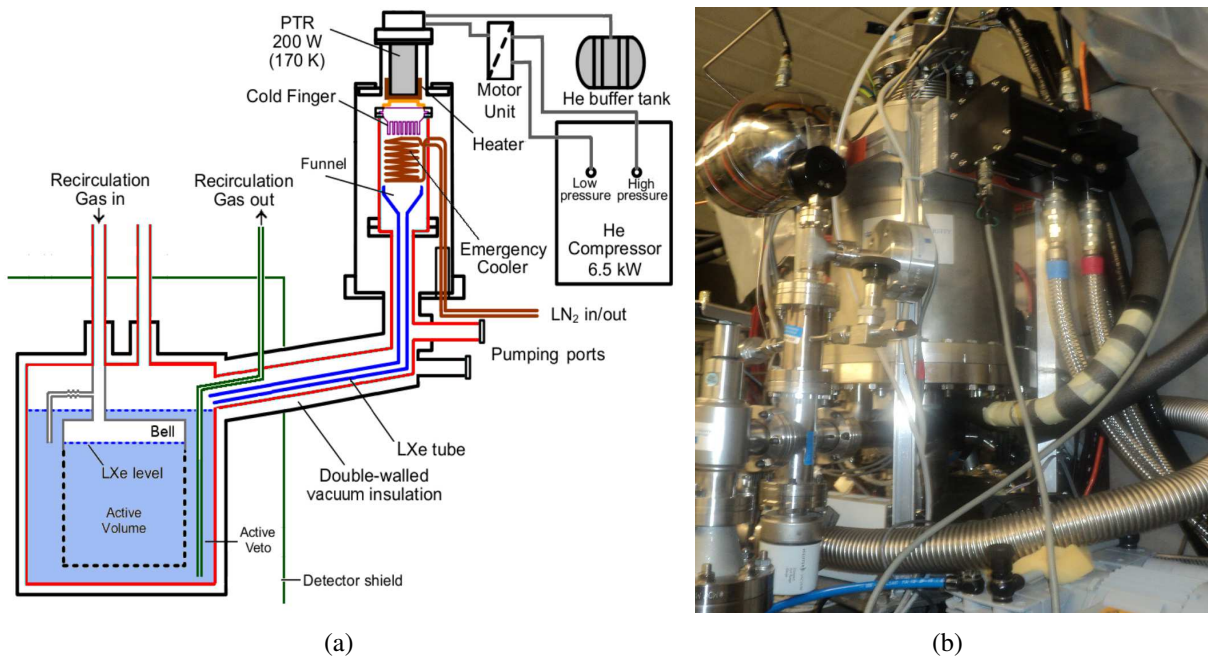


Figure 2.17: XENON100 cryogenic system: (a) Schema of the cryogenic system, from [122], (b) illustration of the XENON100 cryogenic system.

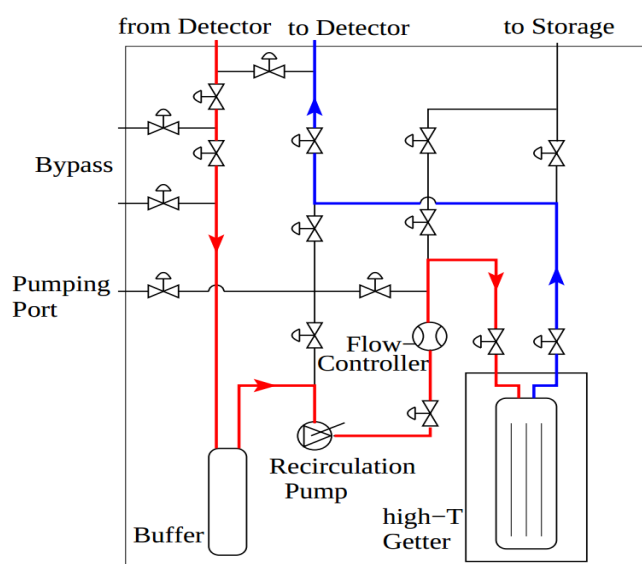
Once the xenon is liquefied, all the liquid drops are collected by a cone-shaped structure and

flow along a ramp back to the detector. In order to reduce all possible external sources of background like radioactivity of the components of these elements, the PTR is mounted outside the passive shield.

In case of emergency, the cooling power is provided by liquid nitrogen injected in a stainless steel coil right below the cold finger, as illustrated in Figure 2.17(a), and can be run during about two entire days. If no cooling power can be used, all liquid xenon start to warm up, increasing the inner pressure of the detector. For safety reasons, a very thin aluminium rupture disc is fixed closed to the PTR, allowing xenon release in such emergency cases.

## 2.4.5 Gas system

It was mentioned previously that some impurities, such as oxygen, carbon and water molecules, were continuously present in the liquid xenon. They mostly come from off-gassing of each component of the detector. Since they can be responsible for the attenuation of the charge signal, a continuous purification of the xenon is needed. For this purpose, a dedicated recirculation gas system has been designed, illustrated in Figure 2.18. The xenon recirculation starts by pumping liquid xenon from the bottom of the detector. It then evaporates in the recirculation gas lines before passing through a high temperature getter for gas purification thanks to zirconium trapper. It is then pushed back into the gas phase of the detector, i.e. below the bell represented in Figure 2.17. The blue device represented in Figure 2.18(b) corresponds to the xenon gas KNF recirculation pump also represented in Figure 2.18(a), while the grey rack contains the getter.



(a)



(b)

Figure 2.18: XENON100 recirculation gas system: (a) Schema of the recirculation gas system, from [122], (b) illustration of the recirculation gas system.

As also represented on Figure 2.18, some additional intermediate valves have been placed, allowing direct maintenance operations and recirculation of the xenon from detector to bottle

storage, illustrated in Figure 2.19(a), and vice-versa. The xenon recirculation flow, usually set between 2 and 4 standard liters per minutes (*slpm*), is also used for changing the liquid level above the ground mesh in the detector, and that is measured by sensor. All of these experimental parameters, like temperature, inner pressure, recirculation flow or events acquisition rate are continuously measured thanks to a Java based software [136], allowing on-line monitoring but also off-line analysis of experimental parameters' stability. This stability is illustrated by Figure 2.19(b) that shows tiny variations of the inner GXe pressure and LXe temperature within 0.24 % and 0.04 % respectively during the first science run.

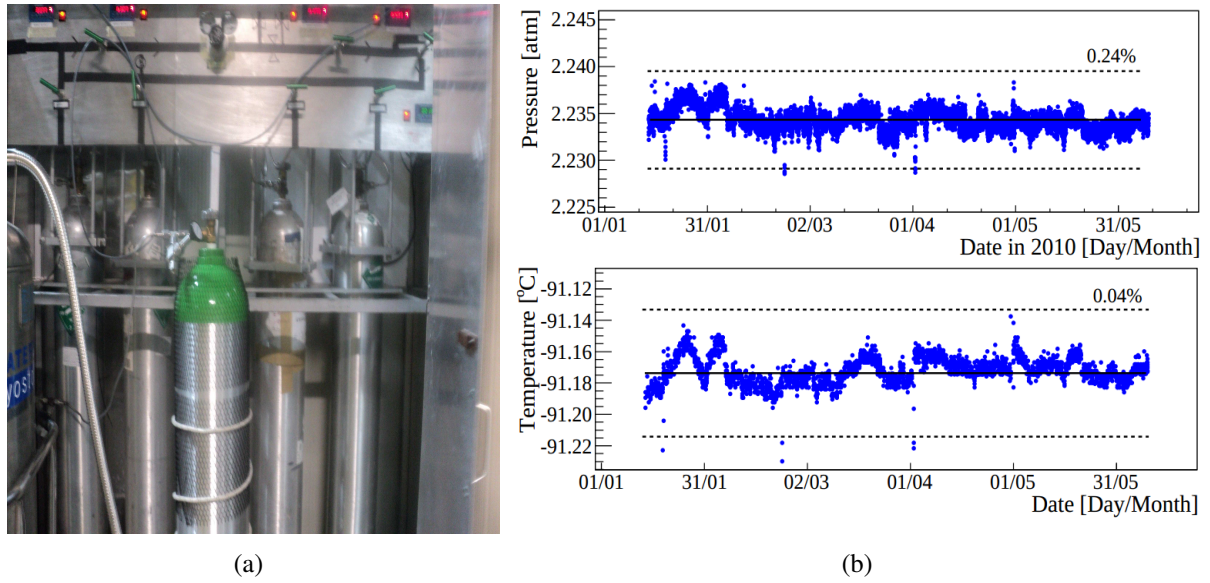


Figure 2.19: (a) Illustration of the xenon bottles used for recuperation and storage between two runs, (b) inner detector pressure and LXe temperature during the first science run, from [122].

As an illustration of the efficiency of the LXe recirculation system, Figure 2.20 represents the improvement of the electron lifetime (left Y-axis), corresponding to the decrease of the impurity abundance expressed as  $O_2$  equivalent (right Y-axis) during the second main science run. Each drop of the purity corresponds to the stopping of recirculation system due to maintenance operations.

The impurities concentration  $N$  is calculated in particle per billion using:

$$N [ppb] = \frac{10^{15} \times M_{Xe} [g/mol]}{\tau_e [\mu s] K_{O_2} [l/mol/s] \rho_{O_2} [g/l]} = \frac{477}{\tau_e [\mu s]} \quad (2.22)$$

where  $M_{Xe} = 131.3 \text{ g.mol}^{-1}$  is the xenon atomic mass,  $\tau_e$  corresponds to the electron lifetime, expressed in microsecond and previously described in Section 2.4.1.1,  $\rho_{Xe} = 2827 \text{ g.l}^{-1}$  is the xenon density, as also reminded in  $\text{g.cm}^{-3}$  in Table 2.1.  $K_{O_2} = 9.73 \cdot 10^{10} \text{ l.mol}^{-1}.\text{s}^{-1}$  is the electron attachment rate constant with  $O_2$  molecules for drift field at 0.53 kV/cm and temperature at 182 K. It is linearly interpolated from the values at 87 K and 165 K coming from [138].

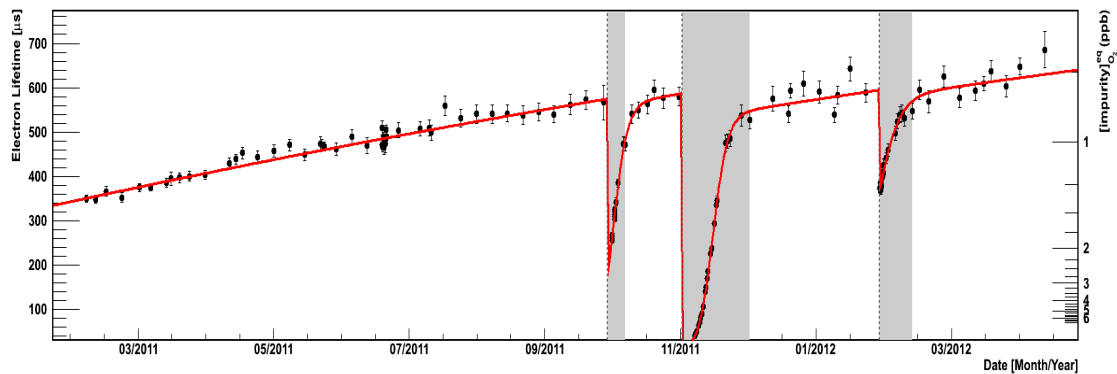


Figure 2.20: Evolution of electron lifetime (left Y-axis) and impurities abundance as  $O_2$  equivalent (right Y-axis) during the second main science run. Figure from [137].

### 2.4.6 Trigger and data acquisition

The XENON100 data acquisition can be divided in several steps. The first one consists in triggering an event. This is done by focusing either on S1 signals or on S2 signals search. In the first science run [139], the trigger was developed to be able to trigger on S2 signals down to  $\sim 300$  PE, corresponding to about 15 electron drifting simultaneously in the gas phase. It consisted then in using only 68 + 16 PMTs from the top + bottom array respectively, for both cases in the centred region. The acquisition starts to record only events that had one pulse summed over all these PMTs above 24 mV (150 PE) for more than 1  $\mu s$  width.

In the second science run, the acquisition trigger was improved in order to be able to trigger on lower energy S2 signals by requesting a majority condition on the number of PMTs that exceeded a 125 mV (0.5 PE) threshold [140]. Thanks to this improvement, the 100% trigger efficiency range was lowered from  $S2 > 300$  PE down to  $S2 > 150$  PE from the first science run to the second one. For all pulses that triggered the acquisition, the width of the associated waveform is 400  $\mu s$ , centred around this pulse, as illustrated in Figure 2.14(a) where the acquisition was triggered by a S2 signal.

Once the waveforms are recorded, an improvement of their resolution is needed to allow the identification of all S1 and S2 peaks that will be then used for data analysis. For this purpose, an off-line raw data reprocessing using a digital raised cosine filter is applied to the summed waveform for signal smoothing [133], corresponding to a 3 MHz frequency cut-off low-pass filter. An example of the smoothed signal can be observed in purple in Figure 2.21. This filtering step allows to identify high energy S2 signals, corresponding to all signals above  $\sim 150$  PE. As described in [133], the used algorithm will then search for time regions where the voltage summed over all PMTs is above 10 mV during at least 0.6  $\mu s$ . The previous and next 0.21  $\mu s$  of each time interval must also have an average voltage below 5% of the maximum of the corresponding time interval.

Due to the known average S2 signal width<sup>8</sup>, such interval could be enough large for being a

<sup>8</sup>From  $\sim 1$   $\mu s$  to  $\sim 2$   $\mu s$ , depending of the electronic cloud dispersion along drift axis due scattering depth, as studied in [141]

combination of two or more S2 signals. In order to establish the border of each of them, each interval is successively re-read from one side to the other, and vice-versa. During each reading, as soon as either the signal drops below 0.5% of the previous local maximum, or the slope's sign changes, a new S2 border is recorded. The reading can then continue on the rest of the interval, following the same rules, with a new local maximum that have to be found first. Among all the S2 peak candidates identified in this way, only those that have a Full Width at Half Maximum (*FWHM*) larger than  $0.35 \mu\text{s}$  will be confirmed as S2 signals and will have their time location and properties (intensity, width...) stored.

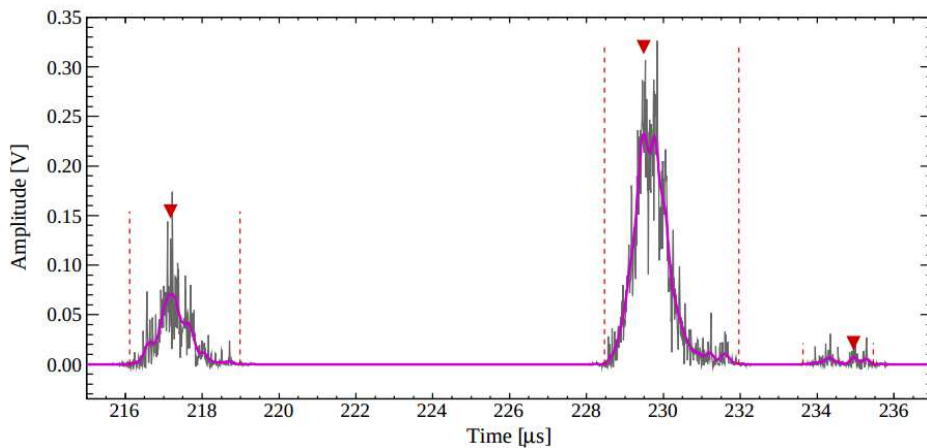


Figure 2.21: Illustration of a waveform smoothing (purple) through low-pass filtering for high energy S2 signal search (peaks identified by red markers, with boundaries represented by red dashed lines), from [133].

The following step of the data processing consists in searching for all lower energy S2 signals, mostly involved by one up to few electrons drifting in time coincidence in the gas phase, as studied in Chapters 4 and 5. For this purpose, the frequency cut-off of the low-pass filter is increased, and the interval search parameter is now changed such that the signal should be above 1 mV for at least  $0.4 \mu\text{s}$ . This is roughly the time needed for one electron to drift across the gaseous amplification region for an electric field at  $\sim 12 \text{ kV/cm}$  [133], the typical running conditions. The previous and next  $0.1 \mu\text{s}$  of each time interval should have an average signal below 5% of the maximum of the corresponding time interval. All low energy S2 candidates identified in this way, and that have a ratio of maximum per interval over interval width larger than  $0.1 \text{ mV/ns}$  are confirmed as S2 signals and are stored in the same way as higher energy S2 signals. Only all the 32 largest S2 peaks are finally kept, stored by decreasing order of size<sup>9</sup>. As an example, if 32 S2 signals are stored, the main one is labelled S2[0], while the lowest one is labelled S2[31].

The last step of the waveform reading consists in identifying all S1 signals in the waveform. Due to the S1 sharper property compared to S2 signals, the used algorithm will now search on the rest of the waveform only for maximums of signals, with no request on time duration compared to previous search. It is then all signals with a maximum above 3 mV that are primary identified as S1 signals. Their left and right boundaries are obtained as soon as the signal drops below 0.5% of the maximum of the corresponding signal. Additional conditions are applied for distinguishing them

<sup>9</sup>Maximum of the signal multiplied by signal time width

from S2 signals. Thus, the previous  $0.5 \mu\text{s}$  and next  $0.1 \mu\text{s}$  of each identified signal region of a S1-candidate signal should have an average signal respectively below 1% and 4% of the maximum of the associated S1-candidate signal region. Then, the distinction from possible single electron S2 signal is obtained by requesting a FWHM below  $0.5 \mu\text{s}$ . In order to reject also waveform base current fluctuations, the maximum of the S1-candidate should be three times bigger than all negative pulses in the neighbourhood of the S1-candidate signal region. As for S2 signals, only the 32 largest S1 peaks' parameters are kept, stored by decreasing order of size. All the algorithms used for the S1 and S2 signals identifications are described in [133].

In the next section, it will be explained how the detector response to the two types of recoil can be calibrated in order to draw the NR and ER bands for background rejection.

## 2.5 Detector calibrations

As mentioned several times in the previous sections, different radioactive sources have been used for the calibration of the detector response to the nuclear and electronic recoils. Among them, the  $^{241}\text{Am}^9\text{Be}$  and  $^{137}\text{Cs}$  source have been already mentioned, and have been used for each type of recoil respectively. Two additional calibration sources were also used: the  $^{60}\text{Co}$ , as quickly seen in the present chapter, and the  $^{232}\text{Th}$ . Both of them have been used for ER calibrations. For each science run, the strategy of the calibration was improved successively, in order to increase the knowledges on the background for dark matter search. These improvements are detailed in the sections below.

In addition, another radioactive calibration source, the 122 keV  $\gamma$  ray emitter  $^{57}\text{Co}$  was used in the early time of the XENON100 detector for the training of the neural network position reconstruction. Moreover, an LED source is also used once a week for PMTs calibration during each science run.

### 2.5.1 First science run

The first science run has taken place during Spring 2010, and has consisted in 100 live days of cumulated data for dark matter search. During this run, some calibrations with  $^{137}\text{Cs}$  source were taken weekly in order to monitor the evolution of the electron lifetime and in order to correct the signals. The nuclear recoil and electronic recoil bands were established with  $^{241}\text{Am}^9\text{Be}$  during commissioning run in Autumn 2009 and with  $^{60}\text{Co}$  during few different periods of the run respectively. The three sources are point-like sources, and can be placed close to the chamber, in external position but inside the shield, thanks to a copper pipe placed at half size of the chamber. This latter is illustrated by a top view of the detector in Figure 2.22, and has been previously mentioned in Figure 2.16(a).

Based on these ER calibrations and a data-MC calibration for nuclear recoils, as discussed in Section 3.3.3.2 for the case of the second science run,  $(1.8 \pm 0.6)$  background events were expected for the 48 kg LXe dark matter search region. This region was defined using the formula of the super-ellipse presented in Section 3.3.2.

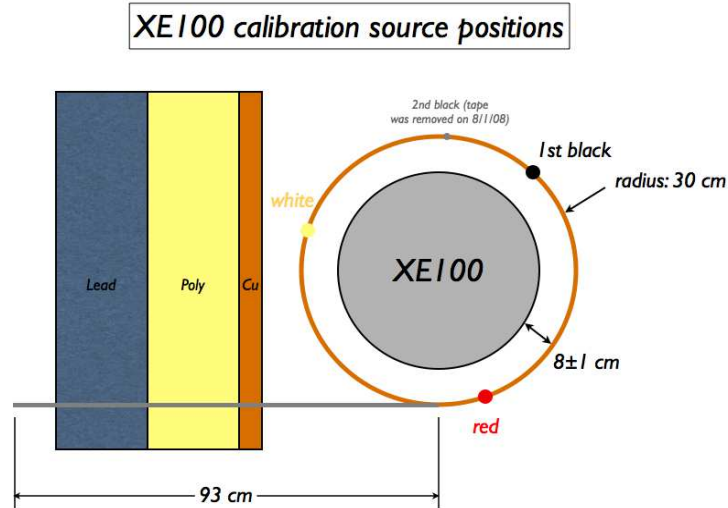


Figure 2.22: Illustration of the calibration process. The radioactive source is inserted inside the stainless tube, and placed closed to the chamber at different position labelled black, white and red inside the copper tube.

## 2.5.2 Second science run

The second science run is also the main one. It consists in about 225 live days of cumulated data for dark matter search acquired during 13 months in continuous operation mode for the detector between March 2011 and April 2012, interrupted only for maintenance. Due to the long time period of data acquisition, two calibration runs with the  $^{241}\text{Am}^9\text{Be}$  source were taken in order to demonstrate the stability of the detector response to NR. Since about one month is needed to wait after a such calibration, due to the activation of the isotopes  $^{129}\text{Xe}$  and  $^{131}\text{I}$  by neutrons, they have taken place during about three consecutive days at the beginning and at the end of the dark matter search. The three consecutive days correspond to the standard rule of the LNGS for the maximum time of a neutron source to be placed in underground laboratory, in order to reduce the perturbations of other low background experiments also installed underground. This maximum time can be however exceptionally extended on demand.

As for the first science run,  $^{137}\text{Cs}$  and  $^{60}\text{Co}$  source were used, for the same purpose respectively. Each of them were used once a week, with about 12 consecutive hours dedicated for the latter, in order to have high calibration statistic. Moreover, an additional ER calibration was used for the first time with XENON100, the  $^{232}\text{Th}$ . It corresponds to a large spectrum of  $\gamma$  ray emissions up to about 2.6 MeV thanks to all the decay products of the  $^{232}\text{Th}$ . One advantage is then to get an artificial background close in energy to the natural background induced by inner components of the detector.

Unlike other calibration sources,  $^{232}\text{Th}$  source consists in a thoriated tungsten wire, borrowed from the past Cuorecino experiment in Gran Sasso. Thanks to this, the emission of the  $\gamma$  rays can be done all around the chamber in the same time, in order to get the corresponding detector response from everywhere for each acquisition dataset. This additional calibration source can be thus used as an efficient independent cross-check of the ER band determined with  $^{60}\text{Co}$  source. As for this latter, about 12 consecutive hours per week are dedicated for ER calibration with

$^{232}\text{Th}$  source. The rest of the week was dedicated to dark matter search. Thanks to all these calibrations, about 35 times more statistics of ER data in the S1 dark matter search energy range were acquired with respect to the dark matter search data. Based on these ER calibrations and a data-MC calibration for nuclear recoils,  $(1.0 \pm 0.2)$  background events were expected for in the dark matter search region, as detailed in Section 3.3.3.2.

### 2.5.3 Third science run

The strategy developed for the third science run is similar to the one of the previous run. The same calibration sources were used by following the almost same time organisation: one NR calibration before the beginning of the science run with  $^{241}\text{Am}^9\text{Be}$  source, and weekly ER calibrations. The main improvement with respect to the previous run has consisted then in a strong increase of the calibration for both the ER and NR calibrations, in order to increase the knowledges on each associated S2 over S1 signals band, and leakages of one on the other. This has been motivated by both the results of the two observed background signals during the second science run with respect to the expectation of only one, and by the aim of reducing the value of the low energy threshold on the S1 signal from 3 PE to 2 PE in order to be more challenging for the search of low mass WIMPs.

As a result, the time dedicated to NR calibration was extended from three days to about five. For each weekly ER calibrations with  $^{60}\text{Co}$  and  $^{232}\text{Th}$  sources, the acquisition was increased by a factor two. At the time of writing, the analysis of the data acquired during this run are not finished. However, it will correspond to about 150 live days of cumulated data acquired during almost all the year 2013. If the corresponding sensitivity is not expected to be as much as constraining than the previous run, this however would provide good result for the sensitivity of the detector to dark matter for only this science run. Combined with previous run(s) this could also slightly increase the total sensitivity of the detector. However, at the time of writing, no clear decision has been taken for the combination of the data from different runs.

Furthermore, since almost one civil year of data was covered during this run, it also provides additional relevant data for the current analysis of the electronic background annual modulation for XENON100, in order to challenge signals claimed by the DAMA Collaboration [83].

### 2.5.4 Additional detector calibration for R&D

The third and last science run has ended in January 2014. Since that time, the XENON100 detector is however still working, and the next generation detector XENON1T is under construction. As a result, it has been decided to perform R&D on XENON100 for future calibration strategies on XENON1T.

In this context, a first intensive calibration campaign with the  $^{137}\text{Cs}$  source has been done in Spring 2014, as it is presented in Section 5.4.3. Since then, efforts have been also made on drawing for a small lead castle inside the shield, in order to insert as close as possible a new low and mono-energetic neutron source at 152 keV, made by the combination of yttrium  $^{88}\text{Y}$  and beryllium  $^9\text{Be}$ . This source takes advantage of the scattering of a  $\gamma$  emitted by the  $^{88}\text{Y}$  on the nucleus of the

$^9\text{Be}$ , releasing a neutron. The remaining  $^8\text{Be}$  will then decay into two  $\alpha$ , with however a lifetime emission larger than the time required for the emission of the neutron from the original  $^9\text{Be}$  [142]. This new calibration source will allow to investigate nuclear recoil almost only below 4 – 5 keV, in order to reduce the threshold sensitivity of the detector. Since no new science run is expected to be started with XENON100, the result from this calibration will benefit to XENON1T.

In addition, it has been also planned to take a longer  $^{241}\text{Am}^9\text{Be}$  calibration run than in the third science run, in order to investigate with enough high statistic the response of the detector at low energy for different electric field configuration, with the aim also to be able to reach a lower energy threshold in the future XENON1T science runs.

## Conclusion

In the present chapter has been explained the operation of a LXe dual phase TPC through the example of the XENON100 experiment, where two different signals  $S1$  and  $S2$  are emitted for a single scatter in liquid phase. The two existing types of recoil were also detailed, nuclear for neutrons and WIMPs, and electronic for  $\gamma$  rays and  $\beta$  particles, that lead to the description of two separated bands in  $S2/S1$  ratio as a function of the deposited energy in the liquid phase.

One of the key points of the direct dark matter search consists in being able to identify clearly these two bands on experimental data during dark matter detection mode. This can be done only by dedicated calibrations of the detector to measure the response for both nuclear and electronic recoil. Combined with the known contamination of each component of the detector, the expected background and sensitivity to dark matter interaction can be then drawn as it will be seen in the next chapter.

In addition, details have been also given on all the past and planned calibrations of the XENON-100 detector. Efforts are currently made for the realisation of these latter, in order to have first outcome before the beginning of the commissioning of the future detector XENON1T.

In the next chapter will be presented the quality rejection cuts applied to XENON100 data in order to draw these two bands for single scatters, and then select only data in the expected dark matter signal region. In addition, it will be presented the expected background and sensitivity to dark matter interactions reached by XENON100, for both spin dependent ( $SD$ ) and independent ( $SI$ ) analysis. For the latter case, the expected sensitivities of the next generation detectors will be also discussed, illustrating the favoured signal regions that will be investigated within the next years.

# Chapter 3

## Direct dark matter search with the XENON100 experiment

All the latest results from the direct dark matter search with the XENON100 experiment are presented here. Details on the general analysis performed for the dark matter search are firstly given, starting by an explanation of the correction of raw signal. The reconstruction of the nuclear and electronic recoiling energies are then presented, completed by an explanation of the dark matter data selection. The results from the WIMPs search during the second science run are then shown, followed by an explanation of the recent results of the search of axions particles, and completed by a presentation of the next steps of the XENON program.

### Contents

---

|  |            |
|--|------------|
| <b>Introduction</b> . . . . .                                  | <b>89</b>  |
| <b>3.1 From light signals to physical quantities</b> . . . . . | <b>90</b>  |
| <b>3.2 Expected background</b> . . . . .                       | <b>99</b>  |
| <b>3.3 Data analysis</b> . . . . .                             | <b>101</b> |
| <b>3.4 Limits on WIMP interaction cross section</b> . . . . .  | <b>107</b> |
| <b>3.5 Search for axions</b> . . . . .                         | <b>111</b> |
| <b>3.6 Towards next detector generation</b> . . . . .          | <b>115</b> |
| <b>Conclusion</b> . . . . .                                    | <b>116</b> |

---

### Introduction

Thanks to both the presentation of the dark matter candidate and their detection media in the first chapter, and then the presentation of the XENON100 detector, the main scientific results of the dark matter search performed with this experiment can be now presented.

For this purpose, the correction of the two signals, S1 and S2, due to the scattering position in the liquid phase is firstly presented. The reconstruction of the kinetic energy transferred to the recoiling particle by using either one of these two signals, or by using both of them is then

detailed, including an explanation of the motivation for the choice of one of these reconstruction method instead of another.

The explanation of the establishment of the nuclear and electronic recoil bands from the standard calibration procedure is also given, including details on the blinding procedure of the nuclear recoil band in the early beginning of each science run.

A qualitative description on the data selection cuts developed for the dark matter analysis is then given, followed by the presentation of the dark matter results during the second science run. For this purpose, the results from WIMPs search is firstly detailed, including both the assumed coupling of WIMP with nucleus (*Spin Independent, SI*) and with nucleons (*Spin Dependent, SD*), completed then by an explanation of the recent results on the axions search with the XENON100 experiment.

The status, the main characteristics and the goals of the next steps of the XENON program will be then introduced.

## 3.1 From light signals to physical quantities

### 3.1.1 Charge and light signals correction

All the analyses performed on the XENON100 experiment are based on the two available signals per scattering, S1 and S2. As mentioned in the previous chapter, an efficient reconstruction of the scattering is reachable thanks to the light pattern of the second one on the top PMTs arrays, and by using the time difference between the two signals. However, for the same amount of deposited energy in LXe, and for the same incident particle, each one of these two signals is position dependent, due to solid angle for the light collection, meshes transparencies, teflon panels reflectivity, electronic cloud attenuation during its drift, etc. As a results, a specific correction has to be applied to each of them.

#### 3.1.1.1 S1 light signal correction

Due to the size of the TPC, the S1 signals need to be corrected not only because of the (x,y) scattering position but also because of the scattering depth position. For each of these positions, the average S1 signal is measured by using internal and external calibration sources, for which the full deposited energy is well known and can be clearly identified. The former type of calibration sources comes from  $\gamma$  lines from both the neutrons inelastic scatterings over  $^{129}\text{Xe}$  isotopes and from neutrons activated lines of  $^{131m}\text{Xe}$ , with an energy set at 40 keV and 164 keV respectively. These two  $\gamma$  rays sources are homogeneously distributed in the TPC. The external source corresponds then to the  $\gamma$  rays emission at 662 keV from the  $^{137}\text{Cs}$  calibration source. In order to test the stability of the signal due to the cylindrical geometry of the chamber, the calibration source is placed at three different horizontal position at half-height around the TPC. Thanks to this, the symmetry has been confirmed.

For each of these three  $\gamma$  rays emission sources, a three dimensional correction map for the light collection efficiency of S1 signals has been drawn [122]. The three measurements have pro-

vided an agreement within 3 % between their results. The final map used for S1 signal correction is represented in Figure 3.1(a). The relative difference between measured signals and the average value for one considered  $\gamma$  rays source is expressed as a function of the scattering (r,z) position. The corrected signal S1 corresponds thus to the measured signal divided by the corresponding relative difference. The maximum light collection efficiency is reached as expected for scattering in the center of the TPC, right above the bottom PMTs array, while the weaker collection efficiency corresponds to scatterings close to the edge, on the top of the liquid volume ( $z \sim 0$  mm).

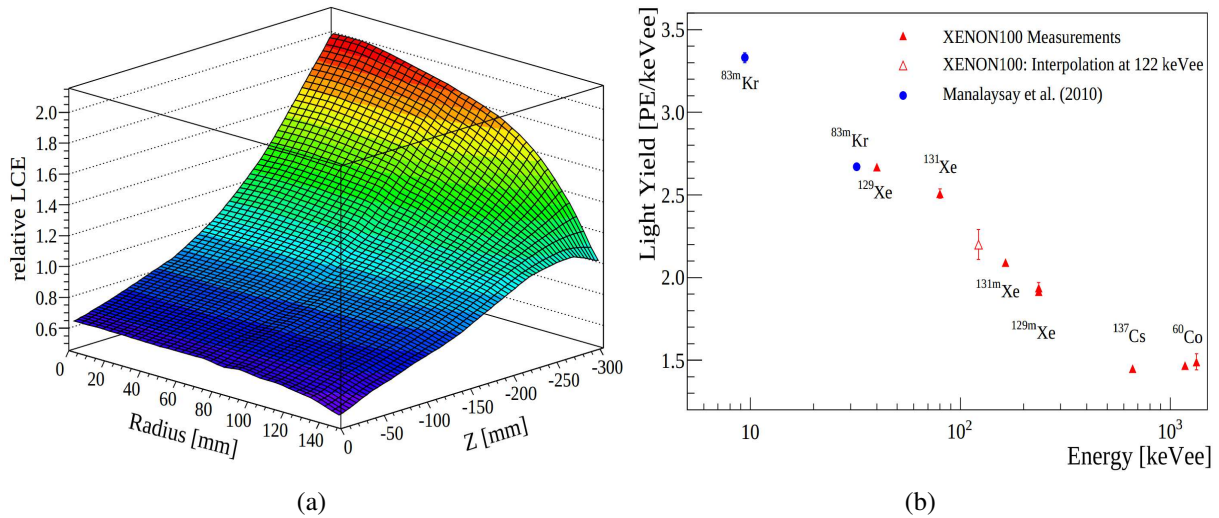


Figure 3.1: (a) Three dimensional light correction map for S1 signal, and (b) light yield extrapolation at 122 keV. Both pictures from [122]

This analysis is also able to provide through an extrapolation a quantity called *Light Yield* (LY), that is crucial for the establishment of the deposited energy in nuclear equivalent scale, as it will be seen in Section 3.1.2.2. This parameter corresponds to all the collected light during a corrected S1 signal for a single scattering in the LXe active volume, and divided by the total deposited energy. It is thus usually expressed in photoelectrons per unit of deposited energy in keV. The definition of this quantity will be also quickly reminded at the end of Chapter 5, since no application of this parameter will be done in between.

For the needs of the nuclear energy scale, this LY has to be calculated for a total deposited energy of 122 keV. However, no internal calibration source with such energy are available, and due to the size of the detector, an external source will be too low penetrating to investigate central region of LXe.

As a result, this value is calculated by investigating the average S1 signal measured for the full deposition of the energy of the ionizing  $\gamma$  ray, by using not only the three sources mentioned above, but also by using the  $\gamma$  rays emitted by neutrons inelastic scatterings over <sup>131</sup>Xe and activated lines from <sup>129m</sup>Xe, with an energy set at 80 keV and 236 keV respectively. Two other values have been also obtained with the external <sup>60</sup>Co calibration source, corresponding to the full absorption of the energy of the two  $\gamma$  rays emitted at 1.1732 MeV and 1.3325 MeV respectively. The corresponding results are presented in Figure 3.1(b) [122]. Additional results from two metastable states of the krypton isotope <sup>83m</sup>Kr are also presented, with an energy set at 9.4 keV and 32.1 keV respectively,

and that come from previous measurements [143].

The value of the LY at 122 keV is inferred from the fit of the data with an empirical function defined to be linear in logarithmic scale for the electric field in the liquid phase. It is equal to  $LY = (2.20 \pm 0.09) \text{ PE/keVee}$ , where the keVee unit corresponds to *electronic equivalent*, and is used to distinguish electronic recoil scale where no quenching factor is applied from nuclear recoil scale. The distinction between the two units will be more detailed in Section 3.1.2, where this LY value will be used.

### 3.1.1.2 S2 light signal correction

As for the S1 signal, the S2 one needs to be corrected as a function of its average position. The strategy used for this purpose is similar to the one described above, and uses the same three calibration sources in order to infer an  $(x,y)$  map for the relative variations of the S2 signal compared to the mean.

As for S1, the corrections obtained from each calibration source are in good agreement. In practice, the correction map used for the first science run corresponds to data measured with  $\gamma$  rays of 40 keV that come from inelastic scatterings of neutrons over  $^{129}\text{Xe}$ , such as it is presented in Figure 3.2. For the second science run, a slightly different map is used, measured with the  $^{137}\text{Cs}$  calibration source. Each of the PMTs arrays are then corrected separately. However, only the bottom array will be used for the S2/S1 ratio discrimination for dark matter search, due to a more homogeneous light distribution with respect to the top array where fluctuations are mostly induced by non-working PMTs, as illustrated by Figure 3.2(b). This is also due to PMTs saturation on top array during calibration as mentioned several times in this chapter. The maximum correction on the bottom PMTs array is thus of the order of 15 % [122].

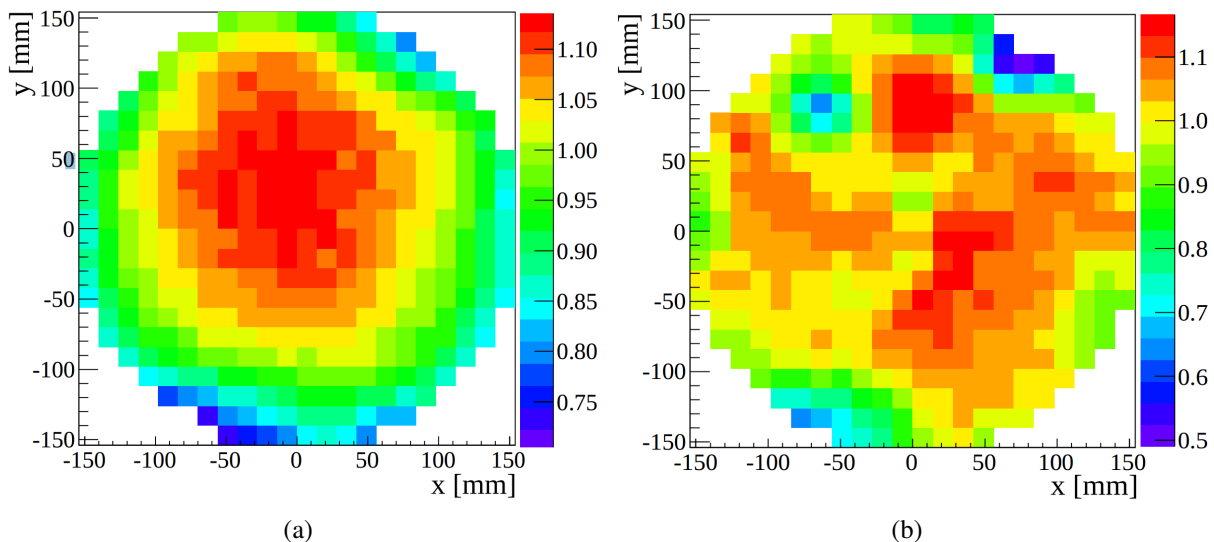


Figure 3.2: Two dimensional light correction map for S2 signal: (a) Bottom PMTs array and (b) top PMTs array. Both pictures from [122].

In addition to this  $(x,y)$  correction, the attenuation of the electronic cloud during the drift needs also to be taken into account. This correction factor corresponds to the Equation 2.21 presented

in Section 2.4.1.1.

As it has been mentioned in the previous chapter, for each S1 and S2 signals, several parameters such as their full intensity – corresponding to the integral of the full signal – are calculated and stored during the processing phase. Thanks to the corrections presented here, the corresponding corrected signals cS1 and cS2 are also stored during this processing. Furthermore, some other parameters need to be corrected. Among them, the temporal width of the S2 signal can be noticed. This parameter is used for establishing the correlation between the S1 and the S2 signal in order to avoid accidental temporal coincidence between the two signals.

The width of the S2 signal have thus to be consistent with the electronic cloud dispersion due to the scattering depth. The time duration of this S2 signal, such as the intensity amplification, depends on the gas gap, which is set between liquid level and anode mesh. Unfortunately, the anode mesh, such as the other grids, is not homogeneously flat. As a result, small modifications of the gas gap, and then also of the electric field, can occur. This leads thus to modifications of the electron drift velocity and amplification electric field in tiny regions of the gaseous phase. Moreover, it has been also observed that the width of the S2 signal follows also an exponential decay as a function of the drift time, due to the elongation of the electronic cloud during the drift [141]. This elongation depends on the type of the interaction and the deposited energy. For nuclear recoil, it can be measured with  $^{241}\text{Am}^9\text{Be}$  calibration source, such as illustrated by Figure 3.3(a).

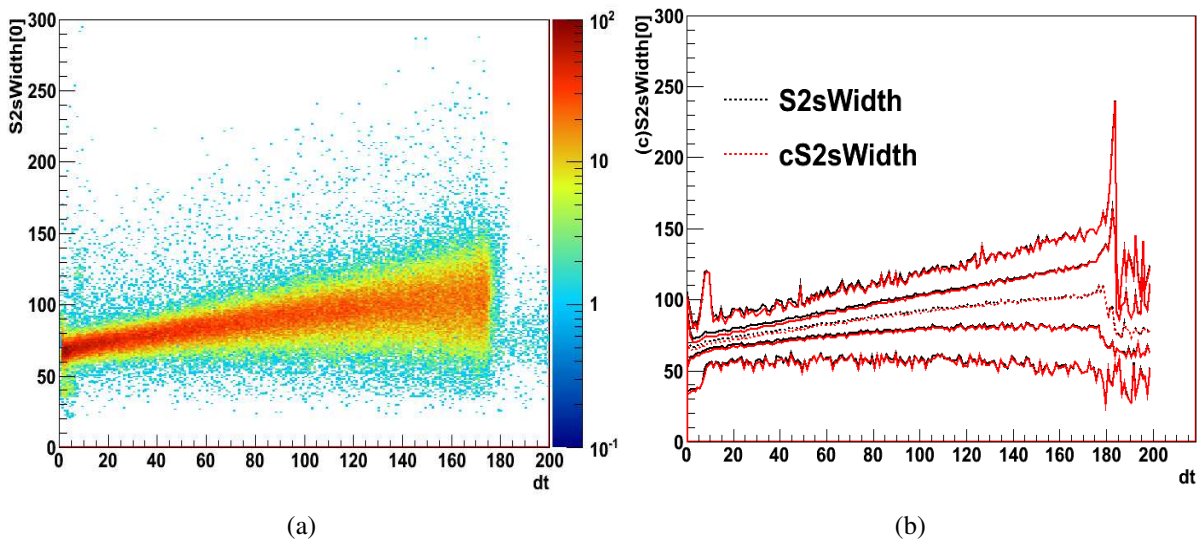


Figure 3.3: (a) Evolution of the width of the S2 signal as a function of the scattering depth, expressed here in term of time delay between S1 and S2 signals. Number of events per bin are represented by a color scale. (b) illustration of a data selection cut based on the width of both the corrected and uncorrected S2 signals. The average of the distribution is represented dashed curve, while the solid curves illustrate the data selection at  $1\sigma$  and  $2\sigma$ . Both pictures from [141].

As a results, for several slices of scattering depth position, a correction map of the S2 time duration with respect to average value needs to be drawn. The resulting distribution of the corrected S2 width as a function of the scattering depth can be then established. The average value,

and the  $1\sigma$  and  $2\sigma$  contour of the corrected and uncorrected distributions can be compared, as illustrated respectively in black and red on Figure 3.3(b). This allows to establish a specific cut for the S2 width that should be within the  $2\sigma$  contours for the dark matter search. Further details on this analysis can be found in [141], while other data selection cuts for dark matter search will be briefly reviewed in the present chapter, as summarized in Section 3.3.2.

### 3.1.2 Estimation of the energy deposit

In addition to the very accurate reconstruction position of the scattering, it is also possible to calculate the energy transferred during the scattering by using either one of the two S1 and S2 signals, or by combining both of them. Depending on the energy of the scattering particle, one of these three methods will be used. As it will be seen in Section 5.8.6, the reconstruction of the deposited energy for the search of low mass WIMP will be done by using only the S2 signal, since it will be the only signal that would be produced and detected.

The remaining two methods, based either on the S1 signal or on the combination of the two signals, are applied to nuclear recoils and electronic recoils respectively. As it is illustrated by Figure 3.4, the former has the lower energy resolution with respect to the other two, while the latter has the highest resolution. As a consequence, this method will be preferred to the others as often as possible, which means that it will be the case for all the ER calibrations. In order to understand why this is not also the case for NR, the explanation of the calculation through this method is firstly needed.

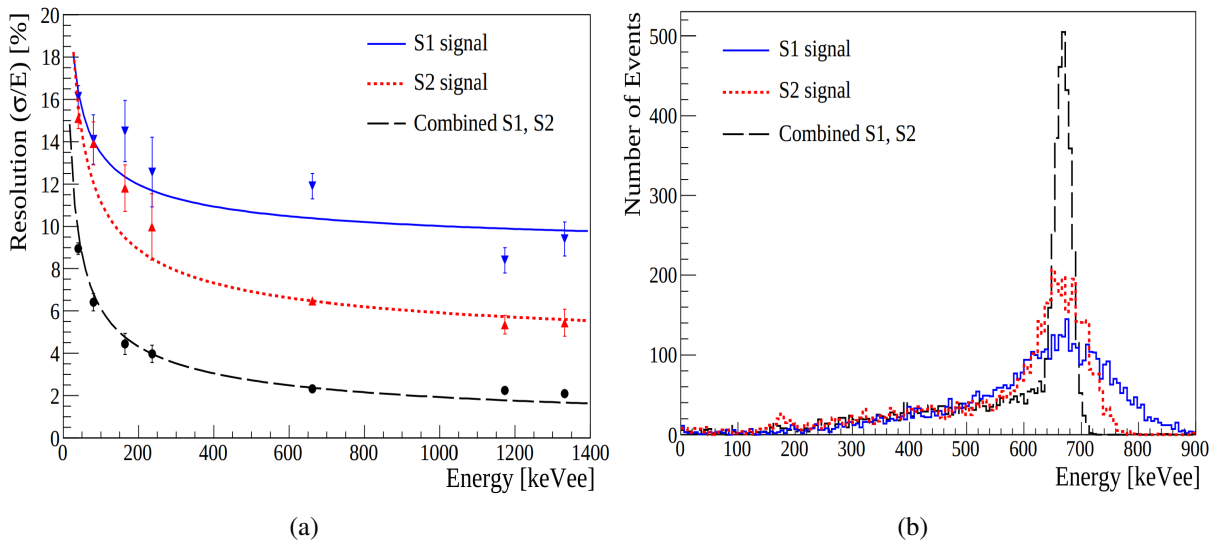


Figure 3.4: (a) Comparison of the energy resolution of the reconstructed deposited energy by using either one of the two signals or a combination of the two signals as a function of the energy of the original ionising  $\gamma$  ray, and (b) comparison of the reconstructed energy spectrum of the  $^{137}\text{Cs}$   $\gamma$  rays with each of the three methods. Only single scatter are selected, including a veto rejection cut in order to reduce the Compton continuum. The resolution of the reconstruction of the full absorption peak at 662 keV at  $1\sigma$  is equal to 12.5 %, 6.5 % and 2.3 % for the S1 based method, S2 based method and (S1+S1) based method respectively. Both pictures from [122].

### 3.1.2.1 Deposited energy in combined energy scale

As mentioned in Section 2.4.1.1, the full absorption peak of a  $\gamma$  ray can be easily identified thanks to the anti-correlation of the light and charge signal, such as it was illustrated previously in Figure 2.11(b) by S1 and S2 signals measured with the  $^{137}\text{Cs}$  calibration source, or such as it will be discussed for the relative light and charge yield in Section 5.6. The ellipse drawn by the full absorption peak of each  $\gamma$  ray in the (S2, S1) plane can be thus clearly selected by using a two dimensional Gaussian, such as illustrated by Figure 3.5(a). This leads then to the evaluation of the anti-correlation angle  $\theta$ , as illustrated in Figure 3.5(b), that represents the charge signal S2 in PE as a function of the light signal S1 in PE.

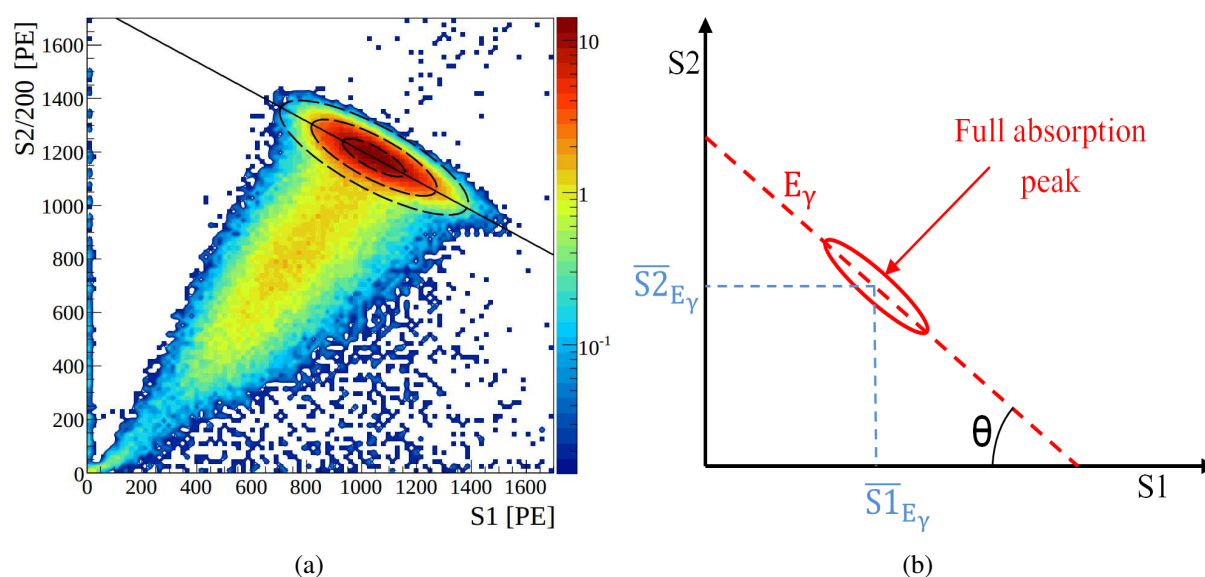


Figure 3.5: (a) Anti-correlation between light and charge signals measured with the  $^{137}\text{Cs}$  calibration source, from [122], and (b) illustration of the reconstruction of the deposited energy as a function of the light and charge signal.

Thanks to the selection of the main ellipse in Figure 3.5(a), the average light and charge signals,  $\overline{S1}_{E_\gamma}$  and  $\overline{S2}_{E_\gamma}$ , for the full absorption peak of the penetrating  $\gamma$  ray and the rotation angle  $\theta$  can be determined. The line drawn by the main axis of this ellipse corresponds to a line of a constant energy equal to the full absorption peak of the original  $\gamma$  ray, expressed in keV. The corresponding equation can be determined thanks to the particular point of this line drawn by the  $\overline{S1}_{E_\gamma}$  and  $\overline{S2}_{E_\gamma}$  signals:

$$S2 = -A(S1 - \overline{S1}_{E_\gamma}) + \overline{S2}_{E_\gamma} \quad (3.1)$$

$$(3.2)$$

where the slope  $A$  of the line is equal to  $\tan(\theta)$ . Since for all the points of this line, the associated energy is constant and equal to  $E_\gamma$ , the equation 3.1 can be rewritten as:

$$\begin{aligned}
S2 + A \times S1 &= \overline{S2}_{E_\gamma} + A \times \overline{S1}_{E_\gamma} \\
&= k \times E_{dep}
\end{aligned} \tag{3.3}$$

where  $k$  is a constant that can be calculated for the specific example of the full deposition of the energy  $E_\gamma$  of the original  $\gamma$  ray by photoelectric effect, knowing the value of  $\overline{S1}_{E_\gamma}$ ,  $\overline{S2}_{E_\gamma}$  and  $\theta$ . The Equation 3.3 is then extended to other (S1, S2) pairs to determine the corresponding deposited energies. It has been actually demonstrated that the rotation angle is constant for all the known energy lines, except for the 40 keV and 80 keV lines, belonging to  $^{129}\text{Xe}$  and  $^{131}\text{Xe}$  isotopes respectively, and that correspond to the combination of a nuclear recoil and a  $\gamma$  ray emission during an inelastic scattering [122]. This reconstructed energy is usually known as the *Combined Energy Scale*, (CES), and is expressed in *keVee*, where *ee* is used for electron equivalent in order to be distinguished from the nuclear recoil energy reconstruction *keVnr* that is presented below. This CES is used for the analysis of the ER background studies, and is expressed as:

$$CES = \frac{1}{k} \times (S2 + A \times S1) \tag{3.4}$$

$$\tag{3.5}$$

where the quantities  $A$  and  $k$  have been presented right above. In practice, only the S2 signals from bottom PMTs array is used, in order to avoid saturation from top PMTs array due to too much energetic signals with respect to the original design of the PMTs, as it will be discussed in Section 5.5.

### 3.1.2.2 Deposited energy in nuclear recoil energy scale

For nuclear recoil, the CES can not be used, since the neutron calibration source is not monoenergetic. As a result, neither the original energy of the neutron, nor the part of this energy that will be transferred to the recoiling nucleus is known. The reconstruction of the energy can be thus done only by using one of the two signals. The selected method for nuclear recoil at high energy, typically above a ten of GeV, is thus based on the S1 signal. The motivation of this choice will be explained after the detail of the energy reconstruction.

In order to infer the deposited energy for nuclear recoil from the S1 signal, this latter needs to be rescaled to a known light yield per unit of deposited energy. This corresponds to the light yield LY previously mentioned, such as in section 3.1.1.1. Since the S1 signal measured here corresponds to a nuclear recoil while the LY of Section 3.1.1.1 corresponds to an electronic recoil, an attenuation factor has to be taken into account. It corresponds to the relative light yield for a neutron scattering with respect to the light yield for the full absorption of a  $\gamma$  with a known energy, when no drift field is applied for the two types of recoil.

For historical reasons, the energy of this  $\gamma$  is equal to 122 keV, corresponding to the  $\gamma$  ray emitted by a  $^{57}\text{Co}$  source. This attenuation factor is known as the  $\mathcal{L}_{eff}$ , and it is an intrinsic property of xenon. It has been measured down to 3 keV for nuclear recoils (*keVnr*) in LXe induced

by neutrons from a monochromatic source [144], as shown by Figure 3.6. For nuclear recoils below 3 keV, no measurements could have been performed, and only extrapolation of the trend of the evolution of  $\mathcal{L}_{eff}$  as a function of the recoiling energy could have been done. As a result, the sensitivity to low mass WIMPs is dramatically reduced with respect to higher mass WIMPs. For the results of the second science run presented later in this chapter, the assumption of  $\mathcal{L}_{eff} = 0$  below 3 keVnr has been also tested, leading to very slightly modifications of the sensitivity to dark matter scattering obtained with the logarithmic extrapolation shown in Figure 3.6.

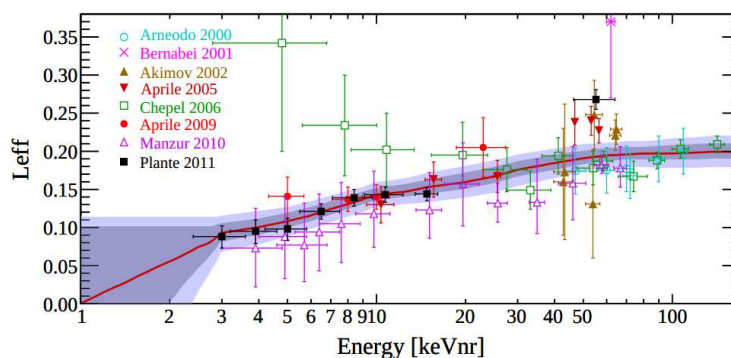


Figure 3.6: All direct measurements of  $\mathcal{L}_{eff}$  as a function of the nucleus recoiling energy. Above 3 keV, the distribution is described by a Gaussian distribution to obtain the mean, represented by the solid line, and the uncertainty bands at  $1\sigma$  and  $2\sigma$ . Below this energy region, the trend is logarithmically extrapolated to  $\mathcal{L}_{eff} = 0$  for a nuclear recoil equal to 1 keVnr. Figure from [139].

In order to be consistent, the associated light yield per unit of deposited energy under the usual drift field of the LXe for this specific 122 keVee  $\gamma$  ray needs to be known. This corresponds to the  $LY$  parameter previously mentioned in Section 3.1.1.1, and it is equal to  $(2.20 \pm 0.09)$  PE/keVee.

Moreover, since  $\mathcal{L}_{eff}$  has been measured for conditions with no applied drift field, some light signal attenuation factors  $S_n$  and  $S_e$ , for nuclear and electronic recoils respectively, have to be applied due to the electric drift field for the measured S1 signal and LY that will reduce the electron-ion recombination. The two quantities have been established independently at 0.95 and 0.58 respectively [145]. The former is independent in energy, while the latter has been measured with the 122 keV  $^{57}\text{Co}$  source.

As a consequence, the deposited energy  $E_{nr}$  in nuclear equivalent energy scale is expressed as:

$$E_{nr} = \frac{S1}{LY} \frac{1}{\mathcal{L}_{eff}} \frac{S_e}{S_n} \quad (3.6)$$

Unlike the CES used for the background analysis, this nuclear energy scale is used for dark matter search. The selection of this reconstruction method, despite of a weaker energy resolution with respect to the remaining reconstruction method, that is based on the S2 signal, is motivated by lower uncertainties on the values of  $\mathcal{L}_{eff}$  than those associated to the model of the relative drifting charge yield  $Q(E)$  under experimental drift field with respect to the drifting charge yield under infinite drift field in LXe,  $Q_0$ , and that is used for the reconstruction of the energy deposition with the S2 signal, as detailed in Section 5.8.6.

### 3.1.3 Example of an interaction signal: the full absorption of a $\gamma$ from $^{137}\text{Cs}$ beta decay

As an illustration, the S1 and S2 signals measured during all  $^{137}\text{Cs}$  calibrations of the first science run [139] has been considered. In these conditions, the cathode voltage was set at 16 kV, and the anode voltage at 4.5 kV/cm, implying an average electric field in gas phase at about 11.9 kV thanks to a gas gap of about 2.5 mm between liquid surface and anode mesh. Such data will be used in Section 5.6 because of the very high electric field condition in the gas phase that insure a 100% electrons extraction yield from liquid to gas phase.

The calculation of the number of emitted photons per S1 and S2 signals for photoelectric effect of  $\gamma$  rays from  $^{137}\text{Cs}$  are detailed in Section 5.7. The corresponding results are summarized in Table 3.1. It includes also the average low energy S2 signal induced by each electron accelerated in the gas phase, usually called *secondary scintillation gain* in this thesis, and widely discussed in Chapter 4 and Chapter 5. As for the S1 and the high energy S2 signals, this signal is expressed in both photoelectrons and photons.

| S1 [PE] | S1 [ph]          | S2 [PE]          | S2 [ph]          | S2 [ $e^-$ ]     | S2 [PE/ $e^-$ ] | S2 [ph/ $e^-$ ] |
|---------|------------------|------------------|------------------|------------------|-----------------|-----------------|
| 1060    | $1.8 \cdot 10^5$ | $5.2 \cdot 10^5$ | $1.1 \cdot 10^7$ | $2.8 \cdot 10^4$ | 18.65           | 390             |

Table 3.1: Summary of the S1 and S2 signals emitted during the photoelectric effect of a  $\gamma$  ray emitted by the  $^{137}\text{Cs}$  calibration source, or by each electron extracted into the gas phase.

### 3.1.4 Nuclear and electronic recoils discrimination

As previously detailed, the ratio between the two S1 and S2 signals allows the discrimination between electronic and nuclear recoils. Figure 3.7 illustrates thus the two S2 over S1 signal ratio for each of these two types of recoil, represented on top and bottom plots respectively. They were obtained with a  $^{60}\text{Co}$  1.17 MeV and 1.33 MeV  $\gamma$  rays emitter and an achromatic  $^{241}\text{Am}^9\text{Be}$  neutrons source with neutron energy emission of the order of few MeV respectively. The latter source consists in the combination of two isotopes. The neutron are emitted by the scattering of the  $\alpha$  particle emitted from the  $^{241}\text{Am}$  source on the  $^9\text{Be}$ . On the two plots of Figure 3.7, the black markers represents the S2 over S1 ratios in logarithmic scale as a function of the deposited energy in the LXe, expressed in  $keVnr$ .

The two red and blue lines represent the median of electronic recoil distribution and nuclear recoil distribution respectively. The dashed curve represents the 300 PE S2 detection threshold, as discussed in section 2.4.6. The two vertical dashed lines correspond to the lower and upper energy range, depending on the S1 detection threshold and the upper limit of the data blinded region used at that time. These two lines correspond to 8.7 keVnr and 32.6 keVnr respectively. In term of S1 signal, it corresponds to 4 PE up to 20 PE. As an illustration, the order of magnitude of the number of emitted photons for each signal and each type of recoil can be calculated, with the quantum and collection efficiencies used in Section 3.1.3. The corresponding numbers are reported in Table 3.2.

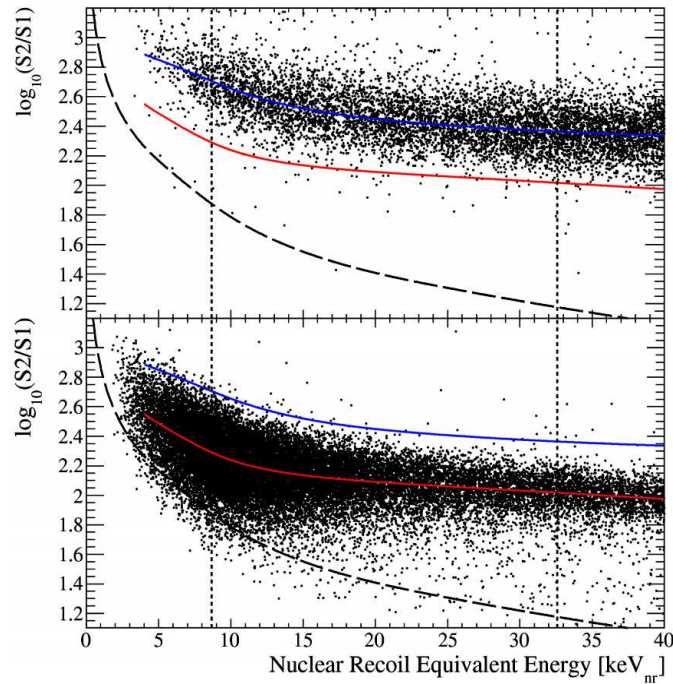


Figure 3.7: XENON100 response for electronic (top) and nuclear (bottom) recoils from calibration during commissioning run in Autumn 2009, from [146].

| Type of recoil | S1 [PE] | S1 [ph] | S2 [PE] | S2 [ph] | $\log_{10}(S2/S1)$ |
|----------------|---------|---------|---------|---------|--------------------|
| Electronic     | 4       | 76      | 2100    | 44000   | 2.72               |
| Nuclear        |         |         | 800     | 16000   | 2.30               |
| Electronic     | 20      | 380     | 4600    | 95000   | 2.36               |
| Nuclear        |         |         | 2100    | 44000   | 2.02               |

Table 3.2: Comparison between nuclear and electronic recoils for S1 and S2 signals

## 3.2 Expected background

For the XENON100 experiment, like for all kind of low-background experiments, the background events come not only from external sources, such as the muon-induced neutron described in the previous section, but also from internal sources. In the specific case of LXe experiments, two other rare gas, the krypton and the radon – that will also affect non-LXe rare gases low background experiment – will have non-negligible contributions to the total background, as presented in the following developments.

Moreover, an additional source of internal background exists, and is made by all the radioactive components of each material that constitute the detector, mostly uranium ( $^{235}\text{U}$  and  $^{238}\text{U}$ ), thorium ( $^{228}\text{Th}$  and  $^{232}\text{Th}$ ) and radium ( $^{228}\text{Ra}$  and  $^{226}\text{Ra}$ ), but also potassium ( $^{40}\text{K}$ ), cobalt ( $^{60}\text{Co}$ ) and caesium ( $^{137}\text{Cs}$ ) that would all lead to either  $\alpha$ ,  $\beta$  or  $\gamma$  emission, directly via their decay, or via the decay of their daughter species. As a consequence, a careful material selection via intensive screening have to be made for the selection of detector's components, as it was already the case for XENON100 [147]

### 3.2.1 The radon background

As mentioned in Section 2.2.3, radon is a radioactive gas. It appears in radioactive decay chains with two important isotopes,  $^{222}\text{Rn}$  and  $^{220}\text{Rn}$ , in the  $^{232}\text{Th}$  and  $^{238}\text{U}$  decay chains respectively. Both of them are produced by  $\alpha$  decay of the radium. This gas will then be distributed either in the detector environmental air because of being released from rock, or will be produced by radium atoms present in the components of the detector.

In the first case, the critical point consists in the reduction of air contamination by all possible tiny leaks on component's connection or in the recirculation gas system, while for the second case it is again only a careful material selection that would reduce this exposure. Due to LXe recirculation, these isotopes will then be present everywhere in the liquid phase, meaning that no fiducialisation would reduce their contribution to the total background of the experiment.

As illustrated in Figure 3.8(a), the two radon isotopes  $^{222}\text{Rn}$  and  $^{220}\text{Rn}$  are followed by two  $\alpha$  decays, two  $\beta$  decays and finally by one  $\alpha$  decay. As widely discussed in [148], the  $\alpha$  decays will lead to a total deposited energy more than two orders bigger than in the expected WIMPs deposited energy region. In parallel, the short decay time of the last  $\beta$  and  $\alpha$  emissions will lead to a very specific signal in the waveform recorded by the PMTs, corresponding to the combination of two S1 and two S2 that belong to these two successive decays. Such events are also called *BiPo* events, due to the involved isotopes.

It is then the remaining  $\beta$  decay that will contribute to the final background of the detector. To measure this contribution, a good continuous measurement of the radon contamination is requested, in order to make a precise prediction from Monte Carlo simulations. This contamination is measured through the signature of both  $\alpha$  decays through their full deposited energy, and BiPo events. In the XENON100 main science run [74] the expected background from radon was evaluated to  $1.51^{+0.03}_{-0.23}$  milliDaily Rate Unit ( $mDRU^{10}$ ) [148].

### 3.2.2 The krypton background

Radon is not the only rare gas that would contribute to the background of a LXe TPC. A second contribution comes from krypton, mostly through its unstable isotope  $^{85}\text{Kr}$ . It is a long-life  $\beta$  emitter with  $E_\beta = 173$  keV. The  $\beta$  emission is followed 1.46  $\mu\text{s}$  after by a  $\gamma$  ray emission at  $E_\gamma = 514$  keV corresponding to the relaxation of the excited state of the  $^{85}\text{Kr}$ 's son, the rubidium  $^{85}\text{Rb}$ . Krypton is naturally present in the xenon because of similar air distillation conditions needed for their both extractions, and a higher relative proportion in air for krypton than for xenon. As a consequence,  $^{85}\text{Kr}$  will be everywhere distributed in xenon, and its contribution to the total background, as for radon isotopes, would not be reduced by fiducialisation.

A solution for reducing the  $^{85}\text{Kr}$  contamination is to use a dedicated distillation column before any detector filling, like for XENON100 with the on-site distillation column illustrated in Figure 3.8(b). Thanks to it, the  $^{85}\text{Kr}$  contamination was lowered down to  $19 \pm 1$  particles per trillion (ppt) in LXe during the main science, measured by Ras Gas Mass Spectrometer (*RGMS*) and confirmed by  $\beta$  -  $\gamma$  coincidence analysis, corresponding to the reduction of more than one order

---

<sup>10</sup>1 DRU = 1 d<sup>-1</sup>kg<sup>-1</sup>keV<sup>-1</sup>

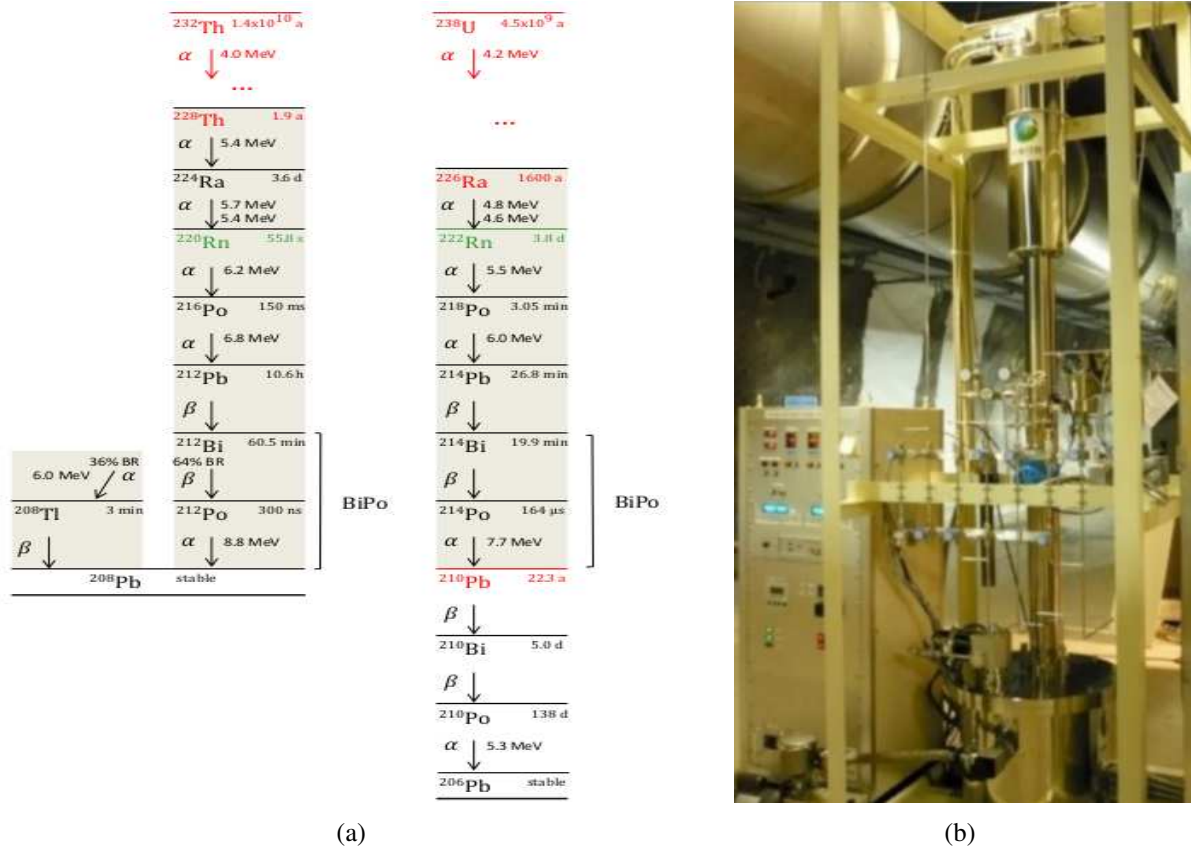


Figure 3.8: (a) Decay chains of  $^{232}\text{Th}$  and  $^{238}\text{U}$ , from [148], (b) XENON100 krypton distillation column.

of magnitude from previous science run. The associated expected background was  $0.74 \pm 0.16$  millidaily rate unit [148].

As presented right above, radon and krypton have signatures that allow to evaluate their proportion in LXe. However, such an identification would not allow for a total rejection since for a given deposited energy in the LXe, the ratio  $S2/S1$  would follow a Gaussian distribution centered around the average of either the nuclear recoil band or the electronic recoil band. There will be thus non-negligible probabilities for all ER events to leak from electronic band to nuclear band, leading to a fake-positive WIMP signature. That is why, in order to take into account this contribution to the final expected background and prevent this leakage, it is important to both measure these contaminations and make efforts to reduce them with distillation, leak check and careful material selection.

## 3.3 Data analysis

### 3.3.1 Dark matter data blinding strategy

In order to not be biased from the expected result, it has been decided to make the analysis of the dark matter search data in blinding mode. As a result, in the early beginning of each science run, the first datasets acquired with  $^{60}\text{Co}$  and eventually  $^{232}\text{Th}$  are used to define the blinded region

for dark matter search. Since, thanks to these datasets, the ER band is available, i.e. the ratio S2 over S1 as a function of S1, for corrected signals in logarithmic scale (using only the S2 signal from bottom array only, as it will be also the case for the rest of this chapter), it is then possible to quickly define a region below the 90 % of the signals population of this band. This can be done thanks to the Gaussian distribution of the profile of the band per each S1 bin.

The lower boundary of this blind region is then defined at 2 PE, below which value the signal is dominated by noise. Thanks to this lower band, the proportion of noisy waveforms can be thus investigated, in order to define a basic quality cut that could reject also noisy events.

The upper band is then fixed at 100 PE, far above the usual upper bound at 20 – 30 PE used for the final dark matter search. Thank to this, the region above 100 PE can be used for test without inducing any bias on the final analysis. Then, before the final unblinding, the procedure can be firstly tested on the 30 – 100 PE region. The corresponding dark matter blinded region for the second science run is thus represented by the red contour in Figure 3.9.

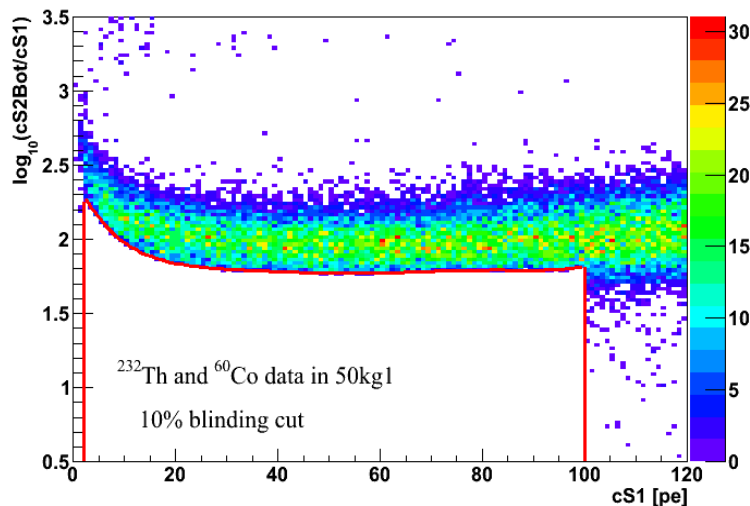


Figure 3.9: Illustration of the blinded region in S2 over S1 signals as a function of the S1 signal for dark matter search used during the second science run. Figure from XENON100 Collaboration.

The data used for the ER band correspond to the combination of the few first datasets acquired with <sup>60</sup>Co and <sup>232</sup>Th in the early beginning of the science run. The outer regions of the chamber have been excluded to analyse a 50 kg cleaner volume. The general formula used for such selection is detailed at the end of the next section. For each S1 signal between 2 PE and 100 PE, the 10 % lower S2 over S1 quantile is blinded.

### 3.3.2 Data selection cuts

Thanks to the calibration of the detector response during science run to each type of recoil, the two corresponding S2 over S1 signals in logarithm scale as a function of the S1 signal for corrected signals, can be drawn. These bands can be also flattered by rescaling to the average of the ER band for simplifying the analysis. Moreover, the features of the waveforms of each type of recoil can be also analysed in order to define data quality selection cuts for the final analysis of

the blinded dark matter data. As a result, only events with only one S1 and only one S2 signals are selected thanks to the very low intensities of the others identified S1 and S2 signals on the same waveform, in order to analyse only single scatter.

In addition, their own properties are also investigated in order to select only real single S1 and S2 signal. For the former type of signal, this can be done by analysing the number of implied PMTs and their spacial distribution in order to reject multiple scatterings events with only one scattering in the active region, while all the other could occur below the cathode. These multiple scatterings events are usually known as  $\gamma-X$  events, where the  $X$  refers to the unknown scatterings below the cathode. For these events, all the individual S1 signals, belonging to each scattering, will be seen in time coincidence. On the contrary, only the scattering in the active region – the usual LXe volume between cathode and ground mesh right below the liquid surface – will lead to the emission of a S2 signal. The electrons released below the cathode will indeed drift in opposite direction toward the very bottom of the TPC, down to be collected by the ground mesh right above bottom PMTs array. Such events are thus very dangerous for dark matter search since, even if they belong to ER, the final measured S2 over S1 signals ratio would be lower than the usual ER band due to the combination of all the S1 signals, and could mimic perfectly the expected ratio for NR. That is why efforts are made for rejecting such events by using the S1 signal PMTs light pattern in order to analyse the number of implied PMTs and their spacial distribution. The contribution of the remaining  $\gamma-X$  events to the total background is then established by Monte-Carlo simulations.

Then, the properties of the S2 signals are also investigated in order to check that both PMTs arrays are effectively implied for these signals. In order to reject unphysical events where a S1 signal is accidentally associated to a S2 signal, the corresponding S2 over S1 signals ratio that are higher than the expected one for ER band are also rejected. This relationship between the S1 and S2 signals is also confirmed by analysing the temporal width of the latter as a function of the depth of the scattering, i.e. the time difference between the two signals, due to vertical dispersion of the electronic cloud during its drift, as discussed in Section 3.1.1.2.

Moreover, the low relative difference of the reconstruction of the position of the scattering between each of the three algorithms is also used to selected good quality events for dark matter search. This quality is also promoted by rejecting events with noisy signals, either in the 99 kg LXe veto region around the chamber, or in the same waveform of the analysed event by investigating the part of the signal summed over the entire waveform that belongs to the combination of the main S1 and S2 signal with respect to the rest of the signal. For noisy events, this proportion is expected to be weaker than half of the entire signal.

Based on these data selection cuts, the trigger efficiency of the recorded events as a function of the S2 signal has been investigated. A trigger efficiency above 99% has been thus reached for a main S2 signal above 300 PE during the first science run and for a main S2 signal above 150 PE during the second science run. The improvements between the two successive science runs were mainly due to the reduction of the electronic noise conditions. Moreover, thanks to these improvements, the acceptance of most of the data selection cuts as a function of the measured S1 signals has been also investigated, allowing to reduce the threshold on the S1 signal from 4 PE down to 3 PE, corresponding to the reduction of the minimum deposited energy from 8.7 keVnr down to 6.6 keVnr, from the first science run up to the second one respectively.

For the rest of this chapter, no more comparisons will be done between these two science runs. The presented results will thus refer only to the second science run since it corresponds to the most performing results released by the XENON100 experiment up to the time of writing where no result from the third science run has been published yet. For more details on the first science run, the reader can refer to [139].

As presented in the Section 3.3.3, two different methods were used in order to investigate any possible excess of the expected background due to WIMPs scatterings inside the chamber. The first one is based on *Profile Likelihood* analysis (*PL*), while the second one is based on the search of signals excesses in a benchmark region. For each analysis, the upper bound of the S1 signal (deposited energy) is set at 30 PE (43.3 keVnr) for practical reasons and at 20 PE (30.5 keVnr) for an optimisation of the signal-to-background ratio respectively [74].

Thanks to the all these data selection cuts, a final LXe volume for WIMP search can be drawn, the *Fiducial Volume* (*FV*). This volume correspond to the larger LXe volume with the minimal exposition to background events from component in the edges of the TPC. Due to the cylindrical shape of the chamber, this volume can be preliminary drawn as a cylinder too. However, in order to reduce the background exposition in the "corner" of the TPC, the shape of this volume is finally set as a rotated *super-ellipse*, usually defined in the  $(r^2, z)$  plane, where  $r$  is the radial position of the scattering and  $z$  its depth, both expressed in  $\text{mm}^2$  and  $\text{mm}$  respectively:

$$\left(\frac{|z|}{Z_{max}}\right)^n + \left(\frac{r^2}{R_{max}^2}\right)^n < 1 \quad (3.7)$$

where  $Z_{max}$  and  $R_{max}^2$  are the two half-axes of the super-ellipse. Due to the origin of the reference system of the depth placed 5 mm below the ground mesh close to the liquid surface, this expression need to be adapted for XENON100 analysis. The formula 3.7 simply corresponds to an extension at higher order of the power  $n = 2$  of the usual ellipse function. In practice, this FV is defined by using the ER calibration data and all the data selection cuts defined previously. The involved quantity of LXe,  $M_{LXe}$ , can be also calculated:

$$M_{LXe} = 4 \times Z_{max} \times R_{max} \frac{(\Gamma(1 + \frac{1}{n}))^2}{\Gamma(1 + \frac{2}{n})} \times \frac{1}{2} \times \pi \times M_{Vol}(LXe) \quad (3.8)$$

where  $\Gamma(x)$  is the mathematical gamma function and  $M_{Vol}(LXe)$  is the liquid xenon volumic mass and is equal to  $2.827 \text{ g.cm}^{-3}$  at XENON100 temperature and pressure [113]. During the second science run, the LXe mass used for the FV was equal to 34 kg.

By using all these criteria for data selection, the two ER and NR bands have been drawn and flattened thanks to the  $^{60}\text{Co}$  and  $^{232}\text{Th}$  calibrations and the  $^{241}\text{Am}^9\text{Be}$  calibration respectively, as shown in the next section. The last data selection cut for the search of WIMP signals is based on these two bands. In order to investigate the expected signal region drawn by the ratio of two signals, only the 97 % upper quantile of the NR band was analysed, whatever is the method used for analysis among the two presented in the next section.

Furthermore, for the method using a benchmark region, this cut is completed by a 99.75 % rejection line of the ER band, in order to exclude almost all signals induced by electronic recoils. These two cuts are illustrated in the next section.

### 3.3.3 Statistical methods

Once all the data selection cut are fixed, all the datasets acquired without calibration source for dark matter search are unblinded. As soon as it is done, two analyses are performed in parallel. As said in the previous section, the first one is based on the *Profile Likelihood* method (*PL*), while the second one is used as cross-check of the former by analysing the excess of signal in a benchmark signal region. The two independent analyses are detailed in the present section.

#### 3.3.3.1 Profile likelihood analysis

The background expectation and the sensitivity of the detector to WIMPs scattering as a function of their energy can be calculated by a profile likelihood function [149]. This likelihood function  $\mathcal{L}$  can be expressed as a product of five terms:

$$\mathcal{L} = \mathcal{L}_1(\sigma, N_b, \varepsilon_s, \varepsilon_b, \mathcal{L}_{\text{eff}}, v_{\text{esc}}; m_\chi) \quad (3.9)$$

$$\times \mathcal{L}_2(\varepsilon_s) \times \mathcal{L}_3(\varepsilon_b) \quad (3.10)$$

$$\times \mathcal{L}_4(\mathcal{L}_{\text{eff}}) \times \mathcal{L}_5(v_{\text{esc}}) \quad (3.11)$$

where  $m_\chi$  is the WIMP mass and  $\sigma$  is its cross section. The first term  $\mathcal{L}_1$  corresponds thus to the dark matter search performed by XENON100 under the assumption of the WIMP velocity escape  $v_{\text{esc}}$ . As a result, the number  $N_b$  describes then the expected number of background events, with the probabilities  $\varepsilon_s$  and  $\varepsilon_b$  for these signals to mimic a WIMP signal or to be identified as a clear background signal.

While this first term of the likelihood function depends only to the measurements made by XENON100, additional correction factors need to be applied, due to the uncertainties that rule each of them. This is the purpose of each of the four remaining terms. While  $\mathcal{L}_4$  and  $\mathcal{L}_5$  correspond to the uncertainties on the values of the  $\mathcal{L}_{\text{eff}}$  parameter and the velocity escape  $v_{\text{esc}}$  that have been determined by other experiments, the second and third terms  $\mathcal{L}_2$  and  $\mathcal{L}_3$  associated to the probabilities  $\varepsilon_s$  and  $\varepsilon_b$  respectively, have to be determined for XENON100. This can be done by investigating the proportion of background signal that fall into the NR signal region in the (S1,S2) plane, as illustrated by Figure 3.10 for previous calibration measurements:

On this figure, the blue circles illustrate ER, while the red circles illustrate NR. They have been drawn by using  $^{60}\text{Co}$  and  $^{241}\text{Am}^9\text{Be}$  calibration sources respectively. The averages of each distribution are represented by thick solid lines, while dashed vertical line illustrated the [4-20] PE S1 range. For the present example, this range is thinner than the signal range used during the second science run since the data used here were acquired before the beginning of the first science run, corresponding to the adaptation of such analysis to XENON100 for the first time.

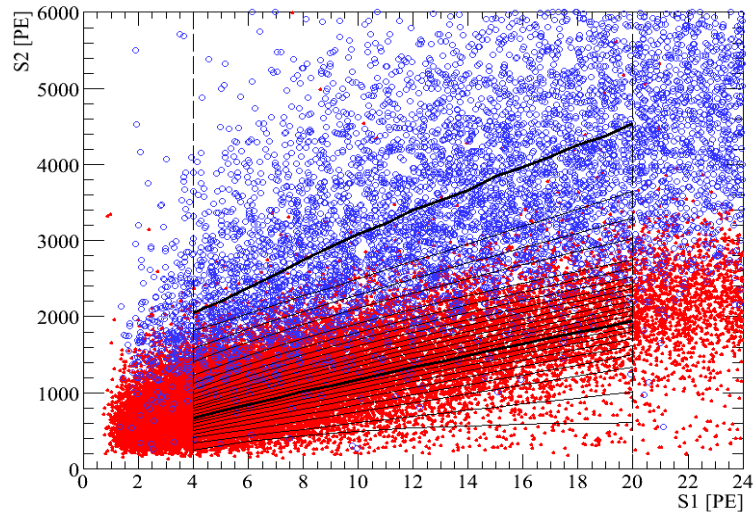


Figure 3.10: Illustration of the scattering signal in (S1,S2) plane for NR (red markers) and ER (blue markers). Figure from [149].

On each side of the average of the NR band, several bands with the same density of NR signal are drawn, represented by thin curves. Thus, the terms  $\mathcal{L}_2$  and  $\mathcal{L}_3$  are calculated by using these bands as reference in order to draw for each of them the proportion of NR signal and ER signals. Same analysis has been done for each science run, with the corresponding calibration data. Once the unblinding has been done, the released data are compared to these reference bands. These latter are scaled to the correct dark matter exposure.

During the second science run, as for the first one, no significant excess above the expected background has been found, corresponding to no signature of a WIMP scattering. For the present step of the analysis, the term  $\mathcal{L}_5$  is not yet used. It will be however used in order to draw the dark matter cross section with standard matter as a function of the WIMP mass. As an illustration, the data selection cuts from NR and ER bands, and from the intensity of each signal can be seen in the next section.

### 3.3.3.2 Analysis with benchmarked signal region

As a cross-check to the PL method, the analysis of the dark matter data is also performed by using the benchmark region. As presented before, this region corresponds to the [4-20] PE S1 signal range, with the ratio S2 over S1 signals below 99.75 % of the ER band, in the 97 % upper quantile of the NR band, and with a S2 signal above 150 PE. This region of ratio of signals as a function of the S1 signal is illustrated in green in Figure 3.11 for flattened results.

The S1 range is thus represented by vertical dashed and dot lines, while the rejection of 99.75 % of the ER band is represented by horizontal dotted line since this band is flattened. Then, the 97 % upper quantile of the NR band is defined by the region above the dashed curve, while the dashed and dot curve illustrates the 150 PE intensity threshold on the S2 signal. The region investigated by the PL analysis can be easily seen by extending the S1 region up to 30 PE and suppressing the ER band 99.75 % rejection line. The NR flattened band from  $^{241}\text{Am}^9\text{Be}$  calibration is also drawn as an illustration in grey-red scale. The average of the ER band corresponds to the

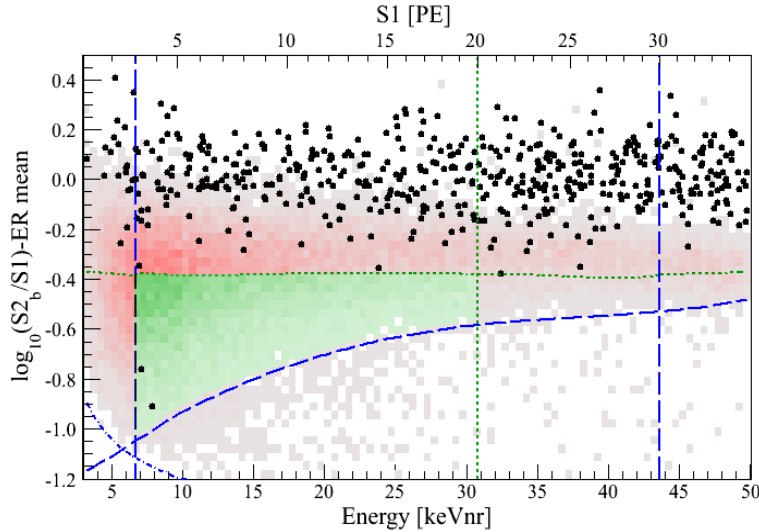


Figure 3.11: Illustration of the benchmark signal region for the second science run. Figure from [74].

ratio S2 over S1 signals in logarithmic scale equal to 0.0.

The expected amount of background signal in this region is established by considering from calibration the contribution of ER signals that could leak into this region during the 225 live days of the science run, due to the Gaussian distribution of the bands and anomalous events such as  $\gamma$ -X. This contribution is estimated at  $(0.79 \pm 0.16)$  events for the whole science run.

The contribution of NR to this benchmark region is inferred from Monte Carlo simulations, thanks to a very good agreement between simulations and background data in a clean centered region. These Monte Carlo simulations take into account the contribution of scatterings of neutrons from  $(\alpha, n)$  reactions production and of muon-induced neutrons, but also spontaneous fission reactions. The expected contribution from this background source is  $(0.17^{+0.12}_{-0.07})$  event for the whole science run. About 70 % of these neutrons background are muon-induced [74].

As a result, the total expected background for the 225 live days of dark matter exposure is  $(1.0 \pm 0.2)$  events. The unblinding of the data has revealed two scatterings that have mimicked WIMPs signatures, that can be clearly seen by the two black markers in the green region of Figure 3.11. This corresponds to statistical fluctuation of the expected background, with a Poisson fluctuation probability of 26.4 % to varie from one up to two events. As a consequence, no dark matter signature have been seen by XENON100 during this science run. The waveforms and PMTs light patterns of these two events are represented in Section 5.8.5.

The benchmark region analysis is only used as a cross check since it is less robust due to the discrete fluctuation of the signals with respect to the expected background.

### 3.4 Limits on WIMP interaction cross section

For the results on dark matter scattering cross-section with standard matter, two different analyses have to be taken into account. The first one consists in assuming that the scattering does not depend on the spin of the involved particle (scalar field) and is known as the *Spin-Independent*

analysis (*SI*). The second one consists in investigating a possible spin-dependency, typically represented as scattering of WIMPs with nucleons in the nucleus, and is known as the *Spin-Dependent* analysis (*SD*). The two analysis are presented below.

### 3.4.1 Spin-independent scattering

The upper limits on dark matter scattering cross-section with nuclei of standard matter can be inferred from the results of direct dark matter experiments. For the present section, the results refer to the XENON100 experiment, and use the profile likelihood analysis method described in the previous section.

The dark matter scattering cross-section with a nucleus  $\frac{A}{Z}X$  without impulsion transfer  $\sigma_0^{SI}$  can be expressed under the general form [72]:

$$\sigma_0^{SI} = \frac{4m_r^2}{\pi} (Zf_p + (A - Z)f_n)^2 \quad (3.12)$$

where  $m_r$  is the WIMP-nucleus reduced mass such as defined in section 1.5.3, and  $f_p$  and  $f_n$  are the diffusion amplitudes of protons and neutron respectively. In case of a dominant coupling process with the quarks from the sea,  $f_p \approx f_n$  [72], that leads to  $\sigma_0^{SI} = 4m_r^2 A^2 f_p^2 / \pi$ .

The cross-section  $\sigma^{SI}(q)$  associated to a transferred momentum  $q = \sqrt{2M_A E_R}$  for the nucleus mass  $M_A$  and the nucleus recoiling energy  $E_R$  is thus expressed as [71]:

$$\sigma^{SI}(q) = \sigma_0^{SI} F(q)^2 \quad (3.13)$$

where  $F(q)$  is the nuclear form-factor already mentioned in section 1.5.3. By applying these calculations to the XENON100 results, a new upper limits on the SI WIMP-nucleons cross section as a function of the WIMP mass can be drawn, such as represented in thick blue curve in Figure 3.12.

The green and yellow bands represents the expected sensitivity at one and two  $\sigma$  confidence level for the second science run before unblinding, due to fluctuations of the expected background. The main results from other experiments described in Section 1.6 are also represented. The SI results from the second science run of XENON100 have been calculated under the assumption of an isothermal WIMP halo with a local density of  $\rho_0 = 0.3 \text{ GeV/cm}^3$ , a local velocity of  $v_0 = 220 \text{ km/s}$  and a Galactic velocity escaped, corresponding to the truncation of the Maxwellian distribution of the dark matter velocity at  $v_{esc} = 544 \text{ km/s}$ . These results were released in late Spring 2012, and up to Autumn 2013, they were the most constraining results for WIMP properties in the whole energy range for WIMP masses range, except for the region below  $8 \text{ GeV}/c^2$  where the best limit was still belonging to the low mass analysis from XENON10 [104].

The sensitivity at low mass WIMP is strongly limited by the recoiling energy detection threshold, and thus by the knowledges on the  $\mathcal{L}_{eff}$  parameter at low recoiling energy. The same effect occurs also at higher WIMP mass, but in a much lesser extend. The increase of the upper limit in this region is more affected by the decrease of events at higher recoiling energy with respect to

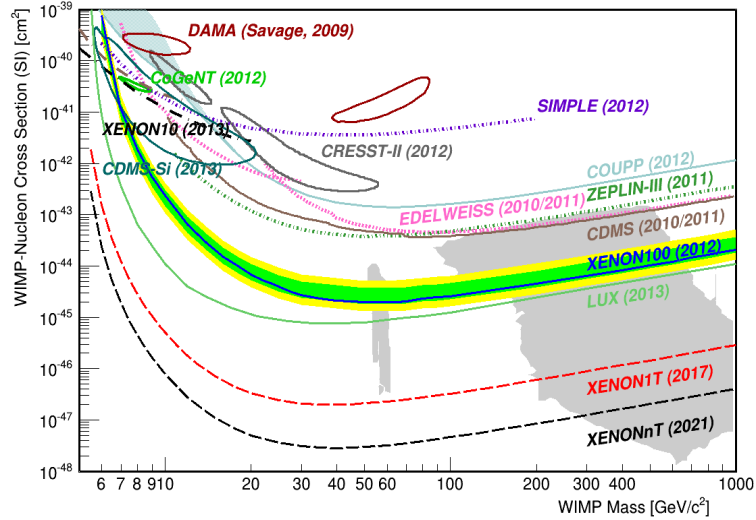


Figure 3.12: Upper limits of the SI WIMP-nucleus cross section as a function of the WIMP mass for the XENON100 second science run data. Figure from [74], adapted because of new results from other experiments.

events at lower recoiling energy.

The lowest value for the SI cross-section was obtained for  $m_\chi = 55 \text{ GeV}/c^2$  with  $\sigma^{SI} = 2.0 \times 10^{-45} \text{ cm}^2$ . This second XENON100 result on direct dark matter search has continued to challenge the interpretation of the DAMA [83], CoGeNT [84, 150], and CRESST-II [92] results as being due to scalar WIMP-nucleon interactions.

In September 2013, another dual-phase xenon TPC, *LUX*, has also provided its first results [105], which were slightly more sensitive than XENON100 thanks to a larger fiducial mass. These results are also represented on Figure 3.12. For illustration purpose, it is also the case for the expected sensitivity of the XENON1T detector, which is still in construction phase, and its future update XENONnT. The grey region represents the favoured WIMPs cross-section versus WIMP mass predicted by supersymmetric models [151]. Thanks to the next steps of the XENON program, a large favoured region for WIMP signal will be investigated.

At the time of submission of this thesis, a new dual-phase xenon TPC, *PandaX-I*, operating at the China Jinping Underground Laboratory, has presented its very first results [106]. It has consisted in 37 kg of liquid xenon as target volume for 17.4 live-days of exposure, where no dark matter signal was found. Due to the low LXe mass and time exposure involved, the resulting sensitivity to dark matter SI coupling is much lower than results from XENON100's second science run, or from LUX. It is however in good agreement with the very first results for dark matter search provided by XENON100, during the commissioning run in Autumn 2009, where LXe target mass and time exposure were similar to *PandaX-I*'s ones. The maximum sensitivity reached by this detector for the SI coupling is  $\sigma_{SI} = 3.7 \cdot 10^{-44} \text{ cm}^2$  for a WIMP mass of  $49 \text{ GeV}/c^2$  at 90 % confidence level. Due to the short delay between the publication of *PandaX-I*'s results and the dead line of the submission of this thesis, no more reference to these results will be done in this chapter.

Furthermore, the results presented here for each experiment have been made under standard

assumption on the dark halo such as it is reminded in Section 1.5.3. As a results, event if one astrophysical parameter is measured with a different value in the future, the outcome of the comparison between all the results will remain almost constant.

### 3.4.2 Spin-dependent scattering

As said in the previous chapter, one of the advantages of using xenon as detector medium is to allow both SI and SD analysis. In this latter case, WIMP is assumed to couple to the total angular momentum of a nucleus. For sensitivity reasons, only nuclei with an odd number of proton or neutron will be considered. As a result, only the  $^{129}\text{Xe}$  and  $^{131}\text{Xe}$  isotopes were used in case of xenon experiment, since these two isotopes have one unpaired neutron, and since they represent about the half of the natural xenon in term of abundance. Compared to the results presented in Table 2.2, the abundance of these two isotopes in the XENON100 detector is slightly different due to the use of a proportion of  $^{124,136}\text{Xe}$  depleted xenon at the beginning of the experiment, and to additional standard xenon between some detector refilling because of xenon loss (i.e. during its distillation through the dedicated column). As a consequence, the proportions of isotopes  $^{129}\text{Xe}$  and  $^{131}\text{Xe}$  during the second science run with respect to their natural abundance have changed from 26.4 % down to 26.2 % and from 21.2 % up to 21.8 % respectively [78].

The scattering cross-section  $\sigma_0^{SD}$  of a WIMP over a nucleon is thus calculated by using [72]:

$$\sigma_0^{SD} = \frac{32G_F^2 m_r^2}{\pi} \frac{J+1}{J} (a_p \langle S_p \rangle + a_n \langle S_n \rangle)^2 \quad (3.14)$$

where  $J$  is the whole spin of the nucleus and  $a_p$  and  $a_n$  the effective WIMP-proton and WIMP-neutron coupling constants respectively for SD interactions. They are equivalent to  $f_p$  and  $f_n$  in SI interactions, with different amplitudes since for the type of scattering considered here, only one of the two species will interact with the incoming WIMP, while for the SI analysis the nucleus is assumed to interact as a whole. The remaining two quantities,  $\langle S_p \rangle$  and  $\langle S_n \rangle$ , are the average spin that are expected to belong to a proton and a neutron respectively. As for SI analysis, the scattering cross-section  $\sigma^{SD}(q)$  for a transferred momentum  $q$  could be also calculated by using the nuclear form factor  $F^2(q)$ . However, since  $a_p$  and  $a_n$  are model dependent, and  $F^2(q)$  spin dependent, it is common to infer the scattering cross-section  $\sigma^{SD}(q)$  for a transferred momentum  $q$  by using the  $\sigma_0^{SD}$  and  $\sigma^{SD}(q)$  [152, 78], assuming that the WIMP-proton coupling is dominant ( $a_n = 0$ ) or vice versa:

$$\sigma_{p,n}^{SD}(q) = \frac{3}{4} \frac{\mu_{p,n}^2}{\mu_A^2} \frac{2J+1}{\pi} \frac{\sigma_{p,n}(q)}{S_{p,n}^A(q)} \quad (3.15)$$

where  $\mu_{p,n}$  is the reduced WIMP-proton or WIMP-neutron mass, and  $\sigma_{p,n}$  is the WIMP-nucleus cross section, assuming pure proton or pure neutron coupling respectively. The remaining term is the nuclear structure function that will hold all the uncertainties. It can be calculated assuming nuclear shell model. For the SD results of the second science run of XENON100, the

very recent nuclear model [153] based on a state-of-art of the valence shell interactions has been chosen. As for the SI analysis, the PL method was applied, using the same datasets and events selection. The resulting XENON100 limits has yields to the most stringent limit for a WIMP mass above 6  $\text{GeV}/c^2$  for neutron coupling, with the lowest limit at  $\sigma_\chi = 3.5 \cdot 10^{-40} \text{ cm}^2$  for a WIMP mass at  $m_\chi = 45 \text{ GeV}/c^2$ , see Figure 3.13(a), and to weaker values for proton coupling because of an even number of proton for the xenon atom as shown on Figure 3.13(b).

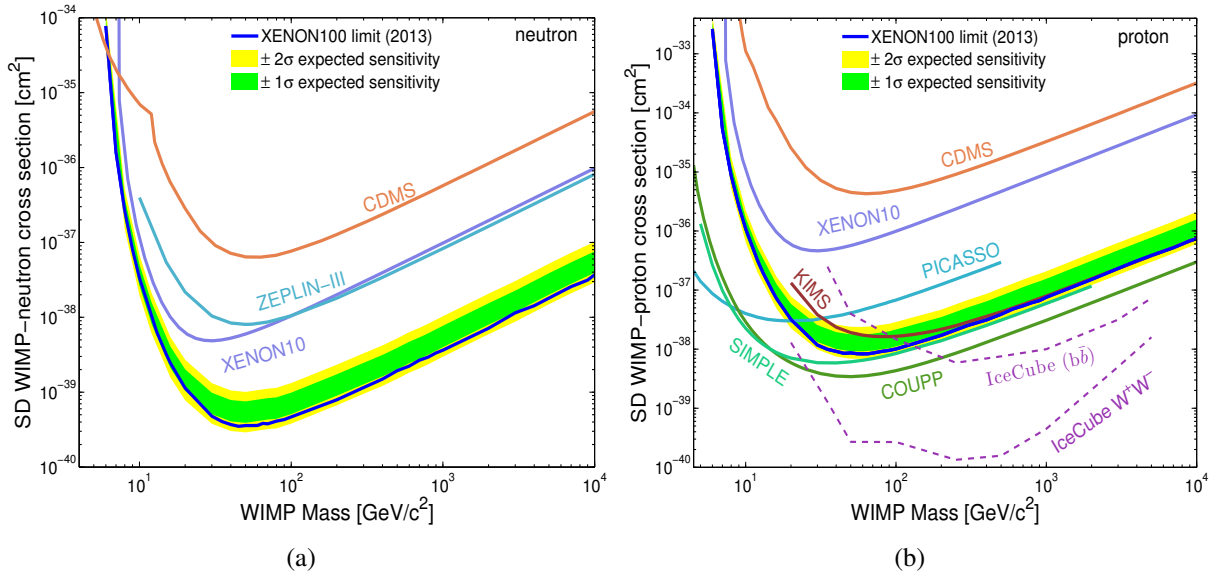


Figure 3.13: Upper limits of the SD WIMP-nucleons cross section as a function of the WIMP mass for the XENON100 second science run data: (a) WIMP-neutron and (b) WIMP-proton. Figure from [78]

As for SI analysis, recent results from other experiments are also shown for comparison. Since no results from the LUX collaboration on a SD analysis of their first data have been published yet, the result from the XENON WIMP-neutron coupling are still the most stringent up to the time of writing.

### 3.5 Search for axions

As a complement to the WIMPs search performed by the XENON100, additional results on the sensitivity to axions particles using the same detector have been also released [53]. As mentioned in Section 1.4.2.2, the axions are cold dark matter candidates that could explain the strong CP problem. Different scale have been thus suggested for their mass, which vary from few  $\mu\text{eV}$  up to few keV. The existence of some other particles with the same properties than the axions but with a higher mass is also investigated. Such particle are named *Axion-Like Particles (ALP)* due to their similarity with the axions. These axions are assumed to be created in the sun, while the ALP are assumed to have been produced in the early Universe. For this purpose, axions are also named as *solar axions* in [53] while the ALP are also named there as *galactic ALP*. These terms are also used here.

As it was also mentioned in Section 1.4.2.2, one possibility for a direct detection of axions and ALP would be to investigate an excess of electronic recoil at the full energy of the scattering axion or ALP mass. This process is explained by the assumed coupling of a such particle with an electron of the encountered atom, in analogy to the photo-electric effect of a photon over such electron and that is illustrated in Figure 2.4(a). For this similarity reason, this process is known as *axio-electric* effect.

The observable that will correspond to the outcome of this analysis is the coupling constant  $g_{Ae}$  between an axion or an ALP and an electron. There is also possibility to infer the scattering cross-section  $\sigma_{Ae}$  from this parameter [53]:

$$\sigma_{Ae} = \sigma_{pe}(EA) \frac{g_{Ae}^2}{\beta_A} \frac{3E_A^2}{16\pi\alpha_{em}m_e^2} \left(1 - \frac{\beta_A^{2/3}}{3}\right) \quad (3.16)$$

where  $\sigma_{pe}(EA)$  is the photoelectric cross-section at the energy  $E_A$  of the axion or the ALP. As for the photoelectric effect, this energy is fully deposited.  $\beta_A$  is then the axion or ALP velocity over the speed of light  $c$ ,  $\alpha_{em}$  is the fine structure constant and  $m_e$  is the electron mass.

As for the WIMPs search results presented in the previous sections, all the data from the second science run were used. The same data selection cuts were also applied. However, since the scattering process analysed here is similar to the photoelectric effect and thus involves the recoil of an electron, only the ER band would be considered for the present analysis. This band is also drawn here by using only the bottom PMTs array for the same reasons as previously, and is calculated and flattened from ER calibrations with the  $^{60}\text{Co}$  and the  $^{232}\text{Th}$  radioactive sources. Only the data within the  $2\sigma$  region around the average of this band are selected, as illustrated by horizontal red lines in Figure 3.14.

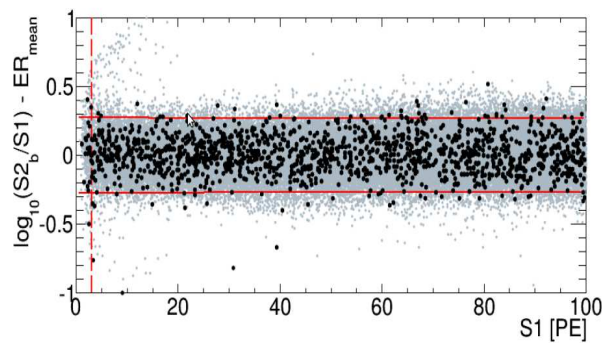


Figure 3.14: Dark matter data selection for axions and ALP search in the ER band in logarithmic scale. As for the WIMPs search, the S1 signal threshold is set at 3 PE, as illustrated by the vertical dashed line. Figure from [53].

Like previously, the analysis is performed by using a PL method. For each bin of S1 signal, i.e  $S1 = 1, 2, 3, \dots$ , the number of events in dark matter search data with respect to the ER calibrations data previously scaled to the total dark matter search exposure is analysed. Due to the axio-electric effect property, an excess of this quantity is assumed in case of axion or ALP scatterings,

depending on their mass. Because of these masses, the two types of axions are thus separately analysed. For the former case, the analysis concerns an axion mass  $m_A$  below 1 keV while for the latter case, the analysis concerns ALP masses above 1 keV. The corresponding results are presented in Figure 3.15 and 3.16 respectively. The threshold at 3 PE for S1 signals is represented on the two figures by the red dashed line.

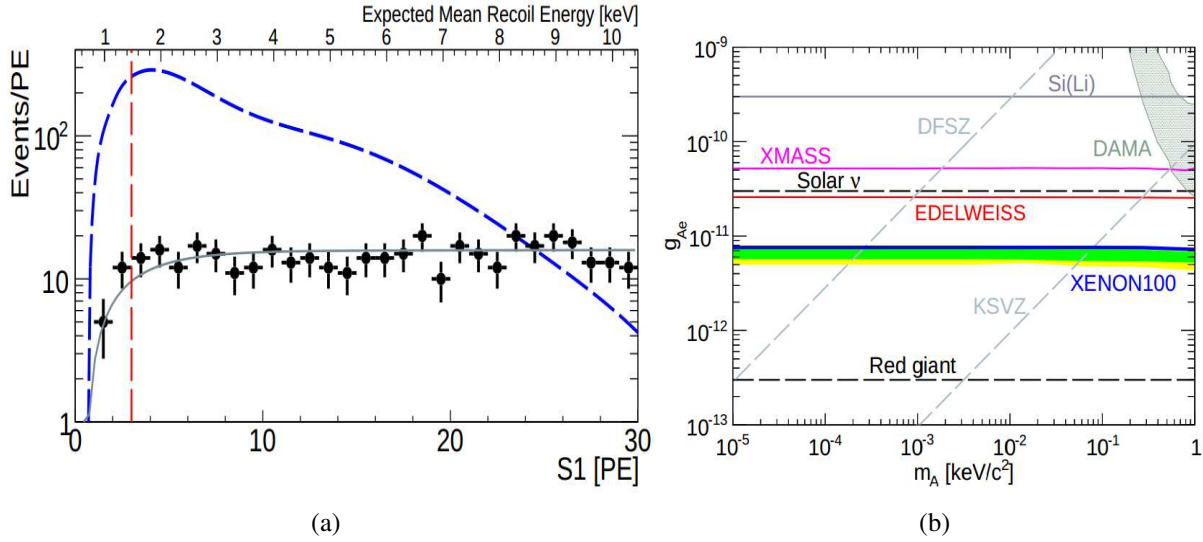


Figure 3.15: (a) Comparison of the number of observed events in ER band per unit of photoelectron for the associated S1 signal (black marker) with respect to the average quantity expected from calibration (grey curve) as a function of the S1 signal. The red dashed line illustrates the threshold at 3 PE for S1 signals. (b) XENON100 limits on solar axions during the second science run. Figure from [53]

In Figure 3.15(a), as in Figure 3.16(a), the number of observed events are also expressed as a function of the expected mean recoil energy on top x-axis. Moreover, it is also added for illustration in Figure 3.15(a), with the blue dashed curve, the expected signal for a solar axion with a mass  $m_A < 1$  keV, assuming the coupling constant  $g_{Ae} = 2 \times 10^{-11}$  which was the best limit in the world reached by EDELWEISS-II [154] before the present results. Data are compatible with the expected background and no excess has been observed.

The XENON100 coupling constant as a function of the axion mass is thus drawn by blue curve in Figure 3.15(b), with the expected background at  $1\sigma$  and  $2\sigma$  represented by green and yellow bands respectively. For comparison, the result from the other experiments are also shown, including the annual modulation signal claimed by DAMA, assuming that the modulation of electronic recoil would be due to axions scatterings. In addition, astrophysical bounds and benchmarks from axion models are also represented by horizontal and inclined dashed lines. The resulting new lowest limit on the coupling constant provided by XENON100 is thus  $g_{Ae} = 7.7 \times 10^{-12}$  at 90 % CL.

On the contrary to axion particles, the signals induced by the ALP scatterings are assumed to be more monoenergetic and would depend only on their mass, since their kinetic energies would be negligible due to their cold properties. For this purpose, several expected signal are also represented in Figure 3.16(a), for different ALP masses, under the assumption of a coupling

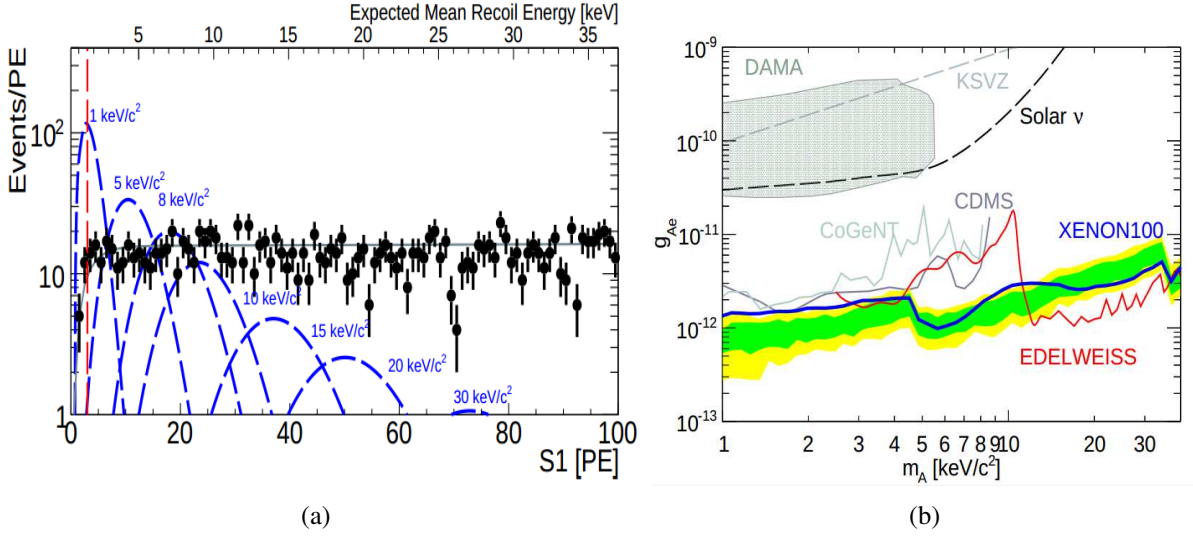


Figure 3.16: (a) Comparison of the number of observed events in ER band per unit of photoelectron for the associated S1 signal (black marker) with respect to the average quantity expected from calibration (grey curve) as a function of the S1 signal. The red dashed line illustrates the threshold at 3 PE for S1 signals. (b) XENON100 limits on galactic ALP during the second science run. Figure from [53]

constant equal to  $g_{Ae} = 4 \times 10^{-12}$ . This value also comes from the results of the EDELWEISS experiment for ALP search [154], and is used for illustration purpose. Moreover, the analysis on S1 signal is also extended to higher value, due to the much higher mass of the ALP with respect to the axion particles. As for the solar axions, the data are compatible with the expected background and no excess has been observed.

The corresponding XENON100 limits for coupling constant of ALP with electrons as a function of their mass is represented by blue thick curve on Figure 3.16(b), with the background at 1 $\sigma$  and 2 $\sigma$  represented by green and yellow bands respectively. Like previously, results from other experiments and astrophysical bounds and benchmarks from ALP models are also represented. The best limit up to date in the [5 – 10] keV ALP mass range is thus provided by the XENON100 experiment.

The two steps on the blue thick curve around  $m_A = 5$  keV and  $m_A = 35$  keV are due to atomic energy level influence on photoelectric cross-section. Moreover, the value of the coupling constant below an ALP mass of 5 keV is higher than the expected background. This is due to a slight excess of events between 3 PE and 5 PE in the S1 energy range. A similar excess at higher S1 signal also explains the fluctuations of the blue curve above this region with respect to the expected signal. In a more general point of view, the sensitivity to ALP is more influenced by the fluctuations of the number of events per unit of deposited energy with respect to the background signals than axion particles, due to the expected monoenergetic signal.

All the results presented in Figure 3.16 have been drawn under the assumption that ALP corresponds to all the galactic dark matter. They also correspond to the latest dark matter results provided by the XENON100 experiment at the time of writing.

### 3.6 Towards next detector generation

The aimed sensitivity of dark matter search has been already reached by XENON100 in 2012. The detector is still running, to collect even more statistics, aiming at an annual modulation study, and to perform R&D for the next generation detector of the XENON program. This new experiment is named XENON1T and consists in a 1m drift liquid xenon dual phase TPC, with more than 2.2 tonnes of LXe in the inner cryostat, corresponding to about 3.5 tonnes by including veto volume. The original purpose of this experiment is to use 1 tonne of LXe as fiducial volume, making XENON1T the first experiment reaching the tonne scale as target search volume. The aim is to increase the dark matter sensitivity by a factor 100 with respect to XENON100, reaching a sensitivity of  $2 \cdot 10^{-47} \text{ cm}^2$  after 2 years of cumulated data, as illustrated in Section 3.4.1. This sensitivity could be reached thanks to not only a careful material selection and detector design, but also thanks to an improved xenon purification, from krypton and radon by new dedicated distillation columns, and from other impurities by a continuous standard xenon purification during storage stage. This latter purification would be done thanks to a storage in liquid phase in a dedicated device, the Xenon Recovery and Storage system (ReStoX), initially proposed and developed by the SUBATECH xenon group [155].

Another major improvement of the detector consists in the external shielding that is replaced by a PMT instrumented water tank, 10 m in height and diameter, acting as a muon veto and illustrated in Figures 3.17(a) and 3.17(b). The tonne-scale size of the detector implies being hosted in one of the three major rooms of the LNGS underground laboratory, the hall B, whose ceil will restrict the size of the whole experiment. A dedicated infrastructure building has been also developed in parallel, in order to host all the electronic equipments, cryogenic systems, and working room, as illustrated in Figure 3.17(b).

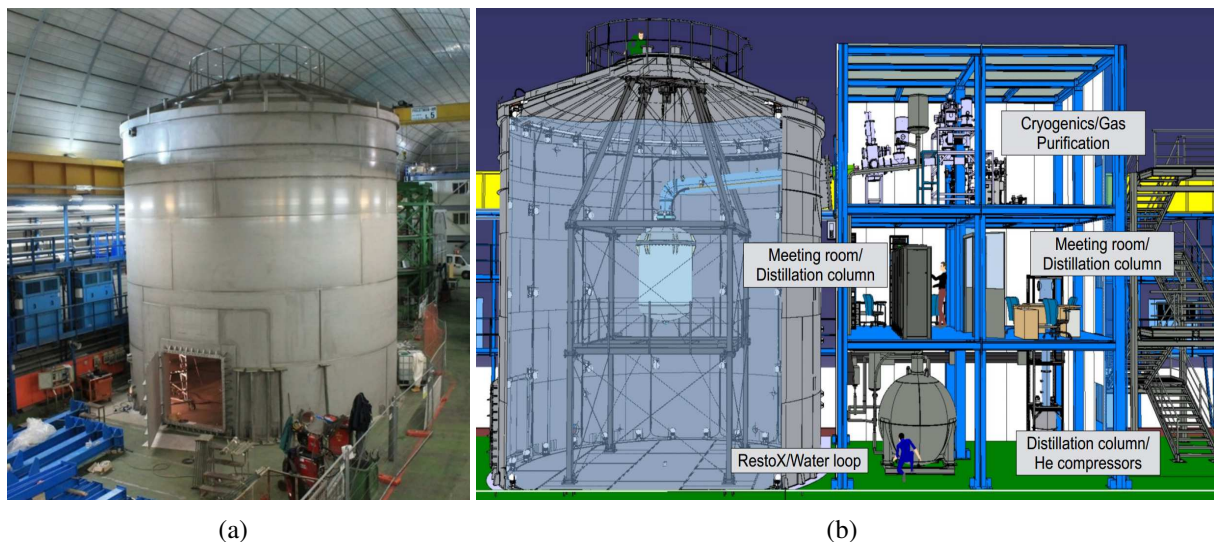


Figure 3.17: (a) Picture of the XENON1T water tank muon veto, with the door allowing the entrance for installation and maintenance, (b) illustration of the infrastructure building of the XENON1T experiment.

Moreover, the XENON1T does not correspond to the end of the XENON program. Indeed,

the whole equipment has been designed to allow a fast update of the detector, namely about two years after the beginning of XENON1T, and called XENONnT, by increasing the total mass of LXe by about a factor two. In these conditions, it would be only the inner cryostat that will be enlarged by adding new rings of PMTs. The aim of this update is to increase the sensitivity of the detector by a factor 10 with respect to XENON1T.

In parallel to these developments, the xenon and argon scientist communities are working together for designing two multi-ton brother-detectors, the DARWIN project [156]. They will use xenon and argon dual phase TPCs respectively, with similar design to the XENON1T and Dark-Side [95] ones. The aim of this project is to increase the dark matter sensitivity and the events statistics in case of a discovery by a previous experiment by employing two independent detectors. The advantage of using two targets consists in the redundancy of dark matter discovery. Furthermore, in case of discovery, since xenon and argon provide different dependency on sensitivity as a function of a WIMP mass, combining the two results would constrain that WIMP mass. Such project will aim to start a construction around 2020.

## Conclusion

In the present chapter were explained all the main results of the dark matter search performed with the XENON100 experiment. As a result, all the aspects of this analysis have been approached. The corrections of each of the two raw signals S1 and S2 have been thus reviewed, completed by the explanation of the method of the reconstruction of the recoiling energy, depending on the type of recoil. An improvement of this reconstruction method for nuclear recoils would be also an advantage for the next generation detector XENONT1T, since the current one used for XENON100 is also the weakest among the three available.

While the analysis of the data of the XENON100 experiment are very robust, and have led to the best sensitive results for a while, as it has been presented in the last sections of this chapter, for both the WIMPs and the very recent axion searches, the detector sensitivity limits are almost reached. Very long time of data taking would be thus needed to challenge new detectors, such as LUX which is currently acquiring new data. That is why it is now the time to move toward the next generation, XENON1T, by keeping all the knowledges on dark matter search acquired by the XENON100 detector.

This third chapter concludes the discussion on dark matter search. In the two next chapters will be presented a dedicated analysis of the very low energy part of the S2 signals spectrum. It will consists in the full understanding of this region and in the characterisation of the S2 signal emitted down to even a single electron extracted in the gaseous phase. This will be completed by a review of applications of such signals to other topics of the analysis, including an application to a specific low-mass WIMP search.

# Chapter 4

## Single electrons charge signals

The observation of single electron charge signals by the XENON100 experiment is presented. A description of the features of these signals is firstly done, followed by the demonstration of their emission process. An explanation of the method used for the evaluation of the average charge signal emitted by a single electron in the gas phase is then given, including details on its first improvements. The search of data quality selection cuts in order to reduce the bias on this evaluation is also presented. The full understanding of these low energy charge signals is finally demonstrated by a large discussion on the systematical errors.

### Contents

---

|  |            |
|--|------------|
| <b>Introduction</b> . . . . .  | <b>117</b> |
| <b>4.1 Single electrons charge signal description</b> . . . . .          | <b>118</b> |
| <b>4.2 Properties of single electrons signals</b> . . . . .              | <b>125</b> |
| <b>4.3 Low energy S2 spectrum analysis</b> . . . . .                     | <b>130</b> |
| <b>4.4 Study of secondary scintillation gain</b> . . . . .               | <b>137</b> |
| <b>4.5 Systematic effects in the determination of the gain</b> . . . . . | <b>146</b> |
| <b>Conclusion</b> . . . . .  | <b>161</b> |

---

### Introduction

The previous chapters have widely demonstrate the challenged for dark matter experiments to reduce all source of background. In this context, the full understanding of the response of the detector is mandatory. For this purpose, the present chapter gives details on the observation of single electron charge signals by the XENON100 experiment.

After a description of the main features of these signals and the description of their observation by previous noble gas experiments, the scenario of their emission process based on experimental observations will be presented. The evaluation process of the average light emitted by a single electron in the gas phase will be then detailed, including a discussion on the limits of the preliminary evaluation method and their improvements.

This discussion will be then followed by a presentation of the strategy developed in order to reduce the bias from the main charge signal on the evaluation of this average light, leading to the establishment of specific data quality selection cuts. The identification and the evaluation of the contribution of each bias factor to the total systematical error per each science run will then conclude this analysis, leading to the full understanding of the XENON100 response to low energy charge signals. Thanks to this demonstration, the variation of this response as a function of the detector settings can be investigated, as it will be presented in the next chapter.

The present and next chapters correspond to the main part of the analysis work done during the three years. The main results have been published [157], and presented in [158].

## 4.1 Single electrons charge signal description

As detailed in Section 2.4.6, the recorded waveform for one triggered event does not only correspond to one S1 and one S2, but can also correspond to few of them, identified by size order. These typical signatures can be induced either by multiple scattering, in cases where only one S1 is identified, but also by simultaneous interactions, that lead to two S1 and S2 signals in the same waveform, like for the BiPo events presented in Section 3.2.1.

However, these processes could not explain all the populations observed in the waveform, especially all the abundant and very low energy S2 signals. Indeed, if the rare additional very low energy S1 signals can be explained by PMTs' base current fluctuations, such an explanation can however not be used for low energy S2 signals, because of their clear signature.

Since it is crucial for a low-background experiment such as XENON100 to be able to identify and reject all possible sources of background, other causes need to be investigated in order to explain these signals. For this purpose, the single electron emission mechanism has been proposed. The main process that leads to this emission is the photoelectric effect of ultraviolet photons on impurities in the liquid xenon, such as organic molecules or components of the detector (grids, field shaping ring, ...). The establishment of this emission process will be discussed in Section 4.2, while the main features of such signals will be detailed in the present section. A detailed study based on experimental data is then presented in the other sections.

### 4.1.1 Single electron and signal electrons emission processes

In order to follow the description of single electron emission, the reader can refer to Figure 4.1. This is a complement of Figure 2.1 that illustrated previously the S1 and S2 signals emission for a single scattering inside the active volume. As already discussed before, the two S1 and S2 signals correspond to ultraviolet photons emissions with a wavelength of  $\lambda = 178$  nm. Their energy is thus equal to about 7 eV.

The photons emitted are very numerous, especially from the S2 signal as presented in Table 3.2, and they are emitted isotropically. Photons from the S1 signal are always emitted from the liquid phase – apart rare events in which the main interaction is in the gas phase – while the one from the S2 signals are always generated in the gas phase because of its productions mechanism. About half of the photons emitted during S2 will penetrate the liquid phase.

If they have almost no probability to scatter with xenon atoms, they can however scatter by photoelectric effect with impurities, as it is discussed in Section 4.2. The single electron emission by Compton scattering is almost excluded due to the very low energy of the emitted ultraviolet photons. Among all the impurities present in the LXe, the most favourite one for being responsible of the single electron emission are the negative ions  $O_2^-$ . They are created during the capture of electrons from a prior drifting electronic cloud by  $O_2$  molecules. Indeed, the average energy needed for the extraction of this additional electron is 0.45 eV [159], while the average energies for first ionisation of the  $O_2$  and  $N_2$  molecules are bigger than 13 eV.

The released electron after the ultraviolet photons scattering will then drift toward the gas phase like the main electronic cloud did right before. If not captured by impurities, it leads to a new S2 signal emission in gas phase, the *single electron signal*. The typical time duration of a single electron signal is of the order of  $1\mu s$  while usual S2 signals are of the order of 2 - 3  $\mu s$  due to the electronic cloud elongation along the vertical axis by diffusion, and that depends from the corresponding interaction depth.

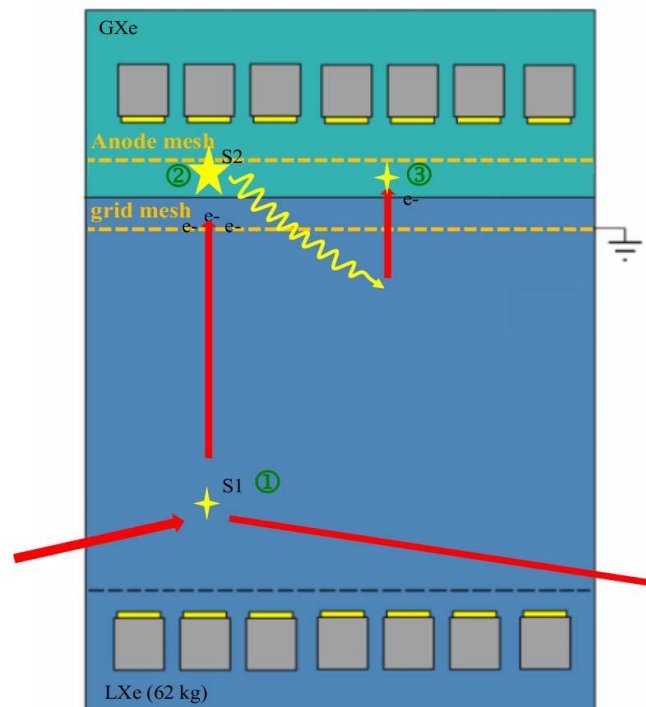


Figure 4.1: Single electron signal emission principle.

Such signals are very small, typically of the order of 20 PE. They correspond to the average light emitted during the drift of one electron in the gas phase. This average light will be defined as the *secondary scintillation gain* in the rest of this thesis. The characterisation of such signals as a function of the detector settings will be done in the next chapter. As calculated in Section 3.1.3, the number of emitted photons during such signals is about 390 photons per each electron accelerated in the gas phase. Due to this very low number of emitted photons, the production of second or third order of single electron signals, i.e. implied by previous single electron signals, will be almost absent. It will be then neglected in all the rest of this work.

Furthermore, single electrons signals can be also few times higher than the typical order of 20

PE. They correspond then to the average light emitted by few electrons accelerated simultaneously in the gas phase, as it is discussed in Section 4.2. **In the rest of this documents, the *single electrons* term will be used for one up to few electrons signals, corresponding to signals below  $\sim 150$  PE, while the term *single electron* will refer only to pure one electron signals.**

### 4.1.2 Previous studies

Before the specific analysis of single electrons signals done by the XENON100 experiment, they were observed by some others xenon dual phase TPCs, like in ZEPLIN-II [160] and in ZEPLIN-III [161]. In both case, a similar analysis to the XENON100 one was done on low energies S2 signals, by however considering only single electron population in such spectra. Few non-demonstrated hypothesis on the origins of single electrons were suggested at that time by the ZEPLIN Collaboration, namely the emission by photoelectric effect by ultraviolet photons or the spontaneous emission of single electron before S1 signals. While the latter was excluded by the observation discussed at the end of Section 4.1.3, the former was confirmed by strong evidences observed by XENON100 [157] and detailed in Section 4.2.

Furthermore, xenon is not the only noble gas that has led to the observation of single electron signals in dual-phase TPC up to date. Prior to ZEPLIN-II, the operation of an argon dual phase TPC in single electron counting mode was reported in [162]. As illustrated by Figure 4.2, that detector is slightly different to the XENON100 TPC. Indeed, the drift fields in liquid phase are in opposition between the two experiments. The purpose of this experimental set up for single electron counting mode is to exclude the possibility of electrons released in liquid phase to be extracted in gas phase. Moreover, the scattering in liquid phase is induced by a pulsed X-ray emitter source instead of a  $\gamma$  rays or a neutrons radioactive source usually used for dark matter experiments calibration. Furthermore, no PMTs are used for signals detections, they are replaced by Gas Electron Multipliers (*GEM*) for charge detection.

As for xenon dual-phase TPC, during the scintillation signal in liquid phase, ultraviolet photons will be emitted. Some of them will scatter with the first electrode of the first GEM. This latter acts as a photocathode, and by photoelectric effect, an electron will be released, accelerated and multiplied through three successive GEM. By taking into account both the quantum efficiency of the first electrode as a photocathode in gaseous argon and the scintillation yield in liquid argon, the drift field is set in order to release only one electron per each scattering X-ray in liquid phase.

If this experiment has not demonstrated the single electron extraction from liquid to gas phase, it has however confirmed the expected extension of such low energies S2 signals to all the noble gas dual phase TPC used in low background experiments.

### 4.1.3 Time features

Figure 4.1 is also expressed schematically in terms of a signal waveform on Figure 4.3. The numbers 1, 2 and 3 reported on the two figures correspond to the emission of the S1, S2 and single electron S2 signals respectively. S2 is the main charge signal, induced by the electronic cloud, and the S2' are the single electron signals. The baseline of this waveform is shown in black, and goes

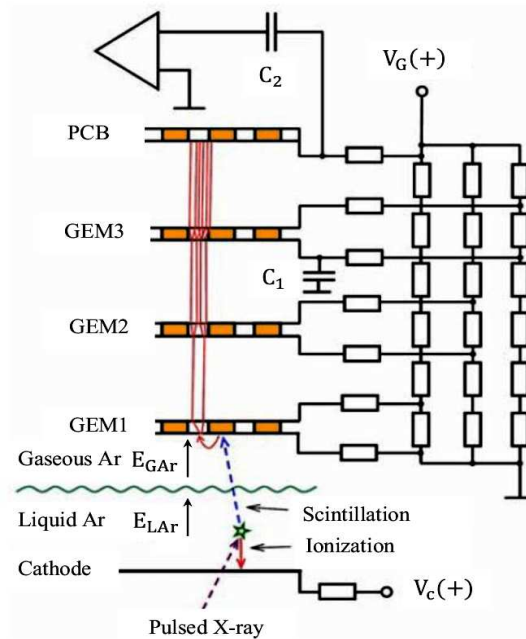


Figure 4.2: Schematic view of a dual phase argon TPC with GEM, operated in single electron counting mode. Figure from [162].

from 0 up to  $400 \mu\text{s}$ , centered around the main S2 signal, as in the standard experimental case. As for the time delay between S1 and S2 signals, the time delay between S2 and the single electron S2 signal labelled 3 on the waveform corresponds to the electronic drift in LXe. It depends from the ultraviolet scattering depth. In this figure, the drift of single electrons are represented by orange arrows while the drift of the main electronic cloud of the considered waveform is represented by the violet one.

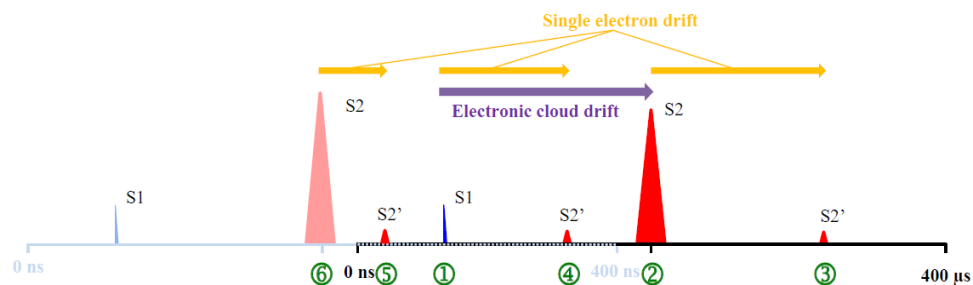


Figure 4.3: Schematic waveform for single electrons emission. See the text for explanation.

As it will be seen in the next section, it may happen that two or more electrons are emitted by coincidence approximation at the same depth, arriving then in the gas phase at the same time. Even if they are located at different positions, involving different PMTs, they would be identified as the same event since the signal is summed over all PMTs of the TPC.

In the general case, the single electrons signal occurs after the main S2, due to their S2's ultraviolet origin. They can however be also observed on the same waveform of this S2 signal, between few microseconds up to few tens of microseconds before this signal. The two cases of single electron signals are thus identified by red marker before and after the main S2 signal on

Figure 4.4, that corresponds to a typical waveform of an event with identified single electrons signals. The single electron signal labelled 4 in Figure 4.3 illustrates also this case. Such signals are mainly involved by photons from the S1 signal. However, due to the very low number of emitted photons during S1 signals, it has a much lower occurrence frequency than single electrons signals detected after S2.

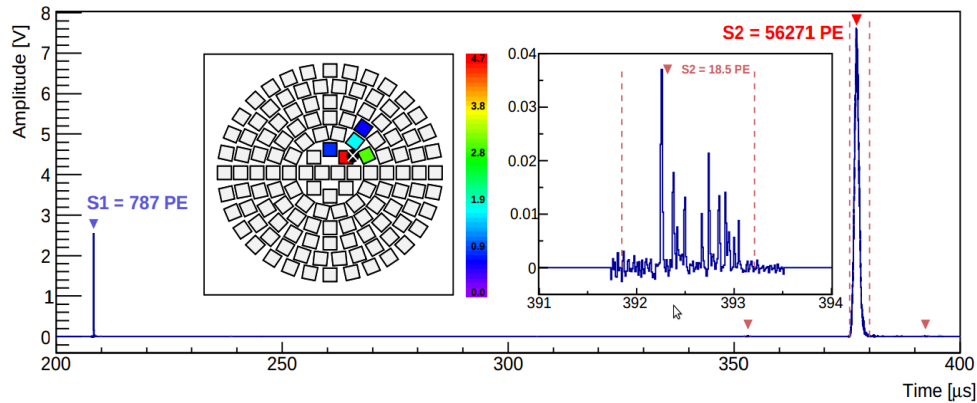


Figure 4.4: Example of a waveform recorded by XENON100. The two S1 and S2 signals correspond to the two main signals from left to right respectively. On both sides of the main S2 signal, two single electrons S2 signals occurs,  $145 \mu\text{s}$  after the S1 and  $17 \mu\text{s}$  after the main S2 respectively. They are both indicated by a red marker. The zoomed part of the waveform and the light pattern on the top PMTs array correspond to the second one. On this latter, the intensity of light in PE received by each PMT is represented by a colors gradient, with hot colors for higher quantities of light. The X marker on the PMT display indicates the reconstructed x-y position of the interaction. For this waveform, the acquisition has been triggered by the S1 signal. Picture from [157].

It has also been observed single electron signal occurring before the S1 signal of the same waveform, such as represented by marker labelled 5 on the waveform of Figure 4.3. The analysis studying the rate of such low energies S2 signals before the S1 signal per waveform has shown a correlation between this number and the differential time between the considered waveform and the previous one. This correlation is presented in Figure 4.5. The colors gradient used for markers is used only to illustrate the increase of the differential time between the considered waveform and the previous triggered one.

The highest rate of low energies S2 signals before S1 per triggered waveform is explained by a minimum acquisition dead time of about  $1000 \mu\text{s}$  between two triggered events. Indeed, due to the electronic dead time, all the scatterings that occur during this time period will never be entirely registered, but could be partially registered in the rare case of a time overlapping with the first next triggered waveform.

The single electrons signals observed before the S1 signal could then correspond to single electrons released by photoelectric effect of ultraviolet photons emitted during a S2 signal prior to the waveform, as illustrated by lighter colors on Figure 4.3. These lighter colors illustrates thus signals that could effectively occur, but that are not registered because of the electronic dead-time. The prior S2 signal corresponds in this case to the S2 signal identified by the marker 6.

However, if such overlapping can exist, it will contribute to single electrons signals observed

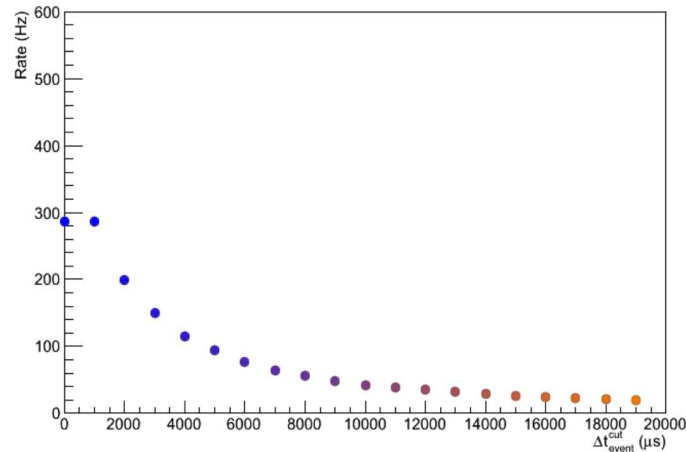


Figure 4.5: Rate of low energy S2 signal prior to S1 signals per each waveform as a function of the differential time between two triggered events.

before S1 only for a differential time between the two successive main S2 signals lower than the maximum drift time of  $176 \mu\text{s}$  from the bottom of the TPC up to the gas phase. As soon as this differential time starts to be higher than this value, this overlapping can not occur anymore. Another process should thus explain all the single electron signals observed before S1 for larger time delay between two successive events.

The almost exponential decrease of the single electron for higher differential time suggests then a delayed electron extraction from liquid to gas phase [157], as also mentioned previously in [161].

In all the analysis presented in the present and next chapter, only single electrons signals occurring after the main S2 signal will be considered, except for the analysis presented in Section 5.3 where single electrons signals occurring between S1 and S2 signals will be considered.

#### 4.1.4 Low energy S2 signals

As already discussed few times earlier in this thesis, many S2 signals with different intensities can be registered per each waveform. Figure 4.6 shows the spectrum of the S2 signals summed over all PMTs, and obtained by combining all the  $^{60}\text{Co}$  calibration data taken during the second science run. The y-axis is in logarithmic scale, and the data used correspond to the raw identified S2 signals, i.e. no quality cuts were applied. The sharp end of the spectrum around  $7 \cdot 10^5$  PE corresponds to the highest S2 signals obtained by photoelectric effect of the most energetic  $\gamma$  ray emitted by the radioactive source, while data above could correspond to background events from higher energetic radioactive sources from component of the detector, or from rare muons scattering events.

In order to study single electrons signals, the very low energy region of S2 signals will be investigated. This region consists in all the S2 signals below about 150 PE, corresponding to less than 7 - 8 electrons accelerated simultaneously in the gas phase. An example of a such spectrum is presented in Figure 4.7, and corresponds to a zoom into the low energy region of the full spectrum for one dataset acquired with  $^{60}\text{Co}$  calibration source during the second science run, i.e.  $5 \cdot 10^5$

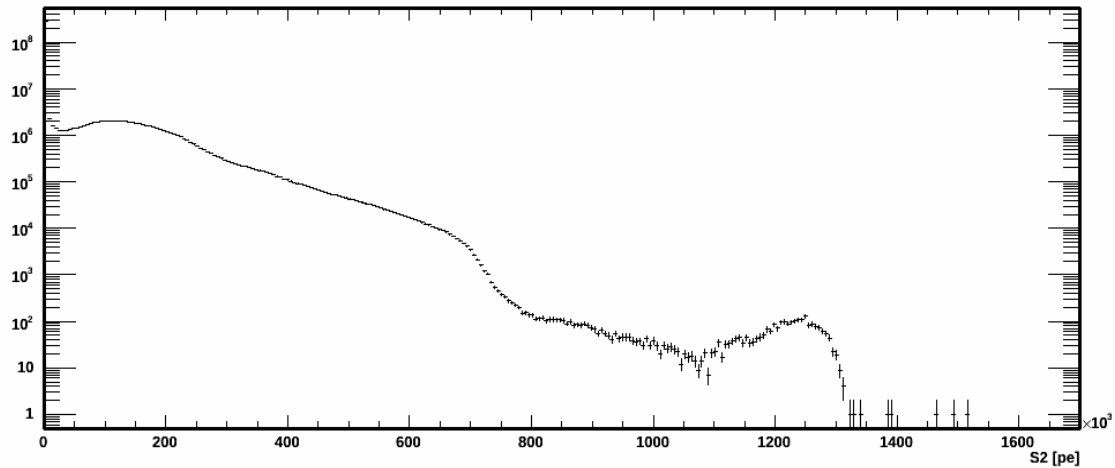


Figure 4.6: S2 signals spectrum obtained with  $^{60}\text{Co}$  calibration source during the second science run.

triggered events, with low energies S2 signals summed over all PMTs of the TPC. No quality cuts have been applied. A very low energy peak around 20 PE appears then. This spectrum illustrates the abundance of single electrons signals per each calibration dataset, allowing a robust analysis when combining all data acquired per science run. All the low energy S2 signals shown in Figure 4.7 are gathered in the first bin of Figure 4.5, explaining the excess of the spectrum in this region.

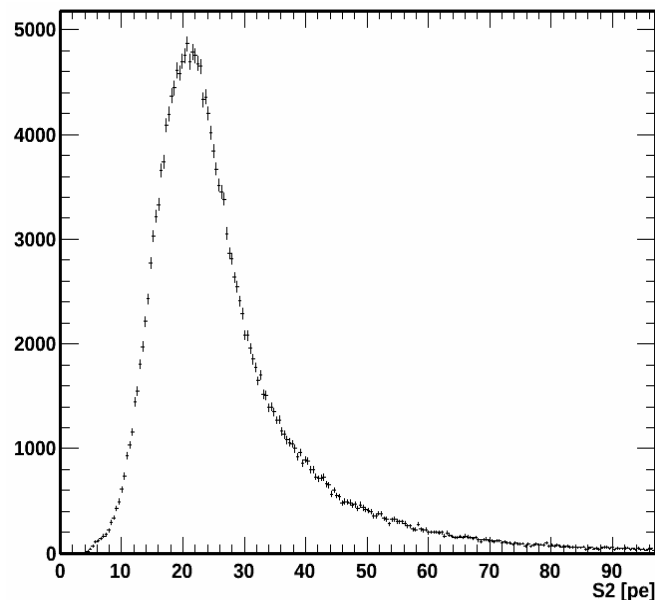


Figure 4.7: Low energy S2 signals spectrum obtained with  $^{60}\text{Co}$  calibration source during the second science run.

All the quantification of the secondary scintillation gain as a function of several specific detector settings and presented in the rest of this thesis will be always done from similar low energy spectra. The details of such analysis are given starting from Section 4.3. The major challenge of this study consists in identifying on this spectrum the contribution of each single electrons popu-

lation, i.e. the contribution of single electron, two electrons and more electrons signals for each range of S2 low energy signals.

As it will be presented all along this present chapter and the next one, several features of single electrons signals will be investigated, such as the coincidence property for multiple electrons signals, or the emission by photoelectric effect from ultraviolet photons. The evaluation of the emitted quantity of light per single electron drifting in the gas phase as a function of the electric field in gas corresponds to the major outcome of this study since it can be used by all the dual phase xenon experiments, for many applications that will be detailed at the end of the next chapter. Furthermore, a similar analysis can be also done for other noble gas dual phase experiments.

In the next section will be presented the main evidences of the single electron emission by photoelectric effect observed by XENON100.

## 4.2 Properties of single electrons signals

As it was mentioned previously, single electrons charge signals are mainly induced by photoelectric effect of ultraviolet photons from a prior S2 signal over impurities in LXe or over metallic components of the TPC. This creation scenario is based on several evidences that are reviewed in the following developments.

### 4.2.1 Rates

The first evidence consists in investigating the rate of identified single electrons signals (S2 signals below 150 PE) per event as a function of either the impurities concentration in LXe, or the intensity of the prior main S2 signals, i.e. the number of emitted photons. The former case is illustrated by Figure 4.8(a) while the latter case is illustrated by Figure 4.8(b).

For each case, a specific time delay between the prior main S2 signal and each single electron signal has been requested. In Figure 4.8(a), this time window is restricted to a delay between 20  $\mu\text{s}$  and 150  $\mu\text{s}$ , in order to select only single electrons potentially generated in the middle of the liquid phase.

In order to not bias the dependency as a function of the impurities concentration in LXe by any effect due to the high intensity of the main S2 signal, the selection on the size of this latter in Figure 4.8(a) is restricted to a narrow window between 5 kPE and 10 kPE. In a similar way, an extended time period of cumulated  $^{137}\text{Cs}$  calibration data acquisition has been considered for this analysis, in order to take benefits of the evolution of the LXe purity such as described in Section 2.4.5.

Figure 4.8(a) shows then that the rate of single electrons signals per waveform is proportional to the impurities concentration in LXe, with a proportionality coefficient of  $3.72 \pm 0.13$  single electrons signals, i.e. S2 signals below 150 PE, and an ordinate at the origin at  $-0.52 \pm 0.12$  single electrons signals per waveform for the corresponding fit, represented in red. The non-null coordinate at the origin is explained by the lack of data at higher impurities concentration, since it is not the purpose of a low background experiment.

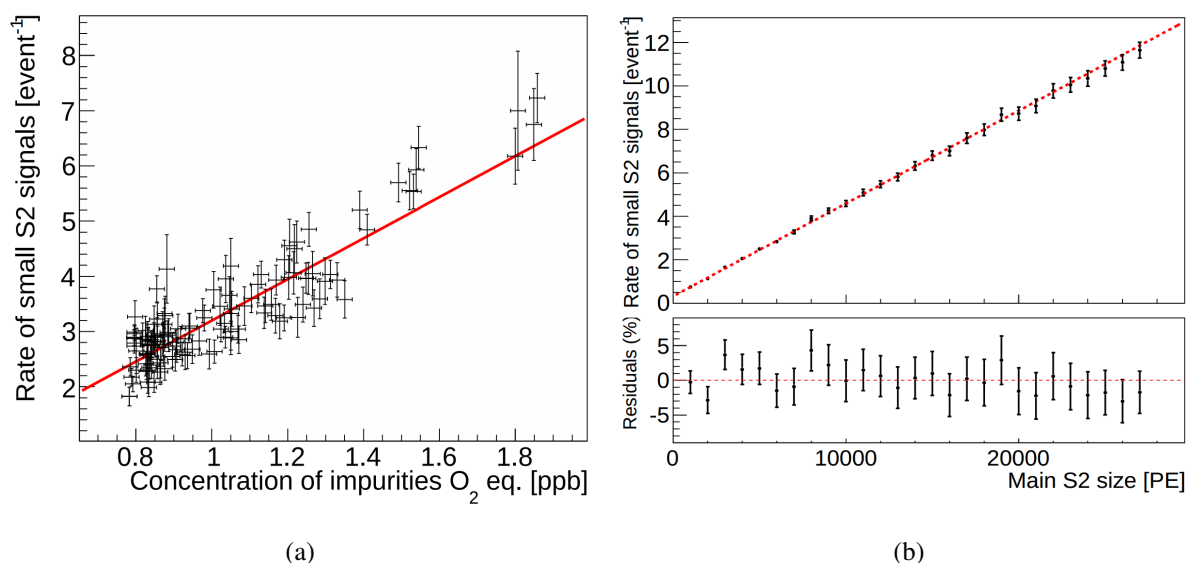


Figure 4.8: (a) Rate of low energy S2 signals per each waveform as a function of the impurity concentration in liquid xenon, (b) rate of low energy S2 signals per each waveform as a function of the intensity of the main S2 signal. Both pictures from [157].

Similar measurements and observations have been repeated without radioactive source for data acquisition, confirming the proportionality property. Because of the very low trigger rate of events without calibration source – of the order of one Hertz with respect to few tens of Hertz – it can be concluded that any fortuitous relationship between impurities concentration and the rate of single electrons signals per waveform, that would be mostly induced by a different phenomenon than the prior main S2 signal, is excluded.

For the rate as a function of the intensity of the main S2 signal, presented in Figure 4.8(b), the time delay between the prior main S2 signal and each single electron signal corresponds to a delay between  $0 \mu\text{s}$  and  $176 \mu\text{s}$ . It corresponds then roughly to the time needed for an electron released in the bottom of the TPC to drift toward the gas phase in the standard drift field conditions. Thanks to this extended time window, the whole drift can be investigated.

Since Figure 4.8(b) illustrates the dependency as a function of the intensity of the prior main S2, all the events with a main S2 above 150 PE have been considered. Moreover, for this analysis, the time period for the combination of  $^{137}\text{Cs}$  calibration data has been restricted to the last five months of the second science run. It corresponds to the period where the xenon purity was the highest and almost constant, right above 0.9 ppb, as illustrated by Figure 2.20.

A linear fit (dashed red line) of the data has been then applied, leading to a proportionality coefficient of  $4.3 \cdot 10^{-4}$  single electrons signals per photoelectrons induced during the prior main S2 signals. The ordinate at the origin is 0.3 single electrons signals per waveform, corresponding to signals that are not induced by the prior main S2 signal. They would correspond mostly to delayed extractions of electrons from the electronic cloud associated to this main S2 signal. Such delayed extraction has been also observed for single electron signals before the S1 signal, as discussed in Section 4.1.3. Furthermore, the residual of the data points with respect to the linear fit shows a very good proportionality between the two quantities.

These two independent observations of the dependency of the rate of single electrons signals seem thus to confirm the emissions by photoelectric effect of ultraviolet photons from a prior main signal. Others evidences of this emission process are presented in the next section.

### 4.2.2 Time distribution

In addition to the proportionality between the rate of single electrons signals and both the intensity of the prior S2 signal and the impurities concentration in LXe, another evidence confirms also the single electron emission by photoelectric effect from ultraviolet photons. It consists in investigating the variation of the rate of single electrons signals as a function of the time delay from the prior main S2 signal, as illustrated by Figure 4.9.

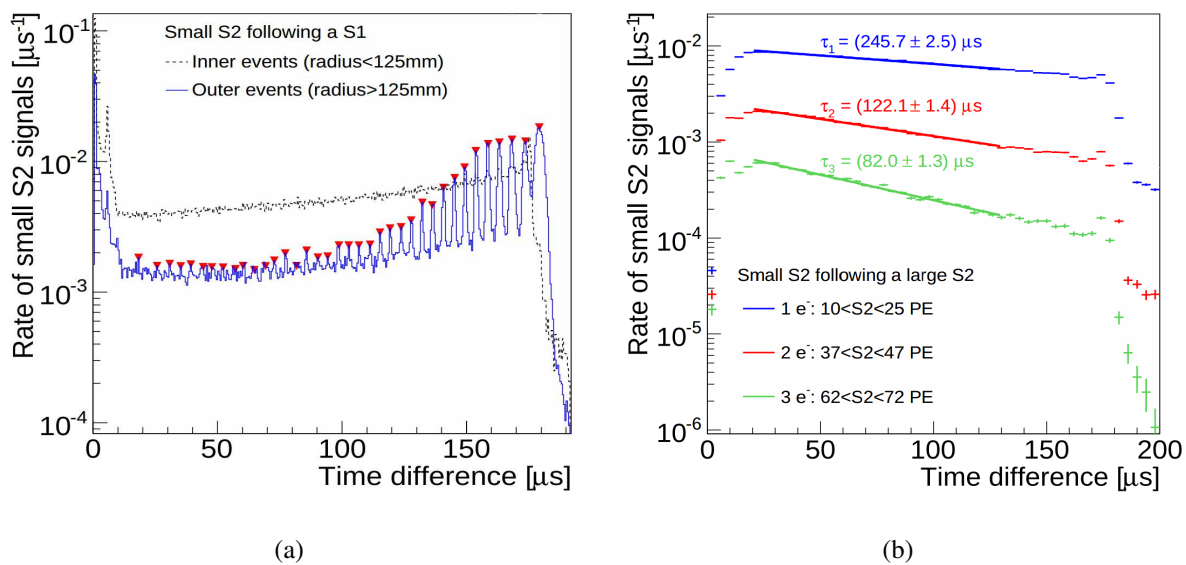


Figure 4.9: (a) Rate of low energy S2 signals (i.e. S2 signals below 150 PE) from either inner horizontal regions of the liquid volume or from outer horizontal region of the liquid volume per each waveform, as a function of the time delay from the prior S1 signal, (b) rate of one, two and three electrons signals per each waveform as a function of the time delay from the prior main S2 signal. Both pictures from [157].

Two different distributions can be studied. The first one consists in looking at the individual time distribution of the inner and outer single electrons signals following a S1 signal, as illustrated by Figure 4.9(a). In such cases, only events with no S2 signals above 150 PE were studied. The second one consists then in investigating the individual time distribution of the first single electrons signal populations (one, two or three electrons drifting in time coincidence) with respect to the main S2 signal, as shown in Figure 4.9(b). The former are electrons induced by the S1 light, while the latter are mainly induced by S2.

For both cases, a sharp decrease of the rate of the considered population of single electrons signals occurs around a time delay of 176  $\mu\text{s}$  from the prior main S2 signal. This signature illustrates the time needed for an electron extracted in the very bottom of the TPC to drift the about 30 cm toward the gas phase, for a drift field of 0.53 kV/cm in liquid phase. This confirms the single electron production mainly by photoelectric effect of photons from the prior main S2

signal, due to the geometrical limit of the time distribution. The very low rate of observed single electron signals above this time delay corresponds to the combination of delayed extractions from the liquid phase to the gas phase, and to a much lesser extent of single electron emission from multiple scatterings. Such multiple scatterings induce also a decrease of the resolution of low energy S2 signals due to overlaps with much higher S2 signals created for each scattering. This leads to the observed decrease of the rate of low energies S2 signals for the shortest time delays, mainly below  $20 \mu\text{s}$ , seen in Figure 4.9(b).

Furthermore, for outer single electrons signals presented in Figure 4.9(a), i.e. electrons released in the edges of the TPC, the rate of such signals per each waveform present several sharp increases, regularly spaced. The distances between them are all of the order of  $4.23 \pm 0.05 \mu\text{s}$ . By taking into account a drift velocity of about  $1.73 \text{ mm}/\mu\text{s}$  under a drift field of  $0.53 \text{ kV}/\text{cm}$  in LXe, this corresponds to a relative difference of depth emission of the order of  $7.32 \pm 0.09 \text{ mm}$ . It is the typical order of the spacing between two successive field shaping rings among the forty that are placed between the cathode mesh and the ground mesh located right below the anode one. It can be calculated by dividing the total drift length of about  $30 \text{ cm}$  by the 41 interstices between two rings, and between rings and meshes. In addition, the ground mesh is also visible through the first sharp peak at the beginning of the histogram.

All of these single electrons signals are induced by the photoelectric effect of photons that come from S1 signals created during one or more successive scatterings below the cathode, since no S2 signals above 150 PE occurs. The increase of the rates for deeper single electrons emissions are due to a less uniform distribution of the electric field in the bottom of the drift region, digressing these electrons from borders and promoting their drift.

For each recorded scattering inside the XENON100 TPC, the average (x,y) position is reconstructed by taking into account the intensity of the signal measured by each PMTs. This algorithm is appropriate for single scatter events, that contain only one cluster of illuminated PMTs on the top array. This is however not the case for multiple scatterings at the same depth, or for single electrons events, where two, three and more clusters of light could be observed on the top PMTs array. This typical feature is then used for the rejection of multiple scattering events for dark matter search. Moreover, single electrons signals are currently used to develop a new rejection algorithm [163], such as mentioned in the next section.

The reconstruction of the scattering positions by the current algorithm for such events is however done by assuming only scattering inside the LXe. As a result, this position is weighted by each cluster of light, and has no physical meaning. For the present analysis, the outer position selection of these single electrons allows however a precise position reconstruction of their emissions. Even if several few electrons (two, three, ...) events can be considered, all of these electrons would arrived in time coincidence in the gas phase, reflecting a same emission depth. Moreover, due to the outer position selection for the average reconstructed position, these electrons have their individual emission position very close one to each others since otherwise the average position will be reconstructed in more centered place.

The three populations presented in Figure 4.9(b) follow exponential decrease, represented by solid curves. Each of these decreases have an associated time constant equal to  $\tau_1 = 245.7 \pm 2.5 \mu\text{s}$ ,  $\tau_2 = 122.1 \pm 1.4 \mu\text{s}$  and  $\tau_3 = 82.0 \pm 1.3 \mu\text{s}$  for the one, two and three electrons signals

population respectively. All of these time constants reflect the accidental time coincidence of  $n$  individual single electrons thanks to the relationship:

$$\tau_n = \frac{\tau_1}{n} \quad (4.1)$$

Such a relation can be easily demonstrated. If  $R_1(t) = R_1(0) e^{-t/\tau_1}$  is the rate of pure single electron signals with a time delay  $t$  after the prior main S2 signal, and  $R_1(0)$  the expected rate of pure single electron signals right after the main S2 signal, assuming a perfect resolution of such signals, then if  $\Delta T \sim 1 \mu\text{s}$  is the time window for coincidence, corresponding to the average single electrons signals time width, the rate  $R_n(t)$  of signals of  $n$  electrons drifting in gas phase in coincidence at the time  $t$  is:

$$\begin{aligned} R_n(t) &= R_n(0) e^{-\frac{t}{\tau_n}} \\ &= R_1(t)^n \Delta T^{n-1} \end{aligned} \quad (4.2)$$

By expressing  $R_1(t)$  as a function of  $\tau_1(t)$ , this leads to the relation 4.1 observed on Figure 4.9(b), confirming the accidental time coincidence of two or more individual single electrons in case of two or more electrons signals.

### 4.2.3 Example of a three electrons S2 signal

The simultaneous drift of few electrons can be easily shown through the (x,y) distribution of the light emitted during S2 signals few times bigger than 20 PE [163], using the results detailed in the present and next chapter. An example of these maps for the top array is shown in Figure 4.10 and corresponds to a S2 signal at about 64 PE, i.e. about three times higher than the typical gain for a single electron S2 signal. The corresponding three independent single electrons can be easily seen in this plot thanks to the three clusters of illuminated PMTs. Each square corresponds to one PMT, identified by a specific number. The external ring corresponds to veto PMTs. The intensity of light in PE received by each of them is represented by a colors gradient, with hot colors for higher quantities of light. The white color corresponds to not illuminated PMTs.

The light observed by the three single PMTs labelled 33, 63 and 45 could correspond to either the reception of photons from one of the three clusters of PMTs, or to PMTs base current fluctuation. At the time of writing, a dedicated analysis on the PMTs pattern is still ongoing, and only further developments would be able to give more details on such behaviours.

Furthermore, such light pattern has also been observed for more electrons drifting in time coincidence, namely up to 7 - 8 individual electrons. However, due to the equivalent number of hotspot of light in the top PMTs array, almost all of them were receiving light, leading to a lower distinction between the edge of each of these hotspots, while it is not case for lower energies S2 signals. That is why, at the time of writing, further analysis are needed in order to identify the contribution of each electron to the light seen by each PMT.

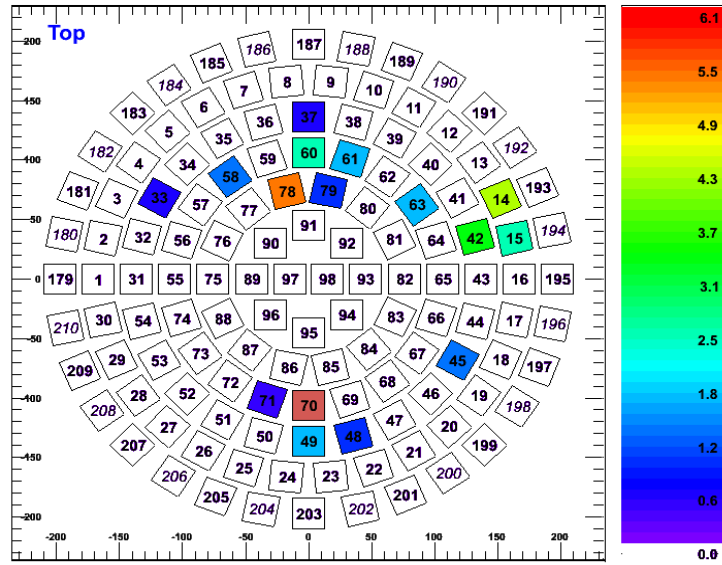


Figure 4.10: Illustration of S2 light repartition on top PMTs array for a three electrons signal. Figure from [163].

### 4.3 Low energy S2 spectrum analysis

As presented in Section 4.1.4, only the low energy part of all the S2 signals spectrum is considered for the characterisation of the secondary scintillation gain. In what follows will be described the method used for this quantification, starting by the explanation of the model used and the data selection criteria, completed by a discussion on the limitation of such primary analysis.

#### 4.3.1 Parametrisation

The S2 low energy spectrum corresponds to all the identified S2 signals that are below about 150 PE, namely the light emitted by about 7 - 8 electrons accelerated simultaneously in the gas phase. In order to characterize the average light emitted by only one electron accelerated in the gas phase, the contribution of each single electrons population have to be identified and taken into account. For this purpose, the spectrum is fitted by a sum of Gaussian distributions that represent the distribution of the emitted light per each population of single electrons signals, i.e. one, two, and more electrons. All of these Gaussian distributions have their mean value  $\mu_i$  and their standard deviation  $\sigma_i$  constrained together following the equations:

$$\begin{aligned}\mu_i &= i \times \mu_1 \\ \sigma_i &= \sqrt{i} \times \sigma_1, \quad i = 1, 2, 3, \dots, n\end{aligned}\quad (4.3)$$

where  $i$  is the number of the Gaussian distribution associated to  $i$  electrons accelerated in time coincidence in the gas phase, since the average light emitted by two, three and more individual single electrons accelerated in time coincidence in the gas phase are supposed to be two, three,

and more times the average light emitted by only one electron. This hypothesis of dependency among the single electrons signals determine also a proportionality of the variance. It will be demonstrated in Section 4.5. The detection efficiency of very low energy S2 signals, i.e. below about 20 PE, is lower than 100 %. This is due to the combination of a reduced differentiation power between PMTs base current fluctuations and S2 signals at such energies, and a non-optimisation of the search algorithm for S2 signals with intensities down to very few PE. Two additional processes are also identified: the influence of prior main S2 signals on the PMTs base current, and the maximum numbers of 32 identified S2 signals on the waveform that are effectively kept after the reprocessing stage. Their identification and the strategies developed to avoid these two processes are detailed in sections 4.4.

Due to this lower detection efficiency at the low energy part of the spectrum, some S2 signals are suppressed in this region. As a result, the Gaussian distribution distribution can not be fully followed. A threshold function has to be used to allow the description of the full spectrum by modelling the detection efficiency as a threshold function based on the Fermi-Dirac distribution.

The function used for the fit of the low energy S2 spectrum with  $n$  Gaussian distributions is presented in Equation 4.4. The left part of this function corresponds to the threshold function presented above, and which takes values between 0 and 1.

$$f(E) = \frac{1}{e^{-\frac{(E-E_t)}{\Delta E_t}} + 1} \sum_{i=1}^n \alpha_i e^{-\frac{(E-\mu_i)^2}{2\sigma_i^2}} \quad (4.4)$$

For a such function, the number of free parameters is equal to  $4 + n$ :

- 3 parameters describing the first Gaussian distribution, corresponding to its amplitude  $\alpha_1$ , average value  $\mu_1$ , and standard deviation  $\sigma_1$ .
- $n-1$  parameters corresponding to the weight of the other Gaussian distributions  $\alpha_i$ ,  $i \in [2, \dots, n]$ .
- 2 parameters describing the threshold function:  $E_t$ , the energy value for half efficiency, and  $\Delta E_t$  the steepness of the function. Both quantities are sometimes referred along the text as *FD1* and *FD2* respectively.

In order to improved the fit stability, the lowest number of free parameters is mandatory. Moreover, the probability of having  $i$  electrons in time coincidence with respect to pure single electron is much lower for  $i$  equal to about 6 - 8 electrons than for about 2 - 3 electrons. Therefore only five Gaussian distributions will be considered in most of the studied presented starting from this point. According to these conditions, the number of free parameters is equal to nine. Analyses with different values for the number of Gaussian distributions will be made only in Section 4.5, in which the stability of the fit with this choice will be also demonstrated.

An illustration of the fit obtained with the function described in Equation 4.4 is presented in Figure 4.11. Data point are in black, barely visible since they are perfectly covered by the fit function in red. The contributions of each of the five Gaussian distributions are presented in other

colors. They correspond to the distribution of low energies S2 signals that are created by one, two, three, four and five electrons accelerated in time coincidence in gas phase. The increase of detection efficiency as a function of the intensity of the low energies S2 signals is represented in purple, with the corresponding amplitude that is reported on the right Y-axis. The spectrum used for this example corresponds to the combination of all the calibration datasets acquired with  $^{60}\text{Co}$  during the second science run. This explains why error bars on data points are so small to be hidden by the size of the marker. The selection cuts applied to this spectrum are not expressed here, but are explained in Table 4.1, at the end of the Section 4.4.3 that details their motivations.

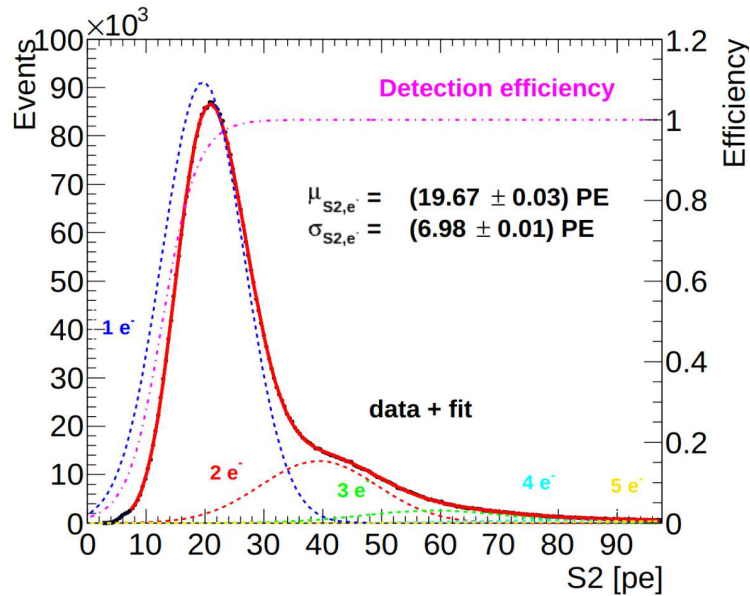


Figure 4.11: Illustration of a low energy S2 spectrum fitted by a sum of five Gaussian distributions and multiplied by a threshold function based on the Fermi-Dirac statistics.

The corresponding secondary scintillation gain and its standard deviation are equal to  $19.67 \pm 0.03$  PE and  $6.97 \pm 0.01$  PE respectively. The very low errors are due to the very high accumulated statistics, and do not take into account the systematic errors, which will be detailed more extensively in Section 4.5.

### 4.3.2 Primary selection cuts

According to all the details that were given in the present chapter up to this section, and in order to quantify the secondary scintillation gain, two primary data selection cuts are needed:

- Since single electrons signals are induced by photons from a previous S2 signal, only low energy S2 signals observed after the main S2 signal will be used.
- Since the rate of single electrons signals per event is proportional to the intensity of the main S2 signal, a threshold value of this intensity has to be fixed in order to increase this rate. As a result, this will also increase the rate of time coincidences of two and more individual single electrons, allowing to improve the height of the second and eventually the third Gaussian distributions, and thus allowing to improve the fit of the spectrum. This is

important since, as it will be seen later, the first Gaussian distribution is correlated with the threshold function and the presence of other Gaussian distributions.

For the time being, the value of the second data selection cut is set at 30 kPE. It will be shown in Section 4.5.5 that this corresponds to the highest threshold value that is convenient to use for a general analysis.

As an illustration, the influence of the intensity of the main S2 signal on the low energy spectrum can be seen in Figure 4.12. The two spectra correspond in each case to the combination of all datasets acquired with the  $^{137}\text{Cs}$  radioactive source during the first science run. The selection threshold on the intensity of the main S2 signal per each waveform is set at 10 kPE and 30 kPE on Figure 4.12(a) and on Figure 4.12(b) respectively. No other selection cut is applied. The quality of the fit of the two spectra around 100 PE is discussed in the next section. The secondary scintillation gain, the standard deviation of the associated distribution and the value of both the position at half size and the width of the threshold function resulting from the fit are presented on each spectrum. This will be also the case for all future spectra presented in this thesis.

While the same detector settings and the same calibration source for the data acquisition have been used for the two spectra, both results are different. As a result, an identification and a reduction of the instability factors of the fit has to be made. This analysis is presented in the next section. The two examples presented in Figure 4.12 have been also selected to illustrate some fit issues that will be discussed in the next section.

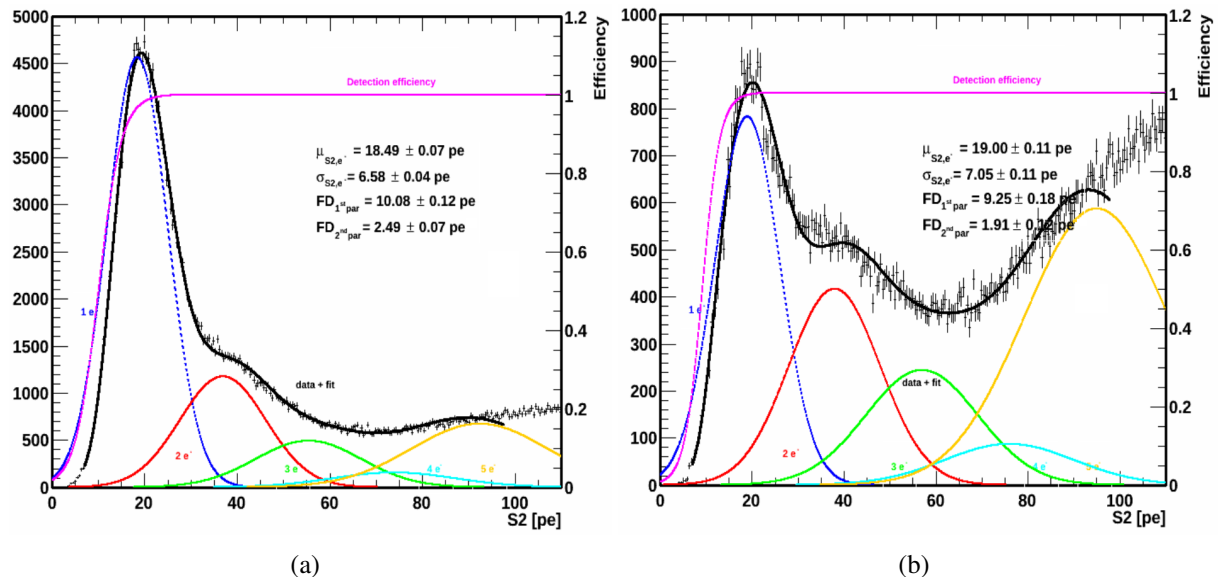


Figure 4.12: Illustration of the influence of the minimum requested intensity of the main S2 signal per waveform on low energy S2 spectrum: (a) main S2 signal above 10 kPE, (a) main S2 signal above 30 kPE. The quality of the fit of the two spectra will be discussed in the next section. Both spectra obtained with the  $^{137}\text{Cs}$  radioactive source during the first science run.

### 4.3.3 Potential fit biases

Starting from the primary cuts presented in the previous section, it was observed that the fit of the spectrum was not optimised, leading to a biased evaluation of the secondary scintillation gain. This phenomenon is illustrated by Figure 4.13(a), that represents the variation of the reduced  $\chi^2$  parameter associated to the fit function as a function of an imposed value of the secondary scintillation gain, for one dataset acquired with the  $^{137}\text{Cs}$  radioactive source right before the second science run. The value naturally obtained from the fit of the low energy S2 spectrum is illustrated by the vertical red dashed line. The green parabola corresponds to a fit of the reduced  $\chi^2$  distribution, and is used only for an optical guidance, illustrating the region of values of the secondary scintillation gain that corresponds to the more accurate fits of the spectrum, with the best value illustrated by the red cross. These latter corresponds then to artificial fits of the spectrum since the secondary scintillation gain value is already imposed in advance, and are used only to investigate the quality of fit as a function of the value of the secondary scintillation gain. They have then to be compared to the vertical dashed line that represents the value of the gain that is effectively measured when no constrains on fit parameter are applied.

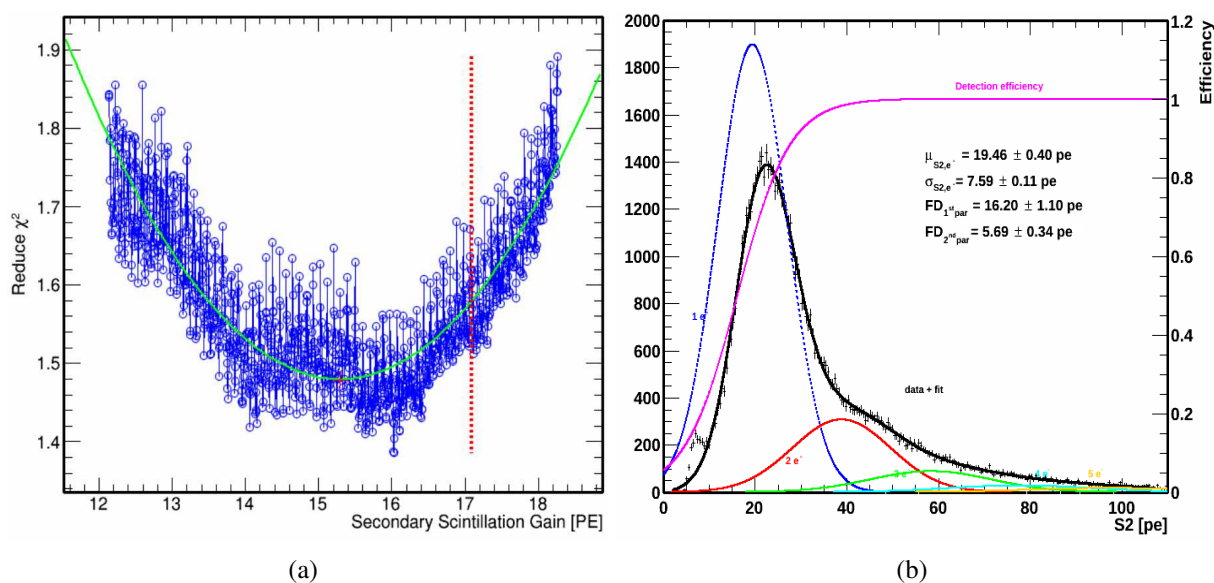


Figure 4.13: (a) Quality of the fit of the low energy S2 signals as a function of the requested secondary scintillation gain. The vertical red dashed line corresponds to the value naturally provided by the fit, that is clearly far from the minimum of the parabola. (b) Illustration of an excess of S2 signals at very low energies ( $S2 \in [5 - 10]$  PE). Both spectra obtained with the  $^{137}\text{Cs}$  radioactive source before the second science run and with the  $^{60}\text{Co}$  radioactive source during the second science run respectively.

The typical difference between the value of the secondary scintillation gain naturally obtained from the fit of the spectrum, and the expected value extracted from the fit of the reduced  $\chi^2$  distribution, corresponding to the minimization of this latter, is of the order of 1.5 PE. Few factors can be responsible for this bias:

1. The upper part of the fit range corresponds to a region where the six, seven and even eight individual single electrons populations are non negligible with respect to the one of five

individuals single electrons. As a result, the lack of the associated sixth, seventh and eighth Gaussian distributions can lead to a divergence between the trend of the spectrum and the fit function, as it is illustrated around 100 PE in Figure 4.12.

2. In a similar way, some very low energy S2 signals, corresponding to either misidentified S1 signals, or noisy S2 signals that can be induced from sparks from the anode, can also bias the fit of the spectrum. Such low energy excess is better illustrated on Figure 4.13(b) that corresponds to the low energy S2 spectrum for one dataset acquired with the  $^{60}\text{Co}$  radioactive source during the second science run, during a period in which a located emission of sparks from the anode are observed. The spatial distribution of this perturbation is presented for illustration purpose in Section 4.5.8.
3. The high number of free parameters for the used fit function can also leads to non-physical value of size of each Gaussian distributions, i.e. negative values or values above few orders higher than the maximum of the spectrum. The other parameters can also not be able to converge to the best values due to the complexity of the fit function.

A typical example of a totally wrong fit corresponds to the association of the main S2 peak of the spectrum with the second Gaussian distribution, and as a consequence the second main peak with the fourth. This has no physical meaning, even without regarding the value of the secondary scintillation gain, which is then two times lower than the expected value.

4. In case of very high impurities concentration in the liquid xenon, the pure single electron signals population and two individual single electron signals population can be dramatically lowered with respect to the other ones, as illustrated by Figure 4.14(a). This spectrum corresponds to one dataset acquired with the  $^{137}\text{Cs}$  radioactive source during the first science run, and only single electrons signals after a main S2 signal higher than 30 kPE are considered.

In such low LXe purity conditions, the decrease of the resolution of the pure single electron signals population is due to the increase of single electrons signals rate per triggered waveform because of high impurities concentration, as discussed in Section 4.2.1. As a consequence, coincidences of few individuals single electrons signals occur with much higher probability than the pure single electron signals. This latter have thus a much lower probability to be part of all the possible 32 S2 signals finally stored per each waveform, leading to a lack of pure single electron signals population with respects to higher single electron signals populations.

Each of these four factors can be treated independently in order to improve the fit quality. Indeed, the two first factors can be reduced by performing a specific choice of the energy range for the fit, typically 7 PE for the lower bound, and the average value of the fifth Gaussian distribution for the upper bound. In case of lower electric field conditions in gas phase, the 7 PE lower bound has been lowered down since the secondary scintillation gain can be about 10 PE or even less. Moreover, as it will be presented in Section 5.3, a specific cut based on minimum proportion of light seen by each PMTs array can be used to reject these excesses at very low energies S2 signals.

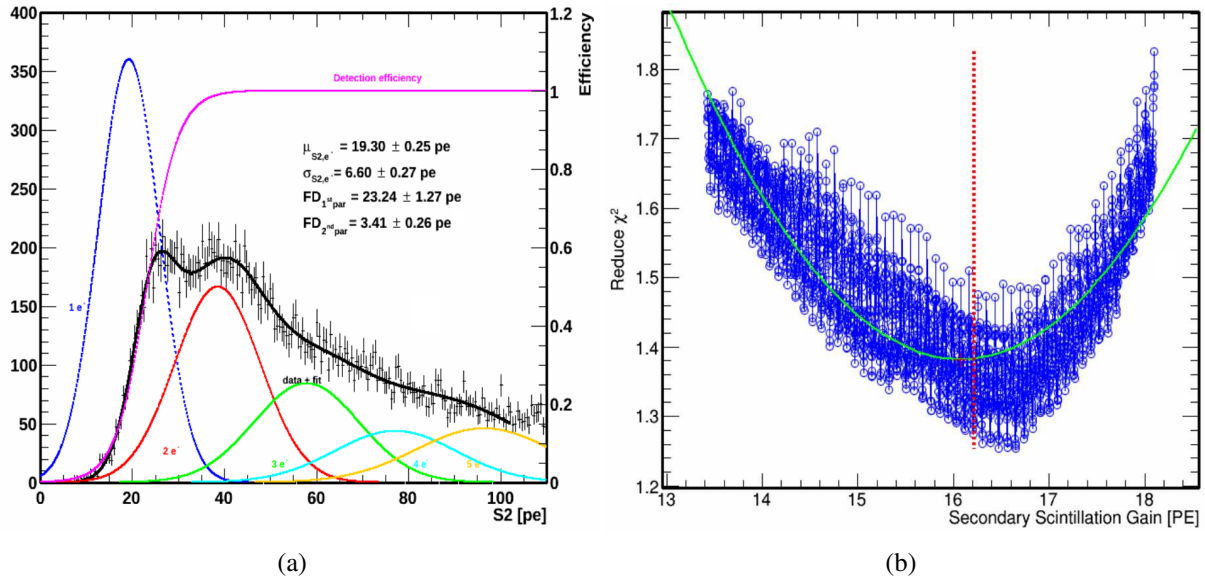


Figure 4.14: Illustration of the decrease of the pure single electron signals population in case of low LXe purity conditions, (b) quality of the fit of the low energy S2 signals as a function of the requested secondary scintillation gain after primary improvement of the fit methods. Both spectra obtained with the  $^{137}\text{Cs}$  radioactive source, during and before the second science run respectively.

However, this kind of cut will be not applied at this primary step of the single electron analysis in order to reject as less as possible data for the analysis presented in the next sections.

Then, the third and partially the fourth factor can be solved by a good choice of the initial parameters on expected regions of values, typically based on the maximum of the spectrum, the expected order of the secondary scintillation gain and its standard deviation. The stability of the fit is enhanced even more by repeating the fit few times up to the stabilization of the results, using values from the previous fit as input for the next one and adapting everytime the domain of the fit. This method increases the capability of identification of each population for difficult spectra similar to Figure 4.14(a). However, this can not increase the real distinction between pure and two individual single electrons signals as it could be for a more general case, like in Figure 4.7. This separation for such low LXe purity conditions can be reached only after using cuts detailed in Section 4.4.1.

Taking all the above mentioned effects into account, the stability and reliability of the fit of the spectrum are improved, and its result is closer to the value corresponding to the minimum reduced  $\chi^2$ , as illustrated by Figure 4.14(b). This figure corresponds to the very same dataset as the one used for Figure 4.13(a). The blue distribution and the red dashed line take now into account the improvements presented above. Since now the instability of the fit of the spectrum has been solved without rejecting datasets with respect to primary cuts, leading to almost 100 % of fit success with coherent fit results, the dependency of secondary scintillation gain as a function of several experimental parameters, such as single electron emission depth or radial position, has to be investigated in order to establish other possible bias for the function. These analyses are presented in next sections.

## 4.4 Study of secondary scintillation gain

As mentioned right above, the dependency of the secondary scintillation gain with the single electron emission position has to be investigated. The purpose of this analysis is to investigate a possible bias on this gain due to the temporal tail of the main S2 signals. As a result, the depth and the radial position of the single electron emission are investigated separately. The results of the two analyses are presented in the following sections.

### 4.4.1 Dependency on single electron depth emission

In the present analysis, the variation of the secondary scintillation gain as a function of the single electron depth emission, i.e. as a function of the time delay from the main S2 signal, is investigated. For this purpose, an additional data selection cut is applied, combined with the two data selection cuts presented in the Section 4.3.2. It consists in considering only single electrons signals that occur during successive windows of  $16 \mu\text{s}$  as time delay from the main S2 signal. Thanks to this selection cut, all depth shells are investigated by keeping an enough high statistics, down to the bottom of the TPC that corresponds to a total drift time of  $176 \mu\text{s}$ , i.e. the end of the eleventh time window.

Moreover, by taking advantage of the high statistics acquired with calibration sources for electronic recoil during the second science run, all the datasets acquired during this period with  $^{60}\text{Co}$  radioactive source are combined and used for the present analysis. As a result, the variation of the secondary scintillation gain as a function of the time delay from the main S2 signal is presented in blue in Figure 4.15. The gain indicated by the red marker corresponds to the case where there is no request on time delay from the main S2 peak, that is why it is represented arbitrary in the middle of the X-axis.

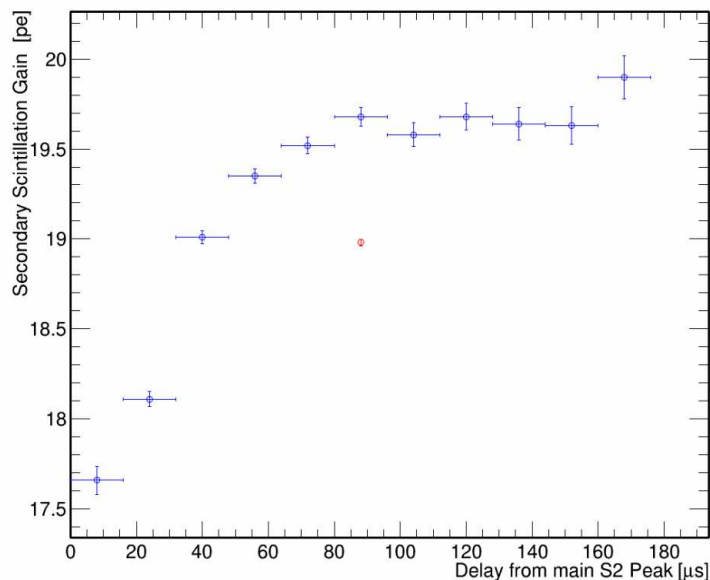


Figure 4.15: Secondary scintillation gain as a function of the single electron depth emission.

Two trends can be observed in this figure. First, the secondary scintillation gain increases from

about 17.6 PE up to about 19.6 PE, with a time delay increasing from 0  $\mu\text{s}$  up to about 70  $\mu\text{s}$ . Then, the gain remains roughly constant. At such a time delay of 70  $\mu\text{s}$  from the main S2 signal, the influence of the tail of this signal is widely excluded. However this time corresponds to the typical time of the PMT base current remaining after the scattering of the photons over its photocathode before vanishing. Thus, since the base current of PMTs enlightened by the main S2 signals is not set back to ground level, the low energy S2 signals occurring less than 70  $\mu\text{s}$  after the main S2 are partially hidden by the PMTs base current since the combination of all the waveform from each PMT are considered for the identification of each signal. This leads to an underestimation of the gain for such emission depth with respect to the plateau value at about 19.7 PE observed above 70  $\mu\text{s}$  after the main S2 signal.

It was therefore discovered that, due to this dependency from the time delay after the main S2 signal, the secondary scintillation gain measured when no request on a time delay is applied was underestimated. As a result, in order to not be biased by the PMTs base current from the main S2 signal, only single electrons signal occurring more than 70  $\mu\text{s}$  after the main S2 signal should be considered.

As a complement, this bias can be also observed by looking at the standard deviation  $\sigma_1$  of the first Gaussian distribution in Figure 4.16(a), or at the ratio of this standard deviation over the secondary scintillation gain  $\sigma_1/\mu_1$ , as illustrated by Figure 4.16(b). For the former case, the bias is much weak, and leads to a plateau value of about 7 PE. It is observable a residual dependency of  $\sigma_1$  from the time delay, however it must be noticed that such a fluctuation is of the order of 0.1 PE only, which is similar to the oscillations of the plateau of the secondary scintillation gain. These two additional figures confirm not only the bias, but also all time boundaries of the plateau, i.e. the time region where the bias from PMTs base current is excluded.

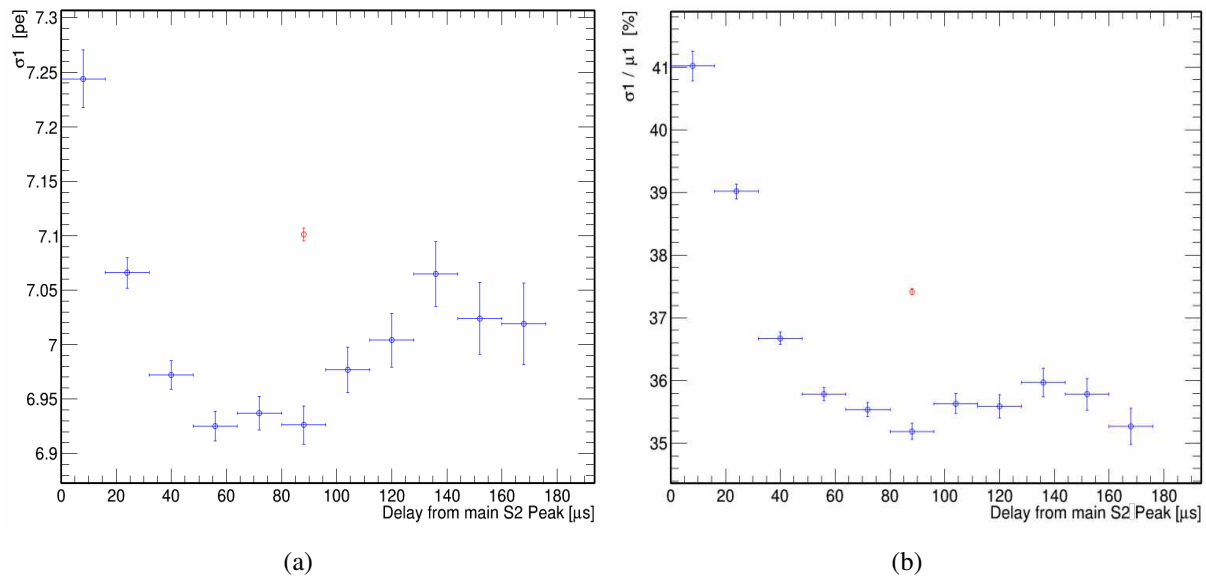


Figure 4.16: (a) Standard deviation of the first Gaussian distribution, and (b) ratio of this standard deviation over the secondary scintillation gain as a function of the single electron depth emission.

### 4.4.2 Dependency on single electron radial location emission

The present section shows the variation of the secondary scintillation as function of the relative reconstructed position of the single electron signal with respect to the position of the main S2 signal. All the datasets acquired during the second science run with  $^{60}\text{Co}$  radioactive source are combined and again used for the present analysis. This is somehow a complementary study of the previous one, since the radial distance between two peaks can produce a similar bias than a distance on  $z$  (hence, the time delay). In order to study these two effects independently, the selection cut of a time delay above  $70 \mu\text{s}$  will be not applied in the present section. In this way, compared to the previous analysis, the data selection cut based on a specific time window of a delay from the main S2 signal is replaced by another one based on a specific window of either 10 mm or 15 mm away from main S2 signal emission location. Both cases are investigated in parallel, increasing both the resolution of the trend of the variation, and the statistics per each considered window respectively. Thanks to this higher statistics, this latter case allows also to extend the analysis to higher relative position than the former case.

Two different values for the minimum threshold of the main S2 signal are tested, set at 10 kPE and 30 kPE respectively. The purpose of lowering the threshold on the main S2 signal is again to increase the statistics per each considered spectrum, in contrast to the analysis on a data selection cut based on the time delay from the main S2 signal, and where a much larger statistics was kept per each spectrum.

The results are presented on Figure 4.17, 4.18, 4.19. The relative position with respect to the main S2 signal's one is shown in the bottom X-axis. On the top X-axis is also shown the time delay from the main S2 signal for the results obtained in the previous analysis, whose data are also presented here in light green. These results from previous analysis have been added for comparison of the two plateaux. There is then nothing that can be learned by comparing the values on the X-axis. For illustration, the values of secondary scintillation gain and the standard deviation of the first Gaussian distribution if no specific cut on either time delay from the main S2 signal or on the relative position from this signal is used are represented by a dark blue dashed line.

As observed in the previous section, there is a bias on the secondary scintillation gain due to the main S2 signal and the associated remaining base current on impacted PMTs, leading to an underestimation of this gain. The trend of this gain up to a plateau value presented in the previous analysis, see Figure 4.17, is clear, and confirmed by all the four analyses that used a higher resolution either of the trend or of the spectra. Moreover, the plateau value reached in the present analysis is compatible to the one reached in the previous analysis. This confirms the need of using an additional data selection for the secondary scintillation gain evaluation, based either on a time delay from the main S2 signal, or from a relative reconstructed position with respect to the position of this signal.

These observations are also confirmed when the standard deviation of the first Gaussian distribution is investigated instead of the secondary scintillation gain, as presented in Figure 4.18. The plateau value is however reached faster than for the secondary scintillation gain, since this value is more stable. This stability is due to a higher correlation with the light collection efficiency and the PMTs fluctuations than with the gain itself.

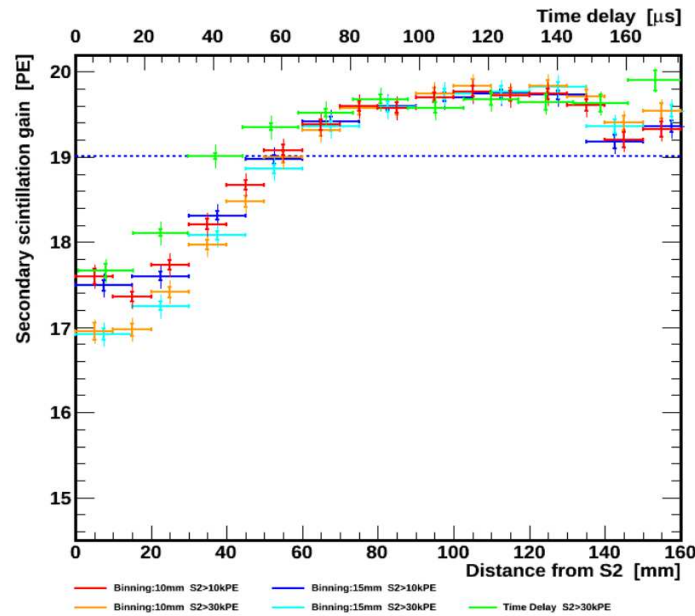


Figure 4.17: Secondary scintillation gain as a function of the single electron reconstructed emission position with respect to the position of the main S2 signal.

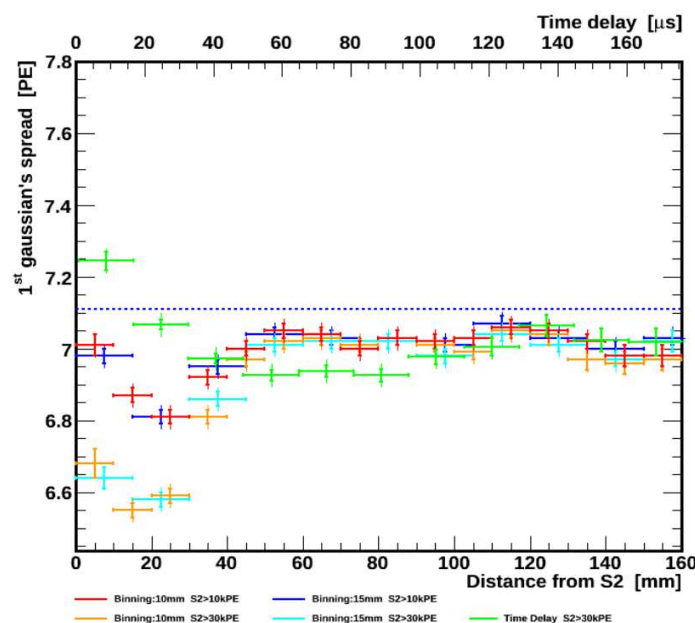


Figure 4.18: Standard deviation of the first Gaussian distribution as a function of the single electron reconstructed emission position with respect to the position of the main S2 signal.

Compared to the previous analysis, the present one can be performed up to a larger distance from S2 after the establishment of the plateau of the gain since a relative position of 15 mm, i.e. equal to the radius of the TPC, does not correspond to the edge of the TPC as long as it is a relative position between the signals. The main S2 signal and single electrons signals can have relative opposite positions with respect to the center of the TPC, with less and less statistics when increasing the relative distance between their position. In the opposite case, in the previous analysis, a 176  $\mu\text{s}$  of time delays really meant an emission at the very bottom of the TPC. Single

electron signals occurring later, if existing, can no longer be related to the main S2 signal.

Figure 4.19 presents the very same analysis as in Figure 4.17, but with extended range on position. For clarity reasons, the result from the previous analysis in light green in Figure 4.19 has been suppressed here. A first behaviour appears here, corresponding to a large discontinuity in the observed plateau for the gain, and located at a relative reconstructed position equal to the radius of the TPC. In such conditions, most of the single electrons signals are at the edge of the TPC, with a S2 signal occurring in the middle, leading to a bias of the secondary scintillation gain due a bad light collection efficiency. These events are dominant in this relative position due to the combination of both effects: the covering of the full ring of the edge of the TPC by the reconstructed emission positions and a decrease of the statistics of single electrons signals far from non-centered main S2 signals due to the distribution of the solid angles of the emission of photons during these signals. Above this discontinuity, the plateau is reached again. At very high distance, the gain starts to be again biased due to a lower collection efficiency at the borders of the chamber. A similar behaviour has been observed for the standard deviation of the first Gaussian distribution.

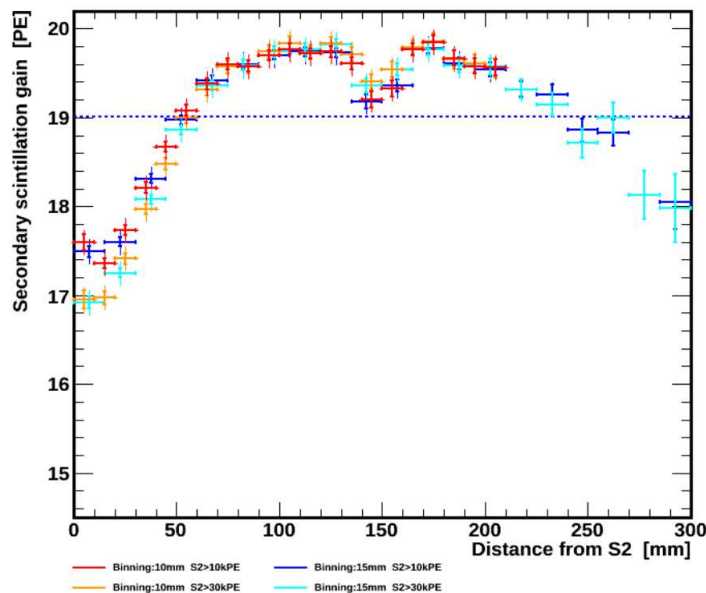


Figure 4.19: Secondary scintillation gain for larger position as a function of the single electron reconstructed emission position with respect to the position of the main S2 signal.

While the present analysis has confirmed the bias of the secondary scintillation gain presented in the previous section, including a plateau value reached after a relative position of about 70 mm, it has however revealed a discontinuity on this plateau. This favours the use of a data selection cut based on a time delay from the main signal, rather than of a radial distance. This choice is also motivated by the definition of a such reconstructed relative position cut. Indeed, in case of a S2 signal induced by a compact cloud of electrons, corresponding to a standard single interaction of a particle inside the liquid phase, the position reconstruction is well estimated. However, in the present case, the reconstructed position of signals induced by few individual single electrons can not be considered as a physical position since each of these electrons can be far from each other, leading to a *center*, reconstructed by the weight of each cluster of light, that has no physical

meaning. In order to use such a data selection cut, the reconstruction of the position of each individual single electron is mandatory. At the time of writing, such a reconstruction is currently investigated [163], but has not been yet implemented in XENON100.

However, if a time delay based data selection cut is preferred to a relative position based data selection cut, namely requesting that single electrons signals should occur only after  $70 \mu\text{s}$  after the main S2 signal such as suggested by Figure 4.15, the discontinuity observed in Figure 4.19 has to be taken into account. Indeed, if it occurs for signals reconstructed close to the border, it seems also to occur for the bottom of the TPC, as suggested by the last data point on Figure 4.15. For such time delay, there is a non negligible probability for events that are not induced by the main S2 signal to occurs. This corresponds to the combination of a S1 signal and a single electron extracted from the last field shaping, since their emission rate is higher than single electron from upper rings, as it has been observed on Figure 4.9(a). That is why it will be safer to also reject single electrons signals occurring more than  $170 \mu\text{s}$  after the main S2 signal.

### 4.4.3 Influence on the number of S2 signals per waveform

The two previous analyses have presented a bias on the secondary scintillation gain and proposed a data selection based on a time delay cut in order to solved it. For these analyses, only the standard deviation and the average value of the first Gaussian distribution have been presented, since only a bias on the secondary scintillation was investigated. However, in order to be complete, the analysis has to be extended to the other majors parameters of the fit function, corresponding to the two parameters of the Fermi-Dirac function used as threshold. While the same discontinuity has been observed for relative position of single electrons signals close to 150 mm, an almost linear trend is observed for the two parameters for both studies, as illustrated by Figure 4.20. This figure corresponds to the very same analysis as in Section 4.4.1, but representing two others quantities: the average position at half efficiency and the width of the threshold function.

This linear trend illustrates the decrease of very low energy S2 signals, i.e. here below 20 - 25 PE, with respect to the other S2 signals. In order to understand this phenomenon, the remaining parameters of the fit function, the amplitudes of each Gaussian distribution, have to be considered. Thus, the proportion of pure single electrons signals among all S2 signals below 150 PE, i.e. the amplitude of the first Gaussian distribution, and the proportion of signals induced by two individuals single electrons, i.e. the amplitude of the second Gaussian distribution, for the full considered data, has been investigated, firstly separately and then the former as a function of the later. This study has been also extended to low energy S2 signals, i.e. the sum of the amplitude of the second up to the fifth Gaussian distribution. The results are presented on Figures 4.21 and 4.22.

The purpose of Figures 4.21(a) and 4.21(b) is to be able to associate a depth emission with a signal rate. The first figure shows an exponential increase of the rate of pure single electrons signals up to a maximum value of about 2.5 %, while the latter shows two different trends: first a very sharp increase up to 0.4 %, at low emission depth, and following the increase of pure single electrons emission, and then an exponential decrease down to 0.3 %. This decrease is due to the decreasing probability of extraction in time coincidence for longer drifts because of the following reasons: the probability of the emission of two individual single electrons at the same

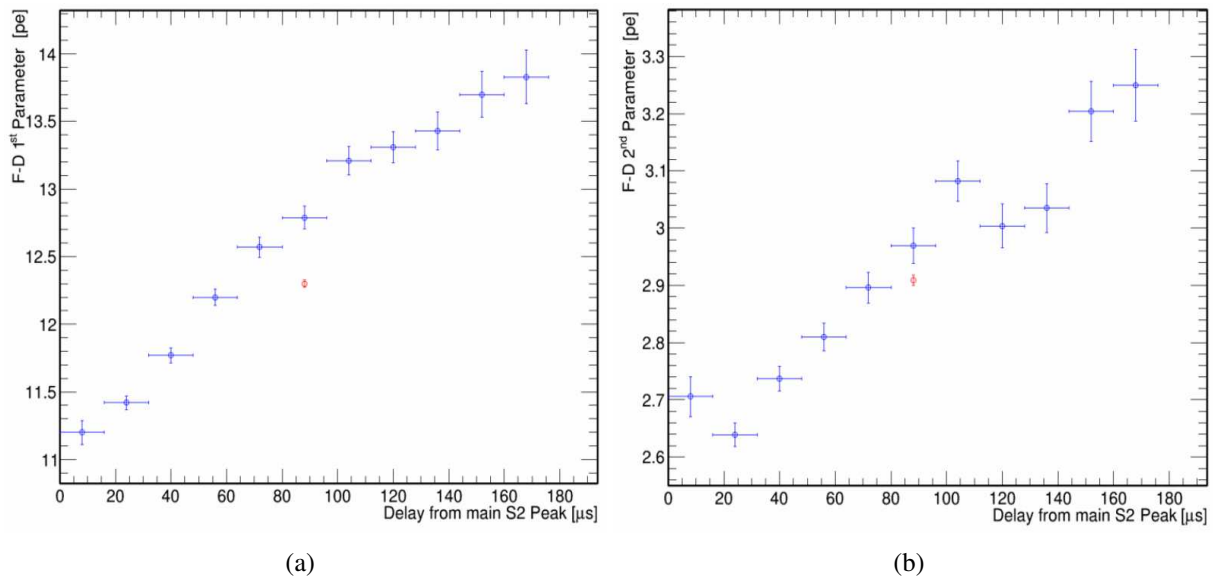


Figure 4.20: Variation of (a) the average position at half height ( $FD1$ ), and (b) the slope of the threshold function as a function of the single electron depth emission ( $FD2$ ).

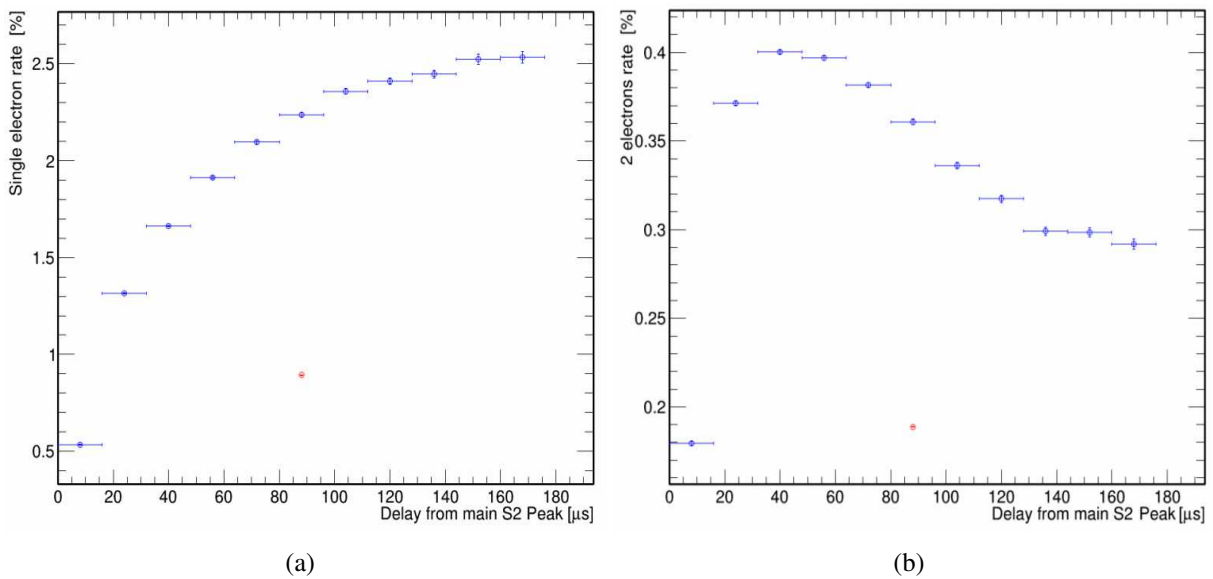


Figure 4.21: Rate of (a) pure single electrons signals, and (b) signals induced by two individuals electrons extracted in time coincidence in gas phase as a function of the single electron depth emission.

depth becomes low, and the probability of a successful drift due to electronic capture become low as well. In these two figures, the very low rate of few tens of percent up to few percent is due to the only consideration of signals effectively at either the secondary scintillation gain, or two time this value, without taking into account the standard deviation of each signals population.

Thanks to these two plots, Figure 4.22(a) can be understood: the proportion of single electrons signal with respect to the signals emitted by two individuals single electrons decreases as soon as the emission depth increases, and becomes almost constant for the highest emission depths. This behaviour is confirmed when considering the combination of the rate of signals induced by two

up to five individuals single electrons, as shown in Figure 4.22(b).

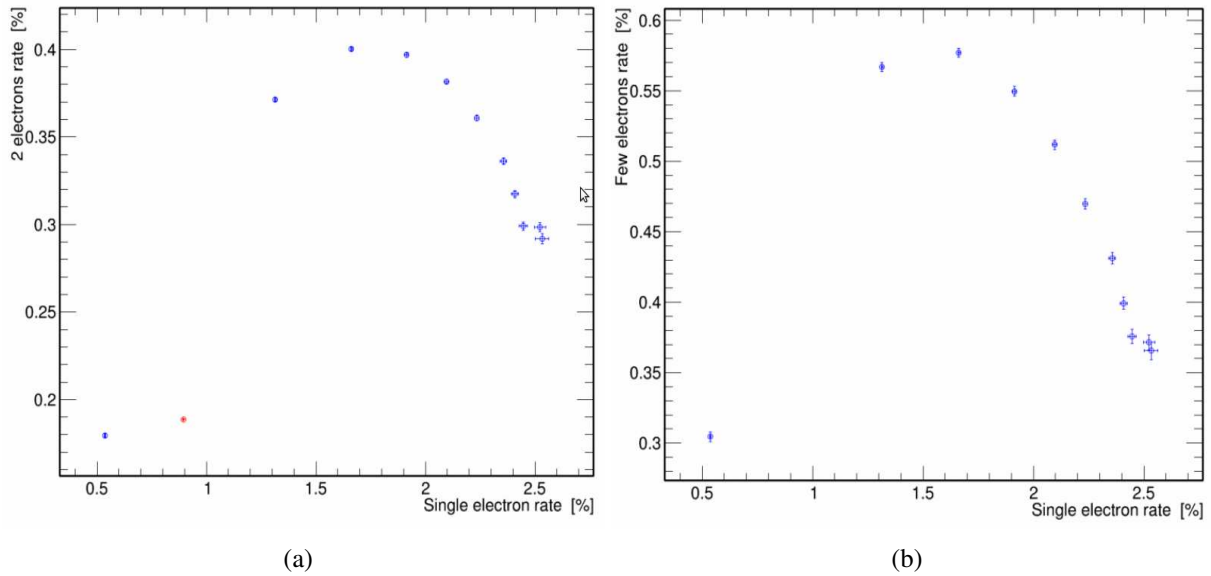


Figure 4.22: Rate of pure single electron signals with respect to signals induced (a) by few individuals electrons extracted in time coincidence in gas phase, and (b) by two individuals electrons extracted in time coincidence in gas phase.

Combined with the observations made from Figure 4.20, this means that the observed decrease of the rate of single electrons is done with respect to much energetic S2 signals. This can be confirmed by investigating the total number of identified S2 signals per waveform for the same datasets, with the same data selection cuts and windows of time delay from the main S2 signal.

A set of spectra of this number of S2 signals for different values of time delay from the main S2 signal is presented in Figure 4.23. The purpose of this analysis is to investigate only the variation of each population of events – events with  $n \in [1 - 2]$ , ...,  $n \in [7 - 8]$ , ...,  $n \in [31 - 32]$  identified S2 signals on the waveform – with respect to the other as a function of the scattering depth. That is why, the several plots on Figure 4.23 have not been rescaled to the same value for the Y-axis.

It is thus illustrated that for the case where S2 signals occur with a short time delay with respect to the main one, as shown in Figure 4.23(a), most of the events have few identified S2 signals per waveform. Due to the considered time window of  $[0 - 16] \mu\text{s}$  as the delay from the main S2 signals, corresponding to a depth between 0 and about 2.7 mm, this means that these events correspond to the combination of Compton scattering and single scatter with most of the emitted photons from the S2 signal that have directly scattered over the grid. In these very rare conditions, the probability of coincidence of several individual electrons extracted in time coincidence in the gas phase is much higher than the extraction of only one or very few individual single electrons in time coincidence. This explains why for short time delay with respect to main S2 signals the proportion of pure single electron signals and signals induced by two individual single electrons seen in Figures 4.21(a) and 4.21(a) is much weaker than for higher time delays.

When increasing the time delay from the main S2 signal, the probability of separation of emission depths for several single electrons is increased, leading to increase both the probability of having pure or few single electrons signals, and the probability of having more S2 signals. This

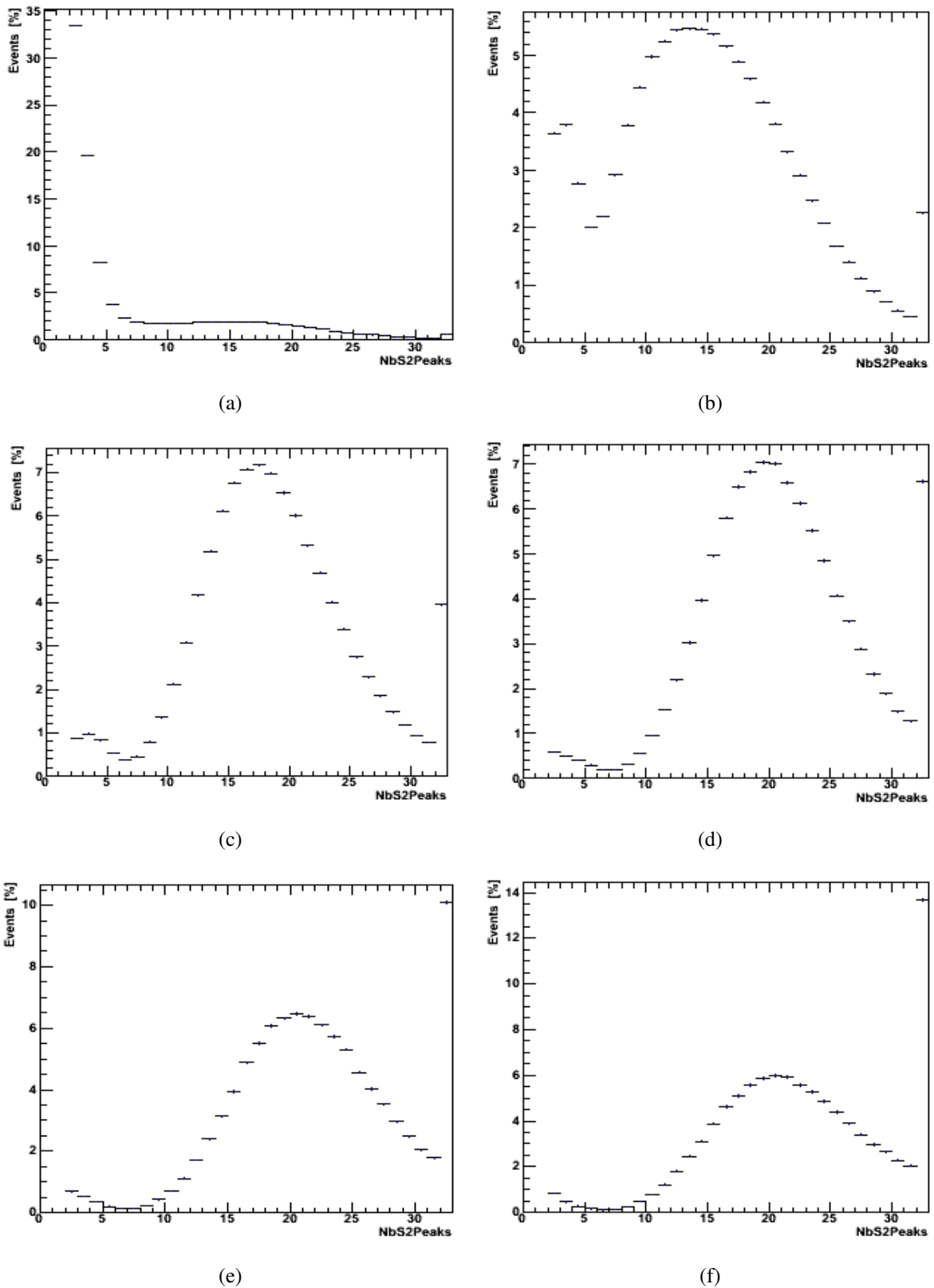


Figure 4.23: Variation of the distribution of identified S2 signals per waveform when increasing the requested time delay window from the main S2 signal. From Figure (a) up to Figure (f), identified S2 signals have a time delay from the main S2 signal included in a time window of [0 - 16], [32 - 48], [64 - 80], [96 - 112], [128 - 144] and [160 - 176]  $\mu\text{s}$  respectively.

can be seen starting from Figure 4.23(b), where the main population of events increases both in terms of number of events and of numbers of signal per events.

However, in parallel to this increase, the last bin of each plot, corresponding to the maximum value (set at 32, assumed to be widely sufficient for dark matter search), starts to be more and more dominant. After a time delay of at least  $96 \mu\text{s}$ , events with 32 identified and recorded S2 signals starts to be the most frequent case. This corresponds to the events that have 32 or more identified S2 signals in the waveform of which only the 32 more energetic ones are effectively recorded. This explains why with the increase of the emission depths, the rate of single electrons signals with respect to higher energies S2 signals decreases. Thus, in order to avoid this case, only events with effectively 31 or less S2 signals will be considered for an unbiased single electron study.

As a conclusion to this section, the set of data selection cuts that will be used for the rest of the work, except when a different one is specified, can be summarized as:

- The main S2 signal intensity should be above 30 kPE, making the fit more stable without reducing too much the statistic.
- Only S2 signals occurring between  $70 \mu\text{s}$  and  $170 \mu\text{s}$  after the main S2 signal will be considered, removing a series of biases on the measurement.
- Only events with 31 or less S2 signals will be considered, to avoid the saturation of peaks.

| Cuts  | Intensity threshold on the main S2 signal [kPE] | Time delay for all the other S2 signals [ $\mu\text{s}$ ] | Maximum number of identified S2 signals per waveform |
|-------|---|---|--|
| Value | 30  | $70 < \Delta t < 170$                                     | 31   |

Table 4.1: Summary of data selection cuts applied for the evaluation of the secondary scintillation gain.

Thanks this set of cuts, the resolution of each single electrons signals population will be improved, allowing a more efficient separation between pure single electrons signals and signals induced by two individuals single electrons in time coincidence in the gas phase, even for low LXe purity, as illustrated by Figure 4.24.

For these spectra, most of the single electrons signals will occurs between few microseconds and few tens of microseconds after the main S2 signals, due to the very low LXe purity. That is why, they correspond to the combination of few datasets taken in similar purity conditions, typically with a concentration of the order of two particles of impurities per billion as  $\text{O}_2$  molecules equivalent. In terms of electron lifetime, this LXe purity is equal to about  $250 \mu\text{s}$ .

## 4.5 Systematic effects in the determination of the gain

As it was presented in Section 4.3.1, the function used for the fit of the low energy part of the S2 spectrum is made by a sum of few Gaussian distributions, usually five, linked together

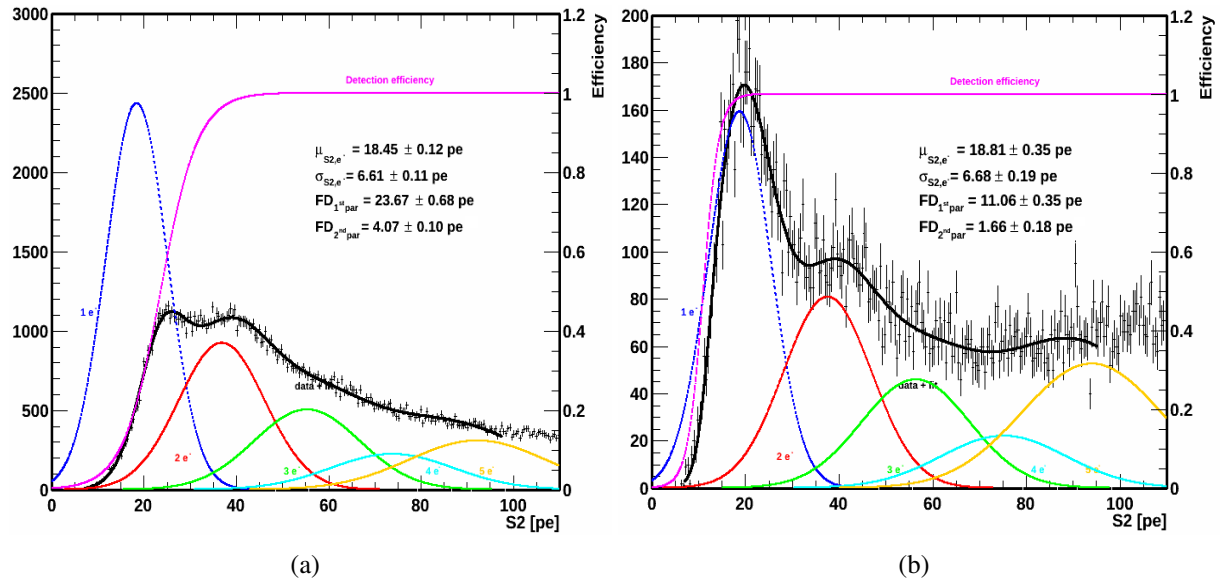


Figure 4.24: Comparison of a low energy S2 spectrum at low LXe purity (a) before and (b) after the addition of a time delay based cut and a restriction on the maximum number of identified S2 signals per waveform. This data have been acquired during the first science run without using any calibration source.

and multiplied by a detection efficiency function. In the different analyses detailed in the present section, the validity of the relationships between all Gaussian distributions will be investigated. For this purpose, all the data taken in stable detector settings during each of the three science runs will be combined, with and without calibration source, in order to take benefits of the very large available statistics from the detector response to single electrons signals.

This analysis is divided in two steps. First, the relationships  $\mu_i = i \times \mu_1$  and  $\sigma_i = \sqrt{i} \times \sigma_1$ , where  $i = 1, 2, 3, \dots, n$ , will be tested by letting each Gaussian distribution free with respect to the first one. This analysis is presented in Section 4.5.2. Then, results will be compared to the case in which Gaussian distributions are constrained, as it will be presented in Section 4.5.3. For both studies, the cuts used are the very same as described in Table 4.1, with a minimum value for the intensity of the main S2 signal that differs from 30 kPE only when it is written.

In addition, the influence of the number of Gaussian distributions used for the fit and the minimum intensity of the main S2 signal will be investigated. The results presented here has been done as a final cross check on the single electrons analysis. That is why they can refer to results that will be presented in the next chapter, or combine data obtained with different sources, since the stability of the results have been demonstrated earlier in time during this analysis, as it will be also presented in Chapter 5.

### 4.5.1 Notations and conventions

Starting from Section 4.5.3, conventions for results presentation and some terminologies used to indicate some special data acquisition runs will be employed:

- Results obtained with one calibration source and combined over the considered science run

are presented independently from others sources. Each of them are thus expressed through a different marker color. A representative set of results is shown in the next section. The same window of values for the secondary scintillation gain between 13.5 PE and 22 PE will be used for all the plots presented in the present and next chapter. They are thus similar to Figure 4.27 in order to ease their comparison.

- The set of events recorded as *Dark Matter* will indicate events in which no radioactive source has been placed close to the detector. It is called in this way because this is clearly the experimental condition to search for a dark matter signal. Since no dark matter signal has been found so far by XENON100 and since in this work any cut that enhance the signal over the background is applied, the totality of these events are coming from well known background, mainly from radioactivity of the detector's components.
- For the second science run, the first run with the  $^{241}\text{Am}^9\text{Be}$  calibration source refers to the NR calibration run for the detector response taken right before starting the regular acquisition of data for dark matter. The second run refers then to a NR calibration run that has been taken right after finishing the second science run, in order to demonstrate the stability of the response of the detector. They will be indicated as  $^{241}\text{Am}^9\text{Be} - \text{first run}$  and  $^{241}\text{Am}^9\text{Be} - \text{second run}$ .

### 4.5.2 Consistency check of the model

In the present section, the relationships  $\mu_i = i \times \mu_1$  and  $\sigma_i = \sqrt{i} \times \sigma_1$ , are tested. Figure 4.25 reports for the second science run both reduced relationships, i.e. in order to be compared to 1, as a function of the number  $i$  of Gaussian distributions used for the fit of the low energy S2 spectrum. Based on the analyses presented in Section 4.3.3, the fit of the spectrum with  $i$  Gaussian distribution is always done from 7 PE up to  $\mu_i$ .

Each point of Figure 4.25(a) and Figure 4.25(b) corresponds to the average value between results from all calibration sources used in the run, including also the case where no calibration source was used, when the fit has been done with  $i$  free Gaussian distributions. The error associated to each point corresponds to the weighted RMS between the results from each calibration source, including datasets without calibration source, in order to take more into account the fluctuation from file acquired with or without calibration source to another one.

Moreover, each color corresponds to a specific cut on the intensity of the main S2 signal. As a result, each colored line corresponds then to the corresponding average value. Basically, an average compatible with 1 would conclude the correctness of the constrained formulas for  $\mu_i$  and  $\sigma_i$ .

Furthermore, by increasing the threshold value on the intensity of the main S2 signal, more and more events, and thus low energy S2 signals, are rejected. As a result, the fits of the spectra can suffer of low statistics starting from a threshold value above 30 kPE. Due to this low statistics, there is a non negligible possibility to get bad quality fits. Thus, for a fix threshold value on the intensity of the main S2 signal, and for a number  $i$  of Gaussian distributions used for the fit, the number of calibration sources that provide a good quality fit results is calculated. This calculation

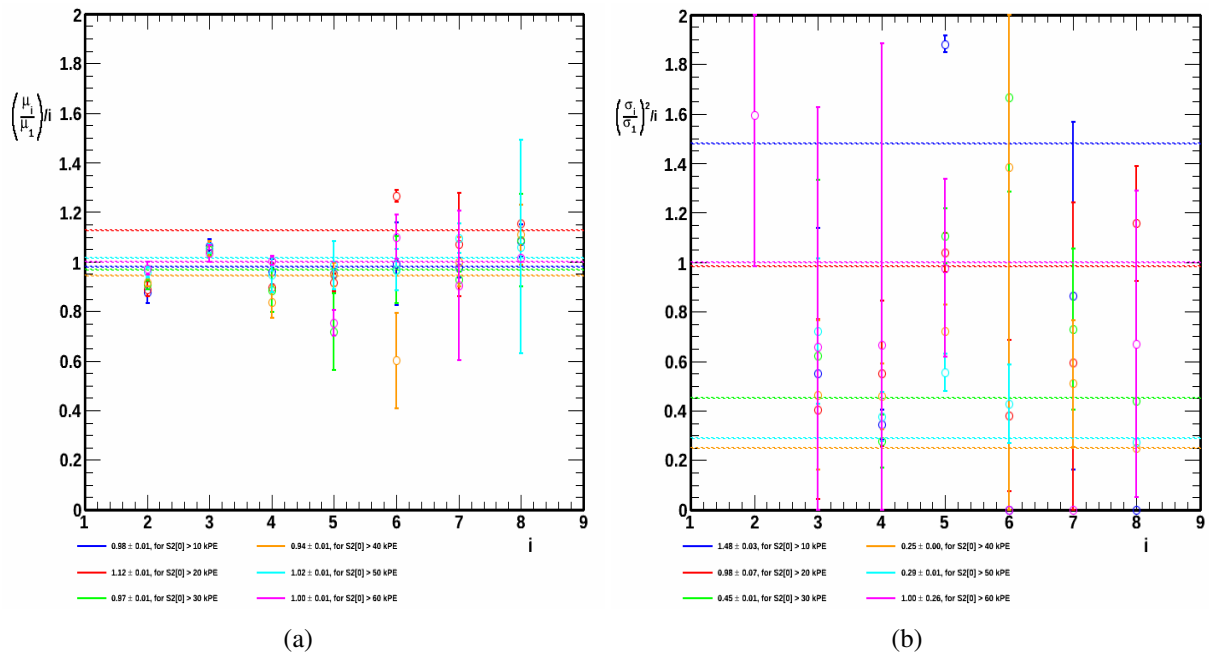


Figure 4.25: Analysis of the reduced relationships between free Gaussian distributions for the fit of the low energies spectra acquired with each calibration sources during the second science run.

includes also the case where no calibration source was used, i.e. datasets used for dark matter search. If less than four spectra, obtained each of them by a specific calibration source, have a good quality fit, then the average value for this data point is artificially set to zero. The purpose of this specific value is simply to be easily excluded and to not bias the average value, i.e. the dashed lines, of the reduced relationship between  $\mu_i$  or  $\sigma_i$  and  $\mu_1$  or  $\sigma_1$  respectively. Since during the first science run, no data were acquired with  $^{232}\text{Th}$  calibration source, this threshold of four spectra is lowered down to three spectra.

Same results have been observed for the first and the third science run. While the trend is clear for the average position of each Gaussian distribution, there are more fluctuations around 1 on the standard deviation results, depending on the S2[0] threshold used. This is mainly due to the free status of each Gaussian distribution that will allow the fit to describe a small fluctuation on the spectrum by a thinner Gaussian distribution than in usual case, and counterbalance with one or more larger Gaussian distributions than what they should be, as it is illustrated on Figure 4.26.

These two spectra correspond to the combination of all the datasets acquired during the second and the third science run respectively, with  $^{137}\text{Cs}$  radioactive calibration source and no calibration source respectively. The former spectrum is fitted by eight Gaussian distributions while only seven are used for the latter spectrum. Due to very small fluctuations on the trend of the spectra, thin Gaussian distributions are respectively used in order to follow the local trend instead of the general one.

As a results of this analysis, the relationships between each Gaussian distribution and the first one have been demonstrated. Moreover, in order to keep the instability of the fit of the low energy S2 spectrum, the position and standard deviation of each Gaussian distribution need to be constrained by the corresponding parameter of the first one.

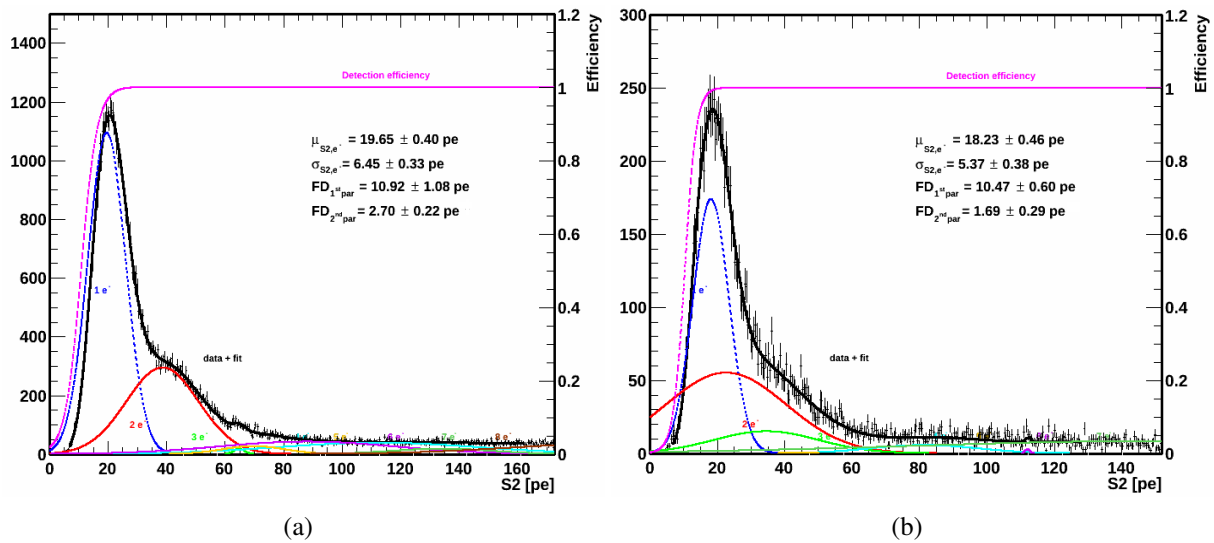


Figure 4.26: Illustration of the influence of very small fluctuations on the fit of low energies S2 spectra by several independent Gaussian distributions making the fit totally wrong: (a) small fluctuation around 65 PE, (b) small fluctuation around 110 PE.

### 4.5.3 Consistency between constrained and unconstrained fits

For the three science runs, the comparison between the results from the two different conditions of the Gaussian distributions used in the fit have been investigated for different numbers of these Gaussian distributions, and for different threshold on the intensity of the main S2 signal. A representative set of these results is shown below. On each of these plots, for a considered calibration source, i.e. a considered marker color, the bottom marker corresponds to results obtained with constrained Gaussian distributions, while the top marker corresponds to results obtained with free Gaussian distributions. The non-existence of data points corresponds to an incoherent fit results regarding either the position of the first Gaussian distribution or its standard deviation. This includes also the associated errors, assuming expected values of the order of few PE up to few tens of PE.

The light blue bands correspond to the optimised values of the gain and the associated error per science run, coming out from the study described in Section 4.5.5. These values are set as reference in order to show how the data points are fluctuating around the final optimised value.

Figure 4.27 demonstrates compatible results within statistical error bars between constrained and not constrained fits. In a lower extend, Figure 4.29 shows the same compatibility for almost all the investigated cases. However, due to the high statistics acquired with most of the sources of the second science run or with the  $^{241}\text{Am}^9\text{Be}$  calibration source during the third one, this compatibility can not be statistically demonstrated. The observed difference is then due to systematic errors that are still remaining even in case of a very high accumulated statistics. These systematic errors are well understood and described starting from Section 4.5.6. For the second and third science run, they are of the order of 0.3 PE and 0.4 PE respectively. Due to a lower accumulated statistics for the first science run, especially with the  $^{60}\text{Co}$  radioactive source, these systematic errors are covered by the statistical ones.

As a results, if this section has shown compatible results between both methods, it is important

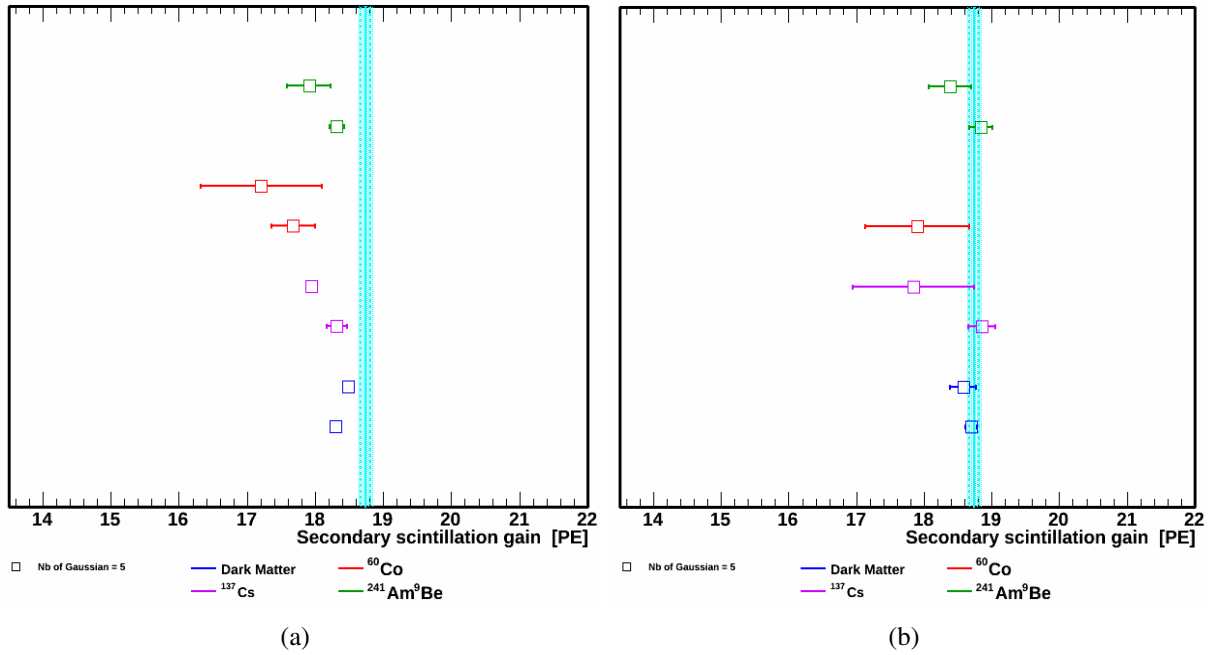


Figure 4.27: First science run. Comparison between results for secondary scintillation gain from fit with five (a) constrained and (b) free Gaussian distributions, for an intensity threshold of 10 kPE and 20 kPE for the main S2 signal respectively.

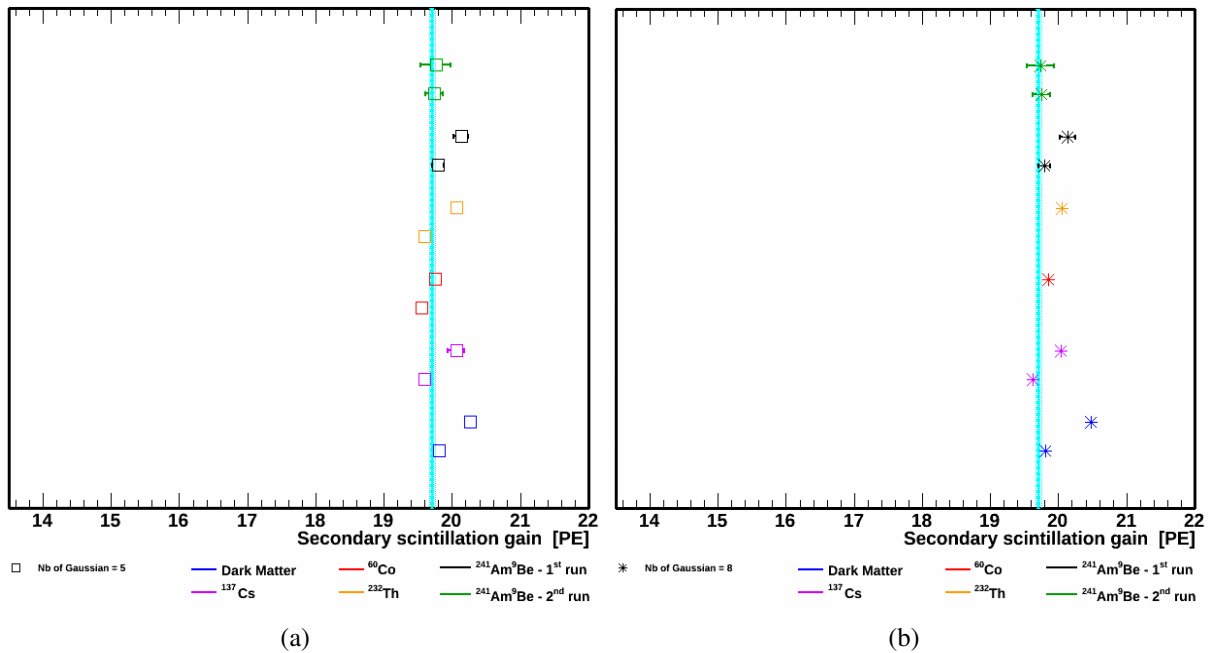


Figure 4.28: Second science run. Comparison between results for secondary scintillation gain from fit with (a) five and (b) eight constrained and free Gaussian distributions, for an intensity threshold of 10 kPE for the main S2 signal.

to notice that the second one, i.e. with free Gaussian distributions, gives much larger errors on parameters. They could sometimes have no-sense, like with  $^{60}\text{Co}$  in the third science run 12 for a main S2 above 20 kPE. That is why it is better to keep the constrained relationship between

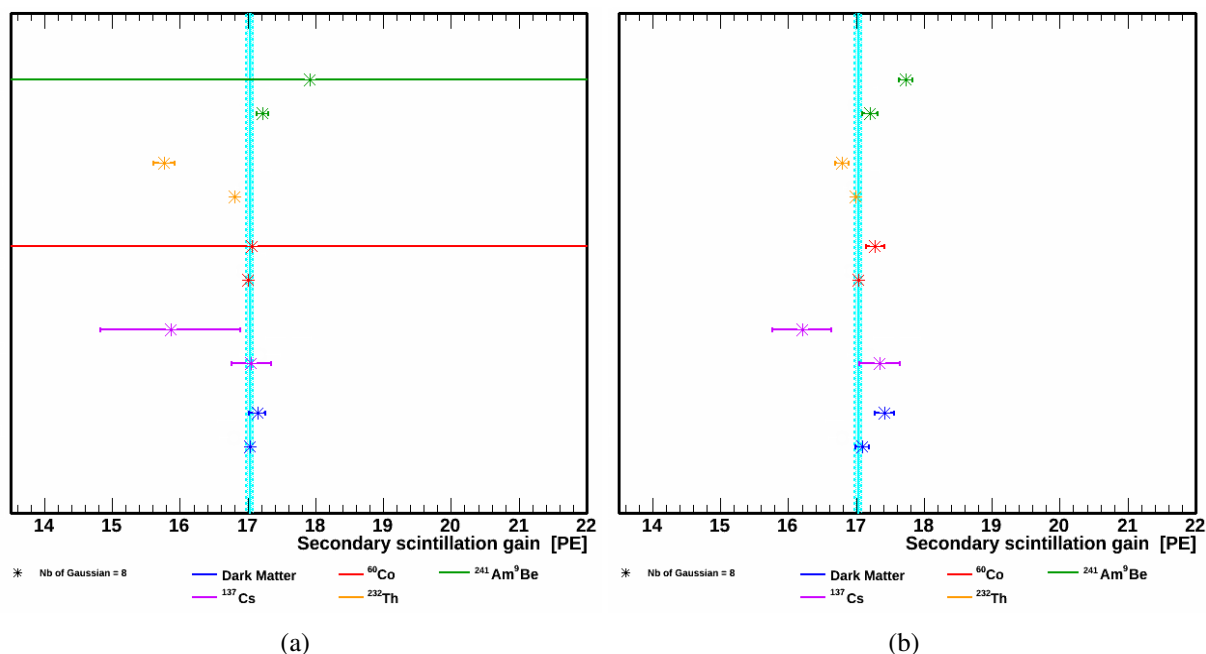


Figure 4.29: Third science run. Comparison between results for secondary scintillation gain from fit with eight (a) constrained and (b) free Gaussian distributions, for an intensity threshold of 20 kPE and 30 kPE for the main S2 signal respectively.

parameters in the fit formula for more accurate results.

Furthermore, it can be observed on Figure 4.27 and Figure 4.29 that the secondary scintillation gain can be slightly different when increasing the requested threshold on the main S2 signal, and thus increasing the proportion of two individual single electrons signals occurring in time coincidence with respect to pure single electrons signals, as it was mentioned previously in this chapter. This is one of the systematic errors that have been studied. The Section 4.5.5 will thus aim to find the best value for the threshold on the intensity of the main S2 signals that will reduce its contribution to all the systematic errors.

#### 4.5.4 Fit stability against number of Gaussian distributions

Before investigating the minimum value of the main S2 signal, it is important to exclude any possible bias from the number of Gaussian distribution used for the fit, that is usually set to five. In agreement with the conclusion presented in the previous section, all of these Gaussian distributions will be constrained by the first one, following the relationships  $\mu_i = i \times \mu_1$  and  $\sigma_i = \sqrt{i} \times \sigma_1$ , where  $i = 1, 2, 3, \dots, n$ . As it was mentioned at the beginning of the Section 4.5.2, the fit is always done from 7 PE up to  $\mu_n$ , where  $\mu_n$  is the average position of the last Gaussian distribution used for the fit.

A set of results for this analysis are presented in Figure 4.30. The combination of all available datasets acquired in stable detector settings during each runs with each calibration source, including the case with no radioactive source (*Dark Matter*), have been investigated separately. The cuts used are very similar to those described in Table 4.1, with however different minimum value for the intensity of the main S2 signal that have been tested.

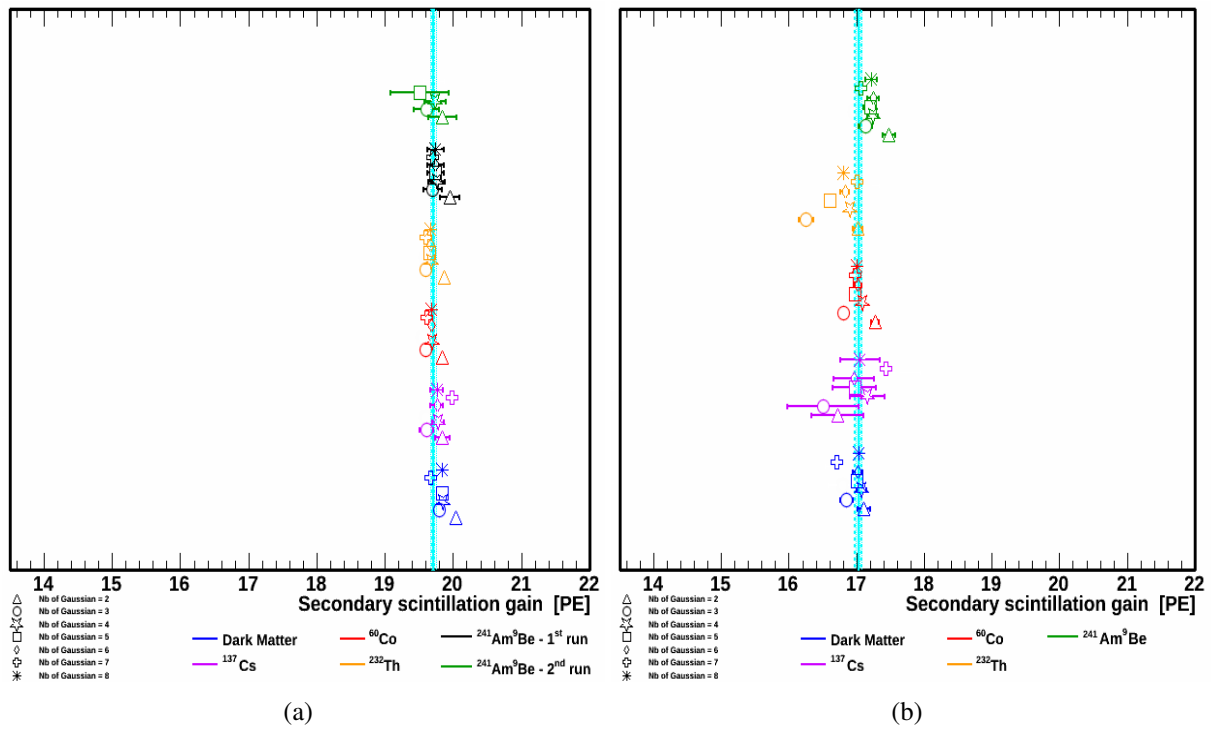


Figure 4.30: Comparison between results for secondary scintillation gain from fit with different numbers of constrained Gaussian distributions, for (a) the second science run and (b) the third science run, for an intensity threshold of 30 kPE and 20 kPE for the main S2 signal respectively.

For each run, for each considered source, i.e. each considered marker color, results for secondary scintillation gain presented on Figure 4.30 from bottom up to top marker correspond to the same spectrum fitted with a sum of  $n$  Gaussian distributions that varies from two up to eight respectively. As mentioned in the previous section, the light blue bands correspond to the optimised values of the gain and the associated error per science run, coming out from the study described in Section 4.5.5, and are set as reference values.

The secondary scintillation gain is then excluded to be biased from missing Gaussian distributions thanks to consistent results between all the values, whatever is the considered source. Same distribution of value for the secondary scintillation gain have been observed for all the three science runs, for different values of the minimum threshold on the main S2 signal. There are however slightly more fluctuations for the first science run, as illustrated by Figure 4.31, due to a lower accumulated statistics, especially for low energy S2 signals delayed by more than  $70 \mu\text{s}$  from the main S2 signal in much lower LXe purity conditions.

As a results, five Gaussian distributions can be kept for the fit of low energies S2 spectra for all the results that will be presented in the rest of this thesis. This corresponds to the maximum number of Gaussian distributions that can be used before suffering from low statistics once only few datasets are combined and analysed together, with respects to an entire run.

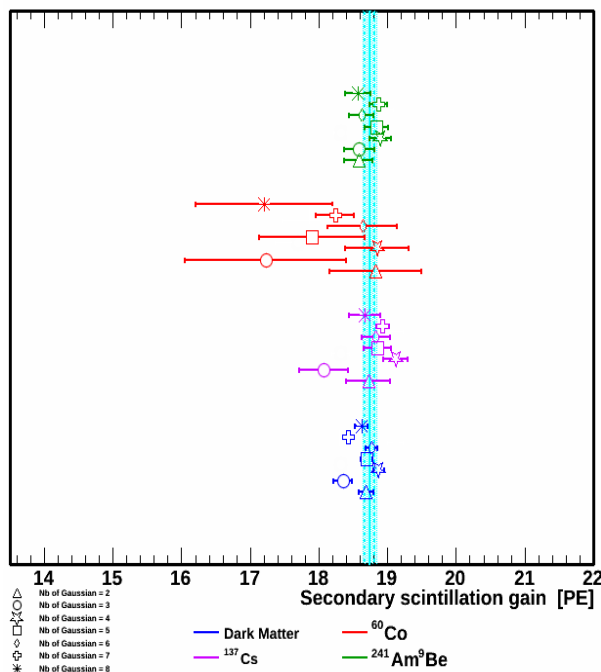


Figure 4.31: Comparison between results for secondary scintillation gain from fit with different numbers of constrained Gaussian distributions, for an intensity threshold of 20 kPE for the main S2 signal, for the first science run.

#### 4.5.5 Fit stability against intensity threshold description

In addition to the number of Gaussian distributions used for the fit, the minimum intensity for the main S2 signal can be also a source of bias on the resolution of the secondary scintillation gain. Indeed, as it was previously observed on Figure 4.27 and Figure 4.29, this gain can slightly change when the minimum threshold on the intensity of the main S2 signal is lowered. Thus, in order to improve the precision of the evaluation of the secondary scintillation per each run for being used as reference values for other analyses on dual phase LXe TPC, the bias should be reduced.

For this purpose, a relevant criteria is needed. It consists then in investigating the stability of the secondary scintillation gain from one source up to another one for fixed value of the minimum intensity for the main S2 signal. This is motivated by the single electrons emission origins, that belong to the ultraviolet photons emitted during the main S2 signal. These source stability of the secondary scintillation gain will be demonstrated in the next chapter, in Section 5.2. The present analysis however uses this property in order to contribute to the demonstration of the full understanding of the systematic errors that are associated to the evaluation of the secondary scintillation gain.

The results of this analysis is presented in Figure 4.32 for the second and third science run. Same results have been observed for the first science run. For each run, for each considered source, results for secondary scintillation gain presented from bottom up to top marker corresponds to the same spectrum fitted with a sum of five constrained Gaussian distributions with a minimum intensity for the main S2 signal that varies from 5 kPE up to 60 kPE, with a step of 5 kPE. As it was mentioned in the Section 4.5.2, starting from 30 kPE the fit can suffer from low statistics.

For each value of the minimum intensity of the main S2 signal, the average value between

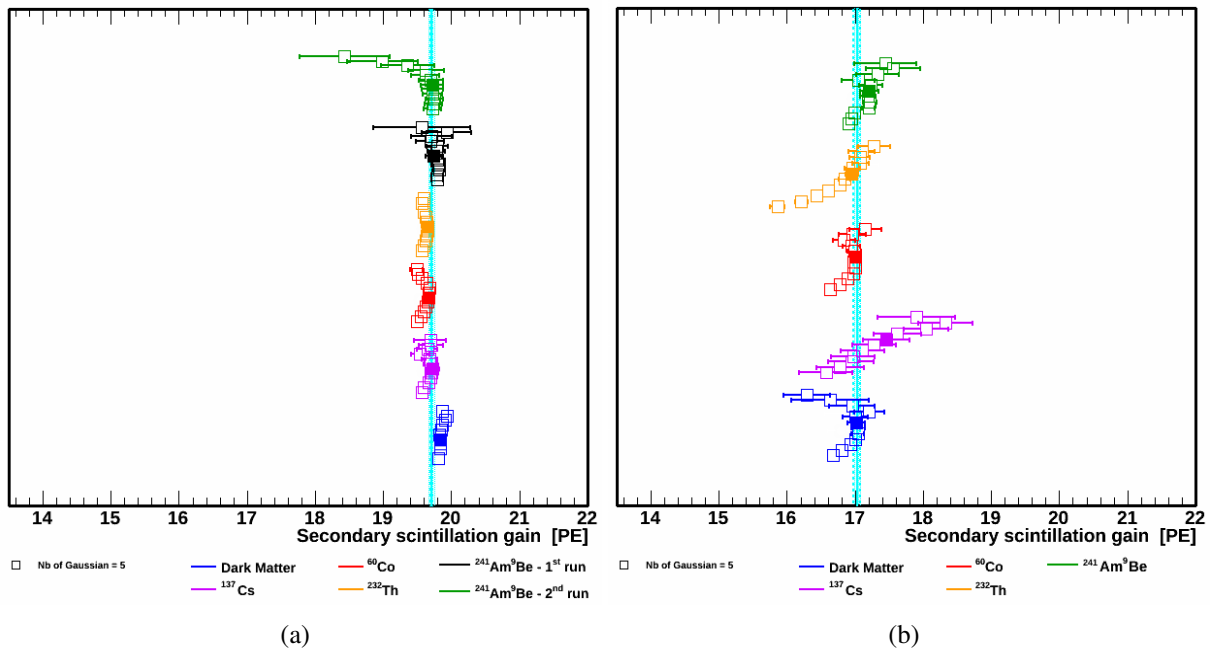


Figure 4.32: Comparison between results for secondary scintillation gain from fit with five constrained Gaussian distributions, varying the low energy cut on the main S2 signal, for (a) the second science run and (b) the third science run. The result is shown from 5 kPE (most bottom marker) up to 60 kPE (most top marker). Filled markers indicate the best value of S2.

secondary scintillation gains measured by each source separately is calculated. In order to take into account the dispersion of these measured gains around this average value, the weighted root mean square is also calculated. Among all the threshold values that provide coherent results from fit for at least four sources (three for the first science run), the associated weighted root mean square are compared together. The configuration of the main S2 signal that provide then the lower value for this weighted root mean is used to calculate the optimised average value of the secondary scintillation gain between all the sources.

This value is illustrated by all the light blue band on Figure 4.32, but also on all the figures that are presented in sections 4.5.3 and 4.5.4. The solid lines in the center of these bands correspond to the average values of the gains, depending on the considered science run, while the associated statistical error is represented by the width of the band from the vertical solid line up to vertical dashed line. These errors are also summarized in Table 4.2.

In the Chapter 5 will be presented a similar analysis, demonstrating the source stability for two more general cases for the minimum value of the intensity of the main S2 signal, typically 10 kPE and 30 kPE, leading to an evaluation of the systematical error associated to the source stability of the secondary scintillation gain. As a result, the value measured per each run during this analysis will be very slightly different to the present ones, with differences of the order of very few cents of PE. They will be however more representative to the general case, while the optimised values calculated here refer to specific case and gives only informations on the statistical errors which belongs to the general values.

The optimised secondary scintillation gains per each source are also identified by solid marker in Figure 4.32, and reported individually on Figure 4.33.

| Science run | Minimum intensity for the main S2 signal [kPE] | statistical error for secondary scintillation gain [PE] |
|-------------|--|---|
| First       | 20   | 0.07  |
| Second      | 30   | 0.02  |
| Third       | 35   | 0.05  |

Table 4.2: Evaluation of the statistical error associated to the secondary scintillation gain per each science run.

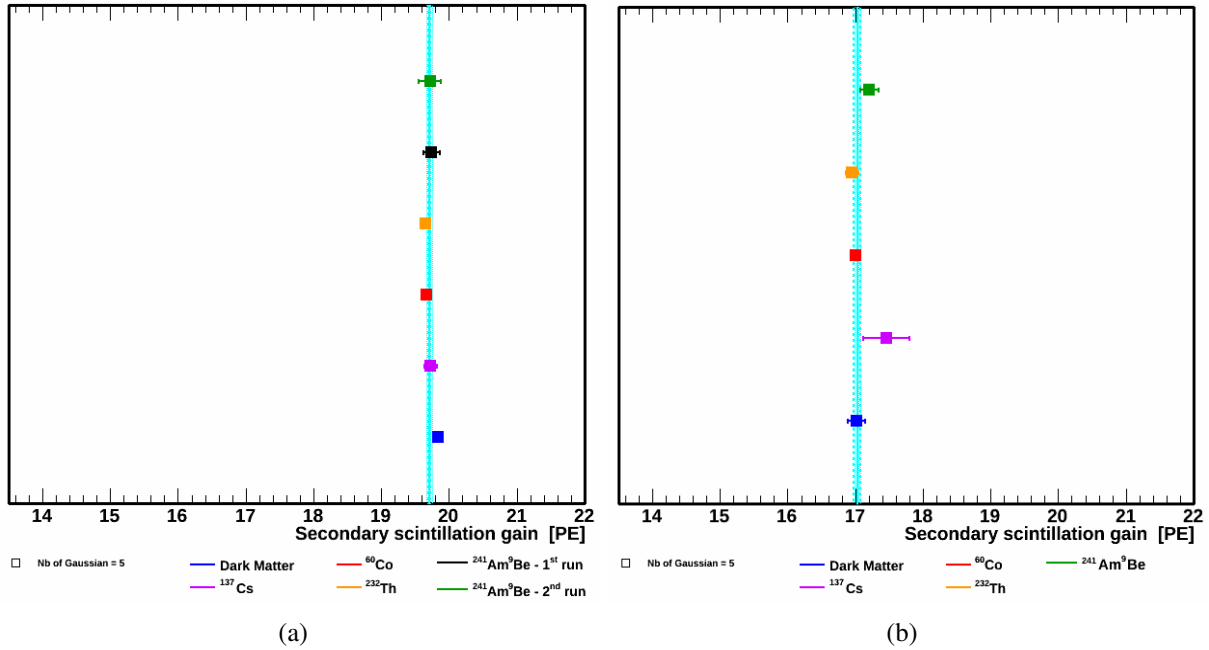


Figure 4.33: Secondary scintillation gain from fit with five constrained Gaussian distributions, for (a) the second science run and (b) the third science run, for an optimised intensity threshold of 30 kPE and 35 kPE for the main S2 signal respectively.

The analysis presented in this section has shown a systematic effect on the evaluation of the secondary scintillation gain with different calibrations sources, that depends from the requested minimum value of the intensity of the main S2 signal. This is however not the only systematic effect suspected to occur. The other factors are:

1. The correlation between the free parameters.
2. The initial choice of the value of free parameters.
3. The lower limit of the energy range in the fit.
4. The upper limit of the energy range in the fit.
5. The systematic error coming from the dependency on the source

Each of them has been separately considered in order to evaluate possible misunderstanding of the fit of low energies S2 spectra.

### 4.5.6 Correlation between the parameters of the fit

The first identified candidate as instability factor consists in the correlation between all the free parameters of the fit that can be wrongly taken into account. In order to investigate the matrix correlation between all the free parameters, all the datasets acquired with the  $^{60}\text{Co}$  radioactive source during the second science run have been combined. The cuts applied in the analysis are the same as those described in Table 4.1. The fit function includes five constrained Gaussian distributions, and is delimited on lower and upper values by boundaries set at 7 PE and  $\mu_5$  respectively. Thanks to an alternative fit routine, *Roofit*, based on probability density function (*pdf*), the correlation matrix can be drawn, as it is represented on Figure 4.34.

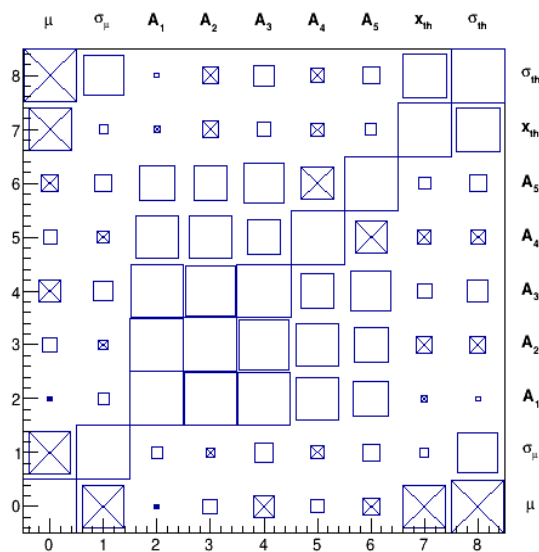


Figure 4.34: Graphical representation of the correlation between the parameters of the fit applied to the low energy S2 spectrum. Negative correlations are marked as crossed.

The position and standard deviation of the first Gaussian distribution correspond to  $\mu$  and  $\sigma_\mu$ , while the  $A_i$  parameters, with  $i = 1, \dots, 5$  correspond to the amplitude of each Gaussian distributions. The remaining parameters,  $x_{th}$  and  $\sigma_{th}$  correspond to the position at half size of the detection efficiency function and its width respectively. The correlation between each parameter is represented by squares, while the anti-correlation are represented by squares with a cross inside. The more the squares are large, the more the correlation or the anti-correlation are strong.

It can be seen that  $\mu_1$  and  $\sigma_1$  are anti-correlated, as expected because of the high sensitivity of the fit to the right side of each Gaussian distribution. As a result, a little increase of the Gaussian distributions at high energies can be compensated by a little decrease of their sigma. In the same way, the secondary scintillation gain  $\mu_1$  is strongly anti-correlated with the two parameters of the Fermi-Dirac. The anti-correlation is expected also in this case since an increase of the position of the first Gaussian distribution requires a decrease of the Fermi-Dirac to lower energies in order to allow the fit of the main peak of the S2 spectrum. The position of the Fermi-Dirac  $x_{th}$  is also strongly correlated with its width  $\sigma_{th}$ , which is expected since the Fermi-Dirac is used as a threshold function for the peak finding algorithm: an ideal algorithm has both parameters equal to

zero, increasing together in a realistic case.

Furthermore, due to the summation of all the Gaussian distributions, all their amplitudes  $A_i$  are correlated to each other, especially the first three of them, in order to continue to draw all the features of the spectrum. For the remaining two, the correlation is weaker because of the very large standard deviation that reduces the importance of each peak. The remaining small correlation between all the  $A_i$  parameters and the others is then very weak, due to the lower importance of these amplitudes with respect to the position and standard deviation of the first Gaussian distribution.

As a conclusion to this analysis, all the correlations among the parameters are well explained, leading to exclude any bias on the evaluation of the secondary scintillation gain due to the fit routine usually used in this work (the usual fit method used in *ROOT*).

#### 4.5.7 Dependency on the initial values of the parameters of the fit

Thanks to the new fit routine, the influence on the parameters initial values on the final value of the secondary scintillation gain can be also investigated. Indeed, for this new routine, no initial advice are mandatory. The results of the main parameters of the fit coming out from the each routine can be thus compared, as it is done in Table 4.3. This leads to the conclusion of very coherent results from both routines. The slope of the detection efficiency function is however very different from one routine to the other one with respect to the statistical error. This is due to a higher instability of this parameter, and corresponds to the major part of its systematic errors. This has however no influence on the evaluation of the secondary scintillation gain, since both methods give the exact same value.

| Fit Parameter | ROOT   |                   | Roofit |                   | Deviation ( $\sigma$ )   |
|---------------|--------|-------------------|--------|-------------------|--------------------------|
|               | Result | statistical error | Result | statistical error |                          |
| $\mu_1$       | 19.81  | 0.03              | 19.81  | 0.03              | 0 (0)                    |
| $\sigma_1$    | 7.000  | 0.007             | 6.974  | 0.009             | $-0.026 \pm 0.010$ (2.2) |
| $x_{th}$      | 12.51  | 0.05              | 12.58  | 0.04              | $0.07 \pm 0.05$ (1.6)    |
| $\sigma_{th}$ | 3.102  | 0.024             | 2.722  | 0.019             | $-0.4 \pm 0.03$ (17)     |

Table 4.3: Comparison of the most relevant parameters between the regular ROOT fit and RooFit

Furthermore, the correlation between parameters observed on Figure 4.34 is also illustrated here, like with the example of the correlation between  $\sigma_1$  and  $\sigma_{th}$ . As a final conclusion on this analysis, neither the choice of the routine nor the initial set of parameters' advices have influence on the evaluation of the secondary scintillation gain.

#### 4.5.8 Fit stability against lower boundary of the energy range

Up to the present section, the lower boundary of the fit was set at 7 PE, due to possible small perturbations on the low energy S2 spectrum. As an illustration of these small perturbations,

usually called *hotspots*, Figure 4.35(a) shows the (x,y) position of each of the S2 signals below 30 PE that were included in the spectrum presented previously in Figure 4.13(b). The spacial position of the perturbation of this spectrum at an energy of the order of 5-10 PE is clearly visible on the top left part of the detector. This is confirmed by restricting the data selection to only S2 signals that have an intensity between 5 and 10 PE, such as it is presented in Figure 4.35(b). In order to ease the comparison, the maximum of color scale is kept constant between the two plots.

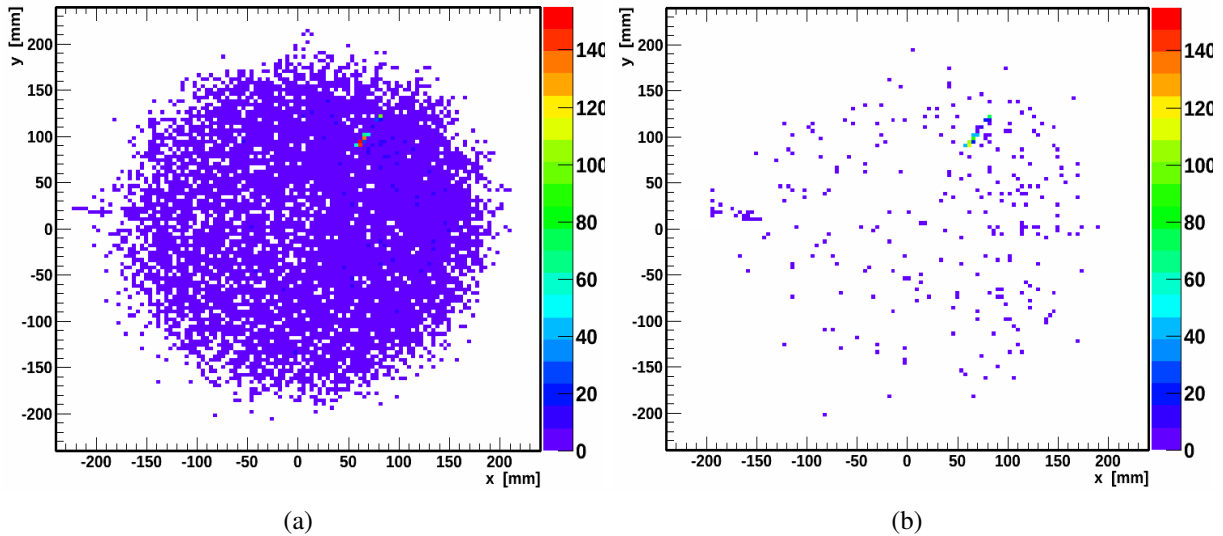


Figure 4.35: Position of the perturbation at low energy, for (a) S2 signals below 30 PE and (b) S2 signals between 5 and 10 PE. Number of events per bin are represented by a color scale. The perturbation is placed on the top right region, with  $x \in [50 - 100]$  mm and  $y \in [75 - 125]$  mm.

Since these very low energy S2 signals are noisy signals, randomly distributed during an entire science run, then their contribution to the cumulated spectrum is strongly reduced with respect to standard signals when many dataset are combined. It is thus mandatory to evaluate the systematic error on the evaluation of the secondary scintillation gain due to the choice of the lower boundary of the fit for spectra with strongly reduced low energies perturbations.

For this purpose, the same combination of data from  $^{60}\text{Co}$  is considered, applying the quality cuts defined in Table 4.1. Different starting values for the fit of the spectrum are then tested. For each of them, the value of the secondary scintillation gain  $\mu_1$ , the standard deviation of the first Gaussian distribution  $\sigma_1$  and the reduced  $\chi^2$  of the quality of the fit are reported on Figure 4.36. The vertical dashed line illustrates the 7 PE position.

This analysis shows a quite stable region of the fit results for a value of lower boundary between 6 PE and 10 PE, which includes thus the original value of 7 PE. The variation observed in this region corresponds to systematic effect due to the choice of this lower boundary, while the observed variation outside this region corresponds to the decrease of the fit quality. The systematic error on the choice of the lower boundary of the fit is then 0.13 PE for  $\mu_1$  and 0.007 PE for  $\sigma_1$ .

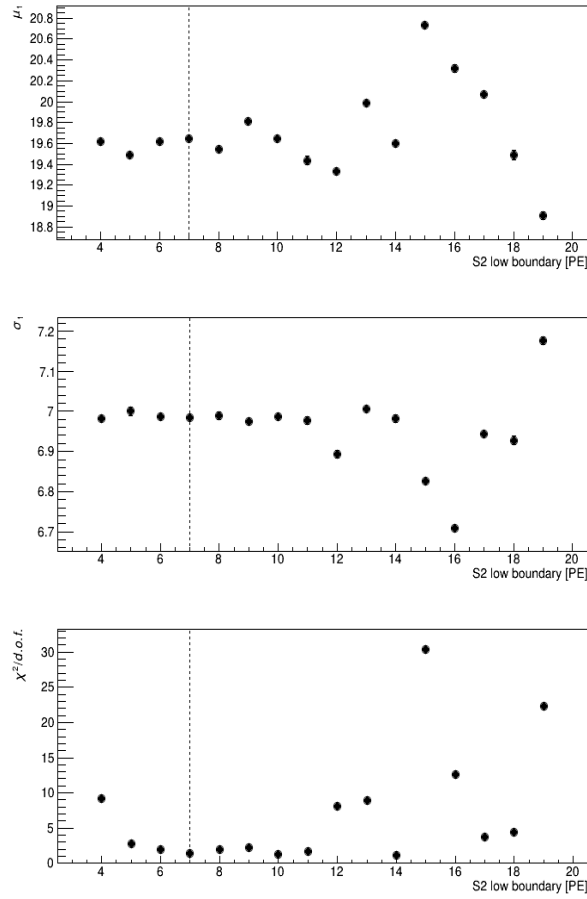


Figure 4.36: Variation of the secondary scintillation gain  $\mu_1$ , the standard deviation of the first Gaussian distribution  $\sigma_1$  and the reduced  $\chi^2$  as a function of the lower boundary of the spectrum fit.

#### 4.5.9 Fit stability against upper boundary of the energy range

In a similar way to the previous analysis, the systematic error on the choice of the upper boundary of the fit can be analysed. Indeed, thanks to the study presented in Section 4.5.4 on the evaluation of the secondary scintillation gain with different number of Gaussian distributions, following the optimised threshold values for the main S2 signals calculated in Section 4.5.5, then for each source the weighted standard deviation of the secondary scintillation gain due to the different numbers of Gaussian distributions can be calculated. Per each science run, the final systematical error on the evaluation of the secondary scintillation gain due to the choice of the upper boundary of the fit corresponds to the average value of these deviations among all available sources. The results are reported in the Table 4.4.

The present analysis has been extended to each science run since the behaviour of the spectra close to 100 PE depends from detector settings and LXe purity. On the contrary, the perturbations on the very low energy part occur randomly during each science run, meaning that the associated systematical error is almost constant along the runs.

| Science run   | Minimum intensity for the main S2 signal [kPE] | Systematical error for secondary scintillation gain [PE] |
|---------------|--|--|
| <b>First</b>  | 20   | 0.18   |
| <b>Second</b> | 30   | 0.07   |
| <b>Third</b>  | 35   | 0.10   |

Table 4.4: Evaluation of the systematical error per each science run due to the upper bound of the fit for the estimation of the secondary scintillation gain.

#### 4.5.10 Fit stability against main S2 signal intensity threshold

The last identified potential source of systematical effect corresponds to the choice of the value of the minimum intensity of the main S2 signal. The associated systematical error will be presented in Section 5.2, when the invariance of the gain from one source up to another one will be investigated. The corresponding results are however reported here in Table 4.5 that summarized all the contributions to systematical errors on the evaluation of the secondary scintillation gain.

| Systematical Errors [PE] | Science run |            |            |
|--------------------------|-------------|------------|------------|
|                          | First       | Second     | Third      |
| <b>Lower boundary</b>    | 0.13        | 0.13       | 0.13       |
| <b>Upper boundary</b>    | 0.18        | 0.07       | 0.10       |
| <b>Source dependency</b> | 0.7         | 0.2        | 0.4        |
| <b>Total</b>             | <b>0.7</b>  | <b>0.3</b> | <b>0.4</b> |

Table 4.5: Summary of the systematical errors associated to the secondary scintillation gain per each science run.

Due to the difference between systematical errors from source dependency and from either lower boundary or upper boundary of the fit, for the first and third science runs, only the contribution to the former is considered for the total systematical error, since it already includes the contribution of the two others. This is also the case for the second science run with the contribution to the upper boundary of the fit that is already included in the combination of the two others.

Based on the analyses presented in this chapter, it can be concluded that the low energy S2 spectrum is fully understood. Thanks to this, the secondary scintillation gain can be used for the characterisation of the response to low energies S2 signals of the XENON100 detector, as it will be presented in the next chapter.

## Conclusion

The observation of single electrons charge signals by the XENON100 detector was presented in this chapter. This analysis takes place in the context of the dark matter search, where the full understanding of the detector response is mandatory, even down to very low energy signals, in order to exclude all possible sources of background.

Results presented here have shown the establishment of specific data selection cuts for the evaluation of the secondary scintillation gain, and demonstrated the full knowledge of all contri-

bution to the systematical effects that can affect this evaluation. This allows to extend the analysis to detector settings that are different from the ones of each sciences run. These additional detector settings corresponds to the acquisition of several calibration datasets between and during each science runs, for the detector settings optimisation and maintenance.

As a results, there are much less experimental data for each detector settings configuration, since the analyses of these datasets, and especially the specific analysis on single electrons signal is not the original purpose of the XENON100 direct dark matter search. The fit of low energy S2 spectra from these datasets will be thus naturally less stable due to lower data statistics, and requests then all the optimisation that were detailed in the present chapter.

Thanks to these additional calibration data, the variation of the secondary scintillation gain as a function of the electric field in the gas phase will be presented in the next chapter. This analysis will then allow to evaluate the proportion of electrons from the main electronic cloud that is extracted from the liquid to the gas phase as a function of a given detector settings. It will also help to define for current and future xenon dual-phase TPCs the detector settings for having an electronic extraction close to 100 %.

# Chapter 5

## Secondary scintillation gain of single electron signals

The stability in time and the average values per science run of the secondary scintillation gain, and of some other main parameters of the fit of the low energy S2 spectrum are presented. The analysis is then extended to the investigation of the dependency of the gain on the electric field in the gas phase. An additional study of the part of the light from S2 signal seen by the bottom PMTs array is also performed in order to draw the dependency of the electrons extraction yield on the electric field. This last chapter is then ended by a set of several single electron applications, including the impact of the dark matter search.

### Contents

---

|  |            |
|--|------------|
| <b>Introduction</b>  | <b>163</b> |
| <b>5.1 Time stability</b>  | <b>164</b> |
| <b>5.2 Dependency on the calibration source</b>  | <b>167</b> |
| <b>5.3 Single electrons signals occurring between the main S1 and S2 signals</b>             | <b>170</b> |
| <b>5.4 Dependency on the electric field</b>  | <b>174</b> |
| <b>5.5 S2 signal repartition over top and bottom PMTs arrays</b>                             | <b>183</b> |
| <b>5.6 Outcome of the analysis: electrons extraction yield</b>                               | <b>187</b> |
| <b>5.7 Outcome of the analysis: from S1 and S2 to drifting electrons and emitted photons</b> | <b>193</b> |
| <b>5.8 Applications and perspectives</b>   | <b>195</b> |
| <b>Conclusion</b>  | <b>203</b> |

---

### Introduction

The demonstration of the observation of single electron signals and of the full understanding of the uncertainties associated to the corresponding gain have been done in the previous chapter.

Thanks to this accurate knowledge, the secondary scintillation gain and the associated distribution per each science run can be calculated by taking advantage of the high available data statistic.

For this purpose, the feasibility of the combination of all the data acquired in stable detector settings with the same source is firstly demonstrated by analysing the stability in time of the secondary scintillation gain measured for each of the datasets from the same exposure. This analysis is also extended to some other main parameters of the low energy S2 spectra. The average final results per science run are then provided. A similar analysis is also performed on single electrons signals occurring between the main S1 and S2 signals.

Thanks to the knowledges on single electrons signals acquired during all previous analyses, the variation of the secondary scintillation gain with the different electric field settings in the gas phase is then investigated, including the analysis of a dedicated calibration campaign. These results are then compared with the corresponding intensity per unit of deposited energy of S2 signals for scatterings occurring close to the liquid surface. Such analysis provides the dependency of the electrons extraction yield from the liquid to the gas phase on the gaseous electric field. The comparison between these two quantities involving different combination of PMTs and expressed in different unit requests the development of a specific algorithm for data selection for the evaluation of the part of the light from S2 signals seen by each PMTs array. An outcome of this analysis is the measure of the average energy needed for the creation of an electron-ion pair in the liquid phase under the usual XENON100 drift field settings, and which is able to strengthen the knowledges on xenon as detector medium.

A review of several identified applications of single electrons signals for dual-phase TPC completes then this study of the single electron charge signals in the XENON100 direct dark matter search experiment. It includes examples with the XENON100 experiment and a discussion on single electrons signals as a possible additional background source for dark matter search.

## 5.1 Time stability

As it was presented in the previous chapter, the study of low energies S2 signals allows to access to a very high statistics for the evaluation of the secondary scintillation gain. This high accumulated statistics is firstly observed on each set of data, since for each recorded event few single electrons events can be identified on the same waveform. It is then also observed by combining together all the data taken in the same detector settings.

Thanks to the very high calibration statistics taken with each radioactive source per each science run, especially during the second one, a precise analysis with almost no statistical errors on the secondary scintillation gain can be performed. This required then a detailed study of all possible source of statistical errors, which have been presented in Section 4.5. In this context, the stability of the secondary scintillation gain from one radioactive source to another one, and with or without calibration source will be analysed, as it will be detailed in the next section. However, since this analysis aims to combine the full available data acquired with each calibration source in stable detector settings, the stability of the secondary scintillation gain needs to be firstly demonstrated.

For this purpose, the variation of the main parameters of the formula used for the low energy S2

spectra fit – namely the average value and the standard deviation of the first Gaussian distribution  $FD1$  – and the position at half-size of the threshold function, during each science run, and per each calibration source have been investigated. This analysis includes also the case where no radioactive calibration source is employed. For this specific section, the width of the threshold function  $FD2$  is not analysed. This is motivated by the aim of this study to demonstrate only the stability in time of the main fit parameters, and thus the stability in time of the secondary scintillation gain, without providing final average values per each science run. These latter will be given in the next section, when the results from each calibration source will be compared. As it have been seen in the previous chapter, this parameter is less stable and relevant for the fit of the spectrum than the three others presented here. That is why it is not investigated here.

The data selections cuts used here are similar to the cuts presented in Table 4.3, with a threshold value of the intensity of the main S2 signal set at 10 kPE. The purpose of this choice is to increase the statistics per each spectrum, since each dataset is individually treated. The analysis is done on the data from each science run, corresponding to the analysis of short time periods (NR calibration files) and long time period (ER calibration and dark matter files). The extension of the analysis to each science run instead of focussing to only one is to investigate different detector settings in order to improve the knowledges of the detector response to low energy S2 signal for different detector settings, and exclude any bias from this energy region for the dark matter search.

Representative plots demonstrating the stability in time of both the secondary scintillation gain and the standard deviation of its distribution are represented in Figure 5.1. They correspond to  $^{232}\text{Th}$  ER calibration data acquired during the second science run (left plot), and to  $^{241}\text{Am}^9\text{Be}$  NR calibration data acquired during the third science run (right plot). The average value of each distribution is represented by a red line, with the associated deviation represented by red dashed lines. Their values are also reported on top of each plot. Due to the very low value of these deviations coming from the high quantity of analysed datasets, they are hardly visible in this figure. It is then preferable to show also the weighted deviations that takes into account the standard deviation of the distributions, represented by orange dashed lines.

The stability in time of the fit parameters, has been observed for the three parameters, for the three science runs, with or without calibration sources. Higher statistical fluctuations have been observed on datasets acquired with  $^{137}\text{Cs}$  calibration, due to a number of recorded events per datasets about ten times lower than in the usual  $^{60}\text{Co}$  and  $^{232}\text{Th}$  files. In a lesser extent, some fluctuations have also been observed for the position at half-size of the threshold function, simply due to its higher dependency on small perturbations on the lower energy part of low statistics spectra with respect to the other parameters. Indeed, thanks to the fit improvements detailed in Section 4.3.3, their instability are strongly reduced. An illustration of these fluctuations for the two cases is done on Figure 5.2. In order to allow the comparison with Figure 5.1(a), these two plots correspond to the second science run. Furthermore, Figure 5.2(b) shows the evolution of the position at half-size of the threshold function for the very same datasets acquired with  $^{232}\text{Th}$  calibration source than Figure 5.1(a).

All the results for the average values of the three parameters from each source and per each science run are summarized from Table 5.1 up to Table 5.3. For comparison, the results from the fit of the combination of all the spectra per each source and per each science run are also detailed,

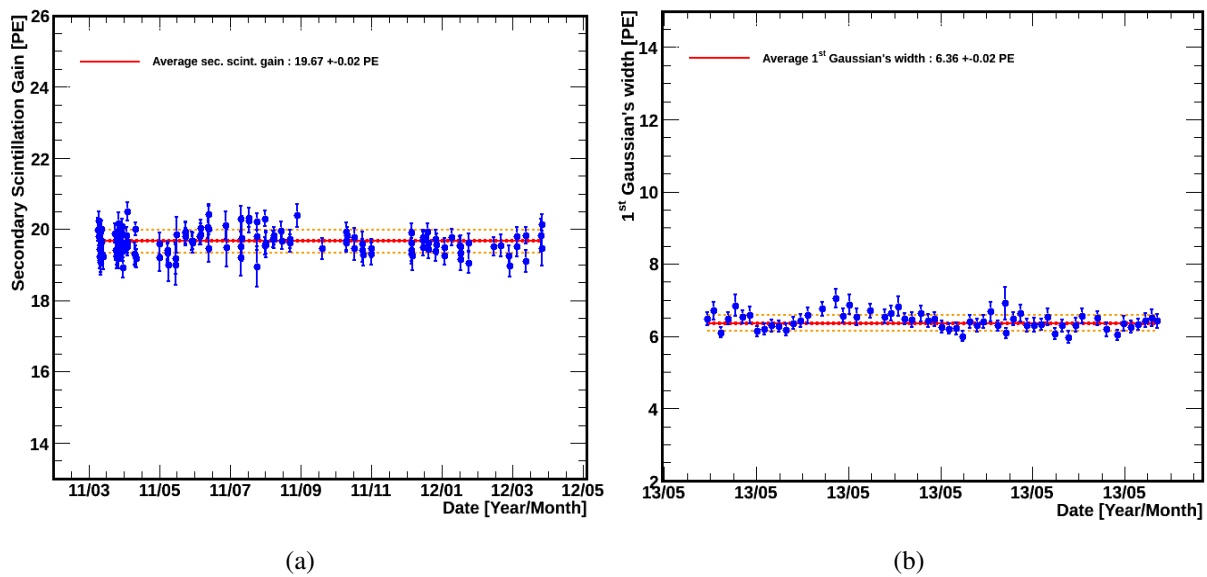


Figure 5.1: Demonstration of the stability in time of the fit parameters: (a) average value of the first Gaussian distribution from  $^{232}\text{Th}$  calibration data acquired during the second science run, published in [157], and (b) standard deviation of the first Gaussian distribution from  $^{241}\text{Am}^9\text{Be}$  calibration data acquired during the third science run.

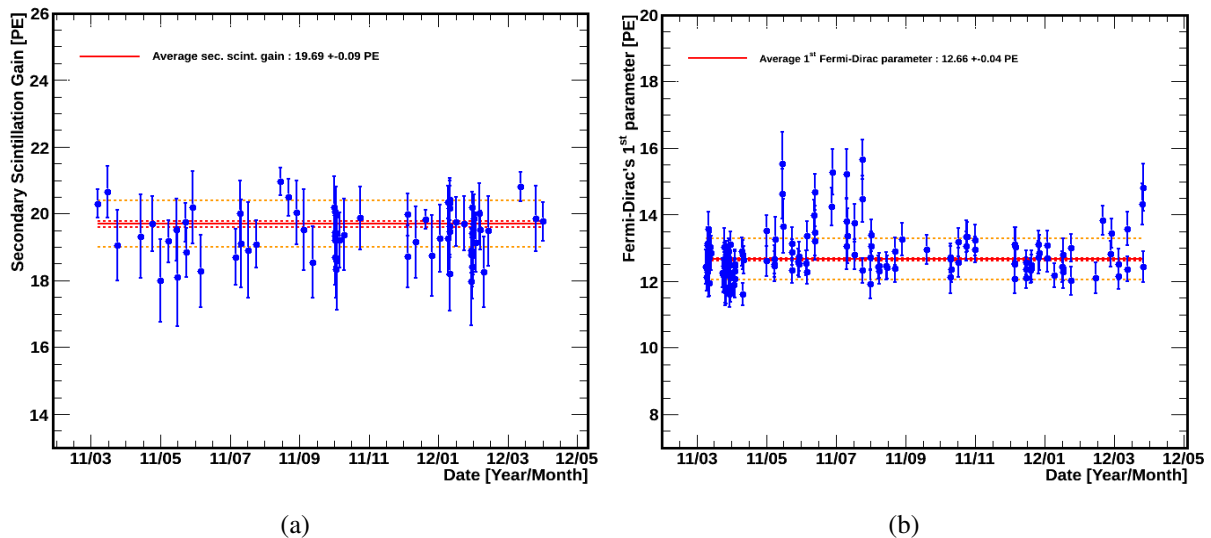


Figure 5.2: Illustration of small fluctuations of the stability in time of the fit parameters: (a) average value of the first Gaussian distribution from  $^{137}\text{Cs}$  calibration data, and (b) position at half-size of the threshold function ( $FD1$ ) from  $^{232}\text{Th}$  calibration. Both pictures correspond to data acquired during the second science run.

using the very same quality cuts than for the study of the stability in time. The purpose of this illustration is to demonstrate through the average value of the stability in time for spectra with low statistics the capability of the fit to reach values of secondary scintillation gain in good agreement with results from spectra with an enough large number of entries to exclude almost all statistical errors.

The errors reported on each of these three tables correspond to statistical errors. The weighted

| Source                            | $\mu_1$ [PE]<br><i>Average</i> | $\mu_1$ [PE]<br><i>Sum</i> | $\sigma_1$ [PE]<br><i>Average</i> | $\sigma_1$ [PE]<br><i>Sum</i> | FD <sub>1</sub> [PE]<br><i>Average</i> | FD <sub>1</sub> [PE]<br><i>Sum</i> |
|-----------------------------------|--------------------------------|----------------------------|-----------------------------------|-------------------------------|--|------------------------------------|
| <b>Dark Matter</b>                | 18.61 ± 0.04<br>(0.51)         | 18.31 ± 0.06               | 6.37 ± 0.02<br>(0.25)             | 6.51 ± 0.02                   | 10.19 ± 0.07<br>(0.98)                 | 10.60 ± 0.09                       |
| <sup>137</sup> Cs                 | 18.75 ± 0.11<br>(0.59)         | 18.32 ± 0.14               | 6.40 ± 0.06<br>(0.30)             | 6.71 ± 0.06                   | 9.84 ± 0.17<br>(1.40)                  | 11.06 ± 0.25                       |
| <sup>60</sup> Co                  | 18.58 ± 0.22<br>(0.47)         | 17.69 ± 0.32               | 6.03 ± 0.11<br>(0.49)             | 6.35 ± 0.10                   | 10.35 ± 0.48<br>(1.01)                 | 11.05 ± 0.58                       |
| <sup>241</sup> Am <sup>9</sup> Be | 18.30 ± 0.10<br>(0.33)         | 18.32 ± 0.10               | 6.13 ± 0.07<br>(0.40)             | 6.19 ± 0.07                   | 9.81 ± 0.17<br>(0.84)                  | 9.42 ± 0.19                        |

Table 5.1: First science run: average values of the main parameters of the fit from the study of the stability in time and comparison with the result from the fit of summed spectra. The weighted standard deviations are also reported between parentheses for the result from time distributions.

| Source   | $\mu_1$ [PE]<br><i>Average</i> | $\mu_1$ [PE]<br><i>Sum</i> | $\sigma_1$ [PE]<br><i>Average</i> | $\sigma_1$ [PE]<br><i>Sum</i> | FD <sub>1</sub> [PE]<br><i>Average</i> | FD <sub>1</sub> [PE]<br><i>Sum</i> |
|--|--------------------------------|----------------------------|-----------------------------------|-------------------------------|--|------------------------------------|
| <b>Dark Matter</b>   | 19.86 ± 0.05<br>(0.52)         | 19.81 ± 0.02               | 6.89 ± 0.02<br>(0.26)             | 6.89 ± 0.01                   | 12.85 ± 0.07<br>(0.87)                 | 12.65 ± 0.04                       |
| <sup>137</sup> Cs  | 19.69 ± 0.09<br>(0.70)         | 19.59 ± 0.08               | 6.84 ± 0.04<br>(0.33)             | 6.91 ± 0.03                   | 12.78 ± 0.13<br>(1.15)                 | 12.41 ± 0.13                       |
| <sup>60</sup> Co   | 19.74 ± 0.03<br>(0.33)         | 19.55 ± 0.02               | 6.97 ± 0.01<br>(0.22)             | 7.03 ± 0.01                   | 12.82 ± 0.04<br>(0.74)                 | 13.08 ± 0.04                       |
| <sup>232</sup> Th  | 19.67 ± 0.02<br>(0.32)         | 19.59 ± 0.02               | 6.92 ± 0.01<br>(0.18)             | 6.97 ± 0.01                   | 12.66 ± 0.04<br>(0.62)                 | 12.76 ± 0.03                       |
| <sup>241</sup> Am <sup>9</sup> Be<br><b>1<sup>st</sup> Run</b> | 19.87 ± 0.11<br>(0.40)         | 19.80 ± 0.09               | 6.60 ± 0.04<br>(0.17)             | 6.62 ± 0.03                   | 12.19 ± 0.20<br>(0.71)                 | 12.13 ± 0.15                       |
| <sup>241</sup> Am <sup>9</sup> Be<br><b>2<sup>nd</sup> Run</b> | 19.98 ± 0.13<br>(0.57)         | 19.74 ± 0.13               | 7.08 ± 0.05<br>(0.22)             | 7.23 ± 0.04                   | 12.90 ± 0.22<br>(0.80)                 | 13.18 ± 0.19                       |

Table 5.2: Second science run: average values of the main parameters of the fit from the study of the stability in time and comparison with the result from the fit of summed spectra. The weighted standard deviations are also reported between parentheses for the result from time distributions.

standard deviations are also reported between parentheses for the result from time distributions. The comparison between the value from the average of the time distributions and the sum of all the datasets leads to very consistent results. The disagreement between small errors on results from both fit methods is due to the consideration of only statistical errors. By taking into account the weighted standard deviations, the agreement between both results is demonstrated.

## 5.2 Dependency on the calibration source

Thanks to the demonstration of the stability in time of the fit parameters, all the data files per each calibration source, including the case with no source, and per each science run can be combined. This will allow to demonstrate the stability of the gain from each source, and to evaluate the average value of the secondary scintillation gain per each of these runs. In the

| Source                       | $\mu_1$ [PE]<br><i>Average</i> | $\mu_1$ [PE]<br><i>Sum</i> | $\sigma_1$ [PE]<br><i>Average</i> | $\sigma_1$ [PE]<br><i>Sum</i> | $FD_1$ [PE]<br><i>Average</i> | $FD_1$ [PE]<br><i>Sum</i> |
|------------------------------|--------------------------------|----------------------------|-----------------------------------|-------------------------------|-------------------------------|---------------------------|
| <b>Dark Matter</b>           | $17.40 \pm 0.12$<br>(0.53)     | $16.79 \pm 0.20$           | $6.32 \pm 0.05$<br>(0.26)         | $6.54 \pm 0.06$               | $10.64 \pm 0.19$<br>(1.00)    | $11.64 \pm 0.30$          |
| $^{137}\text{Cs}$            | $17.21 \pm 0.28$<br>(0.52)     | $17.18 \pm 0.31$           | $6.41 \pm 0.11$<br>(0.39)         | $6.60 \pm 0.11$               | $10.95 \pm 0.37$<br>(1.19)    | $10.76 \pm 0.46$          |
| $^{60}\text{Co}$             | $17.22 \pm 0.08$<br>(0.41)     | $16.92 \pm 0.09$           | $6.33 \pm 0.03$<br>(0.24)         | $6.45 \pm 0.03$               | $10.68 \pm 0.12$<br>(0.72)    | $10.97 \pm 0.13$          |
| $^{232}\text{Th}$            | $17.12 \pm 0.12$<br>(0.46)     | $16.95 \pm 0.13$           | $6.41 \pm 0.04$<br>(0.25)         | $6.51 \pm 0.04$               | $10.74 \pm 0.19$<br>(0.92)    | $10.96 \pm 0.21$          |
| $^{241}\text{Am}^9\text{Be}$ | $17.15 \pm 0.06$<br>(0.54)     | $16.98 \pm 0.07$           | $6.36 \pm 0.02$<br>(0.21)         | $6.44 \pm 0.02$               | $10.42 \pm 0.09$<br>(0.85)    | $10.63 \pm 0.11$          |

Table 5.3: Third science run: average values of the main parameters of the fit from the study of the stability in time and comparison with the result from the fit of summed spectra. The weighted standard deviations are also reported between parentheses for the result from time distributions.

previous chapter, such values were already measured, corresponding to a specific case defined in order to provide statistical errors on these results. The present analysis aims to evaluate a more representative value, which should not depend on the minimum intensity of the main S2 signals.

As a result, two representative cases are investigated. The first one corresponds to a threshold value of 10 kPE, as it is also used in Section 5.4 in order to increase the statistics. The corresponding results have already been presented in the columns labelled *Sum* in Tables 5.1 - 5.3. The second case corresponds then to a threshold value of 30 kPE, that allows to increase the populations of charge signals made by two individuals single electrons in time coincidence. The others data selection cuts and parameters of the fit range are unchanged with respect to those already described in section 4.3.3 and in Table 4.1.

The demonstration of the stability of the gain is achieved by a comparison of the quantities corresponding to each science run, as it is illustrated by Figure 5.3 for the second and third science runs. Circle markers corresponds to the threshold value of 10 kPE, while the triangle markers corresponds to the threshold value of 30 kPE.

For each threshold value of the main S2 signal, the intermediate average gain among all results from each source are then calculated. They are represented by light blue dashed lines. The final average value of the secondary scintillation gain corresponds then to the average between these two intermediate values, and are represented by light blue lines on Figure 5.3. The associated deviations is represented by the light blue bands, and correspond to the half of the difference between the two intermediate average values.

Same observations have been done for the three others parameters. The final results, including deviations calculated with the method described above are presented in Table 5.4, and have also been published for the first two parameters and science runs in [157]. The errors values presented here correspond to the combination of the statistical errors presented in Table 4.2 and the systematic errors coming from the choice of the threshold value of the intensity of the main S2 signal. These values can be considered as reference for calculation and simulation for XENON100, and are very close to the optimised values presented in Figure 4.33.

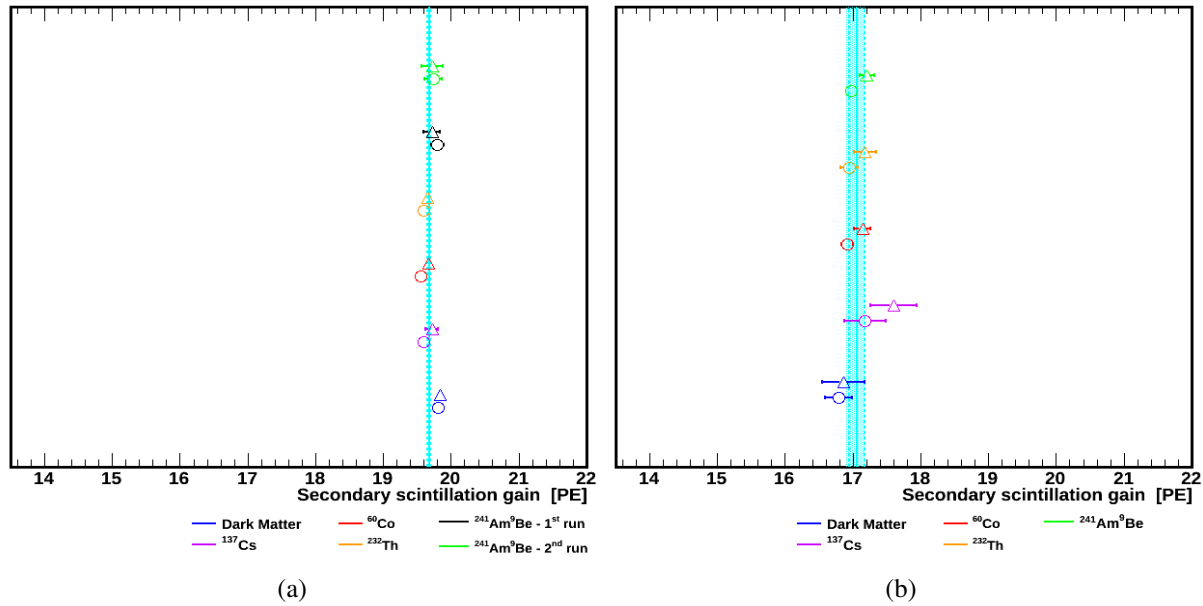


Figure 5.3: Demonstration of the stability of the secondary scintillation gain from triggering source during: (a) the second science run, and (b) the third science run. Circle (triangle) markers indicates a threshold on S2 of 10 (30) kPE.

| Science run   | $\mu_1$ [PE]     | $\sigma_1$ [PE] | $\mathbf{FD}_1$ [PE] | $\mathbf{FD}_2$ [PE] |
|---------------|------------------|-----------------|----------------------|----------------------|
| <b>First</b>  | $18.65 \pm 0.38$ | $6.62 \pm 0.12$ | $10.18 \pm 0.28$     | $2.05 \pm 0.33$      |
| <b>Second</b> | $19.68 \pm 0.02$ | $6.93 \pm 0.02$ | $12.71 \pm 0.09$     | $2.82 \pm 0.01$      |
| <b>Third</b>  | $17.07 \pm 0.12$ | $6.41 \pm 0.05$ | $10.64 \pm 0.21$     | $2.51 \pm 0.12$      |

Table 5.4: Average values of the main parameters of the fit from the study of the stability from calibration sources for the three science runs. Results partially published in [157].

As a complement to this analysis, the systematic errors can be calculated. They are mainly due to the source used for acquisition, but also to the choice of the threshold value. These systematic errors correspond to half of the difference between the minimum and maximum values measured per each science run, whatever is the threshold value. They are reported here in Table 5.5 below, and previously in the Table 4.5 that summarize all the systematic errors.

| Science run                   | First | Second | Third |
|-------------------------------|-------|--------|-------|
| <b>Systematic errors [PE]</b> | 0.7   | 0.2    | 0.4   |

Table 5.5: Systematic errors associated to the secondary scintillation gain per each science run, due to the combination of the used source of calibration and the choice of the threshold value of the minimum intensity of the main S2 signal.

### 5.3 Single electrons signals occurring between the main S1 and S2 signals

The analysis of single electrons charge signals occurring after the main S2 signal can be biased because of the PMTs base current resulting from this main signal, as it has been demonstrated in Section 4.4. In order to be free from this bias, the value of the secondary scintillation gain per each science run have been investigated for single electrons signals occurring between the main S1 and S2 signals. As mentioned in the previous chapter, these single electrons signals are mainly induced by the S1 signal, but also by delayed electron extraction, and to a much lesser extend by a S2 signal occurring before the beginning of the waveform. For this particular low energy S2 spectrum, several problems that will affect the quality of the fit are already known in advance:

- Almost no coincidence of two individual single electrons signals would occur, due to both the large time delay from the corresponding main S2 signal prior to the waveform, that can be usually responsible for delayed electron extraction, and to the much lower intensity of the S1 signal with respect to the main S2 for the single electrons signals production by photoelectric effect. This makes the fit more unstable due to a higher correlation between the first Gaussian distribution and the threshold function.
- The lower rate of single electrons signals makes more evident the already known excess at very low energies, and that could be due to misidentified S1 signals.

The latter identified problem can be however suppressed by requesting a minimum threshold on the amount of light seen by each PMTs. This data selection cut is inspired from an analysis done earlier in time, and presented in Section 5.5. The misidentified S1 signals can be thus avoided by using the results of the proportion of light emitted from a S2 signals seen by bottom PMTs array with respect to the full light from this signal seen by the two PMTs arrays, since due to their lower vertical emission position with respect to real S2 signals, the part of their light seen by bottom PMTs is higher. The less restrictive cut has however been selected in order to also keep as much as possible remaining S2 signals. Thus, for the present analysis, it is requested that at least 20 % of the light emitted during the signal is seen by one of the two PMTs arrays.

Furthermore, since there is no link between the main S2 signal of each studied waveform and the single electrons signals analysed here, no specific cut on the intensity of these main S2 signal such as defined in Table 4.1 can be used. This means that there is no possible improvement for the resolution of the first identified problem with the fit of the low energy S2 spectra considered here.

However, based on the analysis made previously, and that have led to the establishment of the other standard cut presented in Table 4.1, a new set of cut can be defined for the present analysis. Among them, two minimum temporal windows are requested, corresponding firstly to one after the main S1 signal and then one before the main S2 signal. The latter temporal window is set at 15  $\mu\text{s}$  in order to improve the distinction of the single electrons signals from the main S2 signals. In the other hand, several configurations are tested for the former temporal window, corresponding to different minimum time delay from the main S1 signal that are increased from 10  $\mu\text{s}$  up to 90  $\mu\text{s}$  with a step of 10  $\mu\text{s}$ . This is done in order to avoid any bias due to PMTs base current because

of the main S1 signal, even if is expected to not occur because of the low intensity of S1 signals and the low number of involved PMTs.

As a complement, the possibility of a similar bias of the gain than observed for single electrons signals occurring from few microseconds up to few tens of microseconds after the main S2, because of a high energy S2 signal occurring between the main S1 and S2 signal, is considered. Such events could be then induced by multiple scatterings, especially successive Compton scatterings. As a result, several configurations based on the number of identified S2 signals on the same waveform are tested successively. It consists in requesting that if more than  $n$  S2 signals are identified on the waveform, then the  $n - th$  secondary main S2 signal(s) should occur after the real main S2 signal. This analysis is done by increasing the number  $n$  from two up five, for which latter case the available statistics is very weak, even if all the data acquired with one source for one science run are combined. These cuts are summarized in Figure 5.4. Due to the very low available statistics for more than five S2 signals identified on the waveform, this later case is not reminded for clarity reasons on this figure.

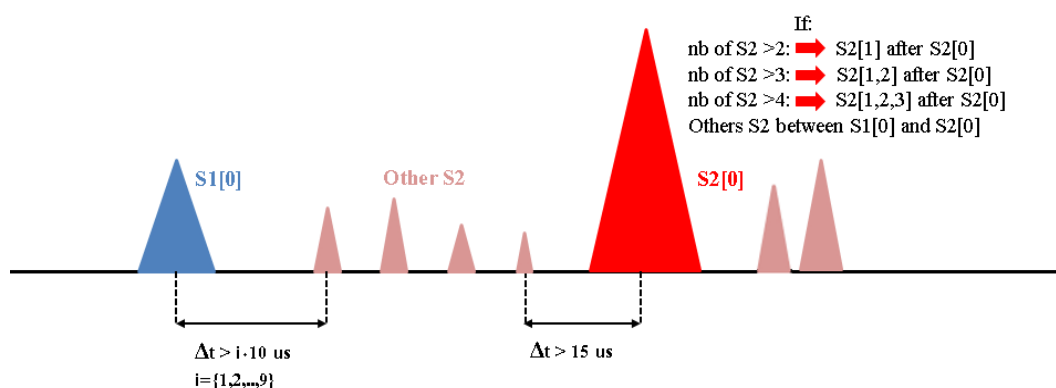


Figure 5.4: Illustration of the different sketches analysed for the single electrons signal occurring between the main S1 and S2 signals.

As for the analysis of single electrons signals occurring after the main S2 signals, all the cuts used for the present analysis can be summarized concisely:

- At least 20 % of the light emitted during the S2 signal is seen by one of the two PMTs arrays.
- Only events with 31 or less S2 signals will be considered.
- Only S2 signals occurring between  $i \times 10 \mu s$  after the main S1 signal, with  $i \in [1, \dots, 9]$ , and  $15 \mu s$  before the main S2 signal will be considered.
- If at least  $n$  S2 signals are identified on the waveform, with  $n \in [2, \dots, 5]$ , the  $n$ -th secondary main S2 signal(s) should occur after the main one.

For each configuration of the requested minimum number of identified S2 signals per waveform, the results of secondary scintillation gain measured from the fit of the low energy S2 spectra

for each configuration of the time delay from the main S1 signal, for each source and for the same science run are compared together. A representative couple of plots is shown in Figures 5.5 and 5.6. The shape of the marker correspond the minimum number of requested identified S2 signals per waveform. It is also legended on the left bottom corner of each figure.

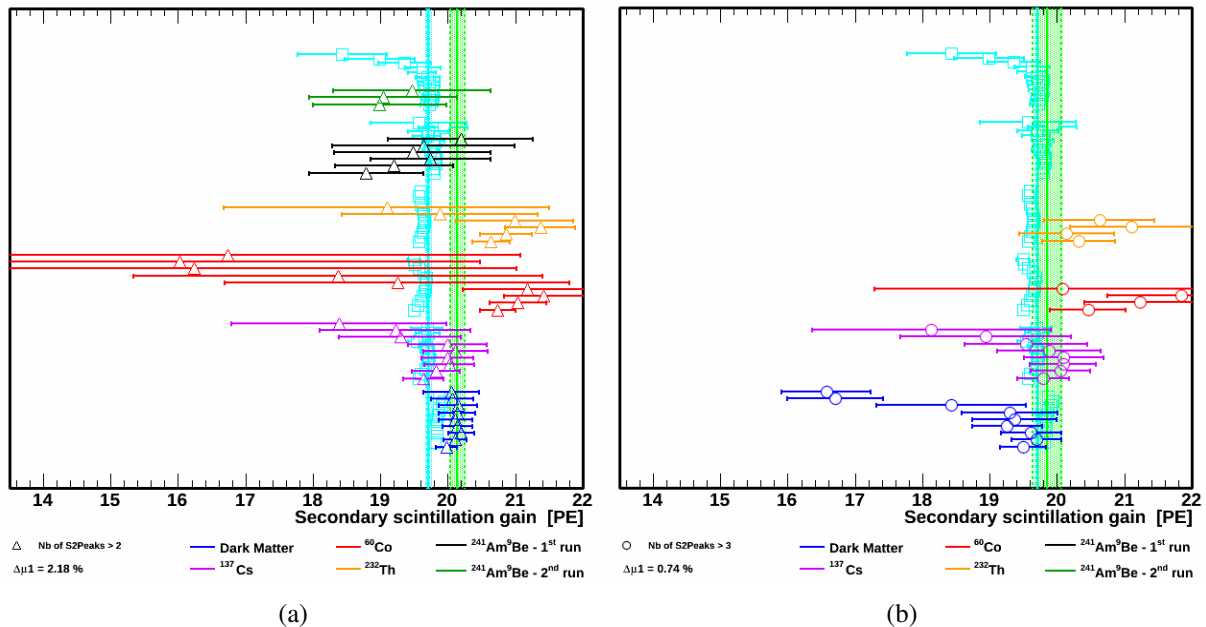


Figure 5.5: Analysis of the secondary scintillation gain results for single electron signals occurring between the main S1 and S2 signals, during the second science run with : (a) more than two identified S2 signals per waveform, and (b) more than three identified S2 signals per waveform. For each source, the delay of single electron signals from S1 increases from  $10 \mu\text{s}$  up to  $90 \mu\text{s}$  with a step of  $10 \mu\text{s}$  from bottom marker up to top marker.

For each source, i.e. each marker color, the result corresponding to each configuration of the time delay from S1 is presented, with the lowest minimum delay for the bottom marker. This delay increases successively from bottom marker up to top marker. Because of being more and more restrictive, the corresponding available statistics of low energy S2 signals is lower and lower. This explains why the errors bars increases from bottom up to top marker, and why results more and more fluctuate. The green solid and dashed lines illustrate the average and standard deviation between all available sources. For their calculation, only the results with the time delay from the main S1 signal above  $10 \mu\text{s}$  for each source are considered, since the others data are also included within this cut.

The comparison between two different sketches of the minimum number of identified S2 signals per waveform, for the same science run, as illustrated by Figure 5.5, gives compatible results. This allows to exclude the possibility of any bias from a secondary main S2 signal occurring between S1 and S2 main signals, and thus the possibility of multiple scattering with more than two interactions for the same event. Moreover, the comparison for the same sketch of identified S2 signals between results from the same source with an enough large available statistics with respect to the other cases, corresponding to error bars below  $0.2\text{--}0.4$  PE, gives also compatibles results. This allows to exclude also any bias on the evaluation of the gain due to the PMTs base current re-

sulting from the main S1 signal. As said before, this was however expected since only few PMTs are involved for this signal, and almost all of them are from the bottom PMTs array.

As a reference, the results from the analysis presented in Section 4.5.5 are also shown here in light blue. The relative difference between average value from each analysis, i.e. between the green and the light blue vertical solid lines is calculated for each configuration of the minimum number of identified S2 signals, and is reported in percent in the bottom left corner. This allows to confirm a compatibility within 5 % for the two methods, even if a statistical overlap is in most of the case excluded due to a much lower accumulated statistics of low energy S2 signals with respect to the analysis presented in the previous chapter. The lack of statistics for single electrons signals occurring between the main S1 and S2 signals, especially individuals single electron signals occurring in time coincidence, explains the difference between the average value. Indeed the comparison between result from the present analysis and the previous one, for a threshold on the intensity of the main S2 signal equal to 5 kPE, corresponding to light blue bottom marker for each source and where the second main peak of the spectrum is strongly reduced compared to the main one, seems to give very similar results. This is especially the case for the first and in a lesser extend for third science runs thanks to larger errors bars, as illustrated by Figure 5.6. The uncertainties on these latter results can be related to the average secondary scintillation gain that is lower for the third run than for the first one. This is then also the case for the intensities of all the S2 signals for the same amount of electron extracted in the gas phase. Combined with a lower drift field in the active volume of the liquid phase, a lower extraction yield as it will be seen at the end of this chapter, and a higher electron lifetime, there are less single electrons induced by the main S2 signal with the same original deposited energy in the two run. That's why for the similar life days of data acquisition, the statistics for single electrons signals occurring during the third science run is worse.

For the second science run, the agreement between the present analysis and the previous one, for a threshold on the intensity of the main S2 signal equal to 5 kPE is less remarkable. While the agreement is clear for dark matter data, corresponding to events triggered by background sources, and for  $^{137}\text{Cs}$  data, it is weaker for the two runs of  $^{241}\text{Am}^9\text{Be}$  data, due to the lower data acquisition statistic. Then, a bias seems to occurs on the two remaining ER calibration source, the  $^{60}\text{Co}$  and the  $^{232}\text{Th}$  during not only the second science run, but also the third one, as illustrated by Figure 5.6(b). The lake of acquisition statistics during the first science run with the  $^{60}\text{Co}$  calibration source does not allow to confirm whether this bias occurs also during this run, or not. This bias could be due to a time overlap between a single electron signal and a non identified small S1 signal, leading to a stronger single electron event. Such event would be more common for higher energetic calibration sources with a higher radiation rate, which correspond to the case of the  $^{60}\text{Co}$  and the  $^{232}\text{Th}$  calibrations sources. This explanation is however not enough to explain alone this bias, because of a too low occurrence frequency of such events. Therefore, further analysis on the shape of these low energy S2 signals would be mandatory to give definitive conclusion on the sketch of the combination of a S1 signal and single electron signal.

As a conclusion to this section, intermediate single electrons can not be used for the secondary scintillation gain analysis, since even if they provide coherent results with single electron signals occurring after the main S2 signal, the lack of coincidence of two individual single electron signals

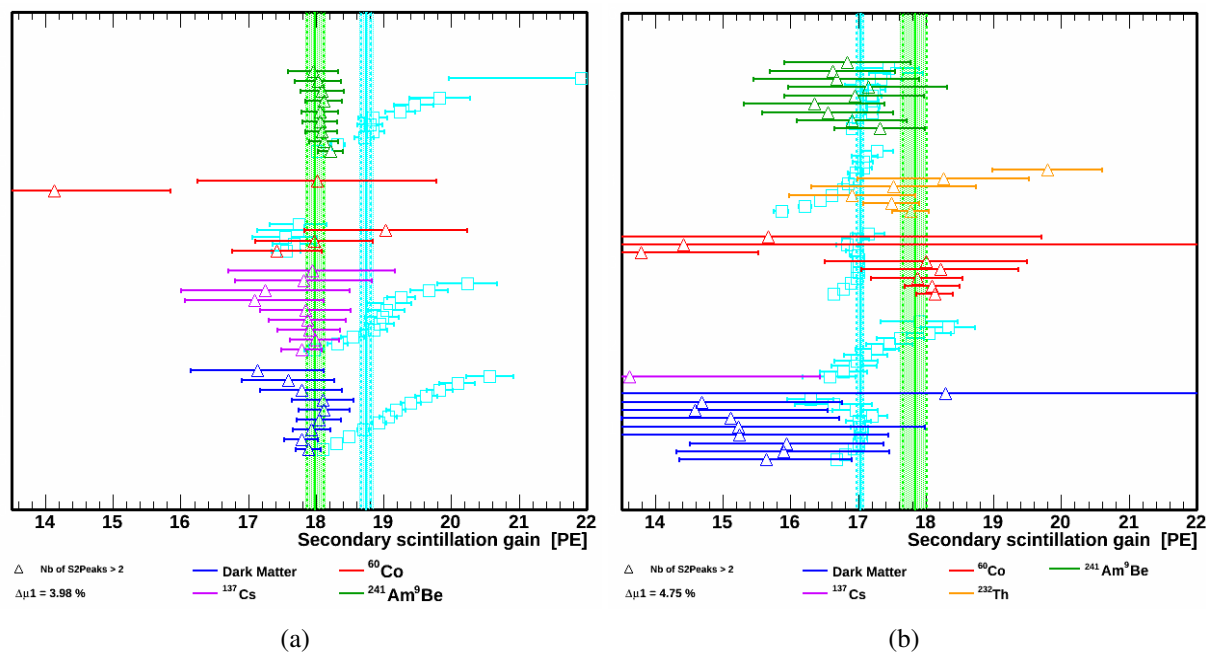


Figure 5.6: Analysis of the secondary scintillation gain results for single electron signals occurring between the main S1 and S2 signals, with more than two identified S2 signals per waveform, during : (a) the first science run, and (b) the third science run. For each source, the delay of single electron signals from S1 increases from 10  $\mu\text{s}$  up to 90  $\mu\text{s}$  with a step of 10  $\mu\text{s}$  from bottom marker up to top marker.

in the spectrum creates an unavoidable bias on the final fit result. The present study concludes all the analysis on single electrons signal made over the three science runs. It what follow will be presented the analysis of the secondary scintillation gain for several other gaseous electric field configurations.

## 5.4 Dependency on the electric field

The previous analysis presented up to this section corresponds mainly to all the data acquired during science runs. However, this does not include all the useful data acquired with XENON100. Indeed, between the end of the refilling of the detector and the beginning of each science run, and eventually during maintenance operations, several measurements have been taken, mainly with  $^{137}\text{Cs}$  calibration source in order to take benefits of the properties presented in Section 2.4.1.1. Each of these measurements corresponds to an investigation of the detector response for different electric fields configurations, in both liquid and gas phase, in order to improve the detector settings for the future science runs. At the same time, thanks to the photoelectric peak of the  $^{137}\text{Cs}$ , the evolution of the purity of the LXe can be monitored. That is why this calibration source is preferred to the two other  $\beta/\gamma$  sources.

Thanks to all of these measurements, one or few datasets per same electric field conditions are available, allowing to extend the study of the secondary scintillation gain for a larger range of electric field in the gas phase. Thus, in addition to the three electric fields configurations belonging

to each science run respectively, two different campaigns can be identified, before the second and third science run respectively. Both of them correspond to modification of the liquid level above the ground mesh and the voltage passing through the anode mesh. Furthermore, some data were acquired with either the liquid level or the anode voltage as a constant value before the second science run.

Since the purpose of the XENON100 detector is not the analysis of the low energy charge signals, but the dark matter search, these data were not originally acquired for the analysis of the secondary scintillation gain. As a result, no specific efforts were made at that time on the choice of the value of the electric field in the gas phase, except for the optimisation of the detector response, corresponding mostly to the suppression of hotspots and sparks emissions from the different meshes by changing liquid level and anode voltage. It is only after the third and last science run that a dedicated and intensive calibration run for the present analysis of the secondary scintillation gain was proposed and performed, as it is detailed in Section 5.4.3.

### 5.4.1 Field calculation

The average electric field in the gas phase below the anode can be calculated thanks to a parallel-plate capacitor approximation of the region of the TPC between the ground mesh and the anode, as it is illustrated by Figure 5.7.

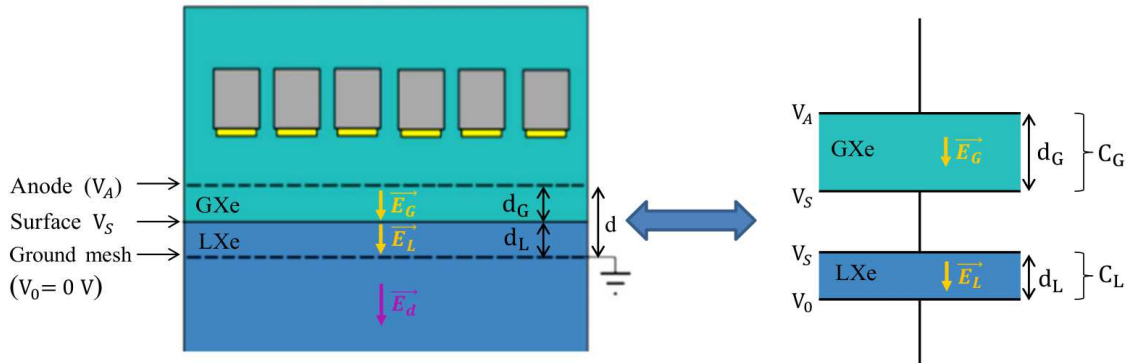


Figure 5.7: Illustration of the approximation of the region of the TPC between the ground mesh and the anode as a parallel-plate capacitor

The liquid and the gas volumes in this region can be seen as two parallel-plate capacitors  $C_L$  and  $C_G$  in series. For each of them, the dielectric constant  $\epsilon_i$  associated to the each of these media is:

$$\epsilon_i = \epsilon_0 \times \epsilon_{r,i} \quad i = L, G \quad (5.1)$$

where  $\epsilon_0$  corresponds to the vacuum permittivity, and  $\epsilon_{r,i}$  correspond to the relative permittivities of the two media. By using these dielectric constants, the capacitance  $C_i$  of each of these two capacitors can be expressed as:

$$C_i = \frac{\varepsilon_i S}{d_i} \quad i = L, G \quad (5.2)$$

with  $S$  the surface covered by each mesh (whose size is not really important since the field is independent of it). The lengths  $d_i$  correspond to the distance between the ground mesh and the liquid surface for the first capacitor, and the distance between the liquid surface and the anode for the second one. The capacitance  $C$  of the capacitor that is equivalent to the combination of these two capacitors is:

$$C = \frac{C_L C_G}{C_L + C_G} \quad (5.3)$$

The distance between the anode and the ground mesh is fixed to  $d = d_L + d_G = 0.5$  cm, therefore  $d_L$  and  $d_G$  are not independent. By combining Equations 5.1, 5.2 and 5.3 and expressing it as a function of the only  $d_L$ ,  $C$  can be written as:

$$C = \frac{\varepsilon_0 \varepsilon_{r,G} \varepsilon_{r,L} S}{\varepsilon_{r,L}(d - d_L) + d_L} \quad (5.4)$$

The definition of the capacitance implies also:

$$C = \frac{Q}{\Delta V} \quad (5.5)$$

with  $\Delta V$  the potential difference between the ground mesh and the anode.  $Q$  corresponds to the absolute value of the charge available on each plate of the equivalent capacitor  $C$ . By combining the definition of the electric displacement field  $D$ :

$$D = \varepsilon_i E_i = \frac{Q}{S} \quad i = L, G \quad (5.6)$$

with Equations 5.4 and 5.5, the electric field in both the liquid and the gas phase between the ground mesh and the anode can be expressed:

$$E_L = \frac{\Delta V}{\varepsilon_{r,L} (d - d_L) + d_L} \quad (5.7)$$

$$E_G = \frac{\varepsilon_{r,L} \Delta V}{\varepsilon_{r,L} (d - d_L) + d_L} \quad (5.8)$$

Equation 5.7 is however written here in a simplified version under the relevant assumption  $\varepsilon_{r,G} \sim 1$ . The value of  $\varepsilon_{r,L}$  is equal to 1.96 [116], as reminded in Table 2.1. As an illustration,

the variation of electric field in the gas phase  $E_G$  as a function of the liquid level  $d_L$  according to Equation 5.8 is represented in Figure 5.8 for different anode voltages.

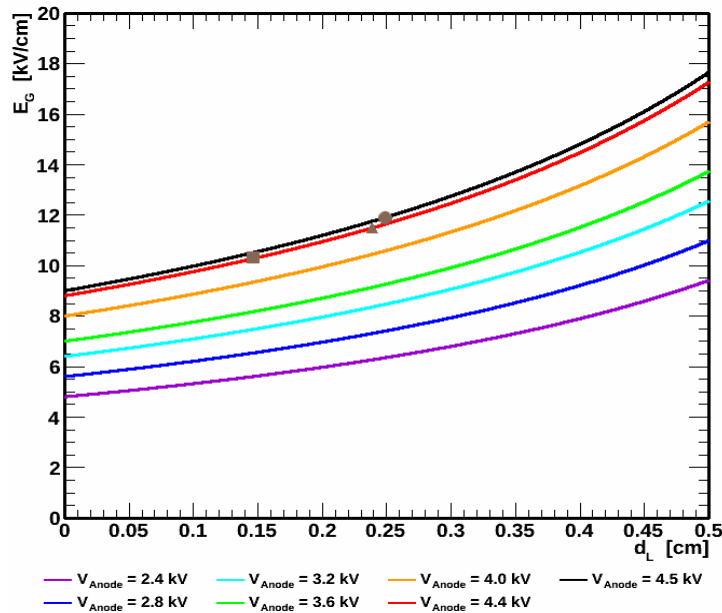


Figure 5.8: Illustration of the variation of the electric field in the gas phase as a function of the liquid level for different anode voltages. The three brown round, square and triangle markers correspond to the liquid level and electric field conditions for the first, second and third science run respectively.

This figure illustrates thus the expected increase of the electric field with the increase of the liquid level, hence the reduction of the gas gap. The three brown round, square and triangle markers correspond to the liquid level and electric field conditions for the first, second and third science run respectively. As demonstrated by Equations 5.7 and 5.8, the variation of the electric field in the liquid phase is proportional to the variation of the electric field in the gas phase for the same liquid level and anode voltage conditions.

## 5.4.2 Measurement of the dependency

Thanks to Equation 5.8, the value of the electric field per each data acquisition conditions can be calculated. The anode voltage is provided by a *CAEN* module which is able to provide a voltage with an accuracy of 5 V. The liquid level is read about each 15 seconds from a sensor. For each dataset, or each combination of datasets in case few of them were acquired in the same detector settings, the distribution of these measurements is drawn, as illustrated in Figure 5.9. The mean values of each of them are identified as the average values of the liquid levels. The associated errors correspond then to the root mean square of these distributions. The zero of the liquid level is set 5 mm below the position of the ground mesh. That is why the measured liquid level is higher than the distance  $d$  between the anode and this mesh.

For each electric field configuration, the corresponding measured secondary scintillation gain is rescaled to a reference value of  $d_L = 0.21$  cm, since the electric field in the gas phase is a function of both the liquid level and the anode voltage. The reference value of  $d_L$  corresponds to the value

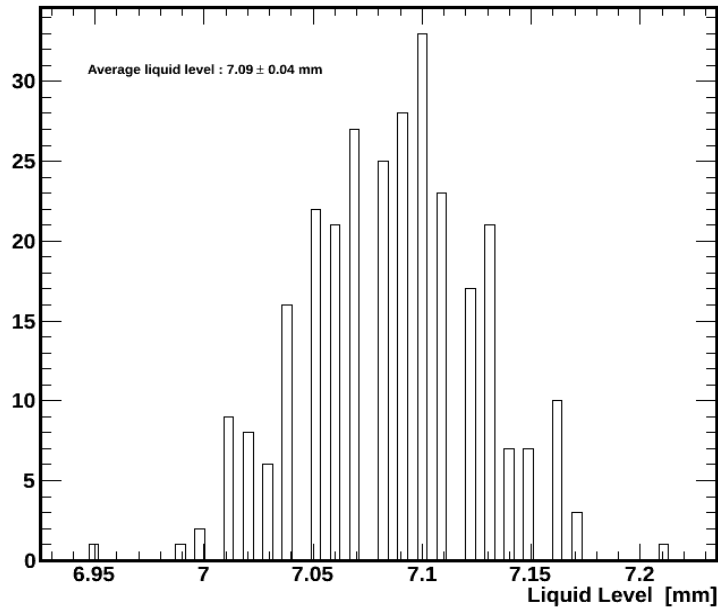


Figure 5.9: Illustration of the liquid level measurements distribution for one dataset acquired with  $^{137}\text{Cs}$  radioactive source right before the second science run.

of the liquid level that was kept constant for the acquisition of several measurements right before the second science run. This is also motivated by the already known empirical formula that rules the variation of the secondary scintillation gain as a function of the electric field, presented later in this section, and from which the two parameters will be calculated thanks to the present analysis. The results from all datasets are reported in Figure 5.10, that draws the variation of the secondary scintillation gain as a function of the electric field in the gas phase.

The datasets acquired right before the second science run are represented in dark blue, while the datasets acquired right before the third science run are represented in light blue. Three other reference datapoints are also added, corresponding to the very high statistics collected during each science run. They are set in orange, violet and pink for the first, second and third science run respectively. In order to both take benefit of the high available statistics per each science run, and to not bias other results by strongly constraining the fit of the secondary scintillation gain distribution, only 16 representative datasets were combined together for each of these three specific detector settings. These 16 datasets are selected among all the available  $^{137}\text{Cs}$  datasets per each science run as being both widely distributed in time, and as having a measured secondary scintillation gain as closest as possible to the corresponding final value presented in Table 5.4. The number 16 is also constrained by the number of  $^{137}\text{Cs}$  calibration datasets taken under the third science run stable conditions and available at the time of this study. The error bars on the Y-axis correspond to the errors on fit parameters, while the error bars on the X-axis correspond to the error on the electric field value. This latter depends from both the errors on the anode voltage and the liquid level measurements. The remaining four datapoints in green correspond to secondary scintillation gain measured with  $^{60}\text{Co}$  radioactive source, before and during the second science run. For the publication of this figure in [157], all the datapoints from data acquisitions with  $^{137}\text{Cs}$  calibration source were presented in dark blue in order to simplify the reading of the figure.

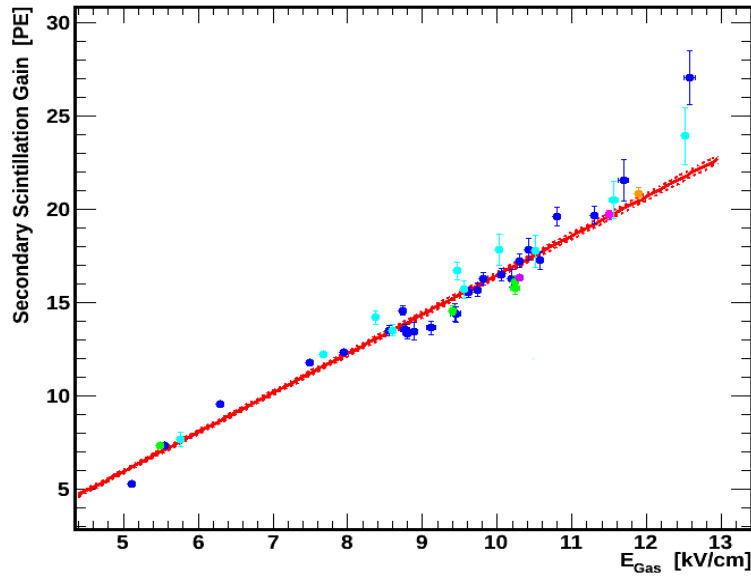


Figure 5.10: Secondary scintillation gain as a function of the electric field in the gas phase. Data from  $^{137}\text{Cs}$  radioactive source: dark blue markers – before second science run, light blue markers – before third science run, orange marker – first science run, violet marker – second science run, pink marker – third science run. Data from  $^{60}\text{Co}$  radioactive source: green markers – before and during second science run.

Several features of the gain can be observed on this figure. First, the invariance of the gain with respect to the used calibration source is again confirmed, and extended down to very low values of the electric field. Then, a linear increase of the gain as a function of the electric field can be observed. This trend, corresponding to the increase of the number  $N_{ph,e^-}$  of emitted photons per electron drifting in the gas phase, has already been observed by other experiments, and quantified through the empirical formula [114, 164]:

$$N_{ph,e^-} = \left( \alpha \frac{E[kV/cm]}{P[bar]} + \beta \right) d_G[cm] P[bar] \quad (5.9)$$

By taking into account the average collection efficiency  $\bar{\delta}$  of emitted photons by each PMTs plane, the average quantum efficiency  $\bar{\eta}$  of the photocathode of the PMTs and average collection efficiency  $\bar{\epsilon}$  of the first dynode of the PMTs to collect the electron released by the photoelectric effect on the photocathode, the number of photoelectrons measured by all the PMTs of the TPC for one electron drifting in the gas phase can be calculated:

$$N_{PE,e^-} = N_{ph,e^-} \bar{\delta} \bar{\eta} \bar{\epsilon} \quad (5.10)$$

This formula is used to fit the distribution of the secondary scintillation gain with the two parameters  $\alpha$  and  $\beta$  let free. Since the pressure of the gaseous phase is almost constant, an average value has been inferred from the distribution in time of this quantity starting from the first

science run up to third one, in order to be used in the fit formula. This distribution is represented in dark blue in Figure 5.11. The average value, equal to about 2.2 atm, corresponding to about 2.25 bar, is illustrated by a line.

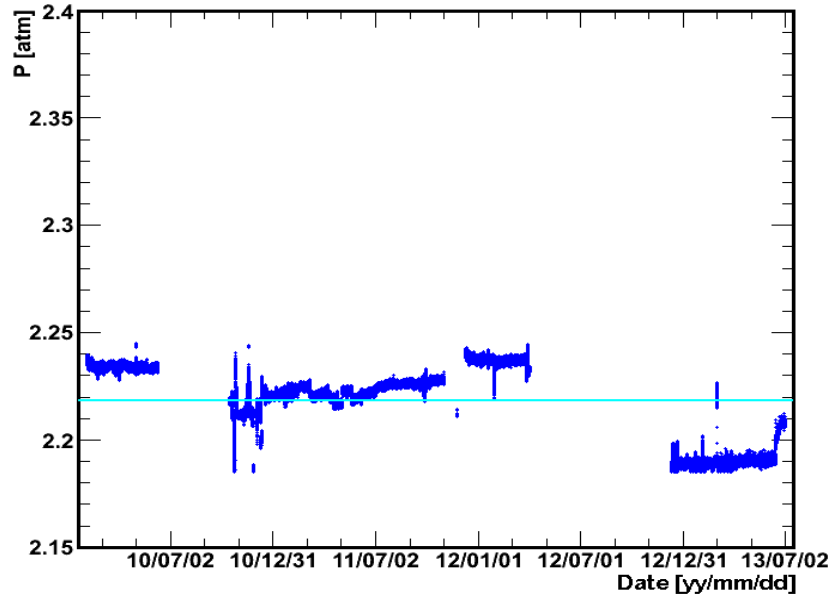


Figure 5.11: Distribution in time of the gaseous pressure from the first science run up to the third one.

The result of the fit of the secondary scintillation gain distribution is then represented by the solid red line in Figure 5.10. The associated errors, coming from the fit parameters statistical errors, are represented by red dashed lines. The two values of these parameters inferred from the fit are:  $\alpha = (151 \pm 19)$  photons/e<sup>-</sup>/kV and  $\beta = -(147 \pm 19)$  photons/e<sup>-</sup>/cm/bar [157]. The uncertainties associated to these results are dominated by uncertainties on the light and electrons collection efficiencies. The two parameters are however in good agreement with previous measurements [164], and with predictions from Monte Carlo simulations [165] at room temperature, but also with measurements for saturated xenon vapour at cryogenic temperature [166].

Furthermore, the highest values of the secondary scintillation gain, corresponding to the highest values of the electric field, start to deviate from the observed linear trend around 12 kV/cm. They seem to be affected by electron multiplication because of the high intensity of the electric field in a similar way to the electron avalanche occurring between two dynodes of a PMTs. Since only two data points seem to be affected, further data are needed to both confirm this multiplication and investigate the threshold value of the electric field at which it starts to occur. This is one of the purpose of the intensive <sup>137</sup>Cs calibration campaign proposed and made in Spring 2014, as presented in the next section.

### 5.4.3 A dedicated single electron calibration run

As mentioned right above and previously in this chapter, a original specific campaign of <sup>137</sup>Cs calibration data has been made in Spring 2014. Since the main scientific goals of the XENON100 detector were already reached by the second science run, and extended by the third one, the

purpose of this intensive run was to take benefits of the last running months of the detector to perform R&D on the optimisation of the running condition for the improvement of the detector response to all S2 signals.

As a results, specific gaseous electric field settings were selected, in order to investigate the dependency of the secondary scintillation on the electric field with first a constant liquid level set at 7.6 mm and then with a constant anode voltage, set at either 2.2 kV or 4.4 kV. A third case was also investigated, corresponding to analysing the response of the detector for different combination of the liquid level and the anode voltage in order to get a constant electric field at either 6 kV/cm or 9 kV/cm in the gas phase. For each of them, the data acquisition algorithm was also optimised to cumulate between five and six times the usual 50 k events from calibration with  $^{137}\text{Cs}$  radioactive source. It was also optimised in order to run continuously the detector in active mode night and day, in order to reduce the duration of the full campaign. Such improvements of the algorithm can be used for future calibrations of either XENON100 for R&D or XENON1T.

Following the same optimisation philosophy, the acquisition was divided into three steps. The first consists in investigating the easiest case, which corresponds to keep the liquid level as constant and decrease the anode voltage. This choice was motivated by the sharp decrease of LXe purity as soon as the liquid level changes. The second one consists then by keeping the anode voltage as constant and decreasing the liquid level. Between each configuration, about three hours were needed before starting the acquisition because of the stabilisation of the liquid level from the LXe recirculation flow. The last step consists in taking data by changing both the liquid level and the anode voltage, in order to keep the gaseous electric field as constant.

During these acquisitions, an unusual acquisition rate of about two times the standard 30 – 33 Hz, was observed, corresponding to an increase of noise events. Despite of these fake events, all the data were acquired and analysed. Unfortunately, some of them, corresponding to the datasets with highest values of the anode voltage during the first step of the acquisition, have presented an unexpected excess at very low energy on the S2 signals, as it is illustrated by Figure 5.12.

These excesses were very similar to those observed sometimes on previous spectra, however no standard quality cuts developed so far, based on either a time delay cut or a cut on the proportion of light from each S2 signal seen by each PMTs arrays, such as it has been presented in Section 5.3, succeeded to remove them. Moreover, no localised hotspots of light in the (x,y) positions reconstruction map have been observed for these signals, excluding any cut based on a specific position. This suggests that these events correspond to misidentified successive S1 signals located between the ground mesh above the bottom PMTs and the cathode, where the electric drift field is of the order of 10 kV/cm. This is motivated because of the combination of their intensity, their non-localisation property for reconstructed positions, and their longer time duration that imply them to be identified as S2 signals instead of S1 signals. Moreover, the high drift field in this region suggests also sparks emission from the bottom ground mesh, that would explain these signals. It was also observed that as soon as the cathode voltage exceeds an absolute value of about 10 kV, this increase of the rate starts to occurs. This seems to confirm the spark emission from the cathode, which are most probably due to a cluster of impurities. Several strategies, up to the almost complete xenon recuperation and detector refilling, were tested to definitely solve the problem, up to a final success few months later.

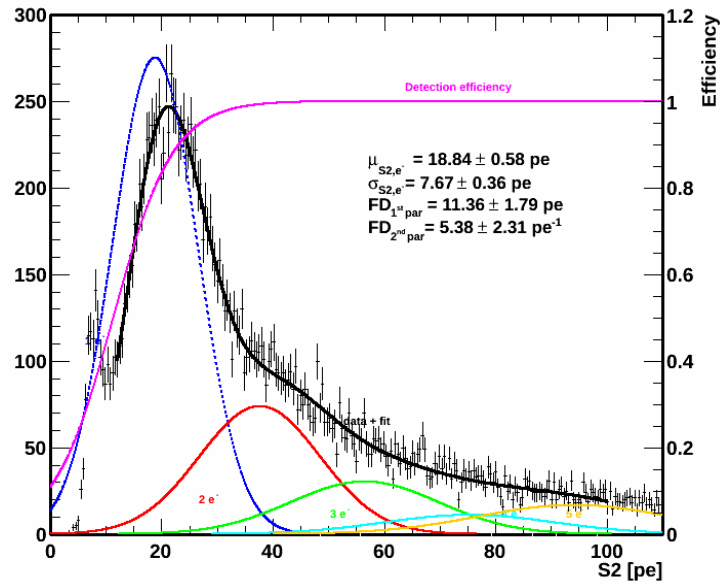


Figure 5.12: Illustration of the unexpected excess on the very low energy part of the S2 spectrum during the  $^{137}\text{Cs}$  calibration campaign.

This issue compromised the analysis of the datasets acquired at an electric field of 9 kV/cm and part of the datasets acquired at an electric field of 6 kV/cm.

The results coming from the remaining new data are shown in black in Figure 5.13, which contains also the old ones presented in Figure 5.10.

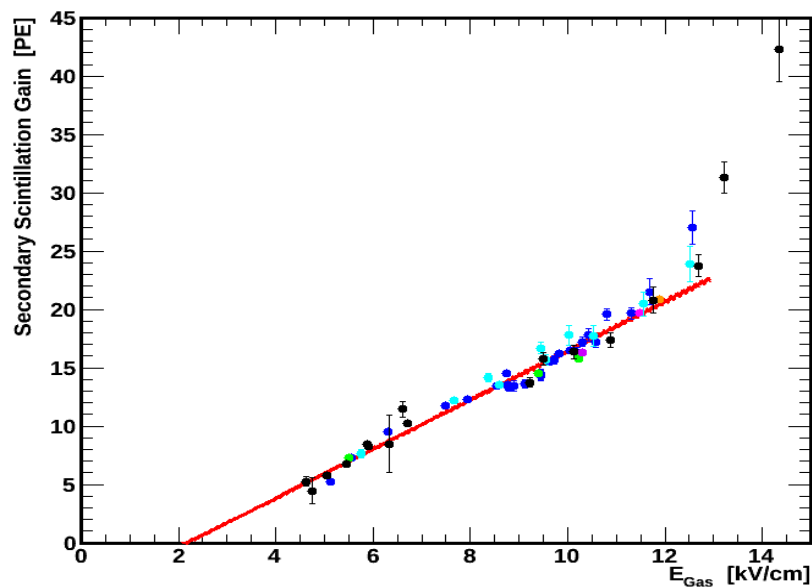


Figure 5.13: Secondary scintillation gain as a function of the electric field in the gas phase during the  $^{137}\text{Cs}$  calibration campaign.

If unfortunately not all the acquired data can be used due to the noise issue, the remaining useful data have however demonstrated the reproducibility of the results previously presented in Figure 5.10. Moreover, the data acquired at low and high electric fields are very useful to confirm the two observed trends. This indeed seems to indicate first that an electric field value of at least

about 2 kV/cm is mandatory to observe a secondary scintillation gain in case the trend continue to be linear. This could correspond to the threshold value of the electric field needed to extract electrons from the liquid phase up to the gas phase. Further measurements at electric fields lower than 4.5 kV/cm would be however needed in order to exclude any changing of the trend. Then, the new results at high electric fields also confirm the apparition of electronic avalanche, improving slightly the knowledges on the electric field conditions for the beginning of this amplification and extending the range to higher fields. The electric field of about 12 kV/cm remains then the maximum limit below which electronic avalanche is excluded. The remaining two datasets acquired during the third step of the acquisition for electric field at 6 kV/cm with different values of both liquid level and anode voltage also confirmed the expected stability of the gain for the same electric field conditions in the gas phase, but with different anode voltage and liquid level configurations.

## 5.5 S2 signal repartition over top and bottom PMTs arrays

Thanks to the analysis presented in the previous section, the dependency of the electrons extraction yield on the electric field can be achieved. This can be done by comparing the light emitted by a single electron with the light emitted by the main S2 signal induced by an interaction with a known deposited energy, such as for the photoelectric effect of a  $\gamma$  ray from  $^{137}\text{Cs}$  calibration source already mentioned before. In order to exclude almost any attenuation of the signal due to electron capture during the drift, the scattering is selected in order to correspond to an interaction close to the liquid gas interface. This selection can be done by extrapolating to a drift time close to zero a curve similar to the one presented in Figure 2.11(a). The S2 signal associated to this scattering and normalised to the energy of 662 keV of the  $\gamma$  is called the *S2 gain*,  $G_{S2}$ . The comparison between the two gains will be done in the next section, since a prior analysis, presented here, needs to be performed first.

For this analysis, the corresponding S2 signal is obtained by a summation of the light observed by the bottom PMTs array only, in order to avoid any bias on the total intensity of the signal due to the saturation of PMTs from top array. Such saturation can effectively occur since this analysis investigates much energetic signals than the expected signals for WIMPs scattering, and thus are too much energetic for the specific setting of the PMTs' gain used by XENON100.

Since the evaluation of the secondary scintillation gain presented in the previous section has been obtained with a summation of the low energy S2 signals per PMT over the two PMTs arrays, two solutions for the comparison can be considered:

1. The analysis of the secondary scintillation gain should be repeated over bottom PMTs array only.
2. The fraction of light seen by bottom PMTs compared to the total amount of light that would be seen by the two PMTs arrays, in case of no PMTs signal saturation from the top array, should be calculated.

The feasibility of the first solution can be investigated by considering the second science run, and by considering only the bottom PMTs array. The value of the secondary scintillation gain is

then lowered from 19.7 PE down to about 8 PE. This illustrative case corresponds however to an optimal case since it corresponds to both a high available data statistics and a high electric field condition. But for the analysis as a function of the electric field, both of them decrease, as it is also the case for the expected gain that can be lowered down to 2 – 3 PE for bottom PMTs array only. As a result, the distinction between each single electrons population is much more difficult, and leads after testing to much more oscillations around the linear trend observed in Figure 5.10. Thus, an analysis of the fraction of light seen by bottom PMTs compared to the total amount of light seen by the two PMTs arrays has been preferred for the comparison of the secondary scintillation gain and the S2 gain. This analysis is detailed in the present section, while the comparison between both quantities, corresponding to the evaluation of the electrons extraction yield from the liquid to the gas phase, is presented in the next section.

### 5.5.1 Data selection

The purpose of the analysis of the fraction of light seen by each PMTs array is to infer the total amount of light that would be seen by the two PMTs arrays for the photoelectric effect of a  $\gamma$  ray from  $^{137}\text{Cs}$  calibration source discussed in the previous section, in the optimal case where no PMT saturation would occur. As a results, the amount of light for low energy S2 signals for one PMTs array as a function of the other one is investigated, as illustrated by Figure 5.14.

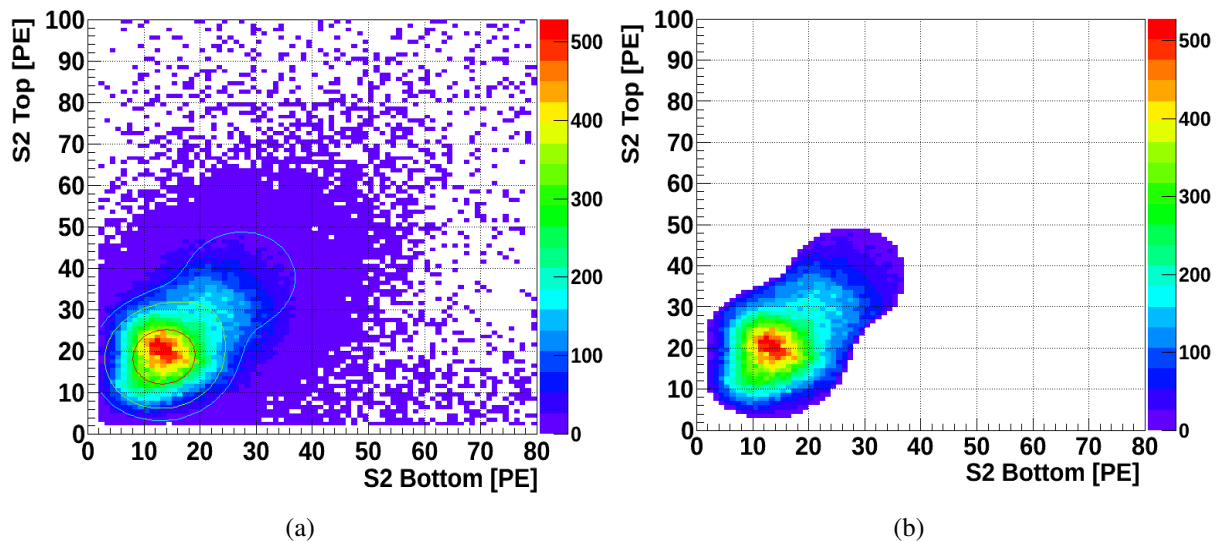


Figure 5.14: Illustration of the comparison without PMTs saturation of the light seen by top PMTs array as a function of the light seen by bottom PMTs array for low energy S2 signals: (a) before data selection, and (b) after data selection.

This figure corresponds to one dataset acquired with  $^{232}\text{Th}$  calibration source during the second science run. Indeed, if the original purpose of this analysis is to investigate the fraction of light seen by each PMTs array for the  $^{137}\text{Cs}$  calibration source for different electric field detector settings, an extension to other calibration source for a science run detector settings is needed to improve the analysis method by taking advantage of much higher available data statistics. Moreover, it is also important to check both the stability in time of this fraction, and the stability from

one calibration source to another one, for stable detector settings.

No specific quality data selection cut has been applied to Figure 5.14(a), except an exclusion of signals seen by only one PMTs arrays, i.e. with a signal lower than 2 PE for the opposite array and corresponding to noisy signals, in order to improve the contrast for the future selection of the main cluster of events. Moreover, these low energy S2 signals used for the present analysis, ie signals below 150 PE, correspond to the main S2 signals per waveform, which means that no bias from a previous high energy S2 signal would occur. They correspond then to delayed extraction of one or few electrons from an interaction prior to the waveform.

Since the data represented here correspond to single electrons signals, a selection of the main cluster of events in order to draw the profile of the distribution of the light seen by PMTs from bottom array is done. For this purpose, a fit of the distribution with a function similar to the previous fit function of the low energy S2 spectra, but defined in a two-dimensional energy space, is applied. As a result, a sum of two bi-dimensional Gaussian distributions multiplied by a threshold function based on the Fermi-Dirac statistics are used. The result of selection of the distribution at one, two and three sigma of confidence level are represented by red, green and blue contours respectively. The purpose of the fit consists only to the selection of relevant data as closest as possible to the shape of the distribution, excluding thus most of possible source of background.

## 5.5.2 Results and stability checks

In order to keep the largest amount of events, the selection is done by using the three sigma contour, as illustrated by Figure 5.14(b). The proportion of light  $R_b$  seen by PMTs from bottom array is then drawn by investigating for each event the intensity of the signal from bottom PMTs array divided by the total signal. For the data selected in Figure 5.14(b), the corresponding distribution is presented in Figure 5.15(a), and is fitted by a Gaussian distribution. The regions excluded by the fit do not follow the Gaussian distribution. The result from the fit of the average value of the Gaussian distribution corresponds then to the average proportion of light seen by the bottom PMTs array with respect to the light seen by the two arrays if no PMT saturation occurs. The stability in time of this proportion of light is also demonstrated by Figure 5.15(b) for  $^{232}\text{Th}$  calibration source, and has been also observed for each source, during each science run. The average value of this distribution in time is represented by a line in Figure 5.15(b).

By taking advantage of this analysis of this stability in time during each science run, with each source, the average value from the distribution in time is firstly compared to the average value from the sum of all the available datasets per source for stable detector settings. This comparison is also done in order to check the performance of the fit for individual datasets, in order to extend the fit method to the analysis as a function of the electric field in the gas phase. Then, the results from sum of datasets per each science run and per source are compared, demonstrating the stability from the selection of the source which was expected since the analysed signals correspond to single electrons signals. The results of the comparison for second science run between results from both time distribution and sum of datasets per each source, and then between results from each source is represented in Table 5.6.

The very low values for errors in Table 5.6 are due to the high considered statistic. That is

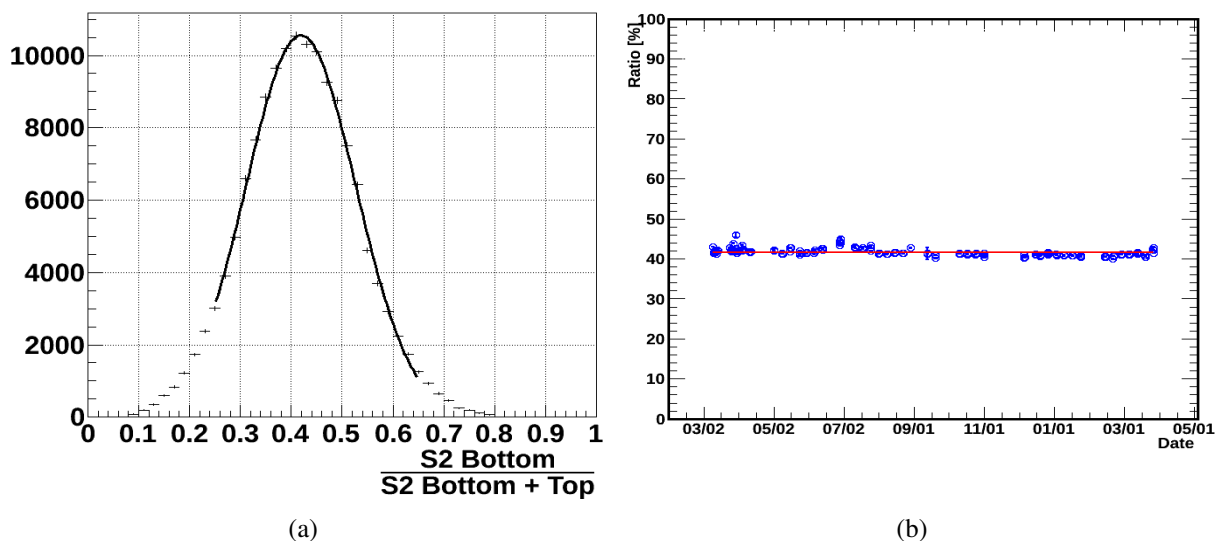


Figure 5.15: (a) Proportion of light from S2 signal seen by bottom PMTs array with respect to the combination of bottom and top PMTs arrays, (b) stability in time of the average value.

| Source  | $R_b$ [%]<br><i>Average</i> | $R_b$ [%]<br><i>Sum</i> |
|---|-----------------------------|-------------------------|
| <b>Dark Matter</b>  | $40.81 \pm 0.02$            | $41.18 \pm 0.02$        |
| $^{137}\text{Cs}$   | $40.40 \pm 0.01$            | $40.97 \pm 0.01$        |
| $^{60}\text{Co}$  | $41.86 \pm 0.01$            | $41.93 \pm 0.01$        |
| $^{232}\text{Th}$   | $41.63 \pm 0.01$            | $41.71 \pm 0.01$        |
| $^{241}\text{Am}^9\text{Be}$<br><b>1<sup>st</sup> Run</b> | $42.94 \pm 0.01$            | $43.27 \pm 0.01$        |
| $^{241}\text{Am}^9\text{Be}$<br><b>1<sup>st</sup> Run</b> | $42.17 \pm 0.02$            | $42.09 \pm 0.02$        |

Table 5.6: Comparison between results from time distribution and from datasets summation of the average proportion of light from S2 signal seen by bottom PMTs array with respect to the light seen by the combination of bottom and top PMTs arrays during the second science run.

why, despite of a non statistical overlap, the two columns give coherent results within 0.5 %, which is much smaller than systematical errors associated to S2. As a result, a larger value for the average results per science run will be used. It will take into account all systematic errors, especially the systematic error between two different source for the same detector settings. Thanks to this analysis, a final value per each science run is evaluated, corresponding to the average value between results from each source. The associated errors correspond to the maximum difference between results from sources and the final values. All of these three average values and errors are reported in Table 5.7.

| Science run | First          | Second         | Third          |
|-------------|----------------|----------------|----------------|
| $R_b$ [%]   | $44.6 \pm 1.1$ | $41.9 \pm 1.3$ | $42.2 \pm 1.6$ |

Table 5.7: Average proportion of light from S2 signal seen by bottom PMTs array with respect to the combination of bottom and top PMTs arrays for each science run.

Since the stability in time and the independence from the choice of the used calibration source have been demonstrated, the same method has been applied to each file used in the analysis of the variation of the secondary scintillation gain as a function of the electric field. Thanks to this extension, the comparison between the secondary scintillation gain, and the gain associated to the main S2 signal for the evaluation of the electrons extraction yield can be done. This is detailed in the next section.

## 5.6 Outcome of the analysis: electrons extraction yield

By using the average proportion of light from S2 signal seen by bottom PMTs array, the secondary scintillation gain  $\mu_1$  and the gain for the main S2 signal  $G_{S2}$  can be rescaled to the same number of PMTs. However, the two quantities are expressed into two different units. The former is expressed in photoelectron per electron, while the latter is expressed in photoelectron per unit of deposited energy expressed in keV. This deposited energy corresponds in this specific case to the full energy of the  $\gamma$  ray from the  $^{137}\text{Cs}$  calibration source, i.e. 662 keV. As a result, the average energy needed for an ionising ray or particle to create an electron-ion pair from the encountered xenon atom can be calculated. This energy is usually known in literature as *W-value*, and is equal to  $15.6 \pm 0.3$  eV [115] for a very large electric drift field, as it is also mentioned in Table 2.1. Thus, the electrons extraction yield  $\epsilon_{extr}$  can be expressed as:

$$\epsilon_{extr} = \frac{G_{S2} [PE/eV] \times W [eV/e^-]}{\mu_1 [PE/e^-]} \quad (5.11)$$

where the W-value  $W$  can be expressed in electron volt per electron since one electron is associated. The term S2 gain is already affected by the attenuation of the signal due to the non-extraction of electron from liquid to gas phase. This is however not the case for the secondary scintillation gain, since either the electron is extracted and thus a 100 % of extraction yield is reached, or the electron is not extracted and no corresponding low energy S2 signal occur.

In order to apply Equation 5.11 to the XENON100 experiment, the W-value needs to be adapted to the experimental field of 0.53 kV/cm. This can be done by using the variation of the charge yield  $Q(E)$  for a drift field  $E$ , and normalized to the charge at infinite drift field  $Q_0$  [167], also called *relative charge yield*, as illustrated in Figure 5.16.

In a similar way, the variation of the light yield in LXe  $S(E)$  for a drift field  $E$  normalized to the light emitted when no drift field is applied  $S_0$  is also represented. This demonstrates thus the anti-correlation between the two quantities because of the electric drift field in LXe that will favourite either electron-ion recombination for low values, or electrons and ions drift in opposite directions for higher values. The experimental set-up used for these measurements correspond to a single phase LXe TPC. The light is detected by two PMTs individually placed at the top and at the bottom of the TPC, while the electrons are collected by an anode mesh. No segmented anode is used since the aim of the experiment is not the reconstruction of the position of the scattering, but the highest collection of the two signals.

In Figure 5.16, the relative charge is affected by a large systematic error due to the uncertainty

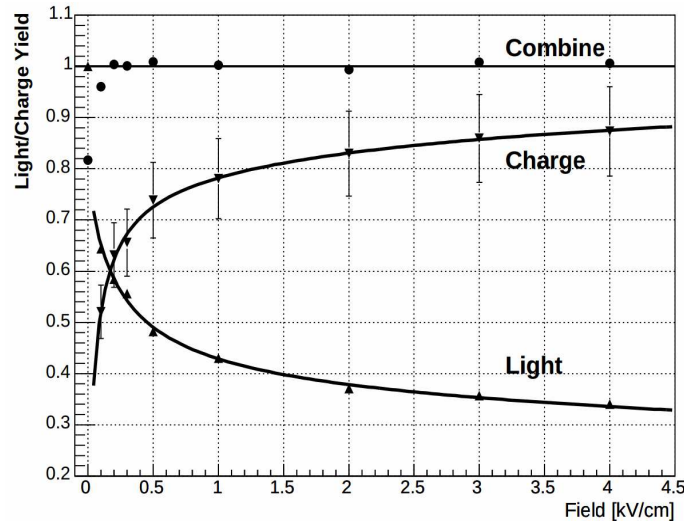


Figure 5.16: Anti-correlation of the variation of the relative light and charge yield as a function of the drifting electric field in LXe. Figure from [167].

in pre-amplifier calibration, and showed by the large error bars on the charge curve. Therefore, while their variation as a function of the field is well known, the absolute value is known only at level of 5 – 10 %.

The relative charge yield value corresponding to a drift field of 0.53 kV/cm is equal to  $T_{ee} = 0.740 \pm 0.075$ . An adapted expression of the W-value can be then inferred from this result by rescaling it with the relative charge yield given above. This leads to a W-value of  $W' = W/T_{ee} = 21.1 \pm 2.2$  eV/e<sup>-</sup>. Due to the large associated error, it is mandatory to calculate a more accurate W-value by using the XENON100 data.

For this purpose, a set of data candidate with the specific following properties should be found:

- The electric field in the gas phase should be enough high to expect a 100 % of electrons extraction yield, so that the calculation of  $W'$  (or  $T_{ee}$ ) will be independent from it.
- Data should be acquired in stable detector settings in order to be combined together.
- The resulting cumulated data statistics should be high enough to reduce the statistical uncertainties, so that almost only systematical errors will remain.
- Since the calculation of  $W$  will be done by using from the Formula 5.11, a very accurate knowledge of the secondary scintillation gain and the S2 gain in the same detector settings is mandatory.

Based on preliminary analysis on the trend of the electrons extraction yield – especially because of a plateau that was observed for the highest part of the analysed region of the electric field – the best candidate corresponds to the combination of all the calibration data acquired with the <sup>137</sup>Cs source under the first science run electric field configurations. The gaseous electric field was then close to 12 kV/cm. For such data, the S2 gain is calculated by combining all the available datasets, as it is shown by Figure 5.17(a) which is similar to Figure 2.11(a). The photoelectric

peak is selected by identifying single scatter events, i.e. events with very low energy secondary S1 and S2 signals, for a deposited energy equal to 662 keV. In order to not be biased from weaker collection efficiency on the border of the TPC, only events inside an horizontal radius of 12 cm from the center of the chamber are selected.

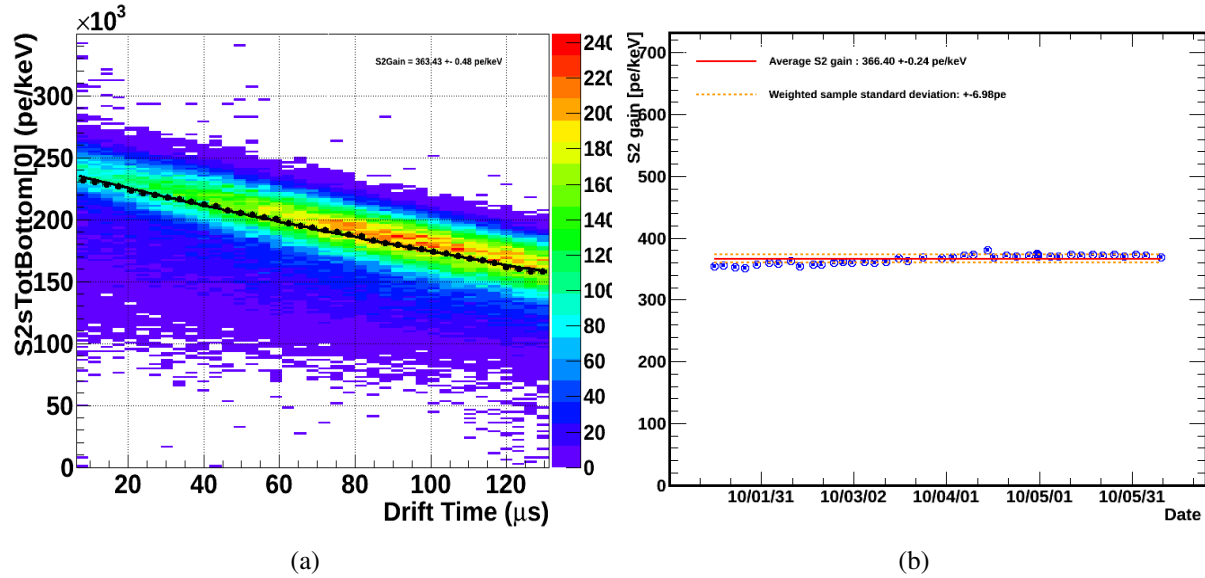


Figure 5.17: (a) S2 gain calculation for the first science run, (b) stability in time of the S2 gain during the first science run.

Thanks to the large amount of acquired data in stable conditions, the S2 gain is measured with a very high statistical precision, and is equal to  $G_{S2} = 363.43 \pm 0.48$  PE/keV. However, in order to also take into account the variations of the S2 gain during this science run, the weighted standard deviation of the distribution in time of the S2 gain will be used for the error associated to the S2 gain in the calculation of the W-value. This weighted standard deviation is equal to 6.98 PE/keV and is represented by the orange dashed lines on the distribution in time of the S2 gain shown in Figure 5.17(b). The red solid line represents the associated average value. The standard deviation is not showed since it is too small to be represented. Their values are equal to 366.40 PE/keV and 0.24 PE/keV respectively.

The W-value can be then calculated using Equation 5.11, assuming an electrons extraction yield  $\epsilon_{extr}$  equal to the unity:

$$W'[eV] = \frac{1000 \times \mu_1 [PE/e^-] \times R_b}{G_{S2} [PE/keV] \times \epsilon_{extr}} \quad (5.12)$$

where the secondary scintillation gain value is equal to  $\mu_1 = 18.65 \pm 0.38$  PE as reported in Table 5.4. This exact average value could be also calculated by using only the  $^{137}\text{Cs}$  calibration source for this specific run, by taking the average result between the fit with either a minimum intensity threshold for the main S2 above 10 kPE, or above 30 kPE. As a result, the reference value for the associated error, presented also in table 5.4, is considered.

The value of the ratio of light from S2 signals seen by the bottom PMT array is then equal

to  $R_b = 45.77 \pm 0.07 \%$ . This latter quantities have been calculated with the combination of all the available datasets acquired with the  $^{137}\text{Cs}$  calibration source during the first science run, in order to effectively consider only results from this specific source for all the parameters of this formula. No weighed standard deviation is used for this ratio, due to its very high stability in time. The W-value obtained with Equation 5.12 is equal to  $W' = 23.5 \pm 0.7 \text{ eV/e}^-$ , in good agreement with  $21.1 \pm 2.2 \text{ eV/e}^-$ . Moreover, by dividing this results with the W-value measured for a very high drift field, i.e. when no electron-ion recombination occurs, the proportion of electrons that effectively escape to recombination for a drift field of 0.53 kV/cm can be calculated. This proportion is equal to  $T_{ee} = 66 \pm 2 \%$ , which is of course still in agreement with the published relative charge yield  $74 \pm 7 \%$  [167], with however a better precision. It is also in good agreement with prediction from the NEST model [131], as illustrated by Figure 5.18.

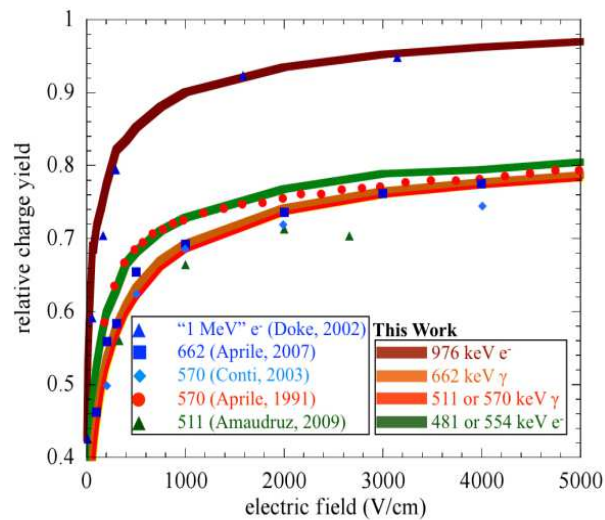


Figure 5.18: Relative charge yield as a function of the electric field in the LXe. Figure from [131].

These results are however valid only for a drift field in LXe equal to 0.53 kV/cm. This means that the data acquired in different electric field conditions right before the third science run can be not used due to the cathode voltage that was lowered from 16 kV/cm down to 15 kV/cm because of noise for higher absolute value. Another specific calculation of the W-value is mandatory before using them, and no data similar to the first science run with the drift field in LXe of the third one are available. Moreover, the data acquired during the specific run in Spring 2014 can also not be used, due to the noisy events also observed at higher energy and that reduced dramatically the proportion of recorded photoelectric effect, preventing the evaluation of the corresponding S2 gain.

Consequently, only the data acquired with the  $^{137}\text{Cs}$  calibration source right before the second science run can be used, since for the same reason than for the third science run, no analysis can be done for the W-value calculated with  $^{60}\text{Co}$  calibration source. This is motivated by the aim to be safe from any small difference due to the energy of the original  $\gamma$  ray, and since the identification of the different photoelectric effect from each  $\gamma$  ray from this source is more difficult. For the remaining data, the S2 gain and the ratio of light seen by bottom PMTs array are calculated. Combined with the corresponding secondary scintillation gain calculated in Section 5.4 and the W-

value calculated in the present one, the electrons extraction yield for each dataset can be calculated.

The electric field calculated for these yield is slightly different from the value used in Figure 5.10. The latter value corresponds to an average electric field between the surface and the anode, and was used since the emission of light during the S2 signals, at high or low energy, occur at different altitudes in the gas, while the extraction investigated here occur exactly at the liquid surface. As a result, a first simulation of this specific electric field has been done by the XENON Collaboration using the software *Garfield*. It was simplified as a two dimensional approximation of the detector. The meshes were then replaced by wires. The resulting electric field were then closer to the real case, with still remaining small differences because of the hexagonal pattern of the real meshes. At the time of writing, it has however not been stated whether this analysis will be extended to three dimensions with the aim of an application for XENON1T, or not.

Several electric field configurations have been tested. Their comparison with the respective results from parallel-plate capacitor model has shown a linear dependency between the two results, due to the inhomogeneity of the electric fields shells. This relationship is illustrated by Figure 5.19(a) that shows the variations of the electric fields values deduced from simulation as a function of the electric fields values deduced from the parallel-plate capacitor model. The dependency is fitted by a linear function, leading to the following relationship:

$$E_{gas_{liq.surf.}} = E_{gas_{average}} \times (0.891 \pm 0.001) + (0.028 \pm 0.010) \quad (5.13)$$

The weaker value of the slope of the dependency with respect to the unity is due to the inhomogeneity of the fields at the liquid surface that make it lower than a constant average field for parallel-plate capacitor.

The variation of the electrons extraction yield as a function of the electric field values inferred from the correction given by the Formula 5.13 is represented by blue markers in Figure 5.19(b) [157]. Three vertical black dashed line represent the electric field for the three science runs, demonstrating an electrons extraction yield at the unity for the first and third one, or very close to unity for the second one, with an electrons extraction yield equal to  $96.45 \pm 3.53 \%$  for this latter. The large errors on this value for the second science run is due to the consideration of only one dataset acquired before the beginning of this run, with different liquid level and anode voltage configurations that lead to the same electric field value in the gas phase. The 100 % extraction yield is reached for electric field at the liquid surface higher than 10 kV/cm. The probability of electron extraction from the liquid to the gas phase could be associated to the quantum tunnelling for which the barrier is the liquid-gas interface [168]. This process is illustrated by Figure 5.20, where the potential energy  $V$  applied to an electron is expressed as a function of the vertical position of the electron during its drift.  $\epsilon_1$  and  $\epsilon_2$  correspond to the dielectric constant in the liquid and the gas phase respectively. As it has been mentioned in Section 4.1.3, the electrons that remain in the liquid phase are finally extracted with a time delay. It is also possible that part of these electrons thermalise and are captured by impurities such as dioxygen molecules.

For comparison with previous published measurements, the results from [128] are also presented in purple in Figure 5.19(b). While a good agreement between results from the two experi-

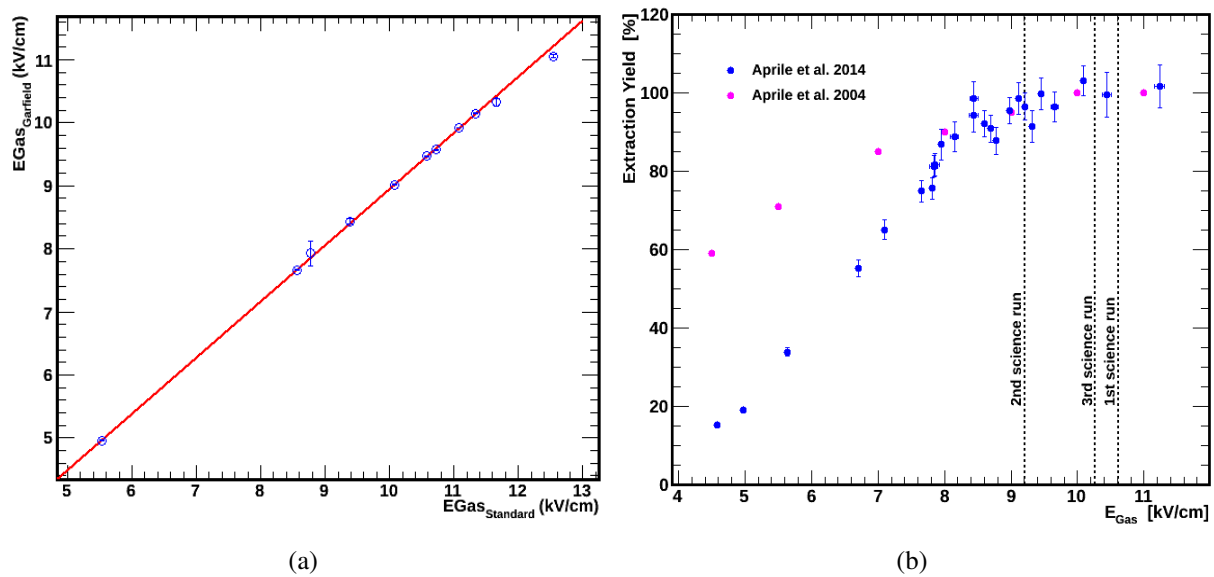


Figure 5.19: (a) Comparison between electric fields values deduced from simulation and electric fields values deduced from the parallel-plate capacitor model, and (b) variation of the electrons extraction yield as a function of the electric field in the gas phase, published in [157]. The results from the present analysis are shown in blue, while results from previous measurements [128] are also shown in purple for comparison.

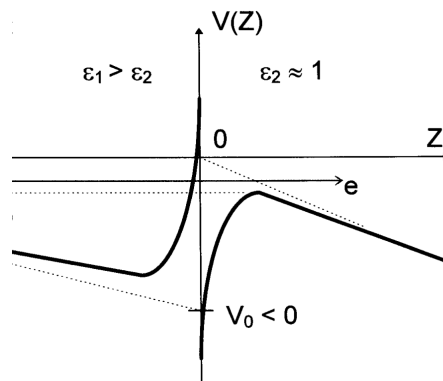


Figure 5.20: Potential energy applied to a drifting electron in a dual phase TPC as a function of its vertical position close to the interface. Figure from [168].

ments is observed for an electric field in gas above 8 kV/cm, a sharper decrease of the extraction yield is noticed for lower fields for XENON100. An uncertainty due to less precision on the liquid level measurements from the other detector could explain the difference between the two trends [158].

## 5.7 Outcome of the analysis: from S1 and S2 to drifting electrons and emitted photons with the $^{137}\text{Cs}$ source as an example

Thanks to the previous sections, all the terms used for the example presented in Section 3.1.3 on the S1 and S2 signals emitted during the photoelectric effect of a  $\gamma$  ray emitted by the  $^{137}\text{Cs}$  calibration source have been detailed. The explanations for their calculation can be now given.

S1 signals can be used to establish a quantity called light yield ( $LY$ ),  $S(E)$ , that depends from the electric field in LXe. This quantity corresponds to all the light detected during a S1 signal, and is expressed in photoelectrons per unit of deposited energy. It will take thus into account all the light emitted during the relaxation of all the dimers created either by the excitation of the encountered xenon atoms, or by the recombination of a part of the electrons previously released during the ionisation of the other encountered xenon atoms. All these emissions follow the corresponding process among the two described in Section 2.3.3.

Under the experimental conditions of the first science run, this LY is of the order of 1.6 PE/keV. Such a signal is furthermore obtained in photoelectric effect conditions, meaning that the 662 keV of the energy of the original  $\gamma$  ray have been transferred during this scattering. The corresponding S1 signal is thus equal to about 1060 PE.

In order to estimate the number of photons emitted during a such S1 signal, some additional experimental quantities should be considered. The first one corresponds to the average collection efficiency of photons by the PMTs,  $\bar{\delta}$ , usually known as the average Light Collection Efficiency ( $LCE$ ). This term is close to 24% [169] for a S1 signal in the middle of the target volume.

The next correction term that has to be considered then corresponds to the average PMTs' capability to release an electron for a scattering photon. This term is usually known as the average PMT's Quantum Efficiency ( $QE$ ),  $\bar{\eta}$ , and is equal to about 25% and 30% for top and bottom arrays respectively [169].

A second geometrical term takes then into account the average part of photons among all those that are collected by each PMT window, and that would effectively extract an electron towards the first dynode of the PMTs, assuming a 100% efficiency of electrons extraction yield from the photoelectric effect. Indeed, due to geometrical configuration, electrons released by photons scattering on the border of each photocathode would not necessarily be focused toward the first dynode, leading to no signal for the concerned PMTs. This correction term is usually known as the average Collection Efficiency ( $CE$ )  $\bar{\epsilon}$ , and is equal to about 80% [169] for XENON100's PMTs.

Thus, the number  $N_{PE}$  of photoelectrons per each signal, S1 or S2, can be expressed as a combination of the number  $N_{ph}$  of emitted photons per each signal, and vice versa:

$$N_{PE} = N_{ph} \bar{\delta} \bar{\eta} \bar{\epsilon} \quad (5.14)$$

The number  $N_{ph}$  depends from the experimental conditions. Thus, in case of a full absorption by photoelectric effect of a  $\gamma$  ray induced by a  $^{137}\text{Cs}$  source under a drift field of 0.53 kV/cm in

LXe, the associated signal S1 corresponds to the emission of about  $1.8 \cdot 10^5$  photons.

Moreover, as illustrated in Section 2.4.1.1, the S2 signal induced by  $^{137}\text{Cs}$  photoelectric effect can be calculated without any correction for the attenuation of the drifting electronic cloud due to electronegative impurities. This can be done by extrapolating the exponential curve of the S2 signal versus the drift time in order to select a scattering close to the ground mesh. Under the same detector settings than for S1, and with this scattering depth condition, the measured S2 signal is about 363 PE/keV. This corresponds to the *S2 gain*  $G_{S2}$  mentioned in Section 5.5 and measured for the first science run detector settings.

In the contrary to S1, such a signal corresponds however to a signal summed over only all bottom PMTs, in order to avoid the saturation of PMTs from top array. The rescaling to the whole TPC is done by using the fraction of light seen by bottom array with respect to the combined two arrays. This fraction  $R_b$  is about of 45.8% for S2 signals under these detector settings, as it has been calculated for  $^{137}\text{Cs}$  calibration source with the method presented in Section 5.5.

Thus, as illustrated by the Equation 5.15, the number of measured photoelectrons for all the PMTs of the TPC for such S2 signal can be calculated. Since the considered S2 signal corresponds to the  $^{137}\text{Cs}$  photoelectric peak, the deposited energy is  $E_{dep} = 662$  keV. The corresponding number of photoelectrons  $N_{PE}$  that create this S2 signal is then of the order of  $5.2 \cdot 10^5$  PE.

$$N_{PE} = \frac{G_{S2} \times E_{dep}}{R_b} \quad (5.15)$$

As for S1, the corresponding average number of emitted photons can be determined thanks to the Formula 5.14, by using for S2 signals an average light collection efficiency of 15.2% and 7% for top and bottom arrays respectively. This number is about  $1.1 \cdot 10^7$  photons.

As a complement to this example, it is also possible to calculate the number of electrons  $N_{e^-}$  drifting in the gas phase during this S2 signal. To do that, the average number of photoelectrons  $N_{PE_{e^-}}$  measured for one electron drifting in gas phase in these very same detector settings has to be considered. A such number corresponds to the *secondary scintillation gain*  $\mu_1$  and is presented in Section 5.2. It is equal to 18.65 PE/e- if calculated either with only the  $^{137}\text{Cs}$  calibration source or with the four sources available during the first science run. The corresponding number of electrons is then defined by Formula 5.16 and is of the order of  $2.8 \cdot 10^4$  electrons.

$$N_{e^-} = \frac{N_{PE}}{N_{PE_{e^-}}} \quad (5.16)$$

By combining results from Equations 5.14 and 5.16, the number  $N_{ph_{e^-}}$  of emitted photons per electrons drifting in the gas phase can be inferred. This number is about 390 emitted photons per electron drifting in the gas phase.

Furthermore, the number of drifting electrons can be also calculated by dividing the total deposited energy, i.e.  $E_{dep} = 662$  keV, by the average energy  $W = 23.5 \pm 0.7$  eV/e<sup>-</sup> needed to create one drifting electron for a drifting field of 0.53 kV/cm, as detailed in Section 5.6. This energy  $W$  includes the LXe ionisation potential of 9.28 eV [114], the part of energy transferred

to excitation states and the proportion of electrons that recombine. This latter term explains the difference between this value of  $W$  and the value of  $W = 15.6 \pm 0.3 \text{ eV}$  per created electron-ion pair [114] usually found in literature, and corresponding to a much higher drift field in LXe.

A similar calculation could be done for the average number of photons emitted in the liquid phase, including photons emission due to recombination. However, no value has been calculated for the average energy needed for a single photon production in LXe under an electric drift field of  $0.53 \text{ kV/cm}$ . The value of  $W_{ph} = 13.8 \pm 0.9 \text{ eV/ph}$  [114] usually found in literature corresponds to an LXe experiment with no drift field and for the perfect case where all the electrons will effectively recombine.

All the results presented in this section have been previously summarized in Table 3.1, in Chapter 2.

## 5.8 Applications and perspectives

In addition to the analysis of the electrons extraction yield for dual-phase noble gas TPCs, single electrons signals have also several other applications that are reviewed in the present section.

### 5.8.1 Detector detector settings optimisation

In order to improve the sensitivity of the detector, it is needed to perform during the early step of any science run the configuration of the electric field that will allow the best compromise between the intensity of the light emitted per electron, and the electrons extraction yield from the liquid to the gas phase. For this purpose, since both terms depend on the electric field in the gas phase, two quantities can be set:

1. The anode voltage
2. The gas gap, determined by the liquid level

In the usual experimental conditions, the anode voltage is however quickly established, since it has been observed starting from the second science run that electronic noise occurs for an anode voltage above  $4.4 \text{ kV}$ . The optimisation of the detector response can be then investigated for several gas gap conditions by changing the liquid level. The optimized detector settings can be defined as the conditions for which a  $100 \%$  of electrons extraction yield from the liquid to the gas phase, combined with the highest possible intensity for the S2 signal. According to Figure 5.19(b), the former condition can be reached for an electric field at the liquid surface above  $10 \text{ kV/cm}$ , corresponding to an average electric field in the gas phase above  $11.3 \text{ kV/cm}$ . The latter condition can be then at least equal to the best case among the three science runs, which corresponds to a secondary scintillation gain equal to 20 PE.

As a result, by combining the formulas 5.8 and 5.10, the variation of the secondary scintillation gain can be investigated as a function of the electric field for a fixed value of the anode voltage, following the parallel-plate capacitor approximation. While experimental conditions have fixed a ceil value equal to  $4.4 \text{ kV}$  for this voltage, the study can however be extended to lower values.

For each of them, the modification of the electric field is thus only due to modifications of the gas gap, corresponding to modifications of the liquid level for the experimental point of view. Such distribution of the secondary scintillation gain is presented in Figure 5.21(a).

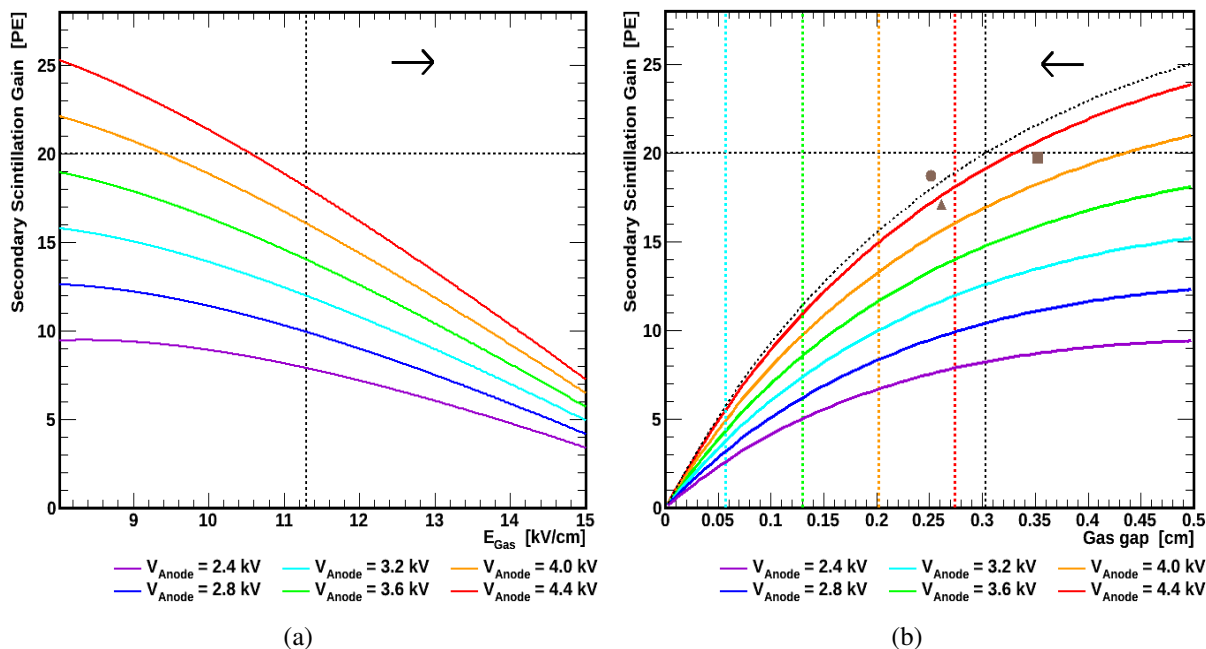


Figure 5.21: Secondary scintillation gain for a fixed anode voltage as a function of (a) the electric field, and (b) the gas gap. The lines are explained in the text. The arrows indicate the direction to follow to increase the extraction yield, and the three brown round, square and triangle markers illustrate also the secondary scintillation gain and liquid level for the first, second and third science run respectively.

Each value of the anode voltage is represented by a different color, with hot colors for higher values. The vertical dashed line corresponds to the 100 % of electrons extraction yield reached at 11.3 kV/cm, while the horizontal one corresponds to the aimed value of 20 PE for the secondary scintillation gain. This analysis shows that no gas gap configuration for an anode voltage lower or equal to 4.4 kV can provide both a 100 % of electrons extraction yield and a secondary scintillation gain at least equal to 20 PE. As expected from the equation 5.8, the secondary scintillation gain decreases with the decrease of the anode voltage. Moreover, this gain also decreases with the gaseous electric field when only the gas gap is modified. This means that higher values of the gain are obtained for lower values of the electric field. This result is important for the full understanding of Figure 5.21(b).

Indeed, the same analysis can be done for the variation of the secondary scintillation gain as a function of the gas gap, as represented in Figure 5.21(b). As for the previous plot, the horizontal dashed line represents the aimed value of 20 PE for the secondary scintillation gain. For each anode voltage configuration, a vertical dashed line with the same color is associated and illustrates the liquid level value for which the electric field is equal to 11.3 kV/cm. Since the trend of the variation of the secondary scintillation gain as a function of the gas gap is in opposition to the variation as a function of the electric field, with lower gain for lower gas gap which is physically expected, each gas gap value on the left side of each dashed line correspond to a 100 % of electrons

extraction yield from liquid to the gas phase. As also observed previously on Figure 5.21(a), this demonstrated that no gas gap configuration for an anode voltage lower or equal to 4.4 kV would provide both a 100 % of electrons extraction yield and a secondary scintillation gain at least equal to 20 PE. This also demonstrates that for an anode voltage lower or equal to about 2.9 kV, no gas gap configuration would provide a 100 % of electrons extraction yield.

For illustration, the black dashed curve represents the optimal case of an anode voltage equal to 4.562 kV, for which the two conditions on the gain and on the extraction yield can be satisfied. The corresponding gas gap configuration is shown by the vertical dashed line, and is equal to 0.304 cm which corresponds to a liquid level equal to 0.696 cm. The three brown round, square and triangle markers illustrate also the secondary scintillation gain and liquid level for the first, second and third science run respectively. They demonstrate that for each of them, only one of the two conditions is satisfied, with a 100 % of electrons extraction yield reached for the first and third one, and a secondary scintillation gain very close to 20 PE reached for the second one since it corresponds to the optimal amplification.

This analysis has been done by using the XENON100 configuration, while the experiment is currently finishing. This has however demonstrated the feasibility of the analysis, that would be extended to XENON1T and XENONnT as soon as all experimental conditions such as the maximum value of the anode voltage, will be fixed. Same method can be also applied to other noble gas dual phase TPC.

## 5.8.2 Multiple scattering rejections

As it was previously mentioned in Section 4.2.3, the single electrons signals can be used for multiple scattering rejections, such as multiple scatterings of neutrons or successive Compton scatterings from  $\gamma$  ray. Since they corresponds to few individual electrons extracted in time coincidence, an algorithm can be performed for the research and the identification of each of the cluster of light in the PMTs pattern that belongs to each of these electrons. At the time of writing, the analysis has been performed first on the identification of each cluster of optically separated single electrons [163], such as for the case represented by Figure 4.10, and will be then improved in order to allow the identification of each individual single electron signal in a long light track made by two or more electrons.

The purpose of this analysis is then to extend such an identification to higher energies by using  $^{241}\text{Am}^9\text{Be}$  calibration data, in order to improve the identification of neutrons but also all other multiple scattering, which will have all a higher probability to occur in XENON1T because of its larger detector size.

## 5.8.3 An homogeneously distributed source of events for light correction

As it has been presented in Section 3.1.1, the two S1 and S2 signals are respectively corrected for the dark matter search in order to take into account for the former the light collection efficiency due to the radial and depth position of scattering, and for the later the light collection efficiency, the elongation of the electronic cloud, and attenuation of the signal again due to the radial and depth

position of scattering. This analysis is usually done with the data taken during each  $^{241}\text{Am}^9\text{Be}$  calibration runs by taking advantage of the homogeneous distribution of activated xenon isotopes  $^{129}\text{Xe}$  and  $^{131}\text{Xe}$ .

Thanks to the very accurate knowledge of the secondary scintillation gain per science run, single electrons signals occurring after a main S2 signal can be very well identified leading to an accurate reconstruction of their electron emission position. As a results this corresponds to another available source for light correction due to emission position. During the third science runs, a first comparison between results from  $^{241}\text{Am}^9\text{Be}$  calibration and single electrons signal for such corrections has been done, with slightly less efficiency for the latter, due to less uniform correction. The two methods are however in very good agreement, allowing single electrons signals to be at least an additional calibration source that can be used for cross check for S2 signals light correction.

Since it was the first time that single electrons signals were used for this purpose, there are still spaces for analysis improvements in order to be used as the main calibration source for S2 signals light corrections for dark matter search with XENON1T.

#### 5.8.4 Charge signal modelling simulation

The simulations of interactions inside the current XENON100 detector, or inside the very next one XENON1T provide only information on the total deposited energy per scattering. In order to be reliable to real data, the corresponding S1 and, if the interaction occurs above the cathode mesh, the S2 signals need to be predicted. Indeed, based on the Thomas and Imel model [124] presented in Section 2.3.2, the number of photons produced during the S1 and the number of electron that effectively start to drift toward the gas phase can be estimated. Then, in order to draw the signal S1, the number of detected photons need to be calculated.

For this purpose, several parameters such as the light collection efficiency by PMTs as a function of the emission position and the PMTs quantum efficiency are used by following the example presented in Section 3.1.3. Combined with the known or expected light yield, and the quenching factor in case of nuclear recoil, the photons detection efficiency for S1 signal can be estimated. The number of detected photons can be then calculated by applying a binomial sampling with this efficiency to the number of emitted photons. A similar process needs also to be applied to the number of detected photons in order to take into account the quantum and electron collection efficiency of the PMTs.

For the S2 signal, the attenuation of the electronic cloud due to the absorption by impurities during the drift and eventually the electrons extraction yield from the liquid to the gas phase have to be taken into account. These correction factors depend on the assumed LXe purity and the aimed electric fields configuration in each phase. The intensity of the S2 signal can be then calculated by using the two formula 5.9 and 5.10. A Gaussian sampling of this signal with a standard deviation close to  $6.5 - 7$  PE, as presented in Table 5.4, can be also done in order to take into account the standard deviation of the secondary scintillation gain.

A complete model should also take into account the z-dispersion of the main cloud in order to be able to draw the time duration of the signal.

### 5.8.5 Single electrons signals for background estimation

As it has been presented in Section 3.3.3.2, two single scatter events were identified as mimicking the dark matter signals signature during the second science run, and are coming from fluctuation of the background. Indeed, as discussed in Section 3.3.3.2, the number of background events in the benchmark region during the 225 live days of dark matter exposure during the second science run was estimated to  $(1.0 \pm 0.2)$  events thanks to robust calibration and Monte-Carlo prediction. The two events finally observed during the data unblinding correspond then to statistical fluctuation of the expected background, with a Poisson fluctuation probability of 26.4 % to varie from one up to two events.

The intensity of the raw S1 and S2 signals associated to these two events, i.e. without including any spatial correction from light distribution, are represented in Table 5.8. Thanks to the results presented in Table 5.4, the number of electrons from each signal of these S2 signals can be inferred, as it is reported below.

| Event | S1 [PE] | S2 [PE] | S2 [ $e^-$ ] |
|-------|---------|---------|--------------|
| #1    | 4.508   | 325.66  | 16 - 17      |
| #2    | 3.622   | 274.423 | 14           |

Table 5.8: Summary of the S1 and S2 signals of the two background events with a dark matter signature observed during the second science run.

In addition, the distribution of the S2 signals from bottom PMTs array over S1 signals in logarithmic scale as a function of the deposited in the LXe such as presented in Figure 3.11 can be extended to lower S2 over S1 values by suppressing the threshold value on the main S2 signal, as presented for illustration in Figure 5.22.

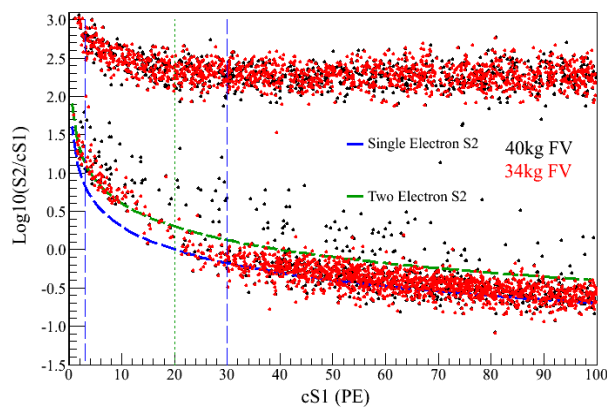


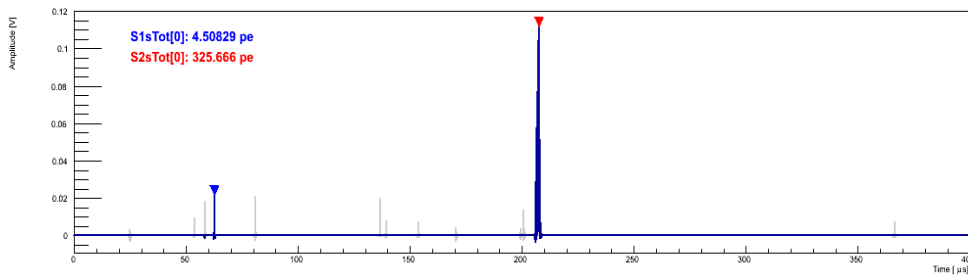
Figure 5.22: Ratio of the S2 signal from bottom PMTs array over S1 signal in logarithmic scale as a function of the deposited energy in the LXe. Figure from the XENON100 collaboration.

The results coming from the dark matter search during the second science run are represented in red and black for results using a fiducial volume of 34 kg and 40 kg respectively. Furthermore, the nuclear recoil band usually drawn from calibration with the  $^{241}\text{Am}^9\text{Be}$  source is not represented on this figure. The electronic recoil band is however very well represented on the top

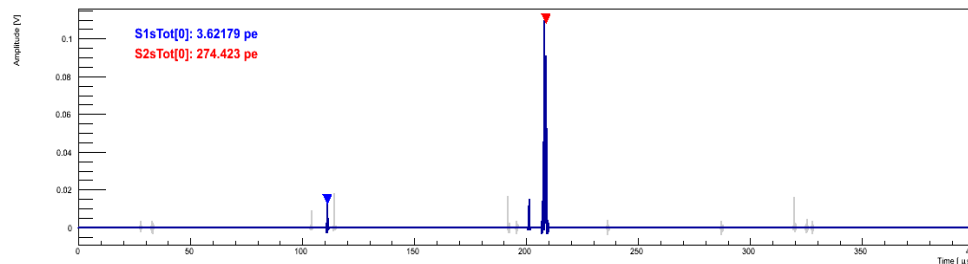
because of the  $\beta/\gamma$  background. Compared to Figure 3.11, the signals S1 and S2 used here are uncorrected signals, and the bands are not flattened.

Another distribution band can be now seen at low S2 over S1 signal ratio. It corresponds to events for which a single electrons signal, the main S2 signal on the waveform, is accidentally associated to a S1 signal. The distribution is thus mainly composed by pure single electron signals, however the contribution of more energetic single electrons signals is not negligible. As an illustration, the average values of the distributions of pure single electron signals and signals induced by two individual electrons extracted in time coincidence are represented by dashed blue and green line.

The two events observed during the second science run correspond to the two red markers close to the left vertical blue dashed line, with a S2 over S1 raw signals ratio in logarithmic scale equal or right below  $-2.0$ . There is thus probability for these events to correspond to a leakage of the single electrons signals band. This probability could be calculated thanks to the average value of the bands or single electrons signals induce by either one, two or event more individual single electrons extracted in time coincidence in the gas phase. This is however quickly excluded here due to the corresponding number of electrons for their S2 signals detailed in Table 5.8. Indeed, by analysing both the shape of their waveform, represented on Figure 5.23, the main S2 signal corresponds to the only one main single electrons signal, while if it was real individuals single electrons extracted in time coincidence and coming from a higher energetic S2 signal prior to the waveform, other signals induced by few single electrons should have also occur.



(a)



(b)

Figure 5.23: Waveform of the two events identified as mimicking the dark matter signals signature during the second science run: (a) event #1, and (b) event #2. The grey pulses correspond to noise signals and are thus not identified as either S1 or S2 signals.

In the same way, by analysing the shape of the light pattern on top PMTs array, represented on Figure 5.24, several individuals cluster of light should occur according to the single electrons

emission process, such as it was the case for the light distribution presented in Figure 4.10. The amplitude of the S2 signal per PMT is represented by color scale, with hot colors for higher energetic signal. The number associated to each color corresponds to the intensity of the signal and is expressed in photoelectron.

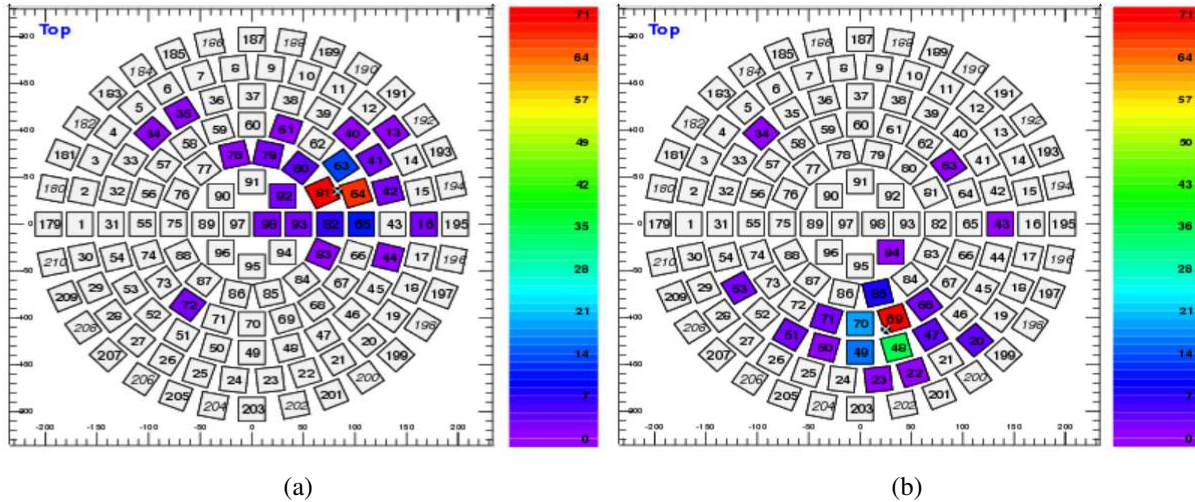


Figure 5.24: Light pattern on top PMTs array of the two events identified as mimicking the dark matter signals signature during the second science run: (a) event #1, and (b) event #2.

As a conclusion, these events do not correspond to a signature of S2 single electrons signals, and are fluctuation of the expected background, with a higher probability of coming from electronic background. It is then also important to remind that the data analysis performed by the XENON Collaboration was done in blinding mode, and that these two events were observed only during the final unblinding, and were not suppressed for the publication of the dark matter search results. As a consequence, this contributes to identify clearly the scientific results provided by the XENON Collaboration as honestest and very robust.

### 5.8.6 A S2-only analysis for Low-mass WIMP

Due to the unknown properties of dark matter, several models for a dark matter particle candidate have to be investigated. For the usual dark matter search made by the XENON Collaboration, the data analysis is focused on WIMP with a mass between few tens of GeV up to few hundreds of GeV. In addition, the search of axions and ALP was also performed by the Collaboration, such as it has been presented in Chapter 3. Some other dark matter search fields can be also investigated by XENON100, such as low mass WIMPs predicted by some theoretical models, and for which several direct dark matter search experiments already claimed in the past for a positive signature, even if some of them have retracted themselves after a while, as it has been presented in Section 1.6.

The nuclear recoil associated to a such WIMP will consist in only one S2 signal. Indeed, due to the weak transferred energy, the scintillation signal S1 will be almost absent. As a result and again because of the very weak transferred energy, the remaining S2 charge signal will be induced by a cloud of few electrons up to few tens of electrons. At the time of writing, this analysis made

by the XENON Collaboration is currently ongoing, with no final data selection cuts, that is why only qualitative explanations are given. More precise results will be published in the dedicated XENON100 S2-only low mass WIMP analysis.

Due to the expected specific signature of a low mass WIMP, the data selection should be slightly different than for the standard WIMPs search. As a result, while qualitative cuts such as for multiple scattering events and noisy waveforms rejection or the rejection of events in the TPC in coincidence with an event in the veto volume are the same or very similar, the selection on the intensities of the S1 and S2 signals is different. Thus, all events with a S1 above very few PE are rejected, since a low mass WIMP can not induce it. The selection window for the S2 signal is then set between about one hundred of photoelectrons up to about one thousand of photoelectrons, which corresponds to a cloud of few electrons up to few tens of electrons. This limit is not lowered in order to not be biased from single electrons signals, even if an additional data selection cut based on the minimum time between two successive events reduces dramatically the probability of time coincidence for delayed extractions of few individuals single electrons.

The deposited energy  $E_{nr}$ , expressed in keV, can be then inferred from the S2 signal expressed in PE thanks to the very accurate knowledges of the secondary scintillation gain  $\mu_1$  during each science run and expressed in PE/e<sup>-</sup>:

$$E_{nr} = \frac{S2}{\mu_1 \times Q_y} \quad (5.17)$$

where  $Q_y$ , expressed in electrons per unit of deposited energy in keV, is the assumed charge yield for a specific drift field in LXe, with a value based on model such as provided by NEST [170]. Due to the only use of the S2 signal, the z-position of the scattering is no longer available, as it is also the case for the discrimination between ER and NR. As a result, this lack of discrimination factor strongly reduces the sensitivity of the detector to dark matter nuclear scattering. As an example, a very similar analysis has been made for the XENON10 detector [104], with a sensitivity decrease by about two order of magnitude with respect to standard dark matter analysis.

### 5.8.7 Application to the detection of coherent neutrino-nucleus scattering

The latest application of the single electrons signal is similar to the one presented in Section 5.8.6, but does not aim specifically to the dark matter detection. The purpose of this application consists in measuring the coherent elastic scattering of neutrinos off nuclei by working also in a few electrons regime for the charge signal. Such a process is predicted by the Standard Model [171] but has never been observed. In case of a discovery, an oscillation of the rate of this signal could provide evidence for the existence of sterile neutrino [161], an hypothetical candidate for hot dark matter. As such, the sterile neutrino distribution would be associated to galaxies, as the WIMPs are. There would be thus a "wind" of sterile neutrinos as it is assumed to be for WIMPs, leading to an annual modulation of the interaction rate such as it has been seen in Section 1.6.1. On the contrary, the distribution of standard neutrinos is not associated to galaxies, and thus will not lead to any annual modulation of the interaction rate.

During the coherent scattering of a neutrino off a nucleus, there is a neutral boson  $Z^0$  exchange between the neutrino and the nucleus, leading to the recoil of this latter. In order to maintain the scattering coherence between neutrino and the nucleus as a whole and not between neutrino and nucleons, the maximum energy of the neutrino should be of the order of about 50 MeV. The minimum energy depends then on the average energy detection threshold  $\bar{E}_A$  of the detector [172], expressed in keV:

$$\bar{E}_A = \frac{2}{3} \frac{(E_\nu)^2}{A} \quad (5.18)$$

where  $A$  is mass number of the scattered nucleus, and  $E_\nu$  is the neutrino energy normalized to 1 MeV. As an illustration, the 6.6 keVnr coming from the lower bound of the sensitivity for the analysis of the second science run would correspond to a lower bound of 36 MeV for the neutrino energy. In a similar way to the S2-only analysis for dark matter search, the detector sensitivity threshold could be assumed to be lower, allowing to explore lower neutrino energy. However, since this analysis of the search for the low mass WIMP is not finished at the time of writing, no more assumption on the lowest neutrino accessible energy can be done.

The feasibility of the detection of this coherent scattering through a xenon dual-phase TPC was recently investigated by the ZEPLIN-III Collaboration [107]. They have identified several neutrino sources at such energies, corresponding to solar neutrinos, reactor neutrinos and stopped pion sources, assuming for each of them an efficient scenario for background rejection. Their conclusions have provided very good feasibility perspectives for the stopped pion source, and detection possibility for reactor neutrinos, with however some concerns for the efficiency of the realistic shielding strategy, that they request to be much higher than for underground WIMP search, and for the strong decrease of the LXe self-shielding efficiency because of the absence of the depth coordinate.

Thanks to a higher target mass, a more precise analysis could be done on current and future dual-phase xenon TPC, especially on XENON100 for which the single electrons signals are very well known. The detection of such neutrinos will however request much larger detector than XENON100.

## Conclusion

Thanks to the full understanding of the low energy S2 signals occurring after the main one of the same event, the average value of the signal induced by a single electron extracted into the gas phase has been calculated.

This analysis has demonstrated the stability of these signals for stable detector settings, both in time and with the selection of the source from which the ionising radiations and particles are coming. It has also provided reference values per science run for these signals, that are crucial for several currents and futures applications to the XENON detectors, for both the full understanding of the detector and the search of rare scatterings of low mass particles, such as it was presented in the last section.

A further similar analysis on single electrons signals occurring between the main S1 and S2 signals has also been performed, in order to investigate low energy S2 signals that were not biased from the main one. This analysis has excluded the possibility of using such signals for the applications mentioned above, due to the lack of temporal coincidence between individual extracted single electrons.

A complementary analysis of these signals as a function of the electric field in the gas phase has been also done. It has confirmed a linear amplification of this gain up to 12 kV/cm where an electronic avalanche starts to occur. These data were also used for the determination of the electrons extraction yield as a function of the electric field, demonstrating a value for this extraction yield close or equal to the unity for the three science runs of XENON100.

Such analysis has included also data coming from a dedicated calibration campaign. Unfortunately, most of the data acquired during this campaign could not have been used, due to electronic noise during the acquisition. For future analysis at low energy, it would be interesting to start a new calibration campaign, with data acquired under an average electric field in the gas phase either very low in order to investigate a new electric field region, or close to 10 – 12 kV/cm. This will thus give more informations on both the beginning of the electronic avalanche, and the region where the 100 % of electrons extraction yield is effectively reached.

Since the XENON100 era is almost over, such analysis will be performed in the early beginning of the XENON1T detector, in order to be able to define the best electric field configuration of the gas phase for both the charge signal and the electrons extraction yield for improving the sensitivity and reduce the background events in future science runs.

# Conclusion

The quest for dark matter detection is nowadays one of the hottest topics in particle physics as well as in astrophysics. While many indirect evidences have strongly indicated and constrained the dark matter contribution to the composition of the Universe, no clear signature of dark matter has been identified up to date. Several candidates were thus successively suggested in order to describe this component, from massive and compact astrophysical object up to hot or cold particles. Among this latter category, the most favoured candidates are the *Weakly Interacting Massive Particle (WIMPs)*.

There is thus a possibility to detect these particles through the identification of their scattering off a nucleus from a target matter. Several detectors, mainly based on crystals, bolometers and noble gas, were thus developed and placed in different underground laboratories for cosmic rays background rejection. The XENON100 experiment, as indicated by its name, concerns the latter detector technology. It consists then in a cylindrical dual-phase time projection chamber (*TPC*) of 62 kg of ultra-pure liquid xenon (*LXe*) used as both target and detection medium, surmounted by a gaseous xenon phase (*GXe*).

The interaction of a particle within the LXe induces the recoil of the encountered element of the xenon atoms: the nucleus (*Nuclear Recoil – NR*) for WIMPs particles and neutrons background, and the electron (*Electronic Recoil – ER*) for the  $\gamma$  rays and  $\beta$  particles from background sources. These two types of recoil create ionization electrons and prompt scintillation photons with different intensities for one type of recoil with respect to the other one. A part of the released electrons, depending again on this type of recoil, escapes to recombination and drifts thanks to a constant electric field towards the top of detector up to be extracted into the gas phase. In this region, they generate proportional scintillation photons. The photon emission in liquid phase is called the *scintillation signal (S1)*, while the photon emission in the gas phase is called the *ionisation signal (S2)*. Both of them are detected by two PMTs arrays placed at the top and the bottom of the TPC.

The direct dark matter search uses thus the different ratio of S2 over S1 signals in order to discriminate nuclear recoils, expected to be induced by WIMPs, from background electronic recoils. Since no clear dark matter signals have been seen up to date, efforts have been made to continue to reduce the exposition to background events for the future experiments, in order to strongly improve their sensitivity to dark matter. For the same purpose, efforts are also made on the development of new calibration strategies in order to reduce the sensitivity threshold to nu-

clear recoils. This is what the R&D calibrations performed on XENON100 aim for the upcoming detector XENON1T.

If the sensitivity limits of XENON100 for WIMP-nucleus scattering have been almost reached during the second science run, further important results for dark matter search achieved with this detector will be released soon, starting by the unblinding of the third science run. The sensitivity of this latter, while assumed to be lower than for the second one, will also provide additional data for the analysis of a possible annual modulation of the ER background because of the Earth's motion around the Sun, and due to the possible scatterings of dark matter particles off electrons according to some less favoured models.

In order to combine data from different science runs, it is thus mandatory to fully understand the two detectable signals S1 and S2. It is even more necessary to perfectly measure the latter signal for the search of low mass WIMPs, due to the expected absence of a truly detectable S1 signal.

Thus, for these signals characterisation reasons, an analysis of the very low energy part of the S2 signals spectrum has been performed and presented in this document. This analysis has been able to provide with a very high precision the average charge signal emitted even by a single electron. The analysis of the evolution of this average signal as a function of the electric field has demonstrated a linear amplification up to an electric field close to 12 kV/cm in the gas phase. This is then the highest electric field value before the apparition of electronic amplification. The results of these gains, and their linear fit by an empirical formula can be thus applied to not only the two applications mentioned above, but also to results from Monte Carlo simulations in order to draw charge signals.

The same data were also used for the calculation of the evolution of the electrons extraction yield from the liquid to the gas phase as a function of the electric field at the liquid surface. This analysis has thus demonstrated an extraction yield close or equal to the unity for the three science runs. It can be thus also used as a criteria for future optimisations of running conditions for any xenon dual phase TPC. The same analysis has also provided a value of the average energy  $W$ -value =  $23.5 \pm 0.7$  eV/e<sup>-</sup> needed for a recoiling particle to create an electron-ion pair. This value is compatible and has been thus calculated with a higher precision than previous published measurements. It has also revealed that under a drift field of 0.53 kV/cm in the xenon liquid phase, about  $66 \pm 2$  % of the electrons extracted by the recoiling one escape to the recombination and drift toward the gas phase. This measurement has been performed for the scattering by photoelectric effect of a 662 keV  $\gamma$  ray inside the liquid phase.

In addition, the study of these low energy charge signals has given clear observables for the validation of the scenario of the single electron emission. They are thus produced by photoelectric effect of ultraviolet photons emitted mainly during the main charge signal on impurities in liquid phase.

Moreover, thanks to the accurate evaluation of the average charge signal emitted by each single electron, all these low energy S2 signals can be then selected in order to be used for light corrections and for the development of an algorithm dedicated to multiple scatterings rejection. These two applications have been firstly tested on XENON100 data, providing very interesting results. They could be then improved with the future calibration data from XENON1T in order to

develop specific quality cuts for future dark matter data analysis.

As a summary, it has been demonstrated in this thesis that robust calculations on the average charge signal induced by one single electron could have been achieved even on bad quality calibrations data acquired during maintenance periods. This has thus shown the capability to perform analysis with low data statistics per each electric field configuration. Thanks to a new calibration campaign, more accurate results could be thus obtained. This would then allow to perform an analysis of the evolution of the relative charge yield, such as extracted during the  $W$ -value calculation, as a function of the applied drift field in LXe. This would thus provide informations on the part of the electrons that effectively escape to recombination.

Moreover, such analysis could be also performed for different calibration sources, in order to investigate different energies of background source. Such a calibration campaign will be carried out in the early running months of XENON1T, with the aim to be also used for the optimisation of the detector running conditions right before starting a first science run, and for simulations of emitted light and charge signals.



**Deuxième partie**

**Partie Française**



# Chapitre 6

## Analyse des signaux d'électrons uniques avec l'expérience de recherche directe de matière noire XENON100

La matière noire est un élément inconnu qui pourrait constituer environ un quart des constituants de l'Univers. Pour la détecter, le programme de recherche XENON, dont l'expérience XENON100 est la phase actuelle, utilise une chambre à projection temporelle au xénon liquide et gazeux. Les résultats reportés ici correspondent aux données acquises aux cours de 224,5 jours d'observation cumulés. Aucun signe d'interaction de matière noire avec des noyaux cibles n'a alors été observé. En complément de ces résultats, une analyse indépendante menée sur la réponse du détecteur aux signaux de charge émis par des électrons uniques est également présentée.

### Sommaire

---

|   |            |
|---|------------|
| <b>Introduction</b> . . . . .                             | <b>211</b> |
| <b>6.1 Le détecteur XENON100</b> . . . . .                | <b>212</b> |
| <b>6.2 La recherche des WIMP avec XENON100</b> . . . . .  | <b>214</b> |
| <b>6.3 Signaux de charge d'électron uniques</b> . . . . . | <b>216</b> |
| <b>Conclusion</b> . . . . .                               | <b>219</b> |

---

### Introduction

Les analyses des distributions de masses au sein de large structures astrophysiques, telles que les galaxies ou leurs amas, menées depuis la première partie du XX<sup>me</sup> siècle ont indiqué la présence d'une matière non-lumineuse qui contribuerait massivement à la dynamique de ces structures [1–12]. Cet élément inconnu s'appelle la *matière noire*. Elle constituerait environ 26,8 % de l'énergie totale de l'Univers [23].

Parmi tous les candidats qui furent tour à tour proposés pour expliquer cette matière noire, la famille de particules la plus favorisée est celle des WIMP [54, 56], difficile à observer car elles interagissent faiblement avec la matière. Pour les détecter de façon directe, il est possible de mesurer le recul nucléaire engendré par la diffusion d'une particule de matière noire sur un atome cible [70]. Pour y parvenir, l'expérience XENON100 [122] – la phase actuelle du programme de recherche directe de matière noire XENON – utilise une chambre à projection temporelle alliant une phase liquide de xénon constituant la cible à une phase gazeuse du même matériel.

Les résultats de recherche de matière noire présentés aux cours de ce chapitre correspondent aux principales données de l'expérience, qui furent acquises aux cours de 224,5 jours d'observation cumulés entre mars 2011 et avril 2012 [74]. Durant cette session de prise de données, aucun indice d'interaction de matière noire avec des noyaux cible n'a été observé. Cette prise de données a cependant permis d'atteindre une sensibilité pour la recherche de la matière noire jamais égalée jusqu'à l'automne 2013 [105].

Une analyse des données du détecteur indépendante de la recherche de matière noire est également présentée ici. Elle porte sur l'étude de la réponse du détecteur aux signaux de charge émis par des électrons uniques en phase gazeuse [157], allant de l'identification et de la compréhension de ces signaux, à leur caractérisation. Cette étude est complétée par une revue de plusieurs applications actuelles et envisagées des signaux d'électrons uniques.

## 6.1 Le détecteur XENON100

Le détecteur XENON100 est une chambre cylindrique à projection temporelle (*TPC*), constituée de deux phases : une phase liquide de 62 kg de xénon (*LXe*) surmontée d'une phase gazeuse (*GXe*). L'ensemble est entouré par 99 kg de xénon liquide supplémentaires, utilisés comme un volume veto scintillant. Il est séparé de la zone active de xénon par des panneaux de téflon sélectionnés pour leurs propriétés de réflectivité. Les deux volumes de xénon sont intégrés à l'intérieur d'un cryostat d'acier inoxydable à double épaisseur, lui-même entouré d'un coffrage de protection contre les rayonnements ionisants, constitué de couches successives de cuivre, polyéthylène, plomb et eau / polyéthylène en allant de l'intérieur vers l'extérieur.

L'objectif de cet assemblage de protections, depuis le volume veto de xénon jusqu'aux éléments d'eau et de polyéthylène à l'extérieur du coffrage, est de réduire au maximum l'exposition du volume cible de xénon au bruit de fond ambiant autour du détecteur. Celui-ci étant par ailleurs placé en laboratoire souterrain, sur le site du Gran Sasso en Italie, afin de se protéger des rayons cosmiques. Le détail de tous ces constituants de l'expérience est présenté dans [122].

Lorsqu'une particule incidente interagit au sein du détecteur, dans le volume cible de xénon, il induit le recul de la particule rencontrée : un électron pour une particule  $\beta$  ou un rayon  $\gamma$  incident, et un noyau pour un neutron ou un WIMP incident [70]. Le recul de ces deux particules va engendrer dans des proportions respectives l'excitation et l'ionisation des atomes de xénon rencontrés. La relaxation des atomes excités et la recombinaison des électrons avec les ions de xénon [124] vont donner lieu à l'émission d'un *signal de scintillation* (*S1*) par des photons ultraviolets [114].

En exerçant un champ électrique constant dans la phase liquide, une partie des électrons libérés va dériver vers la phase gazeuse pour y être extraits à l'aide d'un second champ électrique de plus

grande intensité. L'accélération des électrons dans la phase gazeuse va leur permettre d'engendrer à leur tour un signal lumineux par émission de photons ultraviolets. Ce signal est appelé *signal d'ionisation (S2)*.

Deux plans de photomultiplicateurs, situés au bas et au sommet de la chambre, vont détecter ces deux signaux S1 et S2. La position de l'interaction dans la phase liquide est ensuite reconstruite à l'aide de l'organisation concentrique des photomultiplicateurs situés en haut de la chambre pour la position radiale, obtenue avec une résolution de 3 mm ( $1\sigma$ ) [122]. La profondeur d'interaction est ensuite obtenue à l'aide de la différence de temps entre les deux signaux, correspondant au temps de dérive des électrons, avec une résolution de 0.3 mm ( $1\sigma$ ) [122].

Grâce à la combinaison du très grand pouvoir de reconstruction des positions d'interactions des TPC et de la propriété d'autoblindage de la zone externe de xénon liquide exclue géométriquement du volume final de recherche, la très grande majorité du bruit de fond issu des matériaux constituant le détecteur peut être rejetée. De plus, les différences de rapport des intensités des signaux S2 sur S1 pour les reculs nucléaires (NR) et électroniques (ER) permettent une sélection puissante des ces interactions engendrées par des neutrons ou des WIMP. La discrimination entre ces deux particules s'effectue ensuite en rejetant tous les événements ayant donné lieu à des interactions multiples au sein de la chambre. Ces derniers sont hautement probables pour des neutrons à mesure que l'on augmente la taille du détecteur, mais exclus pour des WIMP du fait de leur très faible taux d'interaction.

La figure 6.1 illustre l'interaction d'une particule incidente au sein de la phase liquide, conduisant à l'émission du signal S1. La dérive des électrons vers la phase gazeuse est également indiquée, ainsi que l'émission du signal S2 dans cette phase, dont la durée temporelle est liée aux différentes altitudes d'émission de photons par des atomes de xénon après excitation ou ionisation par les électrons. En complément, l'allure schématisée pour les deux signaux S1 et S2 sur les formes d'ondes en sortie des photomultiplicateurs est représenté pour les deux types de reculs : nucléaire et électronique.

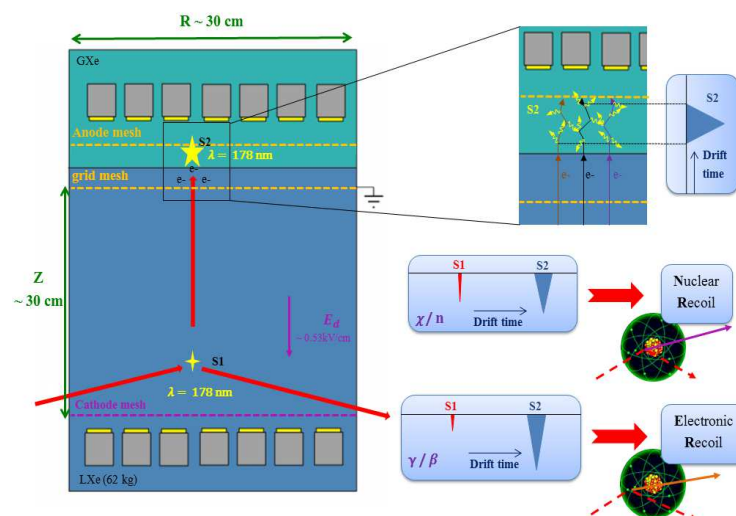


FIGURE 6.1 – Illustration du principe de détection de la chambre à projection temporelle XENON100.

## 6.2 La recherche des WIMP avec XENON100

Les résultats présentés ici correspondent à 224,6 jours d'observation cumulés pour la recherche de matière noire [74]. Ces données ont été régulièrement acquises pendant plus d'une année de fonctionnement continu du détecteur, entre mars 2011 et avril 2012, démontrant d'excellentes stabilités et performances de ce dernier.

Au cours de cette session de prise de données, une procédure pour masquer les données dans la région des signaux S1 et S2 attendus lors du passage d'un WIMP a été appliquée, l'analyse se faisant en aveugle. A l'issus de la session et lorsque toutes les coupures pour la réjection des évènements bruit de fond furent définies, les résultats ont été découverts et l'analyse a été faite selon deux méthodes. La première est fondée sur les profils de vraisemblance des signaux [149], alors que la seconde, utilisée pour vérification, est basée sur l'étude d'excès de signaux dans la région d'intérêt.

Aucun excès notable n'a été observé par l'une des deux méthodes, ce qui signifie qu'aucune interaction de WIMP n'a été enregistrée. Pour illustration, les résultats de la seconde méthode sont présentés figure 6.2. Elle représente les rapports des signaux S2/S1 en fonction du signal S1.

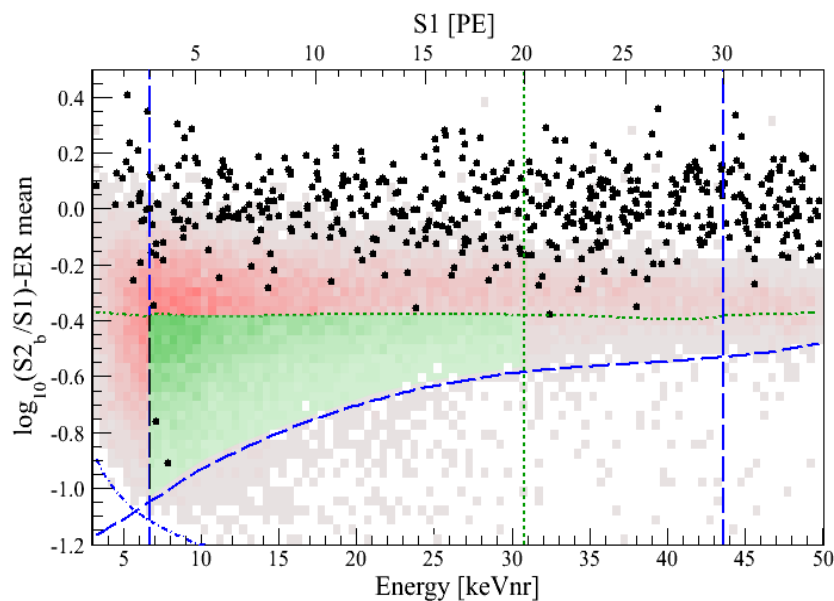


FIGURE 6.2 – Distribution mesurée des rapports des signaux S2 sur S1 en fonction du signal S1 pour les données d'observation pour la recherche de la matière noire. Les différentes courbes en pointillés permettent de sélectionner la région finale de recherche. Pour les détails de ces courbes, voir le texte ci-dessous. Figure adaptée à partir de [74].

Les données pour la recherche de matière noire sont représentées en noir. La région d'intérêt sélectionnée pour la recherche d'excès de signaux est représentée en vert. Les différentes calibrations menées entre deux acquisitions de données de matière noire ont permis d'estimer à  $1.0 \pm 0.2$  le nombre d'évènements de bruit de fond attendus ayant une signature de type WIMP dans cette région pour l'ensemble des 224,6 jours. La découverte des résultats a révélé deux évènements enregistrés dans cette région illustrée en vert. Aucun signe de passage d'un WIMP n'a donc

été enregistré au cours de cette prise de données, la probabilité que le bruit de fond fluctue d'un évènement à deux évènements étant de 26,4 %.

Les différentes courbes en pointillé représente les coupures de sélection des données. Ainsi, pour l'analyse utilisant le profil de vraisemblance, la limite supérieure d'intensité du signal S1 est établie à 30 PE, correspondant à un recul nucléaire engendré avec une énergie de 43.3 keVnr, où  $nr$  représente l'échelle de recul nucléaire qui tient compte du facteur de quenching qui atténue les signaux enregistrés par rapport au reculs d'électrons. Pour des raisons pratiques, cette limite supérieure est abaissée à 20 PE (30.5 keVnr) pour la méthode de la région d'intérêt. Les deux méthodes utilisant une limite inférieure du signal S1 fixée a keVnr, définie à partir de l'acceptance des coupures utilisées. Ces trois limites sont matérialisées par des lignes verticales. La courbe verte horizontale correspond à la limite haute de réjections à 99.75 % des reculs électronique, elle n'est appliquée que pour la méthode de recherche d'analyse utilisant la région d'intérêt. La courbe pointillée bleue en trait long correspond à la limite au-dessus de laquelle se situe 97 % des signaux de reculs nucléaires. La courbe restante illustrant la limite de détection des signaux S2 fixée à 150 PE. Ces deux dernières coupures étant appliquées aux deux méthodes d'analyse.

Les données accumulées au cours de cette session ont cependant permis d'abaisser la limite supérieure de section efficace des WIMP avec les noyaux en fonction de la masse des WIMP, comme cela est illustré en bleu à la figure 6.3.

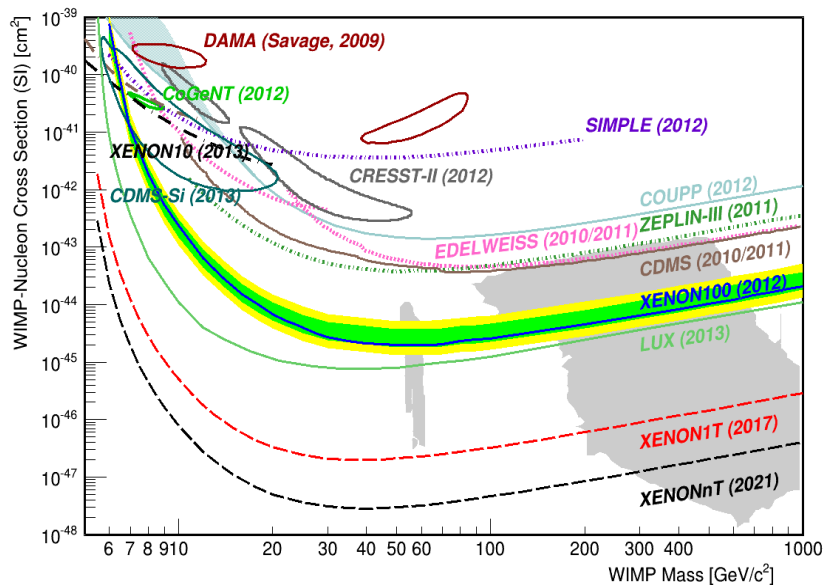


FIGURE 6.3 – Evolution de la limite supérieure de section efficace d'interaction des WIMP avec les noyaux en fonction de leur masse, mesurée lors des 224,6 jours d'observation cumulés. Figure adaptée à partir de [74].

Cette limite a été calculée en utilisant à nouveau la méthode du profil de vraisemblance. Elle a conduit à l'établissement d'un record de limite supérieure de section efficace d'interaction  $\sigma_{\chi} = 2.0 \times 10^{-45} \text{ cm}^2$  pour une masse de WIMP égale à  $55 \text{ GeV}/c^2$ , avec un niveau de confiance de 90 %. En guise de comparaison, les résultats obtenus par les expériences concurrentes sont également indiqués. Ils incluent les récents résultats d'un détecteur très similaire à XENON100,

baptisé LUX [105], et possédant un plus grand volume cible. Cette expérience a ainsi pu abaisser à nouveau la limite supérieure de section efficace d'interaction des WIMP avec les noyaux, atteignant un nouveau record de sensibilité à  $\sigma_\chi = 7.6 \times 10^{-46} \text{ cm}^2$  pour une masse de WIMP de 33 GeV/c<sup>2</sup>, avec un niveau de confiance de 90 %.

Ces résultats confirment la très grande performance des détecteurs aux gaz nobles, et plus particulièrement ceux utilisant du xénon, pour la recherche directe de matière noire. Cette performance est également illustrée par les courbes rouge, puis noire qui représentent les sensibilités du futur détecteur XENON1T dont la mise en service est prévue début 2015, avec une réduction attendue du bruit de fond d'un facteur 100 par rapport à XENON100, et de son amélioration XENONnT. Cette amélioration devrait permettre d'atteindre une nouvelle atténuation d'un facteur 10 du bruit de fond attendu pour XENON1T.

## 6.3 Signaux de charge d'électron uniques

Afin d'améliorer la sensibilité des expériences actuelles et future de recherche directe de matière noire, une excellente connaissance et compréhension du signal est nécessaire. Dans ce contexte, une analyse robuste des signaux S2 de très basse énergie a été menée [157]. Cette analyse est présentée ci-dessous.

### 6.3.1 Origines des signaux de charge d'électron uniques

Comme cela a été décrit dans la section 6.1, deux signaux sont émis successivement pour chaque interaction dans la région active de LXe. La lumière produite durant chacun de ces signaux est donc émise dans toutes les directions. Ceci signifie qu'une partie de la lumière appartenant au signal S2 est orientée vers la phase liquide. Dans cette région, la proportion d'impuretés, parmi lesquels figurent les molécules organiques, ou bien tout autre élément différent du xénon, incluant donc les constituants de la chambre à projection temporelle, n'est jamais nulle.

En conséquence, une partie de la lumière issue du signal S2 et qui pénètre dans la région liquide à une probabilité non négligeable d'interagir avec les impuretés rencontrées. Du fait de la très faible énergie des photons ultraviolets émis lors des signaux S1 et S2, environ 7 eV, ces interactions sont essentiellement des effets photo-électriques, conduisant donc à l'absorption totale de l'énergie du photon incident par l'électron rencontré. Cet électron est alors éjecté du cortège électronique de son atome.

Une fois libéré, l'électron tombe ensuite sous l'influence du champ électrique de dérive, et va être dirigé vers la phase gazeuse pour y être extrait, comme le fut le nuage électronique principal quelques instants auparavant. Lorsqu'il pénètre à son tour dans la phase gazeuse, il va également émettre son propre signal lumineux. Ce signal S2 de très faible énergie est appelé le *signal de charge d'électron unique*. Ce terme désigne non seulement le signal engendré par un seul électron lorsqu'il est écrit au singulier, mais il désigne aussi les signaux engendrés par un à plusieurs électrons uniques extraits en coïncidence temporelle lorsqu'il est écrit au pluriel. Le nombre de ces électrons est généralement inférieur ou égal à cinq, mais il est possible d'observer des signaux engendrés par davantage d'électrons uniques.

### 6.3.2 Caractérisation des signaux de charge d'électron uniques

Du fait de leur création par l'accélération d'un ou plusieurs électrons extraits en coïncidence temporelle en phase gazeuse, les signaux d'électrons uniques ont donc une très faible intensité, généralement inférieure à 150 photoélectrons ( $PE$ ). L'un des principaux objectifs de l'étude de ces signaux est donc de caractériser précisément le gain moyen associé à la dérive d'un seul électron dans la phase gazeuse. Ce gain est alors appelé *gain de scintillation secondaire*. Afin de le mesurer, il est nécessaire de s'intéresser uniquement à l'étude de la partie à très basse énergie du spectre total des signaux S2 enregistrés par le détecteur.

La distribution de signaux S2 correspondante est alors ajustée par une somme de cinq gaussiennes. Elles correspondent respectivement à la distribution des signaux lumineux engendrés et mesurés lors de l'accélération en phase gazeuse d'un électron seul ou d'un groupe de deux à cinq électrons extraits en coïncidence temporelle. Chacune de ces gaussiennes est donc contrainte par la première selon les relations suivantes :

$$\mu_i = i \times \mu_1, \quad \sigma_i = \sqrt{i} \times \sigma_1 \quad (6.1)$$

L'efficacité du détecteur pour enregistrer ces signaux S2 de très basse énergie est également prise en compte en multipliant cette somme par une fonction seuil définie par la statistique de Fermi-Dirac :

$$f(E) = \frac{1}{e^{\frac{-(E-E_t)}{\Delta E_t}} + 1} \quad (6.2)$$

où  $E_t$  et  $\Delta E_t$  sont des paramètres libres déterminés lors de l'ajustement. La figure 6.4 illustre alors, via la courbe rouge superposée aux données, le résultat de l'ajustement d'un spectre typique de signaux S2 de basse énergies.

Les contributions de chacune des gaussiennes et de la fonction de seuil sont également représentés par différentes couleurs. L'échelle de cette dernière étant reportée sur l'axe vertical à droite du spectre. La valeur moyenne du gain de scintillation secondaire  $\mu_{S2,e^-}$  est obtenu à partir de la valeur moyenne de la première gaussienne, alors que la dispersion  $\sigma_{S2,e^-}$  associée à ce gain correspond à la dispersion de cette même gaussienne. Pour cet exemple, les valeurs de ces deux paramètres sont reportés respectivement sur la figure.

La valeur de ces deux paramètres, ainsi que celle des paramètres  $E_t$  et  $\Delta E_t$  de la fonction de seuil, ont été mesurés pour toutes les données de calibrations et de recherche de matière noire accumulées lors des trois sessions principales de prises de données effectuées par XENON100. Cela a notamment permis de démontrer une stabilité de ce gain, tant pour l'aspect temporel que vis-à-vis du changement de source de calibration du détecteur, illustrant ainsi la très grande stabilité et performance du signal de charge S2 dans XENON100 pour la recherche de la matière noire.

Par ailleurs, le gain de scintillation secondaire dépend fortement du champ électrique exercé en phase gazeuse. De ce fait, l'étude de l'évolution de ce gain a été étendue à une large région de valeur pour le champ électrique dans cette phase. Les résultats de cette évolution sont représentés à la figure 6.5.

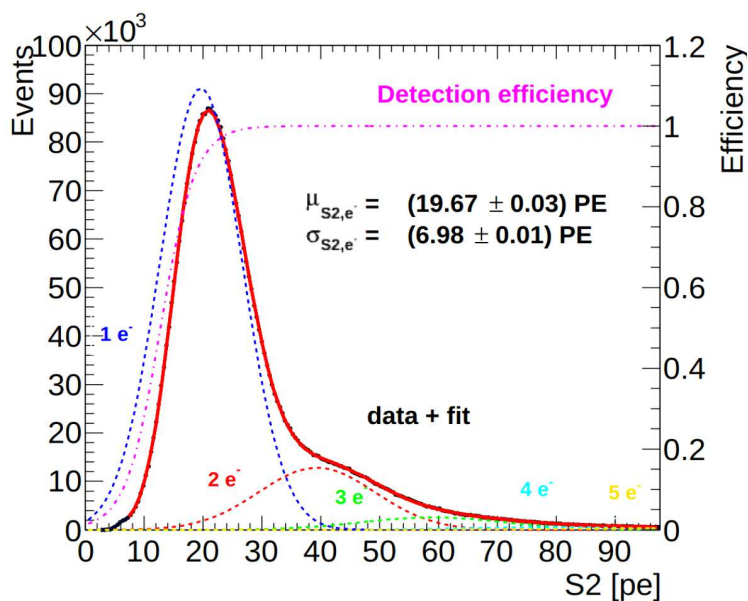


FIGURE 6.4 – Exemple de l’ajustement typique d’un spectre de signaux S2 à très basse énergie. L’ajustement est représenté en rouge, et les contributions de chacun de ses élément par différentes couleurs. Figure publiée dans [157].

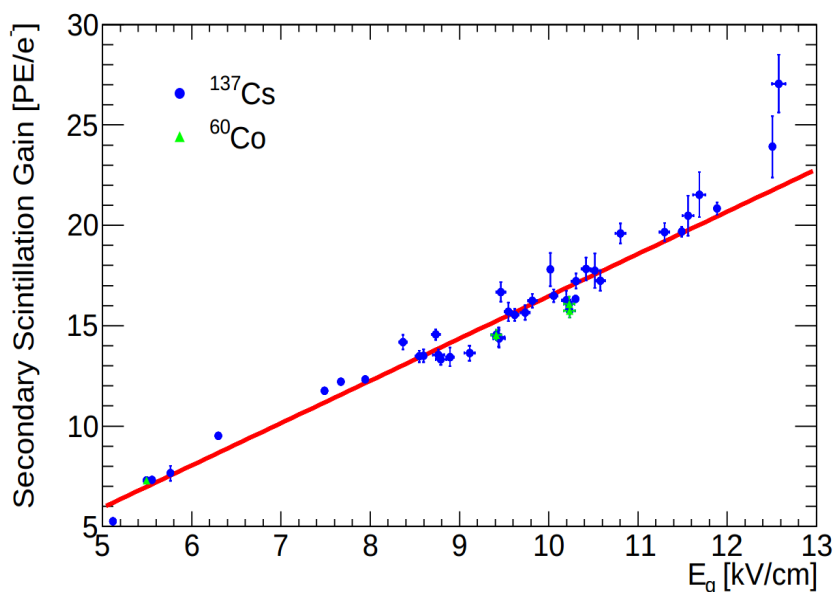


FIGURE 6.5 – Evolution du gain de scintillation secondaire en fonction du champ électrique exercé dans la phase gazeuse. Les données issues de mesures sont représentées en bleu ( $^{137}\text{Cs}$ ) et vert ( $^{60}\text{Co}$ ), et incluent les barres d’erreurs. L’ajustement de ces données par une fonction empirique est représenté en trait plein rouge. Figure publiée dans de [157].

Pour cette figure, les données obtenues avec des sources de calibration  $^{137}\text{Cs}$  (bleu) et  $^{60}\text{Co}$  (vert) pendant et entre chacune des trois prises de données pour la recherche de matière noire sont considérés, illustrant la reproductibilité des résultats. La stabilité du gain de scintillation secondaire vis-à-vis de la source de calibration utilisée est par ailleurs observée pour de plus larges régions de valeur du champ électrique en phase gazeuse. La distribution de gain de scintillation secondaire  $N_{PE,e^-}$ , exprimée en photoélectrons par électron ( $PE/e^-$ ), est ensuite ajustée par une fonction empirique [114, 164] :

$$N_{PE,e^-} = \left( \alpha \frac{E_G}{P_G} - \beta \right) d_G P_G \bar{\delta} \bar{\eta} \bar{\varepsilon} \quad (6.3)$$

où  $E_G$ ,  $P_G$  et  $d_G$  sont respectivement les champs électriques, pression et hauteur de la région gazeuse, exprimés respectivement en kV/cm, bar et cm. Les valeurs moyennes  $\bar{\delta}$ ,  $\bar{\eta}$  et  $\bar{\varepsilon}$  correspondent respectivement à l'efficacité de collection des photons par les photomultiplicateurs, à l'efficacité quantique de ces photomultiplicateurs pour émettre un électron à l'issue de l'interaction d'un photon, et enfin à l'efficacité de la première dynode de chaque photomultiplicateur pour collecter cet électron ainsi libéré et commencer sa multiplication par avalanche électronique. Ces valeurs moyennes sont exprimées en pourcent.

Les deux variables d'ajustement de la fonction sont donc les paramètres  $\alpha$  et  $\beta$ . Elles sont respectivement établies à  $(151 \pm 19)$  photons/ $e^-$ /kV et  $-(147 \pm 19)$  photons/ $e^-$ /cm/bar [157], ce qui est en très bon accord avec les valeurs mesurées par d'autres expériences utilisant du xénon [164, 166], ou encore avec les prévisions issues de simulations [165].

Par ailleurs, cet ajustement permet d'illustrer l'amplification linéaire du gain de scintillation secondaire pour des valeurs de champ électrique en phase gazeuse allant d'environ 5 kV/cm à environ 12 kV/cm. Pour des valeurs de champs électriques supérieurs, les données s'écartent de la courbe de tendance à mesure que le champ augmente. Ceci traduit l'apparition d'un régime d'avalanche électronique dans la phase gazeuse pour ce domaine de champ électrique.

Enfin, cette étude a permis d'effectuer une mesure de l'énergie moyenne nécessaire à la création d'une paire électron-ion,  $W' = 23.5 \pm 0.7$  eV/ $e^-$ , pour un champ électrique de dérive  $E_d = 0.5$  kV/cm appliqué dans la phase liquide. Cette valeur est en très bon accord avec les valeurs publiées [167], mais apporte une plus grande précision du fait de la réduction des erreurs systématiques sur cette mesure.

## Conclusion

Les résultats de recherche directe de matière noire par l'expérience XENON100 présentés ici n'ont pas révélé de signatures d'interaction de WIMP. Il ne s'agit cependant pas des seuls résultats de recherche directes de matière noire menées par la Collaboration XENON. De nouveaux résultats issus de la troisième session de prise de données par le détecteur devraient être bientôt publiés, en attendant le futur détecteur XENON1T, dont la mise en service est prévue début de 2015.

Les résultats de l'analyse de la dernière prise de données de XENON100 devraient présenter

une sensibilités inférieure pour la recherche de matière par rapport à ceux présentés ici, du fait d'une plus faible période d'observation. Ils permettront cependant d'étendre la recherche de la matière noire à d'autres canaux. Parmi ceux-ci figure l'analyse de la fluctuation annuelle du bruit de fond électronique, qui pourrait être un vrai signal engendré par le mouvement de révolution de la Terre autour du Soleil, si l'on postule que les particules de matière noire interagissent non pas avec les noyaux, mais avec les électrons des atomes [83]. L'ajout des nouvelles données avec celle existant déjà, réparties sur environ une nouvelle année civile, va donc permettre d'améliorer la sensibilité du détecteur.

Cette combinaison des données ne peut cependant se faire que par une très bonne maîtrise et compréhension des signaux de réponse du détecteur, et cela pour toutes les échelles d'énergies considérées. C'est dans ce contexte que l'étude menée sur les signaux d'électrons unique va pouvoir s'appliquer. Elle va également être utile pour mener une étude de la sensibilité du détecteur à des WIMP de très basse énergie, et dont le signal S1 engendré lors d'une interaction d'un tel WIMP avec le xénon va être indétectable du fait d'une trop faible intensité. L'étude se faisant alors sur le signal S2, également faible, car engendré uniquement par quelques électrons.

En outre, quelque soit le canal de recherche directe de matière noire envisagé, une optimisation des conditions de fonctionnement est nécessaire afin d'améliorer la sensibilité. L'étude des signaux de charge d'électrons uniques va alors permettre de définir les configurations électriques permettant d'atteindre la meilleure amplification du signal de charge pour un taux d'extraction des électrons de la phase liquide vers la phase gazeuse proche de 100 %.

Enfin, les mesures du gain de scintillation secondaire vont pouvoir être appliquées aux résultats de simulations Monte Carlo afin d'estimer l'intensité du signal de charge qui serait réellement mesuré, connaissant par la simulation l'énergie déposée lors d'une l'interaction dans la phase liquide.

Le détecteur XENON100 approchant de la fin de sa durée de fonctionnement, les signaux d'électrons uniques – dont la compréhension et la maîtrise ont été démontrées par les différentes analyses présentées au cours de cette thèse – vont pouvoir également être utilisés dès les premiers mois du futur détecteur XENON1T, lors de la première phase de prise de données pour la recherche de la matière noire.

# List of Figures

|      |  |    |
|------|--|----|
| 1.1  | Several Galaxies rotation curves . . . . .   | 10 |
| 1.2  | Example of two reference frames linked together by Lorentz's transformations . .   | 12 |
| 1.3  | Distance $dl$ as measured for the surface of a sphere . . . . .  | 15 |
| 1.4  | Combination of cosmological parameters $\Omega_m$ and $\Omega_\Lambda$ from different observables  | 27 |
| 1.5  | NGC 6503 galaxy rotation curve . . . . .   | 27 |
| 1.6  | Illustration of gravitational lensing and Einstein's ring . . . . .  | 28 |
| 1.7  | Mass distribution in galaxies clusters collisions . . . . .  | 29 |
| 1.8  | Abundance prediction for lightest elements from primordial nucleosynthesis . . .   | 30 |
| 1.9  | Sky map of the temperature anisotropies measured by the Planck satellite . . . .   | 31 |
| 1.10 | CMB power spectrum analysis by the Planck satellite . . . . .  | 32 |
| 1.11 | Comparison between observable galaxies distribution and Millennium I simulation  | 34 |
| 1.12 | Thermal relic density $\Omega_\chi$ as a function of the Universe's age, and Wimp mass $m_\chi$<br>as a function of the WIMP contribution to dark matter . . . . . | 38 |
| 1.13 | Illustration of the SUSY theory . . . . .  | 39 |
| 1.14 | Review of few dark matter candidates mass and cross-sections . . . . .   | 40 |
| 1.15 | Summary test of few dark matter candidates . . . . .   | 40 |
| 1.16 | Illustration of the LHC . . . . .  | 41 |
| 1.17 | Possible dark matter annihilation signatures from indirect search . . . . .  | 42 |
| 1.18 | Direct dark matter detection principle . . . . .   | 43 |
| 1.19 | Review of direct dark matter detection experiments . . . . .   | 44 |
| 1.20 | Illustration of the WIMP signal annual modulation . . . . .  | 44 |
| 1.21 | Feynmann diagrams for dark matter scattering . . . . .   | 45 |
| 1.22 | Illustration of expected WIMPs interaction rate for several target materials . . . .   | 45 |
| 1.23 | Illustration of the MIMAC directional direct dark matter detection principle . . .   | 47 |
| 1.24 | CoGent latest annual modulation results . . . . .  | 48 |
| 1.25 | Illustration of the principle and observed NR and ER recoil bands for the EDEL-<br>WEISS experiment . . . . .  | 49 |
| 1.26 | Illustration of a detection module of the <i>CRESST</i> experiment . . . . .   | 50 |
| 1.27 | XMASS low-mass WIMP analysis results . . . . .   | 53 |
| 2.1  | XENON100 TPC principle . . . . .   | 57 |
| 2.2  | Scintillation and ionisation signals emission scenario . . . . .   | 57 |
| 2.3  | Relative contribution of the main photon interaction processes in xenon . . . . .  | 58 |

|      |   |     |
|------|---|-----|
| 2.4  | Sketches of the photoelectric and Compton effects . . . . .   | 58  |
| 2.5  | Illustration of the energy deposition per length unit for a recoiling electron in LXe as a function of its energy . . . . . | 63  |
| 2.6  | Illustration of the two components energy deposition model . . . . .  | 63  |
| 2.7  | Nuclear recoil band and combined energy scale calibration spectra with $^{241}\text{Am}^9\text{Be}$ . . . . .               | 64  |
| 2.8  | Illustration of the relative contributions of each interaction process for a recoiling nucleus . . . . .                    | 65  |
| 2.9  | Illustration of the evolution of the charge collection . . . . .  | 68  |
| 2.10 | XENON100 TPC and Top meshes . . . . .   | 73  |
| 2.11 | S2 signal evolution as a function of scattering depth for $^{137}\text{Cs}$ full absorption peak . . . . .                  | 74  |
| 2.12 | XENON100 PMTS arrays . . . . .  | 76  |
| 2.13 | Illustration of PMT principle . . . . .   | 77  |
| 2.14 | Example of a XENON100 waveform and a PMT gain calibration . . . . .   | 78  |
| 2.15 | Illustration of a muon flux reduction as a function of the depth of underground laboratories . . . . .                      | 79  |
| 2.16 | The XENON100 passive shield . . . . .   | 79  |
| 2.17 | XENON100 cryogenic system . . . . .   | 80  |
| 2.18 | XENON100 recirculation gas system . . . . .   | 81  |
| 2.19 | Xenon bottles storage and illustration of detector pressure and temperature monitoring . . . . .                            | 82  |
| 2.20 | Electron lifetime evolution during second science run . . . . .   | 83  |
| 2.21 | Illustration of a waveform smoothing for S2 signal . . . . .  | 84  |
| 2.22 | Illustration of the calibration process . . . . .   | 86  |
| 3.1  | Three dimensional light correction map for S1 signal and light yield extrapolation at 122 keV . . . . .                     | 91  |
| 3.2  | Two dimensional light correction maps on bottom and top PMTs array for S2 signal . . . . .                                  | 92  |
| 3.3  | Evolution of the width of the S2 signal as a function of the scattering depth . . . . .                                     | 93  |
| 3.4  | Comparison of the energy resolution of the reconstructed deposited energy . . . . .   | 94  |
| 3.5  | Anti-correlation between light and charge signals . . . . .   | 95  |
| 3.6  | All direct measurements of $\mathcal{L}_{eff}$ as a function of the nucleus recoiling energy . . . . .                      | 97  |
| 3.7  | XENON100 response for electronic and nuclear recoils . . . . .  | 99  |
| 3.8  | BiPo events in decay chains and XENON100 krypton distillation column . . . . .  | 101 |
| 3.9  | Illustration of the blinded region for dark matter search . . . . .   | 102 |
| 3.10 | Illustration of the scattering signal in (S1,S2) plane for NR and ER . . . . .  | 106 |
| 3.11 | Illustration of the benchmark signal region . . . . .   | 107 |
| 3.12 | Upper limits of the SI WIMP-nucleus cross section as a function of the WIMP mass . . . . .                                  | 109 |
| 3.13 | Upper limits of the SD WIMP-nucleons cross section as a function of the WIMP mass . . . . .                                 | 111 |
| 3.14 | Dark matter data selection for axions and ALP search in the ER band . . . . .   | 112 |
| 3.15 | XENON100 limits on solar axions during the second science run . . . . .   | 113 |
| 3.16 | XENON100 limits on galactic ALP during the second science run . . . . .   | 114 |

---

|      |  |     |
|------|--|-----|
| 3.17 | The XENON1T experiment . . . . .   | 115 |
| 4.1  | Single electron signal emission principle . . . . .  | 119 |
| 4.2  | Schematic view of the a dual phase argon TPC with GEM, operated in single electron counting mode . . . . .   | 121 |
| 4.3  | Schematic waveform for single electrons emission . . . . .   | 121 |
| 4.4  | Example of a single electron waveform recorded by XENON100 . . . . .   | 122 |
| 4.5  | Rate of low energy S2 signal prior to S1 signals per each waveform as a function of the differential time between two triggered events . . . . .   | 123 |
| 4.6  | Full S2 signals spectrum obtained with $^{60}\text{Co}$ calibration source during the second science run . . . . .   | 124 |
| 4.7  | Low energy S2 signals spectrum obtained with $^{60}\text{Co}$ calibration source during the second science run . . . . .   | 124 |
| 4.8  | Rate of low energy S2 signals per each waveform as a function of impurity concentration in LXe and the intensity of the main S2 signal . . . . .   | 126 |
| 4.9  | Rate of low energy S2 signals per each waveform as a function of the time delay from the prior main S2 or S1 signal . . . . .  | 127 |
| 4.10 | Illustration of S2 light repartition on top PMTs array for a three electrons signal .  | 130 |
| 4.11 | Illustration of a low energy S2 spectrum fitted by a sum of five Gaussian distributions multiplied by a threshold function . . . . .   | 132 |
| 4.12 | Illustration of the influence of the minimum requested intensity of the main S2 signal per waveform on low energy S2 spectrum . . . . .  | 133 |
| 4.13 | Illustration of the quality of the fit of the low energy S2 signals as a function of the requested secondary scintillation gain, and illustration of excess of S2 signals at very low energies . . . . .   | 134 |
| 4.14 | Illustration of the decrease of the pure single electrons signals population in case of low LXe purity conditions and illustration of the quality of the fit of the low energy S2 signals as a function of the requested secondary scintillation gain after primary improvement of the fit methods . . . . . | 136 |
| 4.15 | Secondary scintillation gain as a function of the single electron depth emission .   | 137 |
| 4.16 | Standard deviation of the first Gaussian distribution and of the ratio of this standard deviation over the secondary scintillation gain as a function of the single electron depth emission . . . . .  | 138 |
| 4.17 | Secondary scintillation gain as a function of the single electron reconstructed emission position with respect to the position of the main S2 signal . . . . .   | 140 |
| 4.18 | Standard deviation of the first Gaussian distribution as a function of the single electron reconstructed emission position with respect to the position of the main S2 signal . . . . .  | 140 |
| 4.19 | Secondary scintillation gain for larger position as a function of the single electron reconstructed emission position with respect to the position of the main S2 signal   | 141 |
| 4.20 | Variations of the two parameters of the threshold function as a function of the single electron depth emission . . . . .   | 143 |

|      |  |     |
|------|--|-----|
| 4.21 | Rate of single electron signals as a function of the time delay from the main S2 signal . . . . .  | 143 |
| 4.22 | Rate of single electron signals as a function of the rate of signals of few electrons . . . . .  | 144 |
| 4.23 | Variation of the distribution of identified S2 signals per waveform when increasing the requested time delay window from the main S2 signal . . . . .  | 145 |
| 4.24 | Comparison of a low energy S2 spectrum at low LXe purity before and after the addition of a time delay based cut and a restriction on the maximum number of identified S2 signals per waveform . . . . . | 147 |
| 4.25 | Analysis of the reduced relationships between free Gaussians . . . . .   | 149 |
| 4.26 | Illustration of the influence of very small fluctuations on the fit of low energies S2 spectra by several independent Gaussians . . . . .  | 150 |
| 4.27 | Comparison between results from fit with constrained and free Gaussian distributions for the first science run . . . . .   | 151 |
| 4.28 | Comparison between results from fit with constrained and free Gaussian distributions for the second science run . . . . .  | 151 |
| 4.29 | Comparison between results from fit with constrained and free Gaussian distributions for the third science run . . . . .   | 152 |
| 4.30 | Comparison between results from fit with N constrained Gaussian distributions for the second and third science runs . . . . .  | 153 |
| 4.31 | Comparison between results from fit with N constrained Gaussian distributions for the first science run . . . . .  | 154 |
| 4.32 | Comparison between results from fit with different minimum intensity for the main S2 signal for the second and third science runs . . . . .  | 155 |
| 4.33 | Secondary scintillation gain from fit with optimised minimum intensity for the main S2 signal for the second and third science runs . . . . .  | 156 |
| 4.34 | Graphical representation of the correlation between the parameters of the fit applied to the low energy S2 spectrum . . . . .  | 157 |
| 4.35 | Position of the perturbation at low energy . . . . .   | 159 |
| 4.36 | Variation of the fit parameters as a function of the lower boundary of the spectrum fit . . . . .  | 160 |
| 5.1  | Demonstration of the stability in time of the fit parameters . . . . .   | 166 |
| 5.2  | Small fluctuations of the stability in time of the fit parameters . . . . .  | 166 |
| 5.3  | Demonstration of the stability of the secondary scintillation gain from trigger source   | 169 |
| 5.4  | Illustration of the different sketches analysed for the single electrons signal occurring between the main S1 and S2 signals . . . . .   | 171 |
| 5.5  | Analysis of the secondary scintillation gain results for single electron signals occurring between the main S1 and S2 signals during the second science run . . . . .                                    | 172 |
| 5.6  | Analysis of the secondary scintillation gain results for single electron signals occurring between the main S1 and S2 signals during the first and third science run . . . . .                           | 174 |
| 5.7  | Illustration of the approximation of the region of the TPC between the ground mesh and the anode as a parallel-plate capacitor . . . . .   | 175 |

|      |   |     |
|------|---|-----|
| 5.8  | Illustration of the variation of the electric field in the gas phase as a function of the liquid level for different anode voltages . . . . .   | 177 |
| 5.9  | Illustration of the liquid level measurements distribution for one dataset acquired with $^{137}\text{Cs}$ radioactive source right before the second science run . . . . .   | 178 |
| 5.10 | Secondary scintillation gain as a function of the electric field in the gas phase . . .   | 179 |
| 5.11 | Distribution in time of the gaseous pressure . . . . .  | 180 |
| 5.12 | Illustration of the unexpected excess on the very low energy part of the S2 spectrum during the $^{137}\text{Cs}$ calibration campaign . . . . .  | 182 |
| 5.13 | Secondary scintillation gain as a function of the electric field in the gas phase during the $^{137}\text{Cs}$ calibration campaign . . . . .   | 182 |
| 5.14 | Illustration of the comparison of the light seen without PMTs saturation by Top PMTs array as a function of the light seen by bottom PMTs array for low energy S2 signals . . . . .   | 184 |
| 5.15 | Proportion of S2 light seen by bottom PMTs array with respect to the combination of bottom and top PMTs arrays . . . . .  | 186 |
| 5.16 | Relative light and charge yields as a function of the drifting electric field in LXe .  | 188 |
| 5.17 | S2 gain calculation and time stability for the first science run . . . . .  | 189 |
| 5.18 | Relative charge yield as a function of the electric field in the LXe . . . . .  | 190 |
| 5.19 | Comparison between electric fields values deduced from simulations and electric fields values deduced from the parallel-plate capacitor model, and variation of the electrons extraction yield as a function of the electric field in the gas phase . . . . | 192 |
| 5.20 | Potential energy applied to a drifting electron in a dual phase TPC as a function of its vertical position close to the interface . . . . .   | 192 |
| 5.21 | Secondary scintillation gain for a fixed anode voltage as a function of the electric field and the gas gap . . . . .  | 196 |
| 5.22 | Ratio of the S2 signal from bottom PMTs array over S1 signal in logarithmic scale as a function of the deposited energy in the LXe . . . . .  | 199 |
| 5.23 | Waveform of the two events identified as mimicking the dark matter signals signature during the second science run . . . . .  | 200 |
| 5.24 | Light pattern on top PMTs array of the two events identified as mimicking the dark matter signals signature during the second science run . . . . .   | 201 |
| 6.1  | Principe de détection XENON100 . . . . .  | 213 |
| 6.2  | Distribution mesurée des rapports des signaux S2 sur S1 en fonction du signal S1 pour les données d'observation pour la recherche de la matière noire . . . . .   | 214 |
| 6.3  | Evolution de la limite supérieure de section efficace d'interaction des WIMP avec les noyaux en fonction de leur masse . . . . .  | 215 |
| 6.4  | Exemple de l'ajustement typique d'un spectre de signaux S2 à très basse énergie .   | 218 |
| 6.5  | Evolution du gain de scintillation secondaire en fonction du champ électrique exercé dans la phase gazeuse . . . . .  | 218 |



# List of Tables

|     |  |     |
|-----|--|-----|
| 1.1 | Cosmological parameters from Planck satellite . . . . .  | 32  |
| 2.1 | Xenon main properties . . . . .  | 60  |
| 2.2 | Xenon isotopes natural abundance . . . . .   | 61  |
| 2.3 | Several properties of noble gas . . . . .  | 61  |
| 2.4 | Singlet and triplet lifetime comparison between several noble gas . . . . .  | 70  |
| 2.5 | Drift fields during science runs . . . . .   | 76  |
| 3.1 | Summary of the S1 and S2 signals emitted during the photoelectric effect of a $\gamma$ ray emitted by the $^{137}\text{Cs}$ calibration source . . . . . | 98  |
| 3.2 | Comparison between nuclear and electronic recoils for S1 and S2 signals . . . . .  | 99  |
| 4.1 | Summary of data cuts selection applied for the evaluation of the secondary scintillation gain . . . . .  | 146 |
| 4.2 | Evaluation of the statistical error associated to the secondary scintillation gain per each science run . . . . .  | 156 |
| 4.3 | Comparison of the most relevant parameters between the regular ROOT fit and RooFit . . . . .   | 158 |
| 4.4 | Evaluation of the systematical error per each science run due to the upper bound of the fit . . . . .  | 161 |
| 4.5 | Summary of the systematical errors associated to the secondary scintillation gain per each science run . . . . .   | 161 |
| 5.1 | Average values of the main parameters of the fit from the study of the stability in time for the first science run . . . . .                             | 167 |
| 5.2 | Average values of the main parameters of the fit from the study of the stability in time for the second science run . . . . .                            | 167 |
| 5.3 | Average values of the main parameters of the fit from the study of the stability in time for the third science run . . . . .                             | 168 |
| 5.4 | Average values of the main parameters of the fit from the study of the stability from calibration sources for the three science runs . . . . .           | 169 |
| 5.5 | Systematic errors due to the used source of calibration and associated to the secondary scintillation gain per each science run . . . . .                | 169 |

|     |   |     |
|-----|---|-----|
| 5.6 | Comparison between results from time distribution and from the whole statistics of the average proportion of light from S2 signal seen by bottom PMTs array with respect to the light seen by the combination of bottom and top PMTs arrays during the second science run . . . . . | 186 |
| 5.7 | Average proportion of light from S2 signal seen by bottom PMTs array with respect to the combination of bottom and top PMTs arrays for each science run . .   | 186 |
| 5.8 | Summary of the S1 and S2 signals of the two background events with a dark matter signature observed during the second science run . . . . .   | 199 |

# Bibliography

- [1] F. Zwicky. Die Rotverschiebung von extragalaktischen Nebeln. *Helv. Phys. Acta*, **6**:110, (1933). Cited on pages 8 and 211.
- [2] S. Smith. The Mass of the Virgo Cluster. *Astrophysical Journal*, **83**:23, (1936). Cited on pages 9 and 211.
- [3] E. Hubble. The Distribution of Extra-Galactic Nebulae. *Astrophysical Journal*, **79**:8, (1934). Cited on pages 9 and 211.
- [4] H. Babcock. The rotation of the Andromeda Nebula. *Lick Observatory bulletin*, **498**:41, (1939). Cited on pages 9 and 211.
- [5] L. Volders. Neutral hydrogen in M 33 and M 101. *Bulletin of the Astronomical Institutes of the Netherlands*, **14**:323, (1959). Cited on pages 9 and 211.
- [6] J. Oort. Some Problems Concerning the Structure and Dynamics of the Galactic System and the Elliptical Nebulae NGC 3115 and 4494. *Astrophysical Journal*, **91**:273, (1940). Cited on pages 9 and 211.
- [7] V. C. Rubin and W. K. Jr. Ford. Rotation of the Andromeda Nebula from a Spectroscopic Survey of Emission Regions. *Astrophysical Journal*, **159**:379, (1970). Cited on pages 9 and 211.
- [8] V. C. Rubin, W. K. Jr. Ford, and N. Thonnard. Extended Rotation Curves of High-Luminosity Spiral Galaxies. IV. Systematic Dynamical Properties, SA through SC. *Astrophysical Journal*, **225**:L107, (1978). Cited on pages 10 and 211.
- [9] J. P. Ostriker and P. J. E. Peebles. A Numerical Study of the Stability of Flattened Galaxies: or, can Cold Galaxies Survive? *Astrophysical Journal*, **186**:467, (1973). Cited on pages 10 and 211.
- [10] V. C. Rubin, W. K. Jr. Ford, and N. Thonnard. Rotational properties of 21 SC galaxies with a large range of luminosities and radii, from NGC 4605 ( $R = 4\text{kpc}$ ) to UGC 2885 ( $R = 122\text{kpc}$ ). *Astrophysical Journal*, **238**:471, (1980). Cited on pages 10 and 211.
- [11] A. Bosma. 21-cm line studies of spiral galaxies. I - Observations of the galaxies NGC 5033, 3198, 5055, 2841, and 7331. II - The distribution and kinematics of neutral hydrogen

- in spiral galaxies of various morphological types. *Astronomical Journal*, **86**:1791, (1981). Cited on pages 10 and 211.
- [12] Y. Sofue. Grand Rotation Curve and Dark-Matter Halo in the Milky Way Galaxy. *Publ. Astron. Soc. Japan*, **64**:75, (2012). Cited on pages 10 and 211.
- [13] C. Semay and B. Silvestre-Brac. Relativité Restreinte - Base et applications. *Ed. DUNOD*, (2005). Cited on page 12.
- [14] J. Heyvaerts. Astrophysique - Etoile, Univers et relativité. *Ed. DUNOD*, (2006). Cited on pages 15, 16, and 20.
- [15] B. W. Carroll and D. A. Ostlie. An introduction to Modern Astrophysics. *Internationnal Edition*, (1996). Cited on pages 15, 16, and 20.
- [16] Benoît Revenu. Introduction au modele standard de la cosmologie; developpements sur le rayonnement fossile et sa polarisation. <http://hal.in2p3.fr/in2p3-00012708>, pages 1–115, 2002. Cited on pages 15 and 16.
- [17] J. A. Rich and Trad. de J. Basdevant. Cosmologie. *Ed VUIBERT*, (2010). Cited on page 16.
- [18] Yu. L. Bolotin, V. A. Cherkaskiy, G. I. Ivashkevych, O. A. Lemets, I. V. Tanatarov, D. A. Yerokhin, and O.B. Zaslavskii. Universe in problem. [http://universeinproblems.com/index.php/Friedman-Lemaitre-Robertson-Walker\\_\(FLRW\)\\_metric](http://universeinproblems.com/index.php/Friedman-Lemaitre-Robertson-Walker_(FLRW)_metric). Cited on page 16.
- [19] C. Hirata. Cosmological principle. <http://www.tapir.caltech.edu/~chirata/ph217/lec01.pdf>. Cited on page 16.
- [20] F.-X. Désert. Cours de Cosmologie. <http://ipag.obs.ujf-grenoble.fr/~desertf/cosmologie/cours/coursv2.pdf>. Cited on page 16.
- [21] S. Perlmutter et al. Supernova Cosmology Project, Measurements of Omega and Lambda from 42 high redshift supernovae. *Astrophys.J.*, **517**:565–586, (1999). Cited on pages 18 and 20.
- [22] Adam G. Riess et al. Supernova Search Team, Observational evidence from supernovae for an accelerating universe and a cosmological constant. *Astron.J.*, **116**:1009–1038, (1998). Cited on pages 18 and 20.
- [23] Planck Collaboration. Planck 2013 results. XVI. Cosmological parameters. *ArXiv*, 1303:5076, (2013). Cited on pages 19, 24, 32, 38, and 211.
- [24] J. Beringer et al. Particle Data Group. *Phys. Rev. D*, **86**:010001, (2012). Cited on page 24.
- [25] John C. Mather, D.J. Fixsen, R.A. Shafer, C. Mosier, and D.T. Wilkinson. Calibrator design for the COBE far infrared absolute spectrophotometer (FIRAS). *Astrophys.J.*, **512**:511–520, (1999). Cited on page 24.

- [26] N. Suzuki, D. Rubin, C. Lidman, G. Aldering, R. Amanullah, et al. The Hubble Space Telescope Cluster Supernova Survey: V. Improving the Dark Energy Constraints Above  $Z > 1$  and Building an Early-Type-Hosted Supernova Sample. *Astrophys.J.*, **746**:85, (2012). Cited on pages 26 and 27.
- [27] K.G. Begeman, A.H. Broeils, and R.H. Sanders. Extended rotation curves of spiral galaxies: Dark haloes and modified dynamics. *Mon. Not. Roy. Astron. Soc.*, **249**:523, (1991). Cited on page 27.
- [28] M. Milgrom. A Modification of the Newtonian dynamics as a possible alternative to the hidden mass hypothesis. *Astrophys.J.*, **270**:365–370, (1983). Cited on page 26.
- [29] Jacob D. Bekenstein. Relativistic gravitation theory for the MOND paradigm. *Phys.Rev.*, **D70**:083509, (2004). Cited on page 26.
- [30] Wikipedia. <http://en.wikipedia.org/>. Cited on page 28.
- [31] Richard Massey, Jason Rhodes, Richard Ellis, Nick Scoville, Alexie Leauthaud, et al. Dark matter maps reveal cosmic scaffolding. *Nature*, **445**:286, (2007). Cited on page 28.
- [32] Chandra Website. <http://chandra.harvard.edu/>. Cited on page 29.
- [33] M. Markevitch et al. Chandra observation of the most interesting cluster in the Universe. *ArXiv*, 0511:345, (2005). Cited on page 28.
- [34] Douglas Clowe, Marusa Bradac, Anthony H. Gonzalez, Maxim Markevitch, Scott W. Randall, et al. A direct empirical proof of the existence of dark matter. *Astrophys.J.*, **648**:L109–L113, (2006). Cited on page 28.
- [35] Alain Coc, Jean-Philippe Uzan, and Elisabeth Vangioni. Standard Big-Bang Nucleosynthesis after Planck. *ArXiv*, 1307:6955, (2013). Cited on page 30.
- [36] Brian D. Fields. The primordial lithium problem. *Ann. Rev. Nucl. Part. Sci.*, **61**:47–68, (2011). Cited on page 29.
- [37] Will J. Percival et al. SDSS Collaboration, Baryon Acoustic Oscillations in the Sloan Digital Sky Survey Data Release 7 Galaxy Sample. *Mon. Not. Roy. Astron. Soc.*, **401**:2148–2168, (2010). Cited on page 30.
- [38] R.A. Alpher and R. Herman. Evolution of the universe. *Nature*, **162**:774–775, (1948). Cited on page 31.
- [39] A.A. Penzias and R.W. Wilson. A measurement of excess antenna temperature at 4080 mc/s. *Astrophys. J., Lett.*, **142**:419, (1965). Cited on page 31.
- [40] Esa Website. <http://www.esa.int/>. Cited on page 31.
- [41] P.A.R. Ade et al. Planck Collaboration, Planck 2013 results. XV. CMB power spectra and likelihood. *ArXiv*, 1303:5075, (2013). Cited on pages 31 and 32.

- [42] Wayne Hu. Concepts in CMB anisotropy formation. *Lect.Notes Phys.*, **470**:207, (1996). Cited on pages 31 and 32.
- [43] Petter Callin. How to calculate the CMB spectrum. *ArXiv*, 0606:683, (2006). Cited on page 31.
- [44] David D. Reid, Daniel W. Kittell, Eric E. Arsznov, and Gregory B. Thompson. The Picture of our universe: A View from modern cosmology. *ArXiv*, 0209:504, (2002). Cited on page 31.
- [45] Carlos CHOVER LÓPEZ. Simulations of Structure Formation in the Universe: Hot vs Cold Dark Matter. *Master thesis*, (2010). Cited on page 33.
- [46] Volker Springel, Carlos S. Frenk, and Simon D.M. White. The large-scale structure of the Universe. *Nature*, **440**:1137, (2006). Cited on pages 33 and 34.
- [47] B. Moore, S. Ghigna, F. Governato, G. Lake, Thomas R. Quinn, et al. Dark matter substructure within galactic halos. *Astrophys.J.*, **524**:L19–L22, (1999). Cited on page 33.
- [48] C. Alcock et al. MACHO Collaboration, The MACHO project: Microlensing results from 5.7 years of LMC observations. *Astrophys.J.*, **542**:281–307, (2000). Cited on page 35.
- [49] T. Lasserre for the EROS Collaboration. Not enough stellar mass machos in the galactic halo. *Astron.Astrophys.*, **355**:L39–L42, (2000). Cited on page 35.
- [50] Scott Dodelson and Lawrence M. Widrow. Sterile-neutrinos as dark matter. *Phys.Rev.Lett.*, **72**:17–20, (1994). Cited on page 36.
- [51] Berta Beltran et al. CAST Collaboration, Search for solar axions: The CAST experiment at CERN. *PoS*, **HEP2005**:022, (2006). Cited on page 36.
- [52] Dmitry Lyapustin. The Axion Dark Matter eXperiment. *ArXiv*, 1112:1167, (2011). Cited on page 36.
- [53] E. Aprile et al. XENON100 Collaboration, First Axion Results from the XENON100 Experiment. *ArXiv*, 1404:1455, (2014). Cited on pages 37, 111, 112, 113, and 114.
- [54] Jonathan L. Feng. Dark Matter Candidates from Particle Physics and Methods of Detection. *Ann.Rev.Astron.Astrophys.*, **48**:495–545, (2010). Cited on pages 37, 38, and 212.
- [55] Marco Taoso, Gianfranco Bertone, and Antonio Masiero. Dark Matter Candidates: A Ten-Point Test. *JCAP*, **0803**:022, (2008). Cited on pages 37 and 40.
- [56] E.-K. Park. Contribution to DMSAG report. <http://science.energy.gov/hep/hepap/reports/>, July:5, (2007). Cited on pages 40 and 212.
- [57] ATLAS Collaboration. A general search for new phenomena with the ATLAS detector in pp collisions at  $\sqrt{s} = 8$  TeV. <https://cds.cern.ch/record/1666536/files/ATLAS-CONF-2014-006.pdf>, Marsh:04, (2014). Cited on page 41.

- [58] CDM Collaboration. CMS Physics Analysis Summary. <http://cds.cern.ch/record/1552402/files/SUS-12-030-pas.pdf>, *Mai*:31, (2013). Cited on page 41.
- [59] M. Ackermann et al. Fermi-LAT Collaboration, Dark Matter Constraints from Observations of 25 Milky Way Satellite Galaxies with the Fermi Large Area Telescope. *Phys.Rev.*, **D89**:042001, (2014). Cited on page 42.
- [60] M. Aguilara et al. AMS Collaboration, The Alpha Magnetic Spectrometer (AMS) on the International Space Station: Part I - results from the test flight on the space shuttle. *Phys. Rep.*, **366**:331, (2002). Cited on page 42.
- [61] M. Vecchi et al. The electromagnetic calorimeter of the AMS-02 experiment. *ArXiv*, 1210:0316, (2012). Cited on page 42.
- [62] R. Stokstad for the IceCube Collaboration. Design and performance of the IceCube electronics. <http://indico.cern.ch/event/0510/session/39/contribution/56/material/paper/0.pdf>, page 4, (2005). Cited on page 42.
- [63] J. Masbou. PhD thesis: Study of the Sensitivity of the H.E.S.S. 2 Experiment below 300 GeV and Indirect Search of Dark Matter with the H.E.S.S. Data. *Tel*, 0062:3972, (2010). Cited on page 42.
- [64] L.A. Antonelli, P. Blasi, G. Bonanno, O. Catalano, S. Covino, et al. The Next Generation of Cherenkov Telescopes. A White Paper for the Italian National Institute for Astrophysics (INAF). *ArXiv*, 0906:4114, (2009). Cited on page 42.
- [65] Oscar Adriani et al. PAMELA Collaboration, An anomalous positron abundance in cosmic rays with energies 1.5-100 GeV. *Nature*, **458**:607–609, (2009). Cited on page 42.
- [66] M. Ackermann et al. Fermi LAT Collaboration, Measurement of separate cosmic-ray electron and positron spectra with the Fermi Large Area Telescope. *Phys.Rev.Lett.*, **108**:011103, (2012). Cited on page 42.
- [67] M. Aguilar et al. AMS Collaboration, First Result from the Alpha Magnetic Spectrometer on the International Space Station: Precision Measurement of the Positron Fraction in Primary Cosmic Rays of 0.5-350 GeV. *Phys.Rev.Lett.*, **110**(14):141102, (2013). Cited on page 42.
- [68] D. Grasso et al. FERMI-LAT Collaboration, On possible interpretations of the high energy electron-positron spectrum measured by the Fermi Large Area Telescope. *Astropart.Phys.*, **32**:140–151, (2009). Cited on page 42.
- [69] M. Ackermann et al. Fermi-LAT Collaboration, Search for Gamma-ray Spectral Lines with the Fermi Large Area Telescope and Dark Matter Implications. *Phys.Rev.*, **D88**:082002, (2013). Cited on page 42.

- [70] Mark W. Goodman and Edward Witten. Detectability of Certain Dark Matter Candidates. *Phys.Rev.*, **D31**:3059, (1985). Cited on pages 43, 64, and 212.
- [71] J.D. Lewin and P.F. Smith. Review of mathematics, numerical factors, and corrections for dark matter experiments based on elastic nuclear recoil. *Astropart.Phys.*, **6**:87–112, (1996). Cited on pages 43, 44, 46, and 108.
- [72] Eric Armengaud. Gif Lectures on direct detection of Dark Matter. *ArXiv*, 1003:2380, (2010). Cited on pages 43, 44, 108, and 110.
- [73] Gianfranco Bertone, Dan Hooper, and Joseph Silk. Particle dark matter: Evidence, candidates and constraints. *Phys.Rept.*, **405**:279–390, (2005). Cited on page 43.
- [74] E. Aprile et al. XENON100 Collaboration, Dark Matter Results from 225 Live Days of XENON100 Data. *Phys.Rev.Lett.*, **109**:181301, (2012). Cited on pages 44, 45, 46, 80, 100, 104, 107, 109, 212, 214, and 215.
- [75] Martin C. Smith, G.R. Ruchti, A. Helmi, R.F.G. Wyse, J.P. Fulbright, et al. The RAVE Survey: Constraining the Local Galactic Escape Speed. *Mon. Not. Roy. Astron. Soc.*, **379**:755–772, (2007). Cited on page 44.
- [76] Georges Aad et al. ATLAS Collaboration, Search for squarks and gluinos using final states with jets and missing transverse momentum with the ATLAS detector in  $\sqrt{s} = 7$  TeV proton-proton collisions. *Phys.Lett.*, **B710**:67–85, (2012). Cited on page 45.
- [77] S. Ahlen, N. Afshordi, J.B.R. Battat, J. Billard, N. Bozorgnia, et al. The case for a directional dark matter detector and the status of current experimental efforts. *Int.J.Mod.Phys.*, **A25**:1–51, (2010). Cited on pages 46 and 47.
- [78] E. Aprile et al. XENON100 Collaboration, Limits on spin-dependent WIMP-nucleon cross sections from 225 live days of XENON100 data. *Phys.Rev.Lett.*, **111**:021301, (2013). Cited on pages 47, 110, and 111.
- [79] E. Behnke et al. COUPP Collaboration, First Dark Matter Search Results from a 4-kg CF<sub>3</sub>I Bubble Chamber Operated in a Deep Underground Site. *Phys.Rev.*, **D86**:052001, (2012). Cited on page 47.
- [80] S. Archambault et al. PICASSO Collaboration, Constraints on Low-Mass WIMP Interactions on <sup>19</sup>F from PICASSO. *Phys.Lett.*, **B711**:153–161, (2012). Cited on page 47.
- [81] M. Felizardo, T.A. Girard, T. Morlat, A.C. Fernandes, A.R. Ramos, et al. Final Analysis and Results of the Phase II SIMPLE Dark Matter Search. *Phys.Rev.Lett.*, **108**:201302, (2012). Cited on page 47.
- [82] R. Bernabei et al. Searching for WIMPs by the annual modulation signature. *Phys.Lett.B*, **424**:195, (1998). Cited on page 48.

- [83] R. Bernabei et al. DAMA Collaboration, First results from DAMA/LIBRA and the combined results with DAMA/NaI. *Eur.Phys.J.*, **C56**:333–355, (2008). Cited on pages 48, 87, 109, and 220.
- [84] C.E. Aalseth et al. CoGeNT Collaboration, Search for An Annual Modulation in Three Years of CoGeNT Dark Matter Detector Data. *ArXiv*, 1401:3295, (2014). Cited on pages 48 and 109.
- [85] R. Agnese et al. CDMS Collaboration, Silicon Detector Dark Matter Results from the Final Exposure of CDMS II. *Phys.Rev.Lett.*, **111**:251301, (2013). Cited on page 49.
- [86] E. Armengaud et al. EDELWEISS Collaboration, Final results of the EDELWEISS-II WIMP search using a 4-kg array of cryogenic germanium detectors with interleaved electrodes. *Phys.Lett.*, **B702**:329–335, (2011). Cited on page 49.
- [87] A. Verdier. PhD thesis: Cryogenic scintillators for rare events detection in the EDELWEISS and EURECA experiments. *Tel*, 0055:6620, (2011). Cited on page 49.
- [88] Q. Arnaud. EDELWEISS Dark Matter Search Study of trapping effects in FID detectors. <https://indico.in2p3.fr/getFile.py/access?contribId=39&sessionId=18&resId=0&materialId=slides&confId=8599>. Cited on page 49.
- [89] Z. Ahmed et al. CDMS-II Collaboration, Dark Matter Search Results from the CDMS II Experiment. *Science*, **327**:1619–1621, (2010). Cited on page 49.
- [90] Z. Ahmed et al. CDMS-II Collaboration, Results from a Low-Energy Analysis of the CDMS II Germanium Data. *Phys.Rev.Lett.*, **106**:131302, (2011). Cited on page 49.
- [91] S. Cebrian, N. Coron, G. Dambier, E. Garcia, D. Gonzalez, et al. First results of the ROSE-BUD dark matter experiment. *Astropart.Phys.*, **15**:79–85, (2001). Cited on page 50.
- [92] G. Angloher, M. Bauer, I. Bavykina, A. Bento, C. Bucci, et al. Results from 730 kg days of the CRESST-II Dark Matter Search. *Eur.Phys.J.*, **C72**:1971, (2012). Cited on pages 50 and 109.
- [93] G. Angloher, A. Bento, C. Bucci, et al. Results on low mass WIMPs using an upgraded CRESST-II detector. *ArXiv*, 1407:3146, (2014). Cited on page 50.
- [94] P. Benetti, R. Acciarri, F. Adamo, B. Baibussinov, M. Baldo-Ceolin, et al. First results from a Dark Matter search with liquid Argon at 87 K in the Gran Sasso Underground Laboratory. *Astropart.Phys.*, **28**:495–507, (2008). Cited on page 51.
- [95] T. Alexander et al. DarkSide Collaboration, Light yield in DarkSide-10: A prototype two-phase argon TPC for dark matter searches. *Astropart.Phys.*, **49**:44–51, (2013). Cited on pages 52 and 116.

- [96] A. Badertscher, F. Bay, N. Bourgeois, C. Cantini, A. Curioni, et al. ArDM: first results from underground commissioning. *JINST*, **8**:C09005, (2013). Cited on page 52.
- [97] P. Gorel. Search for Dark Matter with Liquid Argon and Pulse Shape Discrimination: Results from DEAP-1 and Status of DEAP-3600. *ArXiv*, 1406:0462. Cited on page 52.
- [98] R. Hennings-Yeomans. Clean Collaboration, Direct detection of dark matter with Mini-CLEAN. *J.Phys.Conf.Ser.*, **315**:012010, (2011). Cited on page 52.
- [99] K. Abe et al. XMASS-I Collaboration, Light WIMP search in XMASS. *Phys.Lett.*, **B719**:78–82, (2013). Cited on pages 52 and 53.
- [100] H. Uchida et al. XMASS-I Collaboration, Search for inelastic WIMP nucleus scattering on  $^{129}\text{Xe}$  in data from the XMASS-I experiment. *ArXiv*, 1401:4737, (2014). Cited on page 52.
- [101] David Tucker-Smith and Neal Weiner. Inelastic dark matter. *Phys.Rev.*, **D64**:043502, (2001). Cited on page 53.
- [102] David Tucker-Smith and Neal Weiner. The Status of inelastic dark matter. *Phys.Rev.*, **D72**:063509, (2005). Cited on page 53.
- [103] J. Angle et al. XENON10 Collaboration, First Results from the XENON10 Dark Matter Experiment at the Gran Sasso National Laboratory. *Phys.Rev.Lett.*, **100**:021303, (2008). Cited on page 56.
- [104] J. Angle et al. XENON10 Collaboration, A search for light dark matter in XENON10 data. *Phys.Rev.Lett.*, **107**:051301, (2011). Cited on pages 56, 108, and 202.
- [105] D. S. Akerib et al. LUX Collaboration, First results from the LUX dark matter experiment at the Sanford Underground Research Facility. *Phys.Rev.Lett.*, **112**:091303, (2014). Cited on pages 56, 109, 212, and 216.
- [106] M. Xiao et al. PandaX-I Collaboration, First dark matter search results from the PandaX-I experiment. *ArXiv*, 1408:5114, (2014). Cited on pages 56 and 109.
- [107] D. Y. Akimov et al. Wimp-nucleon cross-section results from the second science run of zeplin-iii. *Physics Letters B*, **709**, (2012). Cited on pages 56 and 203.
- [108] A. Manzur, A. Curioni, L. Kastens, D.N. McKinsey, K. Ni, et al. Scintillation efficiency and ionization yield of liquid xenon for mono-energetic nuclear recoils down to 4 keV. *Phys.Rev.*, **C81**:025808, (2010). Cited on page 57.
- [109] J.B. Albert et al. EXO-200 Collaboration, Search for Majorana neutrinos with the first two years of EXO-200 data. *ArXiv*, 1402:6956, (2014). Cited on page 56.
- [110] T. Oger, W-T. Chen, J-P. Cussonneau, J. Donnard, S. Duval, et al. A Liquid xenon TPC for a medical imaging Compton telescope. *Nucl.Instrum.Meth.*, **A695**:125–128, (2012). Cited on page 57.

- [111] T. Oger. PhD thesis: Experimental development of a liquid xenon compton telescope for functional medical imaging. *Tel*, 0067:8767, (2012). Cited on pages 58, 61, and 77.
- [112] National Institute of Standards and Technology. XCOM. <http://physics.nist.gov/PhysRefData/Xcom/html/xcom1.html>. Cited on pages 58 and 61.
- [113] National Institute of Standards and Technology. XCOM. <http://webbook.nist.gov/chemistry/fluid/>. Cited on pages 60 and 104.
- [114] E. Aprile and T. Doke. Liquid Xenon Detectors for Particle Physics and Astrophysics. *Rev.Mod.Phys.*, **82**:2053–2097, (2010). Cited on pages 60, 69, 70, 77, 179, 194, 195, 212, and 219.
- [115] T. Takahashi et al. Average energy expended per ion pair in liquid xenon. *Phys.Rev.*, **A12**:1771–1775, (1975). Cited on pages 60 and 187.
- [116] Istituto Nazionale di Fisica Nucleare. INFN. [http://www.pd.infn.it/~conti/images/LXe/xe\\_properties.txt](http://www.pd.infn.it/~conti/images/LXe/xe_properties.txt). Cited on pages 60 and 176.
- [117] webelements. The periodic table on the web. <http://www.webelements.com/xenon/isotopes.html>. Cited on page 61.
- [118] C. Grignon. PhD thesis: Development of a Liquid xenon Compton telescope dedicated to functional medical imaging. *Tel*, 0028:8738, (2007). Cited on pages 61 and 77.
- [119] J. Thomas, D.A. Imel, and S Biller. Statistics of charge collection in liquid argon and liquid xenon. *Phys. Rev.*, **A38**:5793–5801, (1988). Cited on page 63.
- [120] W.R. Leo. Techniques for Nuclear and Particle Physics Experiments: A How-To Approach. *Springer-Verlag*, Second Ed.:58, (1994). Cited on page 64.
- [121] E. Aprile for the XENON100 Collaboration. New Results from the XENON100 Experiment. *Talk at DarkAttack*, Ascona:18<sup>th</sup> of July, (2012). Cited on page 64.
- [122] E. Aprile et al. XENON100 Collaboration, The XENON100 Dark Matter Experiment. *Astropart.Phys.*, **35**:573–590, (2012). Cited on pages 64, 73, 74, 77, 78, 79, 80, 81, 82, 90, 91, 92, 94, 95, 96, 212, and 213.
- [123] J. Lindhard, M. Scharff, and H.E Schiott. Range concepts and heavy ion ranges. *K. Dan. Vidensk. Selsk. Mat. Fys. Medd.*, **33**:nr. 14, (1963). Cited on pages 64 and 65.
- [124] J. Thomas and D.A. Imel. Recombination of electron-ion pairs in liquid argon and liquid xenon. *Phys. Rev.*, **A36**:614–616, (1987). Cited on pages 67, 68, 198, and 212.
- [125] G. Jaffé. Zur Theorie der Ionisation in Kolonnen. *Ann. Phys.*, **42**:303, (1913). Cited on page 67.
- [126] L. Onsager. Initial recombination of ions. *Phys. Rev.*, **54**:554–557, (1938). Cited on page 67.

- [127] Tadayoshi Doke. Scintillation of liquid xenon and its application to nuclear radiation detectors. *Proceeding IEEE transactions on dielectrics and electrical insulation*, **13**:640–649, (2006). Cited on page 69.
- [128] E. Aprile et al. XENON100 Collaboration, Proportional Light in a Dual-Phase Xenon Chamber. *IEEE TRANSACTION ON NUCLEAR SCIENCE*, **51**:No. 5, October, (2004). Cited on pages 70, 75, 191, and 192.
- [129] W.H. Lippincott, K.J. Coakley, D. Gastler, A. Hime, E. Kearns, et al. Scintillation time dependence and pulse shape discrimination in liquid argon. *Phys.Rev.*, **C78**:035801, (2008). Cited on page 70.
- [130] R.L. Platzman. Total ionization in gases by high-energy particles: An appraisal of our understanding. *The Int. Jour. of Appl. Rad. and Isot.*, **10**:116–127, (1961). Cited on page 71.
- [131] M. Szydagis, N. Barry, K. Kazkaz, J. Mock, D. Stolp, et al. NEST: A Comprehensive Model for Scintillation Yield in Liquid Xenon. *JINST*, **6**:P10002, (2011). Cited on pages 71, 72, and 190.
- [132] U. Fano. Ionization Yield of Radiations. 2. The Fluctuations of the Number of Ions. *Phys.Rev.*, **72**:26–29, (1947). Cited on page 71.
- [133] G. Plante. PhD thesis: The XENON100 Dark Matter Experiment: Design, Construction, Calibration and 2010 Search Results with Improved Measurement of the Scintillation Response of Liquid Xenon to Low-Energy Nuclear Recoils. <http://academiccommons.columbia.edu/catalog/ac%3A143844>, (2012). Cited on pages 73, 83, 84, and 85.
- [134] M. Yamashita, T. Doke, K. Kawasaki, J. Kikuchi, and S. Suzuki. Scintillation response of liquid xe surrounded by ptfе reflector for gamma rays. *Nucl.Intr.Meth.A*, **535**:692, (2004). Cited on page 76.
- [135] M. Ambrosio et al. Vertical muon intensity measured with MACRO at the Gran Sasso Laboratory. *Phys.Rev.*, **D52**:3793–3802, (1995). Cited on page 78.
- [136] E. Aprile, M. Alfonsi, K. Arisaka, F. Arneodo, C. Balan, et al. XENON100 Collaboration, The distributed Slow Control System of the XENON100 Experiment. *JINST*, **7**:T12001, (2012). Cited on page 82.
- [137] Luca Scotto Lavina for the XENON 100 Collaboration. Latest results from XENON100 data. *ArXiv*, 1305:0224, (2013). Cited on page 83.
- [138] G. Bakale, U. Sowada, and W. F. Schmidt. Effect of an Electric Field on Electron Attachment to SF<sub>6</sub>, N<sub>2</sub>O, and O<sub>2</sub> in Liquid Argon and Xenon. *J. Phys. Chem.*, **80**:2556–2559, (1976). Cited on page 82.
- [139] E. Aprile et al. XENON100 Collaboration, Dark Matter Results from 100 Live Days of XENON100 Data. *Phys.Rev.Lett.*, **107**:131302, (2011). Cited on pages 83, 97, 98, and 104.

- [140] E. Aprile et al. XENON100 Collaboration, Analysis of the XENON100 Dark Matter Search Data. *Astropart.Phys.*, **54**:11–24, (2014). Cited on page 83.
- [141] S. Lindemann. PhD thesis: Intrinsic  $^{85}\text{Kr}$  and  $^{222}\text{Rn}$  Backgrounds in the XENON Dark Matter Search. <http://archiv.ub.uni-heidelberg.de/volltextserver/15725/1/d1.pdf>, (2013). Cited on pages 83, 93, and 94.
- [142] B. Hamermesh and C. Kimball. The Photodisintegration Cross Section of Beryllium at 2.185 Mev. *Phys.Rev.*, **90**:1063, (1953). Cited on page 88.
- [143] A. Manalaysay, T.M. Undagoitia, A. Askin, L. Baudis, A. Behrens, et al. Spatially uniform calibration of a liquid xenon detector at low energies using  $^{83}\text{m-Kr}$ . *Rev.Sci.Instrum.*, **81**:073303, (2010). Cited on page 92.
- [144] G. Plante, E. Aprile, R. Budnik, B. Choi, K.L. Giboni, et al. New Measurement of the Scintillation Efficiency of Low-Energy Nuclear Recoils in Liquid Xenon. *Phys.Rev.*, **C84**:045805, (2011). Cited on page 97.
- [145] E. Aprile, C.E. Dahl, L. DeViveiros, R. Gaitskell, K.L. Giboni, et al. Simultaneous measurement of ionization and scintillation from nuclear recoils in liquid xenon as target for a dark matter experiment. *Phys.Rev.Lett.*, **97**:081302, (2006). Cited on page 97.
- [146] E. Aprile et al. XENON100 Collaboration, First Dark Matter Results from the XENON100 Experiment. *Phys.Rev.Lett.*, **105**:131302, (2010). Cited on page 99.
- [147] E. Aprile, K. Arisaka, F. Arneodo, A. Askin, L. Baudis, et al. XENON100 Collaboration, Material screening and selection for XENON100. *Astropart.Phys.*, **35**:43–49, (2011). Cited on page 99.
- [148] M. Weber. PhD thesis: Gentle Neutron Signals and Noble Background in the XENON100 Dark Matter Search Experiment. <http://www.ub.uni-heidelberg.de/archiv/15155>, (2013). Cited on pages 100 and 101.
- [149] E. Aprile et al. XENON100 Collaboration, Likelihood Approach to the First Dark Matter Results from XENON100. *Phys.Rev.*, **D84**:052003, (2011). Cited on pages 105, 106, and 214.
- [150] C.E. Aalseth et al. CoGeNT Collaboration, Results from a Search for Light-Mass Dark Matter with a P-type Point Contact Germanium Detector. *PRL*, **106**:131301, (2011). Cited on page 109.
- [151] O. Buchmueller, R. Cavanaugh, A. De Roeck, M.J. Dolan, J.R. Ellis, et al. Higgs and Supersymmetry. *Eur.Phys.J.*, **C72**:2020, (2012). Cited on page 109.
- [152] D.R. Tovey, R.J. Gaitskell, P. Gondolo, Yorck Alexander Ramachers, and L. Roszkowski. A New model independent method for extracting spin dependent (cross-section) limits from dark matter searches. *Phys.Lett.*, **B488**:17–26, (2000). Cited on page 110.

- [153] J. Menendez, D. Gazit, and A. Schwenk. Spin-dependent WIMP scattering off nuclei. *Phys.Rev.*, **D86**:103511, (2012). Cited on page 111.
- [154] E. Armengaud, Q. Arnaud, C. Augier, A. Benoit, A. Benoit, et al. Axion searches with the EDELWEISS-II experiment. *JCAP*, **1311**:067, (2013). Cited on pages 113 and 114.
- [155] Wan-Ting Chen, D. Chbib, J.P. Cussonneau, J. Donnard, S. Duval, et al. Improvement of xenon purification system using a combination of a pulse tube refrigerator and a coaxial heat exchanger. *ArXiv*, 1205:3874, (2012). Cited on page 115.
- [156] Laura Baudis. DARWIN: dark matter WIMP search with noble liquids. *PoS*, IDM2010:122, (2011). Cited on page 116.
- [157] E. Aprile et al. XENON100 Collaboration, Observation and applications of single-electron charge signals in the XENON100 experiment. *J.Phys.*, **G41**:035201, (2014). Cited on pages 118, 120, 122, 123, 126, 127, 166, 168, 169, 178, 180, 191, 192, 212, 216, 218, and 219.
- [158] J. Lamblin. HDR thesis: XENON100 et MIMAC, des détecteurs à la recherche de matière noire. *Tel*, 0084:5580, (2013). Cited on pages 118 and 192.
- [159] M. J. Travers et al. Reinvestigation of the electron affinities of  $O_2$  and NO. *Chemical Physics Letters*, **164**:449–455, (1989). Cited on page 119.
- [160] B. Edwards, H.M. Araujo, V. Chepel, D. Cline, T. Durkin, et al. Measurement of single electron emission in two-phase xenon. *Astropart.Phys.*, **30**:54–57, (2008). Cited on page 120.
- [161] E. Santos et al. ZEPLIN-III Collaboration, Single electron emission in two-phase xenon with application to the detection of coherent neutrino-nucleus scattering. *JHEP*, **1112**:115, (2011). Cited on pages 120, 123, and 202.
- [162] A. Bondar, A. Buzulutskov, A. Grebenuk, D. Pavlyuchenko, R. Snopkov, et al. A Two-phase argon avalanche detector operated in a single electron counting mode. *Nucl.Instrum.Meth.*, **A574**:493–499, (2007). Cited on pages 120 and 121.
- [163] K. Micheneau. Master thesis: Study of multiple events through single electron signals in the XENON100 experiment. *Subatech laboratory*, (2014). Cited on pages 128, 129, 130, 142, and 197.
- [164] C.M.B. Monteiro, L.M.P. Fernandes, J.A.M. Lopes, L.C.C. Coelho, J.F.C.A. Veloso, et al. Secondary Scintillation Yield in Pure Xenon. *JINST*, **2**:P05001, (2007). Cited on pages 179, 180, and 219.
- [165] F P Santos, T H V T Dias, A D Stauffer, and C A N Conde. Three-dimensional monte carlo calculation of the vuv electroluminescence and other electron transport parameters in xenon. *Journal of Physics D: Applied Physics*, **27**:42, (1994). Cited on pages 180 and 219.

- [166] A.C. Fonseca, R. Meleiro, V. Chepel, A. Pereira, V. Solovov, and M.I. Lopes. Study of secondary scintillation in xenon vapour. *2004 IEEE Nuclear Science Symposium Conference Record*, **1**, (2005). Cited on pages 180 and 219.
- [167] E. Aprile, K.L. Giboni, P. Majewski, K. Ni, and M. Yamashita. Observation of Anti-correlation between Scintillation and Ionization for MeV Gamma-Rays in Liquid Xenon. *Phys.Rev.*, **B76**:014115, (2007). Cited on pages 187, 188, 190, and 219.
- [168] A.I. Bolozdynya. Two-phase emission detectors and their applications. *Nucl.Instrum.Meth.*, **A422**:314–320, (1999). Cited on pages 191 and 192.
- [169] A. Kish. PhD thesis: Dark Matter Search with the XENON100 Experiment. [http://www.physik.uzh.ch/groups/groupbaudis/darkmatter/theses/xenon/Kish\\_THESISelectronic.pdf](http://www.physik.uzh.ch/groups/groupbaudis/darkmatter/theses/xenon/Kish_THESISelectronic.pdf), (2011). Cited on page 193.
- [170] Matthew Szydakis, Adalyn Fyhrie, Daniel Thorngren, and Mani Tripathi. Enhancement of NEST Capabilities for Simulating Low-Energy Recoils in Liquid Xenon. *JINST*, **8**:C10003, (2013). Cited on page 202.
- [171] Daniel Z. Freedman. Coherent effects of a weak neutral current. *Phys.Rev.*, **D9**:1389, (1974). Cited on page 202.
- [172] A. Drukier and Leo Stodolsky. Principles and Applications of a Neutral Current Detector for Neutrino Physics and Astronomy. *Phys.Rev.*, **D30**:2295, (1984). Cited on page 203.



# Remerciements / Acknowledgments

Avant tout, je voudrais remercier Luca, sans qui tout ceci n'aurait pu être écrit. Merci à toi pour ces trois années et demi passées à travailler ensemble, en master puis durant la thèse. Merci pour ta disponibilité quasi-permanente même lorsque nous étions plusieurs personnes à nous succéder dans ton bureau pour discuter, ou pour quérir tes précieux conseils. Tes explications toujours très pédagogiques m'ont permis au cours de ma première année de rapidement comprendre les secrets du détecteur et de ROOT.

Je remercie également Thierry, pour avoir accepté d'être mon directeur de thèse, et pour ton aide des plus précieuses lors de la phase d'écriture de ce manuscrit. Merci aussi à Dominique, pour m'avoir accueilli dans le groupe XENON lors de mon stage de master, puis pour avoir toujours gardé un œil sur l'avancement et l'orientation de mes travaux malgré la multiplication des autres sujets auxquels tu prenais part. Tes conseils, notamment aux cours de ces derniers mois, me furent d'une grande aide.

Je voudrais également remercier les autres membres du Jury d'avoir accepté d'analyser mes travaux de thèse. Un grand merci notamment à Daniel, dont les précieuses suggestions faites au cours de la lecture de ce manuscrit ont permis de l'améliorer et l'enrichir d'avantage. Merci à Sylvie et à Stavros pour leurs précieux conseils et remarques lors de la soutenance.

Cette thèse ayant eu pour cadre le groupe de recherche Xénon, je souhaite remercier l'ensemble de ses membres, actuels ou anciens, que j'ai pu côtoyer, en commençant par Jacob, qui fut le premier à m'encadrer pour cette étude du détecteur XENON100 au cours de mon stage de Master, avec qui j'ai ensuite collaboré durant mes premières années de Doctorat, et qui, avec Dominique, Luca et Thierry, a grandement contribué à la réalisation de cette thèse. Je remercie également Jean-Pierre et Julien pour leur précieux conseils, ainsi qu'Éric, Nicolas, Olivier et Wan-Ting. Merci aux anciens thésards, Abdul, Jérôme, Samuel et surtout Tugdual pour m'avoir transmis l'histoire du groupe et du laboratoire. Merci aussi à Cyril, même s'il est vrai que tu avais déjà quitté le groupe depuis quelques années lorsque je suis arrivé, l'aide que tu m'as apporté en tant que membre de la collaboration XENON m'a été des plus profitables. Merci aux autres thésards du groupe, Aurélien, félicitation Docteur ! Lucia, la prochaine soutenance du groupe c'est toi. Courage ! La moitié de la thèse est faite. Loick, Kevin, vous êtes la relève, comme je peux me permettre de dire en tant qu'ancien. L'aventure commence, bon vent à vous !

I would like also to thank all the member of the XENON Collaboration, starting with Elena, without who the XENON program would not be as such as it is now, and then without who I

would not have the occasion to work on such a nice detector. I would like also to thank the analysis coordinators, Alfredo, Antonio, and Marc S. whose advices for my analyses were very useful. I also thank the two leaders of the simulation working group, Alex K. and more especially Marco S., who helped me a lot during my simulation works. I would like also to thank Andrea T., Bruno M., Marc W., Matteo, and Sebastian, with who I spent some time in shift. Those shifts were also the occasion for me to learn a lot about the detector, and for this I have again to thank a lot Alfredo, who explained me things with a very nice pedagogy. Now, I have left the Collaboration, but for me these three years were a great moment, and for this I would like to thank all of you. I will still keep an eye on the future results from XENON1T, and I wish you all the best for this new detector. Good luck to the students, especially Andrea T., Boris, Ludwig, Fabio Valerio, Nadav, Ran and Shayne that I had the occasion to meet.

I would like to thank the organizers of the ISAPP school hosted at Stockholm in 2013, Lars Bergstrom and Joakim Edsjö, but also the lecturers, namely Torsten Bringmann, Jules Gascon, Subir Sarkar and Mark Vogelsberger, whose presentations helped me a lot for the improvement of the first chapter of this thesis.

Je souhaiterai également remercier les autres membres du laboratoire, et plus particulièrement Noël, qui m'a permis dès ma première année de thèse d'enseigner aux élèves ingénieurs de l'École des Mines. Je remercie aussi Amanda qui prit part avec Jacob à mon comité de suivi de thèse, l'incontournable Arnaud G. et sa bonne humeur, Baptiste L. et Baptiste M., Benoît, Élisabeth, Guy, Lilian, Pol-Bernard, Richard, Vincent Ma. et Vincent Me, ainsi que tous les autres membres. Je remercie également toutes les personnes du service administratif de Subatech, et plus particulièrement Sandrine, Séverine, Stéphanie J. et Tanja pour leur gentillesse et leurs efforts pour que tous les étudiants puissent travailler dans les meilleures conditions.

Je remercie aussi tous les thésards et anciens thésards que j'ai pu côtoyer au laboratoire et avec qui j'ai passé de très bons moments : Alix, Antoine L. et sa rosalie, Antony, Aurélien, Charlotte, Diana, Diego, Florian, François (Benjamin G.), Javier, Jean-Baptiste, Guillaume et sa lutte incessante contre le grand fléau qu'est la fréquente traversée d'armoire sur le chemin lorsqu'une personne (disons Guillaume) passe, ainsi que pour ta dextérité avec la prise électrique lors des JRJC. Merci également à Lucia, Martin, Roland et Zak. Bon courage aux nouveaux arrivants, Dounia, Fanny, Grégoire, Kevin, Loick, et ceux dont je n'ai pas eu le temps de vraiment faire leur connaissance.

Benjamin... Tu ne croyais tout de même pas que j'allais t'oublier ! C'est une tradition maintenant, tu as le droit à ton petit paragraphe dédié ! Merci à toi pour ton amitié, ta bonne humeur, ta musique un peu décalée, le lien vers la vidéo ou tu fais une pub de shampoing (oups, en ai-je trop dit ?). La prochaine soutenance c'est la tienne, mec ! Et on sera tous là, car on connaît tes talents de professeur qui nous avaient épaté en Master avec ta présentation sur les Axions et l'effet Primakoff.

Merci aussi à Antoine C., également connu sous le nom de "Qui" l'Américain. Félicitation pour ta thèse et bon vent à toi aux Amériques.

Merci à Antoine Q. que j'ai connu lors de mon arrivée à Nantes. Merci pour ton amitié indéfectible depuis cette époque, et pour ces grandes discussions enflammées en bord de ligne d'eau à la piscine, à l'appart ou au restaurant. Ça va bientôt être ton tour de soutenir ta thèse, et

d'ici là, courage ! C'est la dernière ligne droite.

Je souhaiterais également remercier ma famille et ma belle-famille, et plus particulièrement mes parents qui m'ont toujours soutenu durant mes études, et sans l'aide de qui je n'aurais pas pu faire cette aventure débutée il y a maintenant quelques années lors de mon installation à Nantes.

Merci également à Zéphir, ce chat physicien incompris, qui nous accompagne, Jeni et moi, depuis nos années de Master, et qui teste régulièrement la flottaison des coton-tiges. A quand une publication ?

Enfin, merci à toi, Jeni. Merci pour ton amour, ton amitié, ton sourire, ta joie, ta compréhension, ta passion. Merci pour tout, pour tous ces bons moments, passés et à venir.



## Abstract

From the observation of the Universe, it has been demonstrated that the mass associated to visible matter represents only few percent of its energetic budget, while the remaining part is composed by dark energy, responsible to the cosmological expansion, and by some hidden matter, the dark matter. The likeliest particles family used to describe this dark matter is called WIMP (Weakly Interacting Massive Particles). That kind of particles could be directly detected by measuring nuclear recoil during an elastic scattering inside a scintillating material. For this, the XENON Collaboration has developed a detector consisting in a time projection chamber (TPC) using xenon dual phase (liquid and gas) detector, and placed underground. The different ionization density of nuclear recoils induced by WIMPs, and electronic recoils induced by  $\beta$  particles or  $\gamma$  rays background source, leads to different ratio between both signals, in the liquid and in the gas phase, and is used to discriminate WIMPs from background. A good knowledge of the ionization signal is strongly required for such a detector. In this context, the XENON100 response to single electron charge signals is investigated. They correspond to very tiny signals emitted in the gas phase by one or few electrons extracted in time coincidence. Thanks to this analysis, an innovative method to establish the extraction yield of electrons from the liquid to the gas phase has been drawn, allowing to explore a key information to reject electronic recoils from nuclear ones.

**Key words :** Dark matter, direct detection, WIMP, low background, dual phase TPC, liquid xenon, XENON100, single electron

## Résumé

A partir de l'observation de l'Univers, il a été démontré que la masse associée à la matière visible ne représente que quelques pourcents de son budget énergétique total. La partie restante est composée de l'énergie noire, responsable de l'expansion cosmologique, et d'une matière invisible, la matière noire. La famille de particules la plus probable pour décrire cette matière noire est appelée WIMP. Ces particules peuvent être directement détectées par la mesure du recul nucléaire induit lors d'une diffusion élastique au sein d'un matériau scintillant. Pour cela, la Collaboration XENON a développé un détecteur placé sous terre, consistant en une chambre à projection temporelle (TPC) et utilisant du xénon sous deux phases: liquide et gazeuse. La différence de taux d'ionisation des atomes rencontrés pour un recul nucléaire induit par un WIMP, par rapport à un recul électronique induit par des sources de bruit de fond  $\beta$  ou  $\gamma$ , conduit à des rapports différents entre les signaux émis en phase liquide et gazeuse. Cette différence est utilisée pour isoler les WIMPs du bruit de fond. Une bonne connaissance du signal d'ionisation est donc requise pour un tel détecteur. Dans ce contexte, la réponse du détecteur XENON100 aux signaux de charge d'électrons uniques est étudiée. Ils correspondent à des faibles signaux émis en phase gazeuse par un ou plusieurs électrons extraits en coïncidence temporelle. Grâce à cette analyse, une méthode innovante pour calculer le rendement d'extraction des électrons du liquide vers le gaz a été établie.

**Mots clés :** Matière noire, détection directe, WIMP, bas bruit de fond, TPC à deux phases, xénon liquide, XENON100, électron unique